

Synthesis and characterisation of novel isoform-selective  
histone deacetylase inhibitors (HDACi) and HDACi-based  
multi-target ligands

**Dissertation**

zur

Erlangung des Doktorgrades (Dr. rer. nat.)

der

Mathematisch-Naturwissenschaftlichen Fakultät

der

Rheinischen Friedrich-Wilhelms-Universität Bonn

vorgelegt von

**Nina Jacqueline Reßing**

aus

Gelsenkirchen

Bonn, Juni 2021

Angefertigt mit Genehmigung der Mathematisch-Naturwissenschaftlichen Fakultät der  
Rheinischen Friedrich-Wilhelms-Universität Bonn

1. Gutachter: Prof. Dr. Finn K. Hansen
2. Gutachter: PD Dr. Martin Schlesinger

Tag der Promotion: 26. Oktober 2021

Erscheinungsjahr: 2022

<b>List of publications</b>	<b>V</b>
<b>List of abbreviations</b>	<b>VII</b>
<b>Summary</b>	<b>XII</b>
<b>Chapter 1: Theoretical background</b>	<b>1</b>
<b>1.1 Epigenetics</b>	<b>1</b>
1.1.1 The chromatin structure	1
1.1.2 The histone code	3
<b>1.2 Histone deacetylases (HDACs)</b>	<b>4</b>
1.2.1 Classes and isoforms	4
1.2.2 Substrates	7
1.2.3 Therapeutic potential	10
1.2.3.1 Approaches in cancer therapy	10
1.2.3.2 Benefits of isoform-selective HDAC inhibitors	12
1.2.3.3 Opportunities in non-oncological conditions	13
1.2.4 Overview of approved drugs and clinical candidates	17
1.2.5 The structure and catalytic mechanism of HDAC6	22
<b>1.3 The 26S proteasome</b>	<b>26</b>
1.3.1 Protein expression and cellular protein disposal systems	26
1.3.2 Structure and catalytic mechanism	27
1.3.2 Targeting of the 20S CP in cancer therapy	29
<b>1.4 References</b>	<b>35</b>
<b>Chapter 2: Synthesis, binding mode and biological evaluation of selective HDAC6 inhibitors with bifurcated capping groups</b>	<b>52</b>
<b>2.1 Introduction</b>	<b>52</b>
2.1.1 LADME: Bioavailability of drugs	52
2.1.2 Bioisosterism	54
2.1.3 Project outline	55
<b>2.2 Results and discussion</b>	<b>58</b>
2.2.1 Synthesis of tetrazole-capped HDAC inhibitors	58

Table of contents

2.2.2 Variable temperature NMR experiments	61
2.2.3 HDAC inhibition	62
2.2.4 Co-crystal structure of II-6I and zebrafish HDAC6 CD2	65
2.2.5 Biological evaluation of II-6I	66
<b>2.3 Conclusions</b>	<b>69</b>
<b>2.4 Experimental section</b>	<b>70</b>
2.4.1 General information	70
2.4.2 Experimental procedures	71
<b>2.5 References</b>	<b>85</b>
<b>Chapter 3: Design, multicomponent synthesis and structure-activity relationships of fluorinated HDAC inhibitors</b>	<b>89</b>
<b>3.1 Introduction</b>	<b>89</b>
3.1.1 Effects and benefits of drug fluorination	89
3.1.2 Project outline	90
<b>3.2 Results and discussion</b>	<b>93</b>
3.2.1 Synthesis of fluorinated HDACi	93
3.2.2 HDAC inhibition	94
3.2.3 Biological evaluation	99
<b>3.3 Conclusions</b>	<b>102</b>
<b>3.4 Experimental section</b>	<b>103</b>
3.4.1 General information	103
3.4.2 Experimental procedures	104
<b>3.5 References</b>	<b>115</b>
<b>Chapter 4: Synthesis and biological evaluation of dual HDAC/20S CP inhibitors</b>	<b>117</b>
<b>4.1 Introduction</b>	<b>117</b>
4.1.1 Polypharmacy	117
4.1.2 Polypharmacology	118
4.1.3 Multi-target drugs	119
4.1.4 Multi-targeted HDAC inhibitors	122



## Table of contents

4.1.5 HDAC6 and the 20S CP as synergistic drug targets	128
4.1.6 Project outline	131
<b>4.2 Results and discussion</b>	<b>134</b>
4.2.1 1st Generation: Design and synthesis	134
4.2.2 1st Generation: Enzyme inhibition	139
4.2.3 1st Generation: Antiproliferative effects	141
4.2.4 1st Generation: Discussion	142
4.2.5 2nd Generation: Design and synthesis	143
4.2.6 2nd Generation: Enzyme inhibition	146
4.2.7 2nd Generation: Antiproliferative effects	149
4.2.8 2nd Generation: Discussion	150
<b>4.3 Conclusions</b>	<b>153</b>
<b>4.4 Experimental section</b>	<b>154</b>
4.4.1 General information	154
4.4.2 Experimental procedures	155
<b>4.5 References</b>	<b>180</b>
<b>Chapter 5: Investigation of (difluoromethyl)-1,3,4-oxadiazole as a novel HDAC6-selective zinc-binding group</b>	<b>189</b>
<b>5.1 Introduction</b>	<b>189</b>
5.1.1 Drawbacks of hydroxamates as HDAC inhibitors	189
5.1.2 Potential new zinc-binding groups	191
5.1.3 Prodrug concepts for HDAC inhibitors	192
5.1.4 Project outline	195
<b>5.2 Results and Discussion</b>	<b>197</b>
5.2.1 Synthesis of (difluoromethyl)-1,3,4-oxadiazole fragments	197
5.2.2 HDAC inhibition of (difluoromethyl)-1,3,4-oxadiazole fragments	198
5.2.3 Synthesis of a (difluoromethyl)-1,3,4-oxadiazole-based HDAC6 inhibitor	198
5.2.4 HDAC inhibition of compound V-8	199
<b>5.3 Conclusions</b>	<b>200</b>

Table of contents

<b>5.4 Experimental section</b>	<b>201</b>
5.4.1 General information	201
5.4.2 Experimental procedures	202
<b>5.5 References</b>	<b>205</b>

## List of publications

### Dissertation-related articles:

Bhatia S\*, Krieger V\*, Groll M, Osko JD, **Reßing N**, Ahlert H, Borkhardt A, Kurz T, Christianson DW, Hauer J, Hansen FK. 2018. Discovery of the first-in-class dual histone deacetylase-proteasome inhibitor. *J Med Chem* **61**: 10299–10309.

doi:10.1021/acs.jmedchem.8b01487.

*The article reports on preliminary work for chapter IV of this dissertation.*

**Reßing N\***, Sönnichsen M\*, Osko JD, Schöler A, Schliehe-Diecks J, Skerhut A, Borkhardt A, Hauer J, Kassack MU, Christianson DW, Bhatia S, Hansen FK. 2020. Multicomponent synthesis, binding mode, and structure-activity relationship of selective histone deacetylase 6 (HDAC6) inhibitors with bifurcated capping groups. *J Med Chem* **63**: 10339–10351.

doi: 10.1021/acs.jmedchem.9b01888.

*The article includes the results presented in chapter II of this dissertation.*

Jenke R, **Reßing N**, Hansen FK, Aigner A, Büch T. 2021. Anticancer therapy with HDAC inhibitors: Mechanism-based combination strategies and future perspectives. *Cancers* **13**: 634. doi: 10.3390/cancers13040634.

*The review includes sections from chapters 1 and 4.1 of this dissertation.*

Okubo K, Isono M, Asano T, **Reßing N**, Schulz WA, Hansen FK, Sato A. 2021. Ubiquitin-proteasome system is a promising target for killing cisplatin-resistant bladder cancer cells. *Anticancer Res* **41**: 2901–2912. doi: 10.21873/anticancer.15072.

*The article follows up on preliminary work for chapter IV of this dissertation.*

*Two more manuscripts with first-authorship contributions based on chapters III and IV of this dissertation are currently in preparation.*

\* The authors share the first authorship.

### Other articles:

**Reßing N**, Marquardt V, Gertzen CGW, Schöler A, Schramm A, Kurz T, Gohlke H, Aigner A, Remke M, Hansen FK. 2019. Design, synthesis and biological evaluation of  $\beta$ -peptoid-capped HDAC inhibitors with anti-neuroblastoma and anti-glioblastoma activity. *Med Chem Commun* **10**: 1109–1115. doi: 10.1039/c8md00454d.

**Poster presentations:**

**Reßing N**, Schöler A, Hansen FK. Design and synthesis of selective HDAC6 inhibitors via the Ugi-azide 4-component reaction. Poster presented at: 7<sup>th</sup> International Conference on Multicomponent Reactions and Related Chemistry; 2018 Aug 26–31; Düsseldorf, Germany.

**Reßing N**, Schöler A, Hansen FK. Design and synthesis of selective HDAC6 inhibitors as potential anti-tumour agents. Poster presented at: DPhG Annual Conference 2018; 2018 Oct 3–5; Hamburg, Germany.

**Reßing N**, Schöler A, Hansen FK. Development of novel dual histone deacetylase-proteasome inhibitors. Poster presented at: 15<sup>th</sup> Research Festival for Life Science; 2019, Jan 18; Leipzig, Germany.

**Reßing N**, Sönnichsen M, Schöler A, Borkhardt A, Bhatia S, Hansen FK. Design and synthesis of dual histone deacetylase-proteasome inhibitors. Poster presented at: DPhG Annual Conference 2019; 2019 Sep 01–04; Heidelberg, Germany.

## List of abbreviations

<b>A</b>			
Å	Ångström (1 Å = 0.1 nm)	br s	broad singlet
A549	adenocarcinomic human alveolar basal epithelial cell line	BTZ	bortezomib
Ac	acetyl	<b>C</b>	
Acetyl-CoA	acetyl coenzyme A	c	concentration
ADP	adenosine diphosphate	c-Hexyl	cyclohexyl
AIBN	azobisisobutyronitrile	c-Src	proto-oncogene tyrosine- protein kinase Src
Ala	alanine	calcd	calculated
ALL	acute lymphoblastic leukaemia	cCP	constitutive proteasome
AML	acute myeloid leukaemia	CD1	catalytic domain 1 of HDAC6
aq.	aqueous	CD2	catalytic domain 2 of HDAC6
arom.	aromatic	CDCl <sub>3</sub>	deuterated chloroform
Asp	asparagine	CDH1	epithelial cell marker
ATP	adenosine triphosphate	CDK	cyclin-dependent kinase
<b>B</b>		ChTL	chymotrypsin-like
BCP-ALL	B-cell precursor acute lymphoblastic leukaemia	Cl	clearance
BDNF	brain-derived neurotrophic factor	CL	caspase-like
BET	bromo- and extra-terminal domain	conc.	concentration
BMF	Bcl-2-modifying factor	CP	core particle
Bn	benzyl	CYP	cytochrome
Boc	<i>tert</i> -butyloxycarbonyl	Cys	cysteine
		<b>D</b>	
		d	doublet
		δ	chemical shift
		DCM	dichloromethane
		dd	doublet of doublets
		decomp.	decomposition

List of abbreviations

DFAA	difluoroacetic anhydride		<b>H</b>
DFMO	2-(difluoromethyl)-1,3,4-oxadiazole	h	hour(s)
DFT	density functional theory	H3	histone 3
DIPEA	<i>N,N</i> -diisopropylethylamine	HAL-01	B-cell acute lymphoblastic leukaemia cell line
DMF	<i>N,N</i> -dimethylformamide	HAT	histone acetyltransferase
DMSO	dimethyl sulfoxide	HATU	<i>O</i> -(7-azabenzotriazol-1-yl)- <i>N,N,N',N'</i> -tetramethyluronium hexafluorophosphate
DMSO- <i>d</i> <sub>6</sub>	deuterated dimethyl sulfoxide	<i>h</i> CD2	second catalytic domain of human HDAC6
DNA	deoxyribonucleic acid	HDAC	histone deacetylase
	<b>E</b>	HDACi	histone deacetylase inhibitor(s)
EDC	1-ethyl-3-(3-dimethylaminopropyl)carbodiimide	HDM	histone demethylase
EGFR	epidermal growth factor receptor	HIF-1 $\alpha$	hypoxia-inducible factor 1 $\alpha$
EMA	European Medicines Agency	His	histidine
eq	equivalent	HIV	human immunodeficiency virus
ER $\alpha$	estrogen-related receptor $\alpha$	HK	histone kinase
ESI	electrospray ionisation	HL-60	human acute myeloid leukaemia cell line
Et	ethyl	HL-60R	bortezomib-resistant human acute myeloid leukaemia cell line
	<b>F</b>	HLM	human liver microsomes
F	phenylalanine	HMT	histone methyltransferases
FAERS	U.S. Food and Drug Administration Adverse Event Reporting System	HPLC	High performance liquid chromatography
FDA	U.S. Food and Drug Administration	HRMS	high resolution mass spectrometry
Foxp3	forkhead box P3	HSB-2	human T cell leukaemia cell line
	<b>G</b>		
Gly	glycine		

List of abbreviations

Hsp	heat shock protein	Lys	lysine
Hz	Hertz		<b>M</b>
	<b>I</b>	m	multiplet
<i>i</i> -Pr	<i>iso</i> -propyl	M	molar (mol/L)
IC <sub>50</sub>	half maximal inhibitory concentration	MCF-7	human breast cancer cell line
iCP	immunoproteasome	Me	methyl
ID	identification code	MEF2	myocyte enhancer factor-2
IκB	natural inhibitor of the nuclear factor kappa-B	MeOH- <i>d</i> <sub>4</sub>	deuterated methanol
IL-6	interleukin 6	Met	methionine
Ile	isoleucine	MHz	Megahertz
	<b>J</b>	min	minute(s)
<i>J</i>	coupling constant	MLM	mouse liver microsomes
JAK	janus kinase	MM	multiple myeloma
Jurkat	human T cell leukaemia cell line	μM	micromolar (μmol/L)
	<b>K</b>	MOLM-13	human acute myeloid leukaemia cell line
K562	human chronic myelogenous leukaemia cell line	MOLT-4	human T cell leukaemia cell line
kDA	kilodalton(s)	mp	melting point
	<b>L</b>	mRNA	messenger ribonucleic acid
LADME(T)	liberation, absorption, distribution, metabolism, excretion, (toxicity)	MS	molecular sieve(s)
LC-MS	liquid chromatography–mass spectrometry	MSH2	MutS protein homolog 2
Leu	leucine	mSin3	mSin3 interaction domain
<i>log</i> D	distribution coefficient	MV4-11	human acute myeloid leukaemia cell line
<i>log</i> P	partition coefficient	MW	microwave
LSD1	lysine-specific demethylase 1		<b>N</b>
		N-CoR	nuclear receptor co-repressor 1
		NAD <sup>+</sup>	nicotinamide adenine dinucleotide
		NBS	<i>N</i> -bromosuccinimide
		NF-κB	nuclear factor kappa-B

List of abbreviations

nm	nanometre(s)		
NMM	<i>N</i> -methylmorpholine	RNA	ribonucleic acid
NMPA	National Medical Products Administration (China)	Rpd3	reduced potassium dependency 3
NMR	nuclear magnetic resonance	Rpn	regulatory particle non-ATPase
<b>P</b>			
P1–4	protein residues residing in specificity pockets 1–4 of the 20S core particle	Rpt	regulatory particle ATPase
p21	cyclin-dependent kinase inhibitor 1	rt	room temperature
p53	tumour suppressor protein p53	RTK	receptor tyrosine kinase
PARP	poly (ADP-ribose) polymerase	<b>S</b>	
PDB	protein data bank	s	singlet
PET	positron emission tomography	S	Svedberg sedimentation coefficient
petrol	petroleum ether	S1–4	specificity pockets 1–4 of the 20S core particle
Ph	phenyl	SAHA	suberoylanilide hydroxamic acid
Phe	phenylalanine	SAR	structure-activity relationship
PI	propidium iodide	sat.	saturated
PI3K	phosphoinositide 3-kinase	SEM	human B cell precursor leukaemia cell line
pK <sub>a</sub>	acid dissociation constant	Ser	serine
pK <sub>b</sub>	base dissociation constant	SI	selectivity index
POI	protein of interest	SirT	sirtuin
PP	histone phosphatase	SMC3	structural maintenance of chromosomes protein 3
ppm	parts per million	SMRT	silencing mediator for retinoid or thyroid-hormone receptor
PROTAC	proteolysis targeting chimera	SnAAP	small neutral amino acid preferring
<b>Q</b>			
q	quartet	SUMO	small ubiquitin-like modifiers
quant.	quantitative		



List of abbreviations

SUP	T-cell lymphoblastic lymphoma cell line	Tyr	tyrosine
SUP-B15	human acute lymphoblastic leukaemia cell line	U4CR	Ugi four-component reaction
SUP-B15R	imatinib-resistant human acute lymphoblastic leukaemia cell line	UA4CR	Ugi-azide four-component reaction
	<b>T</b>	Ub	ubiquitin
t	triplet	UBD	ubiquitin binding domain
t <sub>1/2</sub>	half-time	Ubps	ubiquitin hydrolases
<i>t</i> -Bu	tertiary butyl	UPS	ubiquitin-proteasome system
T-PLL	T-cell prolymphocytic leukaemia	UV	ultra violet
TALL-1	human T cell leukaemia cell line		<b>V</b>
TAP	thiol activated prodrug	vdW	van der Waals
tCP	thymoproteasome	vs	versus
TFA	trifluoroacetic acid		<b>W</b>
TFMK	trifluoromethyl ketone	W	Watt
THF	tetrahydrofuran		<b>Z</b>
THP	tetrahydropyran	ZBG	zinc-binding group
THP-1	acute monocytic leukaemia cell line	zCD2	second catalytic domain of zebrafish HDAC6
THP-1R	bortezomib-resistant acute monocytic leukaemia cell line	ZnF	HDAC6 zinc finger
Thr	threonine		<b>0-9</b>
TIPS	triisopropylsilane	20S CPi	20S core particle (proteasome) inhibitor(s)
TL	trypsin-like	393	patient-derived acute myeloid leukaemia cell line
TLC	thin layer chromatography		
t <sub>R</sub>	retention time		
Treg	regulatory T cell		
Trityl	triphenylmethyl		

## Summary

Epigenetic events define the post-translational phenotype of a cell and occur through a complex interplay between different enzyme families that are classified as writers, readers, and erasers. One relevant mechanism in this context is the balancing of acetylation levels on histones and other substrates by histone acetyltransferases (HATs) and histone deacetylases (HDACs). Controlling the conformation and accessibility of DNA, some of the eleven zinc-dependent HDAC isoforms are known to have direct impact on gene expression and cellular processes, including tumorigenesis, and are therefore considered as valuable drug targets. Extensive research in this direction culminated in the development of a characteristic

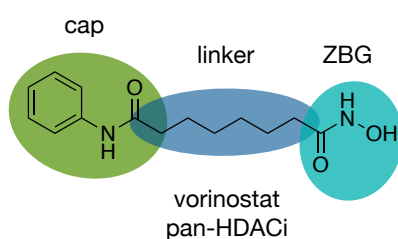


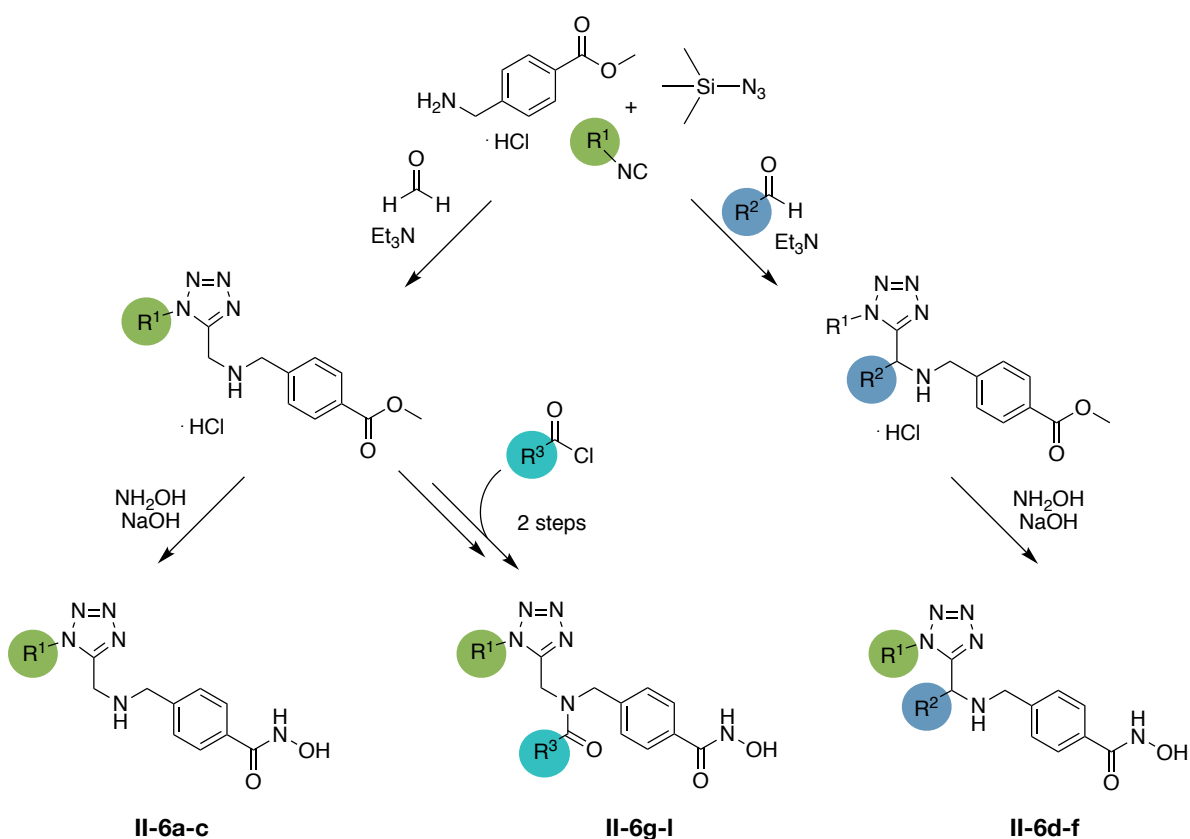
**Figure I.** The first FDA-approved HDACi vorinostat was based on the established pharmacophore model.

pharmacophore model comprising a cap group, a linker moiety, and a zinc-binding group (ZBG) which is supposed to bind to the zinc ions present in the active sites of all four zinc-dependent HDAC classes. Based on this model, vorinostat (Figure I) became the first FDA-approved HDAC inhibitor (HDACi) for cancer therapy in 2006 and was succeeded by two more pan-HDACi, panobinostat and belinostat, and two class I-selective drugs, romidepsin and tucidinostat, over the following years.

With class I HDACs being the most prominent targets to elicit cytotoxicity, the non-selective nature of pan-HDACi has long been suspected to account for severe adverse effects, aside from the desired efficacy. Since such complications limit the scope of the altogether promising HDACi to short-term treatments and chemotherapy, it has become a priority to design isoform-selective compounds, particularly those inhibiting HDAC6 with its unique substrate spectrum including Hsp90,  $\alpha$ -tubulin, and tau. A detailed overview of HDACs as therapeutic targets is given in chapter 1.

Following prior research on HDACi in the Hansen group, chapter 2 presents a study on HDAC6i with bifurcated capping groups featuring a tetrazole moiety. Unlike earlier libraries built on a peptoid scaffold, this new set of HDACi was designed to display higher rigidity and metabolic stability. In order to locate the appropriate position for cap group branching, three different types of scaffolds were prepared by means of the Ugi-azide four-component

reaction (UA4CR) and subsequent attachment of the hydroxamate ZBG (Scheme I). Once identified through biochemical HDAC inhibition assays, the most promising scaffold was further diversified within a brief SAR study yielding **II-6I** ( $IC_{50}$  HDAC1:  $5.18 \pm 0.313 \mu\text{M}$ ; HDAC6:  $0.030 \pm 0.0002 \mu\text{M}$ , SI: 173) as the most selective HDAC6i among a total of twelve compounds.



**Scheme I.** Multicomponent-synthesis of the tetrazole-based HDACi **II-6a-l** featuring three different types of capping groups.

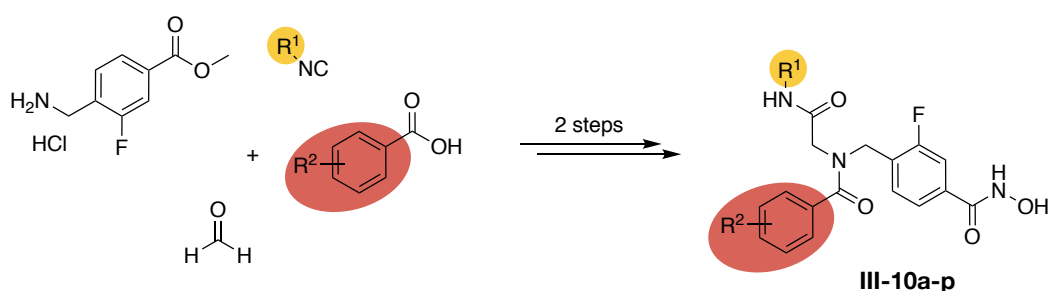
To confirm the inhibitory potential and the cellular selectivity for HDAC6, **II-6I** was subjected to immunoblotting experiments.<sup>1</sup> A co-crystal structure of HDAC6 in complex with **II-6I** was analysed to gain detailed information on the binding mode.<sup>2</sup> In microsomal stability assays, **II-6I** turned out to be sufficiently stable in presence of human and mouse liver enzymes.<sup>3</sup> As expected for selective HDAC6i, **II-6I** had no significant cytotoxic effect on selected leukaemia cell lines but enhanced the efficacy of the proteasome inhibitor bortezomib. Hence, **II-6I** may serve as a potent, isoform-selective tool compound for drug combination experiments.

<sup>1</sup> Western blotting experiments and cytotoxicity screenings for all projects were performed by the group of Sanil Bhatia, HHU Düsseldorf.

<sup>2</sup> X-ray experiments were carried out by the group of David W. Christianson, University of Pennsylvania.

<sup>3</sup> Microsomal stability assays were performed by Bienta/Enamine Ltd., Kiev, Ukraine.

Chapter 3 focuses on the design and synthesis of novel, fluorinated HDACi. The project was inspired by recent findings suggesting that the HDAC6-selective PET probe [ $^{18}\text{F}$ ]bavarostat, which comprises a fluorinated linker moiety, adopts a different binding mode than the otherwise identical linker of peptoid-based HDACi developed by the Hansen group. To illuminate the impact of the linker variation on HDAC6 selectivity in further detail, several fluorinated analogues were to be compared with their non-fluorinated parent compounds in biochemical inhibition assays against HDAC1 and HDAC6. An additional SAR study entailed modifications of the aromatic cap group region and was supposed to shed light on the question whether substitution patterns can be tweaked to steer between different isoforms. With this goal, sixteen new HDACi were designed. Upon successful 4-step linker synthesis via the Staudinger reaction as key step, all desired compounds could be obtained from scratch and in sufficient purity > 95% within less than 4 h by using an optimised, microwave-assisted 2-step protocol for the Ugi four-component reaction (U4CR) and the subsequent hydroxylaminolysis (Scheme II).

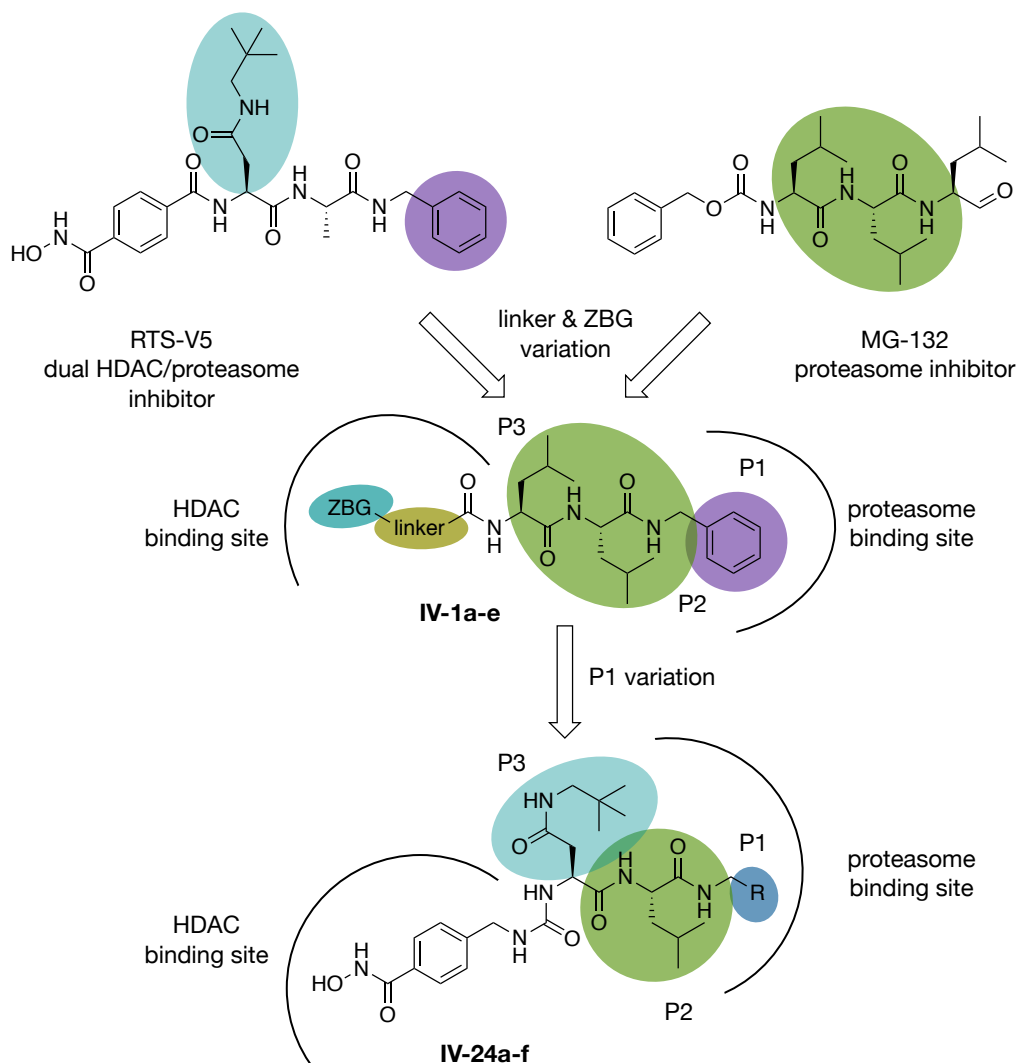


**Scheme II.** The synthesis of the peptoid-capped HDACi **III-10a-p** was accomplished using a microwave-assisted two-step protocol.

The HDAC inhibition data obtained for the resulting library confirm that linker fluorination has a slight effect on the selectivity profiles. The main driver of HDAC6 selectivity, however, appears to be the cap group in which the alteration of particular residues correlates with preferences for either HDAC1 or HDAC6. Matching the data obtained for its non-fluorinated analogue and exceeding all other derivatives of this set in terms of HDAC1 inhibition and cytotoxicity against selected leukaemia cell lines, the pan-inhibitor **III-10h** ( $\text{IC}_{50}$  HDAC1:  $0.013 \pm 0.001 \mu\text{M}$ ; HDAC6:  $0.010 \pm 0.00004 \mu\text{M}$ , SI: 1.3) comprising a dimethylamino group in *para*-position of the acyl ring was singled out as the most promising candidate for future biological evaluation. Compound **III-10p** ( $\text{IC}_{50}$  HDAC1:  $8.01 \pm 0.22 \mu\text{M}$ ; HDAC6:  $0.042 \pm 0.006 \mu\text{M}$ , SI: 191), on the other hand, features a large and branched *iso*-propyl group in the *meta*-position of the acyl moiety and outmatched the HDAC6 selectivity of both

**II-6I** (chapter 2) and the widely-used tool compound tubastatin A ( $IC_{50}$  HDAC1:  $2.49 \pm 0.14 \mu\text{M}$ ; HDAC6:  $0.014 \pm 0.0006 \mu\text{M}$ , SI: 178).

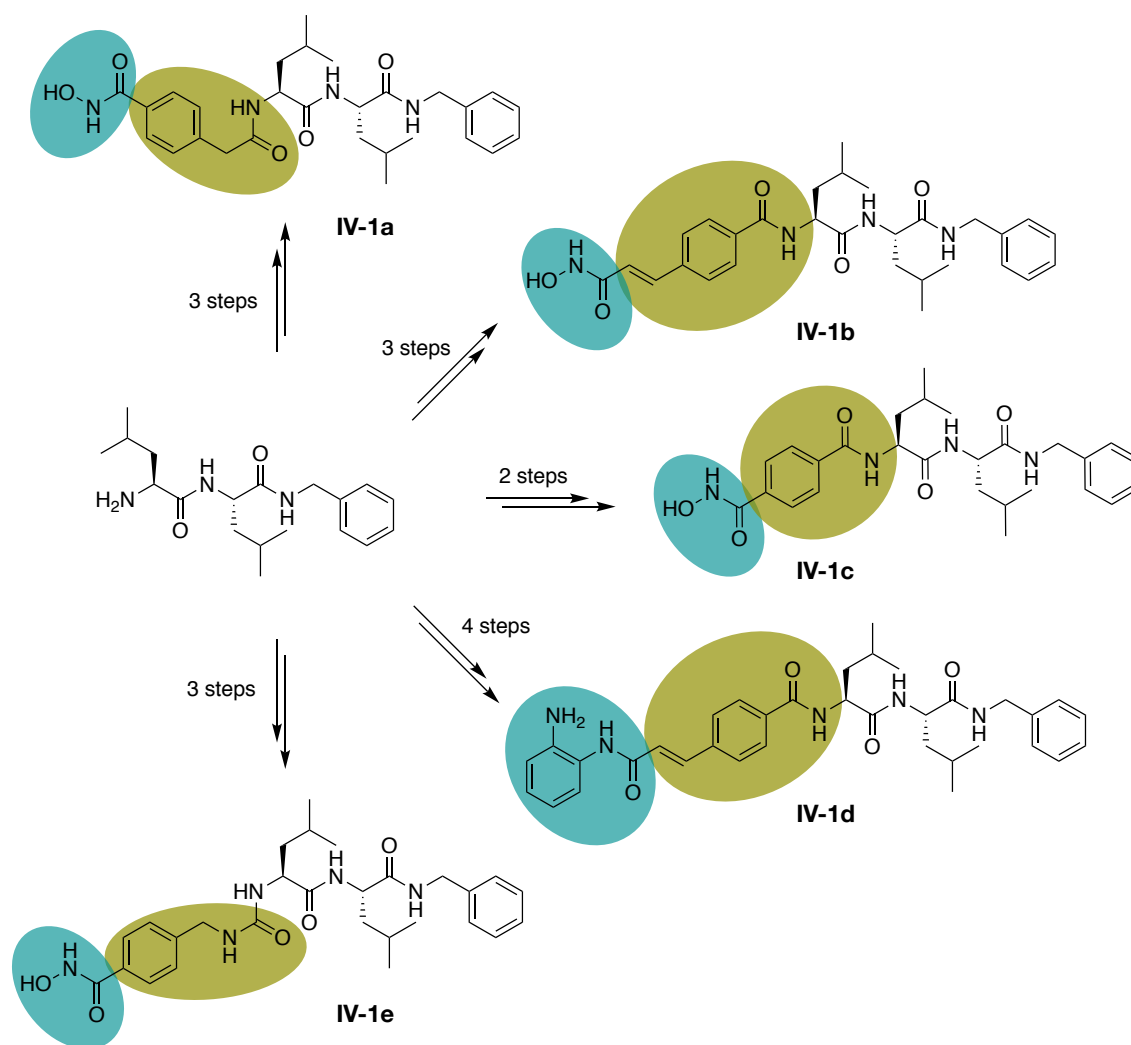
The underlying mechanisms contributing to the abovementioned synergistic interaction between proteasome inhibitors and HDAC6i affect the cellular protein disposal systems and are further elucidated in chapter 4. Misfolded or otherwise dispensable proteins are typically tagged with polyubiquitin chains that initiate recognition by the 26S proteasome where the degradation process takes place. If necessary, the ubiquitin-proteasome system is assisted by the aggresome-autophagy pathway which relies on HDAC6 for the transport of polyubiquitinated proteins. In absence of both disposal systems, protein waste may accumulate and induce apoptosis owing to proteotoxic stress. In cancer therapy, this interplay can be addressed to reverse acquired resistance to proteasome inhibitors.



**Scheme III.** Design of dual HDAC/proteasome inhibitors inspired by RTS-V5. The first library (**IV-1a-e**) focuses on optimising the HDAC binding site through linker and ZBG variations; the second generation (**IV-24a-f**) comprises different P1 residues at the proteasome binding site.

## Summary

Generally offering additive efficacy, combination therapies are a common phenomenon but come at the risk of inducing unfavourable drug-drug interactions and increased side effects with a negative impact on patient compliance. Polypharmacology is an emerging alternative to this concept and seeks to design multi-target drugs in which characteristic parts of two or more individual pharmacophore models are merged into one molecule.

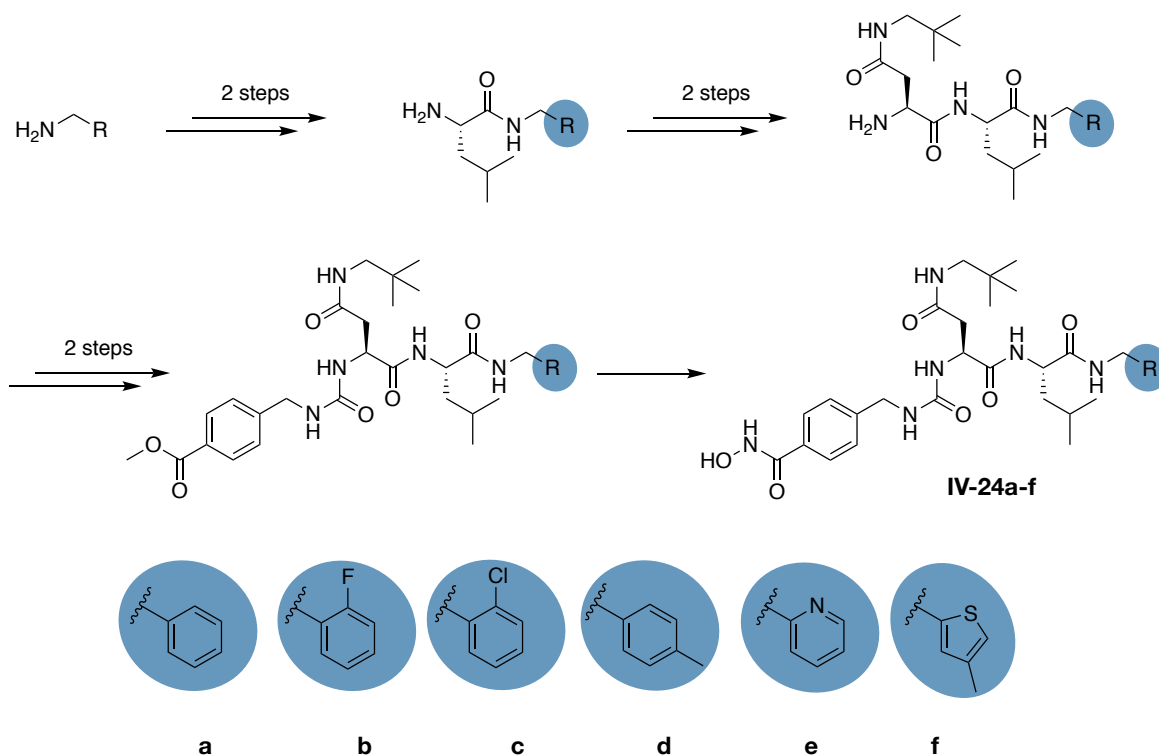


**Scheme IV.** Overview of compounds **IV-1a-e**, the first generation of dual HDAC/proteasome inhibitors with variations on the HDAC binding site.

In 2018, the Hansen group succeeded in designing the first dual HDAC/proteasome inhibitor, RTS-V5. On the basis of this preliminary work, eleven new dual HDAC/proteasome inhibitors are presented in chapter 4. Intending to increase the inhibitory activity and selectivity for HDAC6, a linker screening using the easily accessible RTS-V5/MG-132 hybrid scaffold and hydroxamate ZBGs was performed in the first optimisation cycle (Schemes III & IV); an additional *ortho*-aminoanilide derivative with selectivity for class I isoforms was included to

## Summary

evaluate the impact on HDAC1. After individual synthesis of each linker fragment, amide coupling reactions were carried out to introduce the hybrid scaffolds upon which the ZBGs were either generated via hydroxylaminolysis or released through protecting group removal. HDAC inhibition assays of the five resulting analogues revealed **IV-1e** to be the most potent HDAC6i of this set ( $IC_{50}$ :  $0.122 \pm 0.006 \mu\text{M}$ ). The urea-based linker motif of this compound was then featured in the **IV-1e**/RTS-V5 hybrid scaffold on which the second library was built.

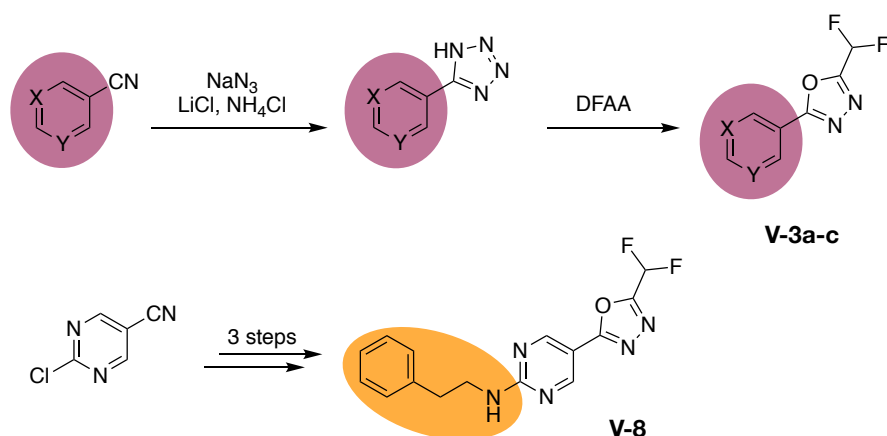


**Scheme V.** Synthesis of compounds **IV-24a-f** with different P1 residues at the proteasome binding site.

With diversification of the aromatic substituent at the proteasome-binding P1 site, the second optimisation cycle aimed to improve the non-covalent proteasome inhibition (Scheme III). Requiring a seven-step protocol upon successful building block synthesis, six analogues were synthesised and evaluated with regard to target inhibition and cytotoxic potential (Scheme V). As a result, all screened compounds ( $IC_{50}$  HDAC1: 1.17–3.20  $\mu\text{M}$ ; HDAC6: 0.146–0.328  $\mu\text{M}$ ) clearly outmatched RTS-V5 ( $IC_{50}$  HDAC1:  $2.31 \pm 0.04 \mu\text{M}$ ; HDAC6:  $0.413 \pm 0.038 \mu\text{M}$ ) in terms of HDAC6 inhibition but failed to achieve similar levels of proteasome inhibition. Nevertheless, several analogues, and particularly **IV-1b** and **IV-24d**, displayed similar or even higher antiproliferative potential against different cancer cell lines than RTS-V5 and were selected for further biological evaluation. Both libraries moreover

provided the first set of valuable SAR data on non-covalent dual HDAC/proteasome inhibitors which can be used to fine-tune succeeding analogues in the future.

Chapter 5 addresses the issue of hydroxamates being controversial groups in drug development. The excellent metal-binding properties of the hydroxamate motif still seem to be unrivalled and essential in order to inhibit certain metalloenzymes; however, the danger of off-target interactions and the formation of toxic metabolites, such as isocyanates, remain a concerning source of unwanted side effects. Over the last years, various efforts to develop alternative but equally potent ZBGs have yielded a range of candidates among which the HDAC6-selective (difluoromethyl)-1,3,4-oxadiazole (DFMO) motif seems to bear the greatest potential. Patented by Yates in 2019, information on this novel ZBG is yet scarce and therefore, the presented study focused on the evaluation of the DFMO group in combination with (hetero)aromatic linker residues other than the pyrimidine ring mentioned in the patent.



**Scheme VI.** Fragment-synthesis and screening of the DFMO derivatives **V-3a-c** was performed to identify the most promising linker which was then featured in the prototype **V-8**.

Pursuing a fragment-based approach, three different analogues featuring the DFMO moiety in absence of a cap group were synthesised from carbonitriles using a microwave-assisted two-step procedure (Scheme VI, top). HDAC inhibition assays of the resulting fragments detected the highest potential for the pyrimidine analogue which then formed the basis for the first full-drug prototype **V-8** (Scheme VI, bottom). Albeit displaying amendable inhibitory potential, this novel compound clearly reduced the activity of HDAC6 ( $\text{IC}_{50}$ :  $1.31 \pm 0.09 \mu\text{M}$ ) without affecting HDAC1 ( $\text{IC}_{50}$ :  $> 30 \mu\text{M}$ ). With the synthetic procedure being proven and adjusted to provide a high overall yield of 79% after 3 steps, compound **V-8** may thus act as a starting point for more elaborate future studies on DFMO-based HDAC6i.



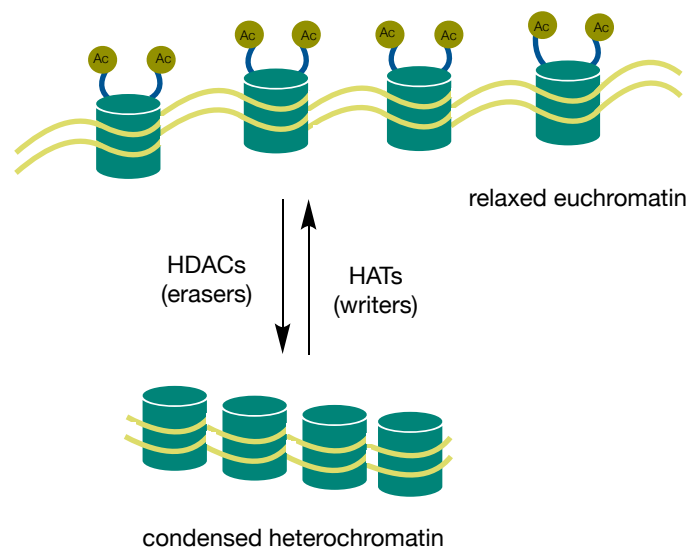
# Chapter 1: Theoretical background

## 1.1 Epigenetics

### 1.1.1 The chromatin structure

Originally describing the phenomenon of post-translational trait variations of cell phenotypes, the term *epigenetics* now encompasses a wide range of chromatin structure modifications and related mechanisms (Bannister & Kouzarides 2011).

In every eukaryotic cell, the entire genetic information is encoded by deoxyribonucleic acid (DNA), a polymer consisting of nucleotides that are arranged in two strands of complementary base pairs forming a double helix. Apart from a particular pattern of nucleobases which is unique for every living creature, the DNA strands further contain ribose and phosphate groups that build the DNA backbone. Coiled around histone octamers comprising the histone proteins H2A, H2B, H3, and H4, the smallest subunits of packed DNA count approximately 146 base pairs and are known as nucleosomes; each of which is marked by another histone protein, H1, and connected by linker DNA (Luger et al. 1997). The ensemble of coiled DNA and proteins forms the chromatin which carries the chromosomes on a dynamic structure shifting between a condensed (*heterochromatin*) and

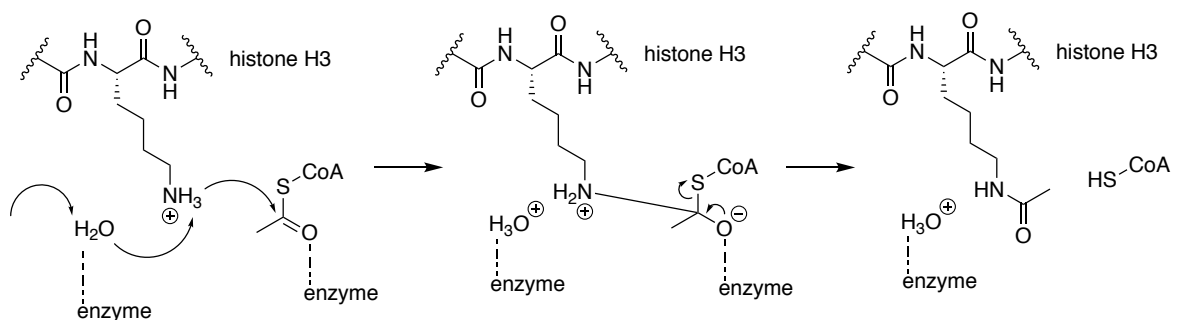


**Scheme 1.1.** HATs and HDACs regulate the chromatin structure.

a relaxed (*euchromatin*) conformation (Scheme 1.1; Jenuwein & Allis 2001). In the relaxed state, a specific section of the DNA template may be exposed to ribonucleic acid (RNA) polymerase which transcribes the respective gene into messenger RNA (mRNA) that can subsequently be translated into the corresponding protein (Jenuwein & Allis 2001). Heterochromatin, in turn, blocks gene expression by denying access to the required DNA template (Jenuwein & Allis 2001).

The dynamic changes of the chromatin structure are regulated by different groups of enzymes: histone acetyltransferases (HATs) and, catalysing the reverse reaction, histone deacetylases (HDACs), histone kinases (HKs) and histone phosphatases (PPs), and histone methyltransferases (HMTs) counteracting the demethylases (HDMs; Biel et al. 2005). Other enzymes are involved in the attachment (small ubiquitin-like modifiers; SUMOs) and removal (ubiquitin hydrolases; Ubps) of ubiquitin groups or participate in DNA repair processes (poly (ADP-ribose) polymerases; PARPs; Biel et al. 2005).

Nucleosomes are globular structures of which only the N-terminal amino acid tails are exposed to the surface where they are susceptible to modifications (Biel et al. 2005). Lysine residues in this position are known to undergo acetylation and deacetylation reactions mediated by HATs (Scheme 1.2) and HDACs, respectively (Greer & Shi 2012). Substrates for methylation mediated by HMTs are lysines, arginines and histidines (Greer & Shi 2012). So far, demethylation reactions were reported for lysines and arginines (Shi & Tsukada 2013), whereas serines, threonines, and tyrosines can be subjected to phosphorylation by HKs and dephosphorylation by PPp (Rossetto et al. 2012). As a result of deacetylation, histone termini remain ionised and bind to the negatively charged DNA backbone, thus enabling heterochromatin formation (Jenuwein & Allis 2001). Upon acetylation, such ionic interactions are no longer retained so that the easily accessible euchromatin structure can be restored (Scheme 1.2; Jenuwein & Allis 2001).



**Scheme 1.2.** Mechanism of the HAT-mediated acetyl transfer from acetyl-CoA to histone-bound lysine residues. Adapted from de Lera & Ganesan 2016.

The occurrence of DNA-related processes, such as transcription, repair, and replication; and cellular events, like apoptosis, are now considered to depend on epigenetic mechanisms rather than the genetic information encoded by DNA (Tiffon 2018; Biel et al. 2005). The fact that such epigenetic events are mainly influenced by environmental factors, for example air pollution, diet, and exposure to toxins, could serve as an explanation for the phenomenon that identical twins, who share the same genotype, are likely to develop vastly dissimilar phenotypes in terms of health and appearance if they lead different lifestyles (Tiffon 2018).

### 1.1.2 The histone code

The complex interplay between the different histone modifications appears to follow particular patterns in order to evoke specific cellular events and is generally referred to as the *histone code* (Strahl & Allis 2000; Biel et al. 2005). First proposed in 2000 but yet remaining to be elucidated in full, the histone code hypothesis has been extended and refined over the last two decades (Strahl & Allis 2000; Jenuwein & Allis 2001; Rothbart & Strahl 2014). The model classifies enzymes that attach functional groups or residues to histone proteins, such as HATs, HMT, and PKs, as *writers* and opposes them to the *erasers* which remove the respective fragments, e.g. HDACs, HDMs, and PPs (Jones et al. 2016). The information thus conveyed is meanwhile recognised by *readers* that bind to the chromatin in order to initiate cellular responses such as the activation of transcription factors (Fujisawa & Filippakopoulos 2017). Among others, the most prominent reader enzymes are bromodomains, which bind to acetylated lysines, and chromodomains, which recognise methylated lysines (Holdermann et al. 2012; Fujisawa & Filippakopoulos 2017; Owen et al. 2000).

## 1.2 Histone deacetylases (HDACs)

### 1.2.1 Classes and isoforms

**Modified sections from this subchapter have previously been published in:**

Jenke R, Reßing N, Hansen FK, Aigner A, Büch T. 2021. Anticancer therapy with HDAC inhibitors: Mechanism-based combination strategies and future perspectives. *Cancers* **13**: 634.

Histone deacetylases (HDACs) are a family of eukaryotic enzymes of which eighteen human isoforms are known to date (Roche & Bertrand 2016). Owing to their homology to the *Saccharomyces cerevisiae* yeast proteins, HDACs are divided into four classes (Figure 1.1; Roche & Bertrand 2016). The class I HDACs 1, 2, 3, and 8 are ubiquitously expressed homologues of the *S. cerevisiae* protein Rpd3 (reduced potassium dependency 3) which are composed of less than 500 amino acids (Gregoretto et al. 2004). Except for HDAC8, which shuttles between the nucleus and the cytoplasm, all class I HDACs are localised in the cell nucleus (Gregoretto et al. 2004; Wang et al. 2020). The class II enzymes are homologous to the *S. cerevisiae* histone deacetylase Hda1 and are further divided into the subgroups IIa, covering the signal proteins HDACs 4, 5, 7, and 9 that shuttle between the nucleus and cytoplasm; and IIb, comprising HDACs 6 and 10 which operate in the cytoplasm (Verdin et al. 2003). Unlike class I enzymes, the class II isoforms assemble approximately 1000 amino acids in length and are expressed in a tissue-specific manner with the class IIa isoforms being prevalent in the heart, brain, and skeletal muscle (Verdin et al. 2003; Wang et al. 2020). The class IIb isoform HDAC10 acts in the liver, kidney, and spleen (Hai et al. 2017). Since the protein sequence of HDAC11 does not reveal sufficient concordance with either class I or class II, it has been deemed a class IV isoform (Gregoretto et al. 2004). Apart from being the only HDAC enzyme that was not found in fungi, HDAC11 is also unique in showing no homology to yeast proteins (Gregoretto et al. 2004).

class I	class IIa	class IIb	class III	class IV
HDAC1 HDAC2 HDAC3 HDAC8	HDAC4 HDAC5 HDAC7 HDAC9	HDAC6 HDAC10	sirtuins Sirt1–7	HDAC11

**Figure 1.1.** Overview of the HDAC classification system based on the homology to yeast proteins.

Despite their belonging to the same enzyme family, the class III isoforms Sirt1–7 differ from other HDACs by the fact that they are NAD<sup>+</sup>-dependent and homologues of the *S. cerevisiae* protein Sir2, whereas the classic HDACs 1–11 happen to be zinc-dependent (Gregoretta et al. 2004). Accordingly, the class III HDACs are referred to as *sirtuins* (Gregoretta et al. 2004).

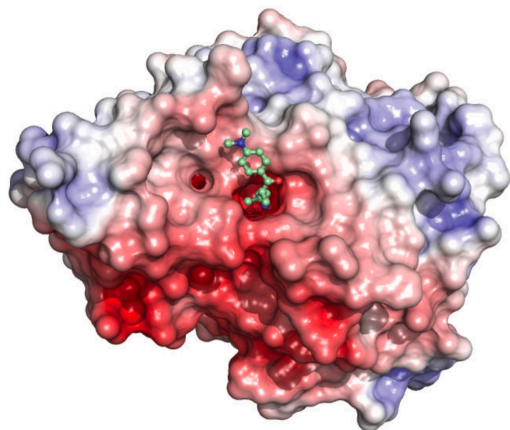


**Figure 1.2.** Molecular surface of human HDAC6 CD2 (*hCD2*) in complex with trichostatin A (PDB ID: 5EDU). The picture was created by the Christianson group, University of Pennsylvania. Reprinted with permission from Hai Y, Christianson DW. 2016. Histone deacetylase 6 structure and molecular basis of catalysis and inhibition. *Nat Chem Biol* **12**: 741–747. Copyright (2016) Springer Nature.

In medicinal chemistry, accurate structural data on biological targets is most valuable as it facilitates binding mode predictions for potential drugs. This is helpful to eliminate poor candidates at early design stages and may thus supersede elaborate synthesis. To perform reliable computational docking experiments on sketched compounds, X-ray structures of crystallised target proteins are essential as they offer a maximum of structural information. For highly similar proteins, such information can moreover be used to create homology models if crystallisation experiments with particular targets remain unsuccessful.

Regarding HDACs, X-ray data on co-crystal structures of most zinc-dependent isoforms are available, with HDAC10 being the most recent addition to the protein data bank (PDB; Hai et al. 2017). Five years after the publication of co-crystallised HDAC homologues in 1999 (Finnin et al. 1999), Vannini and co-workers were the first group to obtain a crystal structure of a human isoform, HDAC8 (Vannini et al. 2004), which thereupon served as a valuable tool for docking experiments until the structures of HDACs 1–3 were solved between 2010 and 2013 (Bressi et al. 2010; Millard et al. 2013; Watson et al. 2012).

Since its first structural analysis by the Christianson group in 2016, HDAC6 has become the most prominent class II isoform for X-ray experiments which now makes up for about one third of all HDAC crystal structures accessible in the PDB (Hai & Christianson 2016). Other co-crystal structures of class II isoforms presented to date are HDAC4 (Guo et al. 2007; Bottomley et al. 2008) and HDAC7 (Schuetz et al. 2008).

So far, the available crystallographic data confirmed a highly conserved nature for all HDACs. Each isoform features a variably sized cavity on the surface, a zinc ion located in the centre

of the active site, and a narrow tunnel of mutable length and width connecting the two units. Figures 1.2 and 1.3 illustrate this structure by the example of HDAC6 in complex with trichostatin A (Hai & Christianson 2016). While this structural motif can generally be applied to all isoforms, there are also several unique properties distinguishing the enzymes.

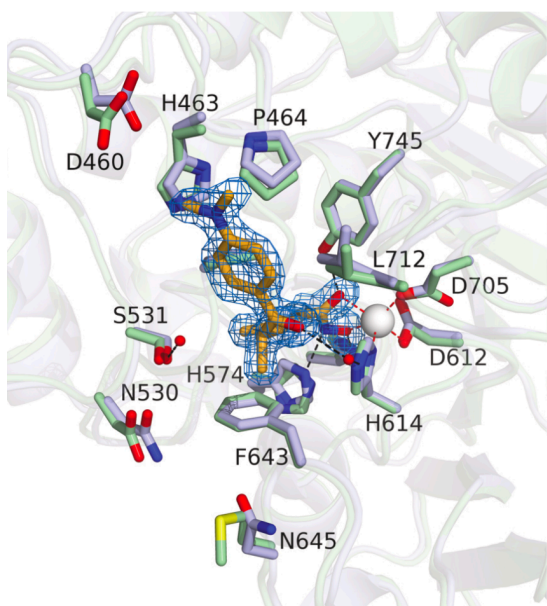


**Figure 1.3.** Trichostatin A (orange) in complex with zebrafish HDAC6 CD2 (zCD2) (light blue; PDB ID: 5EEK). The residues from human HDAC6 CD2 (hCD2; pale green) are overlapped for comparison. The zinc ion in the catalytic centre is depicted as a grey sphere. The picture was created by the Christianson group, University of Pennsylvania. Adapted and reprinted with permission from Hai Y, Christianson DW. 2016. Histone deacetylase 6 structure and molecular basis of catalysis and inhibition. *Nat Chem Biol* **12**: 741–747. Copyright (2016) Springer Nature.

Within class I, HDACs 1 and 2 were found to share more than 80% sequence homology with each other and 50% resemblance with HDAC3 (Ho et al. 2020). A 14 Å long cavity adjacent to the zinc ion in the active site, the so-called *foot pocket*, was only found in HDACs 1 and 2, which are further characterised by particularly narrow tunnel areas and rather small openings on the outside (Bressi et al. 2010; Wambua et al. 2014; Methot et al. 2008; Paris et al. 2008). HDAC8, on the other hand, is smaller than HDACs 1–3 and lacks a C-terminal domain capable of joining multiprotein complexes (Ho et al. 2020).

A characteristic feature of all class IIa isoforms is the replacement of a catalytically crucial tyrosine residue by a histidine which can rotate to open the *lower pocket* (Lahm et al. 2007; Bürli et al. 2013). Possibly required for engaging in protein-protein interactions, HDAC7 further possesses a hydrophobic binding site in proximity to the catalytic centre (Schuetz et al. 2008).

As highly-conserved proteins, HDACs depend on minor structural differences in order to ensure target specificity. Some peptidic residues located in crucial positions around the active site may therefore act as *gatekeepers* that allow specific interactions with the preferred substrates. For the class IIb isoforms HDAC6 and HDAC10, such gatekeepers have been identified by X-ray analysis (Hai et al. 2017; Porter et al. 2018; Osko & Christianson 2019). Both class IIb isoforms moreover contain two catalytic domains but HDAC6 turned out to be unique in featuring a zinc finger (ZnF) that serves as a ubiquitin-binding domain (HDAC6 UBD; Hook et al. 2002; Hai & Christianson 2016; Hai et al.

2017). Compared to other isoforms, the tunnel of the second catalytic domain (CD2) of HDAC6 appears slightly more spacious but shorter, whereas the large entrance area on the surface was found to be defined by characteristic *loop pockets* (Figures 1.2 & 1.3; Hai & Christianson 2016; Porter et al. 2018).

### 1.2.2 Substrates

Serving as key regulators of histones and a number of non-histone proteins, HDACs have considerable impact on cellular processes. Extensive and ongoing research on biological substrates of the different isoforms has revealed that the classification as histone deacetylases, which is shared by the entire enzyme family, mainly applies to the class I HDACs 1–3 and 8, since those were found to control acetylation levels on all four histones (Grozinger et al. 1999; Hu et al. 2000; Johnson et al. 2002, Seto & Yoshida 2014; Ho et al. 2020). Thus, they regulate the expression of several proteins, including the tumour suppressor protein p53, which is also subjected to direct deacetylation by HDAC1 and HDAC8 (Stojanovic et al. 2017; Luo et al. 2000; Seto & Yoshida 2014; Wolfson et al. 2013). Other proteins regulated by class I HDACs are the androgen receptor, which is a substrate of HDAC1 and associated with the development of male phenotypic traits, and the glucocorticoid receptor, which is targeted by HDAC2 (Dokmanovic et al. 2007; Gaughan et al. 2002; Ito et al. 2006). According to a recent study, HDAC1 may also be involved in histone decrotonylation as one of several newly discovered but yet poorly understood histone modifications (Kelly et al. 2018).

As for HDAC8, interactions with  $\alpha$ -actin, the mitosis-related structural maintenance of chromosomes protein 3 (SMC3), and the estrogen-related receptor  $\alpha$  (ER $\alpha$ ), which influences energy homeostasis, have been proposed (Heimburg et al. 2017; Waltregny et al. 2004; Waltregny et al. 2005; Wolfson et al. 2013). Potentially accounting for the small number of identified substrates and opening up new options for its physiological role, recent findings hint at the possibility of HDAC8 exhibiting a preference for long chain fatty acid acyl lysines (Ho et al. 2020; Aramsangtienchai et al. 2016).

Unlike other class I isoforms, HDAC3 appears to depend on the nuclear receptor co-repressor 1 (N-CoR) or the silencing mediator for retinoid or thyroid-hormone receptor (SMRT) to retain its stability and catalytic activity (Emmett et al. 2019; Ho et al. 2020). The resulting SMRT/N-CoR–HDAC3 complex associates with class IIa isoforms which are believed to function as scaffolding proteins that recruit acetyl lysines for their eventual deacetylation by HDAC3 (Ho et al. 2020).

Unless bound to the SMRT/N-CoR–HDAC3 complex, HDACs 4, 5, 7, and 9 are known to exhibit poor deacetylase qualities which presumably result from the lack of catalytically active tyrosines in the active sites (Schuetz et al. 2008; Fischle et al. 2002; Verdin et al. 2003; Ho et al. 2020). Hence, in their most recent review, Ganesan and co-workers question the *in vivo* enzymatic activities of class IIa isoforms altogether (Ho et al. 2020). Experiments on this matter have shown that a catalytic domain of HDAC7 mutant with a tyrosine in place of His843 exhibited significantly higher deacetylase activity than the wild-type enzyme, thus matching the results of a similar study on the replacement of His976 in HDAC4 (Schuetz et al. 2008; Lahm et al. 2007; Mielcarek et al. 2015). Nevertheless, class IIa HDACs reportedly take part in the regulation of gene expression by undergoing interactions with transcription factors and other proteins. To assume this action, they depend on kinases and phosphatases that control the phosphorylation status of the N-terminal serine residues (Wang et al. 2020; Mielcarek et al. 2015; Parra & Verdin 2010). Bound to the chromatin in the unphosphorylated state, class IIa HDACs are capable of repressing transcription in the cell nucleus until phosphorylation allows them to relocate to the cytoplasm, thereby leaving the genes derepressed (Parra & Verdin 2010).

The class IIb isoforms HDAC6 and HDAC10 are now considered to be a tubulin deacetylase and a polyamine deacetylase, respectively (Hubbert et al. 2002; Hai et al. 2017). Owing to its ability to deacetylate  $\alpha$ -tubulin and cortactin, HDAC6 regulates the cytoskeleton and, consequently, exerts influence on cell mitosis, adhesion and migration (Zhang et al. 2007; Valenzuela-Fernández et al. 2008). HDAC6 also participates in complex formation with the class III HDAC isoform Sirt2, which was found to be another tubulin deacetylase, and HDAC11 (Boyault et al. 2007; Valenzuela-Fernández et al. 2008; Deubzer et al. 2013). Another connection between HDAC6 and HDAC11 is their role in immunosuppression through the deacetylation of the Forkhead box P3 (Foxp3) protein which controls the function of regulatory T (Treg) cells (Xiao et al. 2016; Huang et al. 2017). Decreasing immune responses, Treg cells are relevant for the treatment of autoimmune diseases as well as cancer and may require careful balancing for those purposes (Xiao et al. 2016). Similar to HDAC9, inhibition or deletion of HDACs 6 and 11 was observed to increase the Treg cell production, whereas downregulation of HDACs 3 and 5 resulted in the reverse effect (Xiao et al. 2016; Huang et al. 2017).

Enabling the correct folding of proteins, the heat shock protein 90 (Hsp90) acts as a chaperone protein that responds to direct deacetylation by HDAC6 (Boyault et al. 2007; Valenzuela-Fernández et al. 2008). In absence of HDAC6, hyperacetylation of Hsp90 leads to



limited chaperone function and, as a consequence, to the accumulation of misfolded proteins (Boyault et al. 2007; Valenzuela-Fernández et al. 2008). To escape apoptotic stress, cells usually dispose of misfolded proteins via several degradation mechanisms and one of which, the aggresome-autophagy pathway, is also regulated by HDAC6 (Kawaguchi et al. 2003). Both mechanisms, the chaperone function of Hsp90 and the aggresome-mediated protein degradation, are of significant importance to fast-growing tumour cells (Kawaguchi et al. 2003).

In 2017, Hai et al. succeeded in characterising the catalytic domain of the transcriptional repressor HDAC10 and reported on the discovery of a glutamate gatekeeper which appears to be unique among HDACs (Hai et al. 2017; Koeneke et al. 2015; Ho et al. 2020). Inspired by this finding, the group concluded that HDAC10 serves as a *N*<sup>8</sup>-acetylspermidine-specific deacetylase rather than an acetyllysine deacetylase and that its activity might be linked to autophagy function (Hai et al. 2017).

Similar to HDAC8, the only class IV isoform HDAC11 is presumed to interact with long chain fatty acids instead of acetyllysines (Ho et al. 2020). In spite of further information on HDAC11 substrates being extremely scarce, it has been suggested that the involvements in transcriptional modifications may affect immunomodulation (Ho et al. 2020).

Acetyl-Lys Peptide Hydrolases	Longer Chain Acyl-Lys Peptide Hydrolases	Ac-Polyamine Hydrolase	TrifluoroAc-Lys Peptide Hydrolases
HDAC1 HDAC2 HDAC3 HDAC6	HDAC8 HDAC11	HDAC10	HDAC4 HDAC5 HDAC7 HDAC9

**Figure 1.4.** Overview of the *in vitro* substrate-based HDAC classification system proposed by Ho et al. (Ho et al. 2020).

Although far from complete, this overview of HDAC substrates demonstrates that the enzyme family's name *histone deacetylases* is somewhat misleading. Ever since their discovery and initial classification about two decades ago, the knowledge on structural details and biological roles of the different HDAC isoforms has evolved and in light of today's understanding, the established terminology might no longer seem entirely appropriate. Hence, Ho et al. recently proposed to reorganise the HDAC isoforms in accordance with their preferred *in vitro* substrates (Ho et al. 2020). In this model (Figure 1.4), HDACs 1–3 and 6 would be considered as *In vitro Acetyl-Lys Peptide Hydrolases*, whereas HDAC8 and

HDAC11 could be termed *In vitro Longer Chain Acyl-Lys Peptide Hydrolases* (Ho et al. 2020). The newly identified characteristics of HDAC10 would justify its classification as an *In vitro Ac-Polyamine Hydrolase* (Ho et al. 2020; Hai et al. 2017). Due to the increased catalytic activity in presence of more electrophilic, fluorinated acetyllysines, HDACs 4, 5, 7, and 9, hitherto considered as class IIa isoforms, would be redefined as *In vitro TrifluoroAc-Lys Peptide Hydrolases* (Ho et al. 2020). In consequence to their conclusions, the authors also point out that current *in vitro* assay methods employed for isoforms other than HDACs 1–3 and HDAC6 might be unsuitable and yielding results of little relevance unless they are built around the actual substrates (Ho et al. 2020).

### **1.2.3 Therapeutic potential**

#### **1.2.3.1 Approaches in cancer therapy**

So far, most pharmaceutical attempts towards HDAC inhibitors (HDACi) have been made in the field of cancer therapy. Apart from regulating gene expression through histone modifications and protein complex formation in healthy cells, HDACs are known to impact and support the genesis and growth of malignant cells (Witt et al. 2009; West & Johnstone 2014; Li & Seto 2016). Aberrant expression levels of particular HDAC isoforms are thus typical for some tumour entities and may be used as markers for disease progression, hinting at either good or poor patient prognosis (Aldana-Masangay & Sakamoto 2011; Li & Seto 2016; Yano et al. 2018; Witt et al. 2009; Chun 2015). A detailed overview of the cancer-related processes influenced by different HDAC isoforms is given in a review by Li and Seto (Li & Seto 2016) and several earlier works, including those by Roche and Bertrand (Bertrand 2010; Roche & Bertrand 2016), West and Johnstone (West & Johnstone 2014), and Oehme and co-workers (Witt et al. 2009). A more recent article by Jenke et al. elaborates on the potential of HDACi for combination therapies (Jenke et al. 2021).

As drivers of tumourigenesis, oncoproteins initiate the development of cancerous cells and are counteracted by tumour suppressor proteins, such as p53, which are supposed to preclude the growth of mutated cells by causing cell cycle arrest or apoptosis (West & Johnstone 2014; Li & Seto 2016; Santoro et al. 2013). Concerning the latter group, HDACs 1 and 2 have recently been linked to the occurrence of mutant p53 (Stojanovic et al. 2017). Typically found in pancreatic cancer and other tumours but failing to induce cell-protective mechanisms, this mutant is believed to account for poor prognosis and decreased

sensitivity to chemotherapy (Stojanovic et al. 2017). The deacetylation of p53 is generally attributed to the HDAC1/mSin3 (mSin3 interaction domain) complex, but a study on lung cancer cells gave evidence suggesting that p53-mediated activation of the pro-apoptotic factors p21 and Bax may also depend on the absence of HDAC2 (Jung et al. 2012; Mrakovcic et al. 2019; Li & Seto 2016). In colon cancer cells, inhibition of HDAC8 led to increased activity of the pro-apoptotic Bcl-2-modifying factor (BMF; Kang et al. 2014; Li & Seto 2016).

Once formed, a tumour proliferates aggressively and sustains this growth through angiogenesis, which results in the formation of new blood vessels, and metastasis, which spreads the tumour to previously unaffected sites. Highly reliant on cytoskeletal rearrangements, both processes are affected by HDAC6 and its impact on the acetylation status of cortactin (Michaelis 2014; Zhang et al. 2007; Aldana-Masangkay & Sakamoto 2011). According to *in vivo* studies on pancreatic cancer, metastasis may also be facilitated by a lack of the tumour suppressor protein E-cadherin; however, requiring complexes of transcriptional repressors and HDACs 1 and 2, the silencing of the respective gene (*CDH1*) could be reversed upon HDAC inhibition (von Burstin et al. 2009; Li & Seto 2016). Angiogenesis is associated with HDACs 4–6 which regulate the hypoxia-inducible factor 1 $\alpha$  (HIF-1 $\alpha$ ) by means of direct deacetylation or indirect stabilisation through activation of the chaperone proteins (Geng et al. 2011; Chen et al. 2015; Li & Seto 2016; Kong et al. 2006; Qian et al. 2006). By initiating the expression of HDAC3 as a co-repressor of epithelial genes, HIF-1 $\alpha$  furthermore promotes metastasis via epithelial-mesenchymal transition (Wu et al. 2011; Serrano-Gomez et al. 2016).

Another factor contributing to the survival of tumour cells is the interplay of class I HDACs with cell cycle-related proteins functioning as either activators (cyclins) or inhibitors (p21) of the cyclin-dependent kinases (CDKs; Chun 2015; Sandor et al. 2000). In this context, HDAC3 is of particular importance as it undergoes interactions with cyclin A, CDK1, and a protein complex featuring A-kinase-anchoring proteins and the Aurora B kinase, all of which are presumed to support mitotic progression (Jiang & Hsieh 2014; Li et al. 2006; Li & Seto 2016).

Despite their role in tumour progression, HDACs are known to protect healthy cells by controlling proteins involved in DNA-damage repair (Li & Seto 2016; Miller et al. 2010). In tumour cells, however, this effect seems to be equally powerful and thus, it affects the susceptibility to some of the most effective treatments options, e.g. DNA-damaging drugs, such as cisplatin, and radiation therapy (Miller et al. 2010; Ozaki et al. 2008). Class I HDAC

inhibition, in turn, has effectuated increased chemosensitivity in several cancer cell lines, including the often cisplatin-resistant high grade serous ovarian cancer (Diedrich et al. 2016, Ozaki et al. 2008; Bandolik et al. 2019). Other entanglements of HDACs in the DNA-repair network appear to include class IIa enzymes and the class IIb isoforms HDAC6 and HDAC10 which function as MutS protein homologue 2 (MSH2) deacetylases, thereby governing the DNA mismatch repair system (Li & Seto 2016).

The fact that all selective and non-selective FDA-approved HDACi available on the market act as potent inhibitors of class I isoforms coincides with the observation that numerous cancer-sustaining mechanisms depend on the function of those particular enzymes. Thus, it cannot be ruled out that cytotoxic effects achieved by inhibitors of other isoforms may come as a result of unintentional class I inhibition (Lin et al. 2019). As a consequence, HDACs 1–3 are now regarded as primary cancer targets and an increasing number of class I-selective inhibitors is currently being evaluated in clinical trials for the treatment of solid and haematological malignancies. The class IIb isoform HDAC6, in contrast, exhibits negligible cytotoxicity as a single agent but is facing growing attention as a target for combination therapies or dual approaches due to its unique substrate spectrum (Hideshima et al. 2011; Kalin & Bergman 2013; Gaisina et al. 2016; Bhatia et al. 2018; Depetter et al. 2019; Luan et al. 2019; Liu et al. 2020; Reßing et al. 2020). Suspected to be a regulator of the autophagy, HDAC10 is emerging as a promising target for the treatment of neuroblastoma (Oehme et al. 2013).

With less than thirty years gone by since their discovery, the information on HDACs and their involvements in cancer progression is indeed incomplete but certain to be complemented as research is proceeding at an enormous rate.

### **1.2.3.2 Benefits of isoform-selective HDAC inhibitors**

***Modified sections from this subchapter have previously been published in:***

Jenke R, Reßing N, Hansen FK, Aigner A, Büch T. 2021. Anticancer therapy with HDAC inhibitors: Mechanism-based combination strategies and future perspectives. *Cancers* **13**: 634.

Over the last three decades, knowledge on the biological roles of HDACs has evolved and it is now clear that each isoform serves an individual substrate spectrum (Ho et al. 2020). Thus involved in numerous individual epigenetic pathways, HDACs contribute to the development of various cancers and non-oncological conditions, including neurodegenerative disorders,

viral infections, and rare diseases. The fact that all approved HDACi as well as the majority of compounds in clinical trials address oncological conditions is therefore not a consequence of lacking therapeutic opportunities, but the result of poor target selectivity and unfavourable pharmacokinetics (Zhang et al. 2018). With few exceptions, all of the current clinical candidates feature a hydroxamate zinc-binding group (ZBG) which is prone to undergoing off-target interactions and reactions that may produce toxic metabolites (Shen & Kozikowski 2016). The polar nature of this ZBG also complicates the passage of the blood-brain-barrier which would be a crucial requirement for treating disorders located in the central nervous system (Bertran et al. 2020; Kazantsev & Thompson 2008). Displaying potent class I HDAC inhibition, both hydroxamate-based pan-inhibitors and compounds featuring *ortho*-aminoanilide ZBGs may moreover be associated with the danger of severe adverse effects that cannot be tolerated in long-term treatments or in the therapy of non-life-threatening diseases (Witt et al. 2009; Subramanian et al. 2010; Shen & Kozikowski 2016). Such unwanted complications typically include fatigue, bone marrow toxicity, diarrhoea, peripheral neuropathy, asthenia, cardiac abnormalities, neutropenia, thrombocytopenia, and lymphocytopenia (van Veggel et al. 2018; Ho et al. 2020). In this context, it is noteworthy that experiments on knockout mice lacking class I HDACs or the class IIa enzyme HDAC7 resulted in pre- or perinatal lethality due to impeded cell proliferation (HDAC1), cardiac conditions (HDAC2), cell cycle interruption (HDAC3), or failing endothelial cell-cell adhesion (HDAC7; Witt et al. 2009). Related studies on the depletion of other class IIa isoforms produced viable phenotypes suffering from cardiac conditions and complications in bone formation (Witt et al. 2009). Causing high acetylation levels of  $\alpha$ -tubulin and Hsp90, the absence of HDAC6 had no damaging effect on the viability and entailed no obvious defects except impaired Hsp90 function (Witt et al. 2009). Together, those data allude to the idea that developing isoform-selective inhibitors with a focus on HDAC6 could be desirable in order to circumvent off-target interactions. If successful, this approach could give way to a more targeted chemotherapy, thereby extending the scope to applications beyond cancer.

### 1.2.3.3 Opportunities in non-oncological conditions

**Neurodegenerative diseases.** In the field of neurodegenerative diseases, the class I HDACs 1–3, the class IIa isoform HDAC4, and the class IIb enzyme HDAC6 have gained interest as relevant drug targets (Simões-Pires et al. 2013). In a review published in 2013, Cuendet and co-workers summarise that the neuroprotective properties of nuclear HDAC1 cease upon the enzyme's relocation to the cytoplasm where increased HDAC1 levels are associated with

axonal damage (Simões-Pires et al. 2013). The authors further point out that inhibition or absence of HDACs 2 and 3 in mice led to improved memory processes and an increase in synapse formation, whereas overexpression of HDAC2 caused the opposite effect (Simões-Pires et al. 2013; Fischer et al. 2010; Guan et al. 2009; McQuown et al. 2011). As for HDAC4, increased neuronal apoptosis appeared to be related to the enzyme's shuttling from the cytosol to the nucleus but could be prevented by its inactivation (Chen & Cepko 2009; Simões-Pires et al. 2013). Depletion of HDAC4 moreover turned out to have positive effects on learning and long-term memory (Wang et al. 2011; Simões-Pires et al. 2013).

The neurodegenerative effects of HDACs 1–4 are generally linked to their impact on the regulation of genes and transcription factors, for example the myocyte enhancer factor-2 (MEF2), while the involvement of HDAC6 stems from the enzyme's influence on Hsp90-mediated protein folding and from its pivotal role in protein degradation via the aggresome-autophagy pathway (Bolger & Yao 2005; Chen & Cepko 2009; Fischer et al. 2010; Simões-Pires et al. 2013; Kovacs et al. 2005; Ouyang et al. 2012). The concurrence of insufficient proteasome activity and protein aggregation, e.g. tau (Alzheimer's disease),  $\alpha$ -synuclein-based Lewy bodies (Parkinson's disease), and huntingtin (Huntington's disease), is a common complication in neurodegenerative diseases and thus, sufficient HDAC6 function may seem essential to prevent apoptosis in affected cells (Simões-Pires et al. 2013). In fact, some studies implied that HDAC6 has no worsening but negligible or even beneficial effects on Huntington's disease (Simões-Pires et al. 2013; Bobrowska et al. 2011; Ragot et al. 2015). Other findings on the effect of the HDAC6i tubastatin A in Parkinson's disease accentuate the enzyme's role as a promising therapeutic target (Francelle et al. 2020; Yan et al. 2020; Simões-Pires et al. 2013). Nevertheless, such observations must be considered alongside the fact that the underlying mechanisms invoking the emergence and progression of both diseases are yet unclear.

In the case of the equally enigmatic Alzheimer's disease, significant overexpression of HDAC6 in the hippocampus and cortex parts of the brain were found to coincide with increased  $\alpha$ -tubulin acetylation levels (Ding et al. 2008). This may indicate a loss of deacetylase activity due to HDAC6 inhibition by the co-localised tau protein which also happens to be among the prime suspects for driving the disease (Ding et al. 2008). Acting as a cytoskeletal protein in the brain under normal circumstances, tau is believed to initiate the dementia by forming aggregates after hyperphosphorylation (Ding et al. 2008). Upon treatment with the selective HDAC6i tubacin *in vitro*, the interaction between HDAC6 and tau remained unaffected but the tau phosphorylation at specific sites decreased, thus hinting at a possible regulatory function of HDAC6 (Ding et al. 2008). In addition to phosphorylation, tau

acetylation was found to promote aggregation and in the same study, HDAC6 was exposed as a tau deacetylase (Cohen et al. 2011). Overall, this evidence suggests that HDAC6 regulation could be employed to treat Alzheimer's disease which is the most common form of dementia (Cohen et al. 2011; Ding et al. 2008; Simões-Pires et al. 2013).

As a tubulin deacetylase, HDAC6 controls the microtubule network and is therefore essential for mitochondrial transport and the trafficking of the brain-derived neurotrophic factor (BDNF) which enables neurogenesis and differentiation in adult brains (Hubbert et al. 2002; Dompierre et al. 2007; Simões-Pires et al. 2013). Accordingly, HDAC6 inhibition was found to correlate with high tubulin acetylation and enhanced microtubule stability, thus allowing for a more efficient transport of BDNF (Brindisi et al. 2020). Beside Huntington's disease, this process is proposed to play an essential role in the progression of rare disorders, especially Rett syndrome and Charcot-Marie-Tooth disease (Brindisi et al. 2020; Simões-Pires et al. 2013; Adalbert et al. 2020; Dompierre et al. 2007). Early clinical trials elucidating HDAC6i of yet undisclosed structures for the treatment of such rare diseases are currently under way.

**Viral infections.** A common viral disease associated with HDACs is the influenza A virus (Banerjee et al. 2014; Yamauchi et al. 2011). Through their role in organising the microtubule network with influence on centrosome function and the endosome transport, HDAC3 and HDAC8 are presumed to assist the virus' entry into host cells (Yamauchi et al. 2011). In studies using A549 cells, it turned out that depletion of HDAC8 decreased the infection levels due to centrosome splitting, but interestingly, absence of HDAC1 favoured the opposite effect so that infection became more efficient (Yamauchi et al. 2011). Once transferred into the cell, the virus' capsid, which mimics ubiquitinated misfolded proteins, depends on the aggresome-mediated decoating process induced by HDAC6 in order to release the enclosed RNA-containing ribonucleoproteins into the cell nucleus where the replication takes place (Banerjee et al. 2014). *In vitro* assays on mutated cells lacking function in either CD1, CD2, or ZnF as well as experiments using HDAC6 knockout mice confirmed this mechanism to solely rely on the HDAC6 UBD with assistance by motor proteins and the cytoskeleton (Banerjee et al. 2014).

One of the few non-oncological conditions against which HDACi are currently tested in clinical trials is the human immunodeficiency virus (HIV-1). The established HIV therapy aims at suppressing the viral reproduction in order to keep the viral load to a minimum but fails to address the complication of latency in HIV-infected CD4<sup>+</sup> T cells (Spivak & Planelles 2018). In

the latent state, viral reproduction remains silenced but spontaneous reactivation of reservoirs may suddenly increase the viral load so that permanent and life-long antiretroviral therapy is yet inevitable (Spivak & Planelles 2018). Owing to their regulatory function in the expression of particular genes, the class I HDACs 1–3 are presumed to support HIV latency. The application of HDACi is therefore supposed to help initiate the reproduction of the latent-state virus which could then respond to the antiretroviral approach (Margolis 2011; Spivak & Planelles 2018). This *shock and kill* method has already been the subject of clinical trials using pan-HDACi, but the levels of induced HIV latency reversal did not suffice to achieve complete reservoir elimination (Stoszko et al. 2019; Spivak & Planelles 2018). Meanwhile, preclinical *in vivo* studies succeeded in identifying the combination of the class I-selective inhibitor entinostat and the protein kinase C modulator bryostatin-1 as a powerful initiator of latent virus reactivation, whereas reduced Hsp90 deacetylation after inhibition of HDAC6 appeared to impede the desired gene expression (Zaikos et al. 2018). In accordance with the authors' suggestion to focus on class I HDACi for HIV therapy, first studies using the selective inhibitor tucidinostat are currently being conducted (Zaikos et al. 2018).

**Inflammatory diseases.** The attenuating effect of HDACi on the progression of inflammatory diseases, e.g. several types of arthritis, in mice models is well-documented (Nishida et al. 2004; Nasu et al. 2008; Joosten et al. 2011; Sellmer et al. 2018). Some studies suggest that HDACi are valuable tools to regulate cytokine responses but the extent to which this effect can be attributed to particular isoforms remains to be elucidated in detail (Sellmer et al. 2018). Promising antiinflammatory effects could be achieved with the pan-HDACi givinostat and were investigated in clinical trials for the treatment of juvenile idiopathic arthritis (Joosten et al. 2011; Vojinovic & Damjanov 2011; Vojinovic et al. 2011); however, preclinical studies had previously shown that inhibition of class I HDACs with entinostat or romidepsin may suffice to elicit the desired antiarthritic effects (Nishida et al. 2004; Lin et al. 2007). In a different approach, Koh and co-workers discovered considerable antirheumatic potential of the class IIb HDACi tubastatin A and linked this effect to the regulation of interleukin IL-6 (Lee et al. 2015). Ruling out the inhibition of HDAC10 as the source of efficacy for tubastatin A, Mahboobi and colleagues followed up on this work and designed the highly selective HDAC6i marbostat-100 which turned out to have considerable ameliorating effects on rheumatic mice (Sellmer et al. 2018). Remarking that arthritic diseases are typically chronic conditions, both groups emphasise that the major advantage of targeting HDAC6 instead of other isoforms lies in the superior safety profiles of HDAC6i (Lee et al. 2015; Sellmer et al.



2018). One candidate, the HDAC6i CKD-506, has since been admitted to phase II trials against rheumatoid arthritis (Zhang et al. 2021).

## 1.2.4 Overview of approved drugs and clinical candidates

*Modified sections from this subchapter have previously been published in:*

Jenke R, Reßing N, Hansen FK, Aigner A, Büch T. 2021. Anticancer therapy with HDAC inhibitors: Mechanism-based combination strategies and future perspectives. *Cancers* **13**: 634.

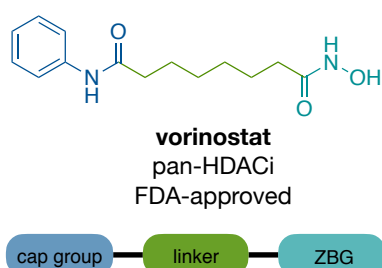


**Figure 1.5.** HDAC pharmacophore model exemplified by the structure of the first FDA-approved HDACi vorinostat.

In compliance with structural characteristics of the different isoforms, a reliable pharmacophore model for HDAC inhibitors has been established (Jung et al. 1997). As illustrated using the example of vorinostat (Figure 1.5) which was first introduced by Marks and Breslow, HDACi typically comprise a cap group occupying the entrance area to the active site, a zinc-binding group interacting with the zinc ion in the catalytic centre, and a hydrophobic linker connecting the two units through the enzyme's channel rim (Marks & Breslow 2007). Following the

discovery of epigenetic drug targets only a few years earlier, vorinostat, also known as suberoylanilide hydroxamic acid (SAHA), was the first HDACi to be approved by the FDA and has been used to treat cutaneous T-cell lymphoma since 2006. Over the following years, more than 27 HDACi were investigated in phase I trials against conditions within and beyond oncology but only three other compounds have yet been granted permission by the FDA (Figure 1.6). The second FDA-approved HDACi based on the established pharmacophore model was belinostat which was introduced into peripheral T-cell lymphoma therapy in 2014. Featuring a phenylvinyl linker, the multiple myeloma drug panobinostat was released in the

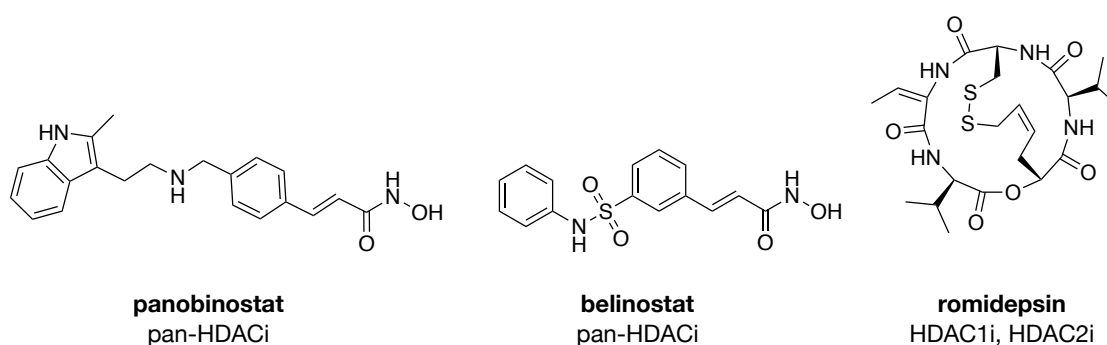


**Figure 1.6.** Further FDA-approved HDACi.

following year. While all three drugs function as non-selective HDACi, vorinostat and belinostat have been approved as single agents, whereas panobinostat is supposed to be administered in combination with the proteasome inhibitor (20S CPI) bortezomib and the corticosteroid dexamethasone.

The fourth FDA-approved inhibitor, romidepsin, is a natural compound built on a different scaffold. Originally isolated from *chromobacterium violaceum* in 1994, the depsipeptide romidepsin was soon found to be active against several tumour cell lines, but at the time, the mode of action remained unclear (Ueda et al. 1994). In 1998, the anticancer activity of romidepsin was finally linked to potent class I HDAC inhibition and after successful development of a total synthesis, the drug was FDA-approved to treat cutaneous T-cell lymphoma in 2009 (Nakajima et al. 1998; Li et al. 1996). Two years later, the FDA expanded the approval of romidepsin to the therapy of peripheral T-cell lymphoma.

Despite extensive studies on potent drug candidates, the four approved inhibitors still dominate the majority of all clinical studies on HDACi throughout phases I to III. Beside various solid and non-solid tumours, several conditions ranging from neurological and neurodegenerative disorders to inflammatory diseases and viral infections are covered by current clinical trials, including HIV (vorinostat, panobinostat, romidepsin, tucidinostat), chronic graft-versus-host disease (vorinostat, panobinostat, romidepsin), Alzheimer's disease (vorinostat), Crohn's disease (vorinostat), epilepsy (vorinostat), and rheumatoid arthritis (CKD-506).

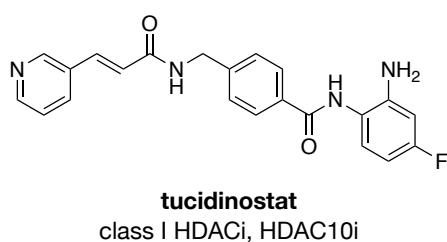


**Figure 1.7.** Structure of the NMPA-approved drug tucidinostat.

The second generation of HDACi entering the clinical stage already included several fine-tuned compounds with improved selectivity profiles. In 2015, tucidinostat (Figure 1.7), formerly known as chidamide, was the first *ortho*-aminoanilide-based class I-selective inhibitor to be approved for the treatment of peripheral T-cell lymphoma by the NMPA in China. Later, it was also granted orphan drug status in Japan. Most recently, after two decades of unsuccessful clinical trials of HDACi against solid tumours, tucidinostat and the aromatase inhibitor exemestane were granted NMPA-approval for the combination therapy of breast cancer (Ho et al. 2020). In other regions, tucidinostat is currently being investigated as a phase III candidate against HIV, haematological malignancies, and solid tumours, including breast and bladder cancer.

Two other drug candidates in phase III studies are the pan-HDACi and possible kidney

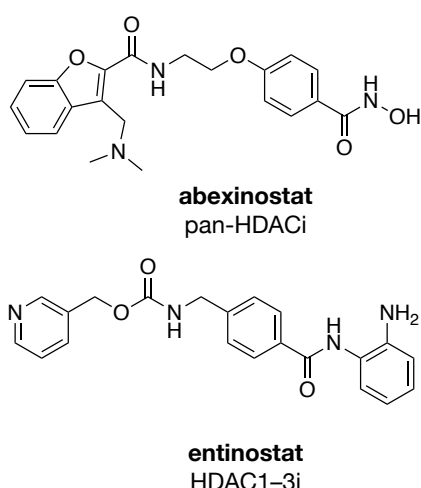


**Figure 1.8.** HDACi in phase III clinical trials.

cancer agent abexinostat in combination with the tyrosine kinase inhibitor pazopanib and the class I-selective entinostat (Figure 1.8). Like tucidinostat, the latter is being considered as an additive for exemestane in the therapy of breast cancers. A study on pracinostat against acute myeloid leukaemia was terminated due to a lack of efficacy.

It is striking that more than half of the current phase II candidates show preferences for class I isoforms (Figure 1.9). Such isoform selectivity is typically achieved by using *ortho*-aminoanilide ZBGs. Now a common motif found in many HDACi including mocetinostat, CXD-101, and tacedinaline, this group was specifically designed to address the foot pockets of class I HDACs. Other class I-selective drug candidates in early clinical trials are resminostat, quisinostat, and fimepinostat featuring hydroxamate ZBGs in combination with olefinic linkers inspired by panobinostat or pyrimidine-based linkers, respectively. As one of only few dual

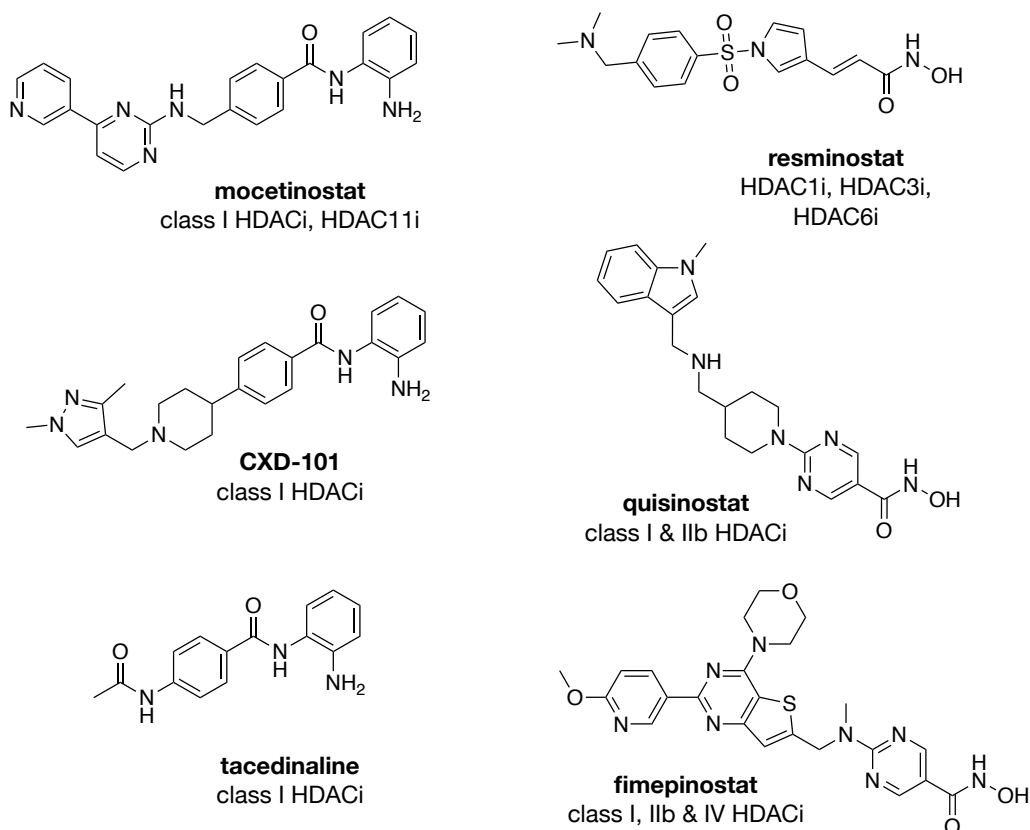


**Figure 1.9.** HDACi with a preference for class I HDACs in current phase II trials.

HDAC inhibitors in clinical trials, fimepinostat acts against the phosphoinositide 3-kinase (PI3K) as well.

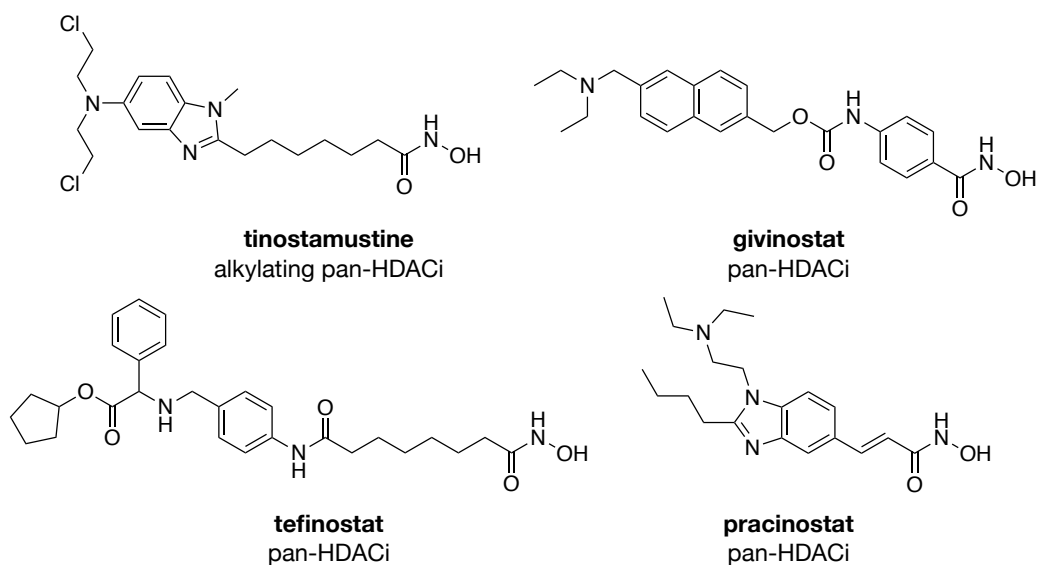


**Figure 1.10.** Pan-HDACi in current phase II trials.

Additional phase II studies (Figure 1.10) involve the pan-inhibitors pracinostat and tefinostat and the non-selective dual agents tinostamustine and givinostat. A hybrid of the alkylating agent bendamustine and vorinostat, tinostamustine is currently being evaluated for the treatment of haematological diseases, breast cancer, and glioblastoma. So far, it is the only phase II candidate capable of DNA alkylation as a second mode of action. In 2020, tinostamustine has been granted orphan drug status for the treatment of T-cell polymphocytic leukaemia by the European Medicines Agency (EMA). Givinostat, on the other hand, appears to affect both HDACs and the janus kinase 2 (Calzada et al. 2012).

Noteworthy, some fatty acids, e.g. butyric acid, phenylbutyric acid, and the antiepileptic drug valproic acid, have long been linked to HDAC inhibition and are still being assessed in clinical trials. However, it is now clear that the carboxylate group present in those compounds acts as a poor ZBG so that fatty acids are typically inferior to rationally designed HDACi in terms of HDAC inhibition (Ho et al. 2020).

The dominance of pan-HDACi and class I-selective drugs in clinical development conforms with their excellent antiproliferative potential due to histone regulation. In contrast, HDAC6i exhibit only poor cytotoxicities as single agents but may be useful for combination therapies, synergistic approaches, and, indeed, for the treatment of specific diseases evolving through

HDAC6-mediated pathways (Depetter et al. 2019; Jenke et al. 2021). The interest in developing preferential HDAC6i is hence widespread and one candidate, ricolinostat (selectivity index (SI<sup>1/6</sup>): 10), is currently being evaluated in phase I and II trials against haematological and gynaecological tumours, breast cancer, and diabetes while its slightly more selective derivative citarinostat is a phase I candidate for the treatment of multiple myeloma (Figure 1.11). Although a number of highly selective HDAC6i have been presented over the last years, there are only three candidates of yet undisclosed structures in clinical trials: CKD-504 for the therapy of Huntington's disease, CKD-510 against Charcot-Marie-Tooth disease, and CKD-506 as a candidate for rheumatoid arthritis.

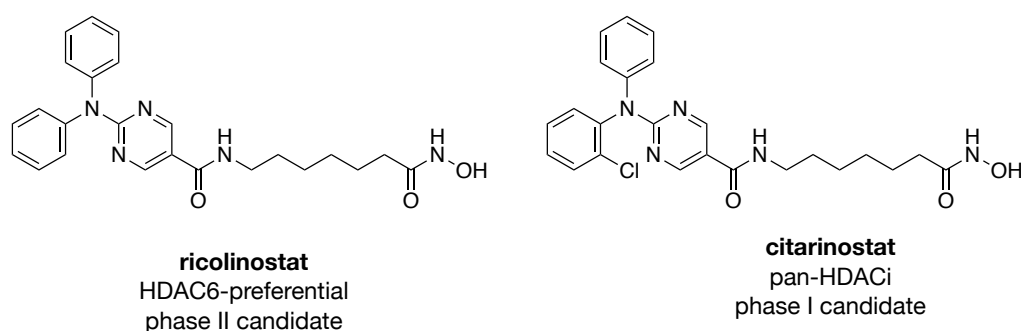


**Figure 1.11.** HDAC6-preferential drug candidates in clinical trials.

To date, the majority of preclinical attempts towards HDAC6i focuses on targeting the second catalytic domain, CD2. An exception is the work of Arrowsmith and co-workers who pioneered in the design of HDAC6 UBD inhibitors in 2017 (Harding et al. 2017; de Freitas et al. 2018).

Apart from clinical and preclinical candidates, there are several hydroxamate-based tool compounds (Figure 1.12) that are frequently used for experimental purposes. Some examples for HDAC6i are tubacin with its large, bifurcated capping group, the bulky tubastatin A, nexturastat A, and HPOB (Wong et al. 2003; Bergman et al. 2012; Lee et al. 2013; Butler et al. 2010). The linear antifungal trichostatin A features an olefinic linker and acts as a potent pan-inhibitor (Vigushin et al. 2001).

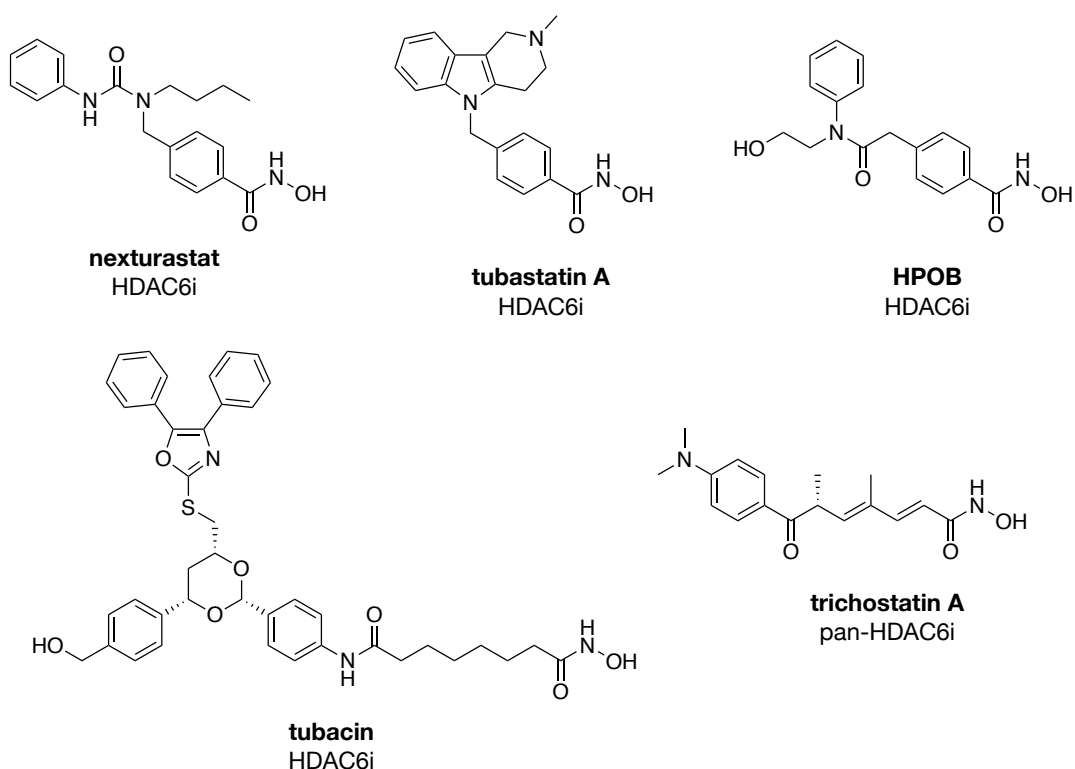


**Figure 1.12.** HDAC6-preferential tool compounds for research purposes.

Beside therapy, HDACi may also be used for diagnostic purposes. Attempts to develop adamantyl-capped radiolabelled HDACi as probes for positron emission tomography (PET) by Hooker and colleagues yielded the brain-penetrant and radiofluorinated HDAC6i [ $^{18}\text{F}$ ]bavarostat and the non-selective phase I candidate [ $^{11}\text{C}$ ]martinostat (Figure 1.13; Strebl et al. 2017; Wang et al. 2014).

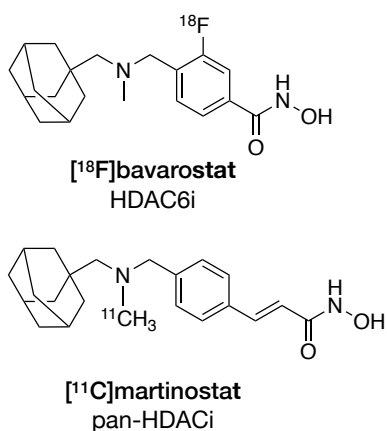


**Figure 1.13.** Radiolabelled HDACi as PET probes.

### 1.2.5 The structure and catalytic mechanism of HDAC6

Featuring two catalytic domains, CD1 and CD2, and a zinc finger capable of binding polyubiquitin chains, HDAC6 is unique among HDACs. Although both catalytic domains appear to be fully functional, there is yet no information on biological substrates of CD1 so that the catalytic activity elucidated so far is generally attributed to CD2 (Osko & Christianson 2019). Following the characterisation of both zebrafish (*Danio rerio*) and human CD1 and CD2 by X-ray crystallography, Christianson and colleagues point out

structural differences between the two domains (Hai & Christianson 2016; Osko & Christianson 2019).

Possibly acting as gatekeepers in CD1, Tyr225 and Lys353 are proposed to account for the narrow substrate specificity with a preference for peptides carrying a C-terminal acetyllysine residue and a free  $\alpha$ -carboxylate group (Osko & Christianson 2019). In CD2, the respective Lys353 is replaced by a leucine, but substrate specificity is instead conferred by the two loop pockets L1 and L2 which define a binding site for bifurcated capping groups in the entrance area (Hai & Christianson 2016; Osko & Christianson 2019). Also, sitting between L1 and L2, Ser531 is proposed to serve as a gatekeeper with the ability to form hydrogen bonds with preferred substrates (Osko & Christianson 2020; Porter et al. 2017). In CD1, the binding site was found to be wider than in CD2, thus allowing for larger aromatic substrates in the tunnel area between the entrance and the active site (Osko & Christianson 2019). With regard to drug design, the narrow tunnel of CD2 may be of interest as it seems to be an ideal match for benzylic linkers that can be stabilised by  $\pi$ - $\pi$  interactions with two surrounding phenylalanine residues (Figure 1.14; Porter et al. 2018; Osko et al. 2020; Hai & Christianson 2016). Compared to the aliphatic linker of vorinostat which is known to undergo metabolic cleavage, benzylic linkers could moreover help improve the pharmacokinetic profiles of the resulting drugs (Ho et al. 2020).

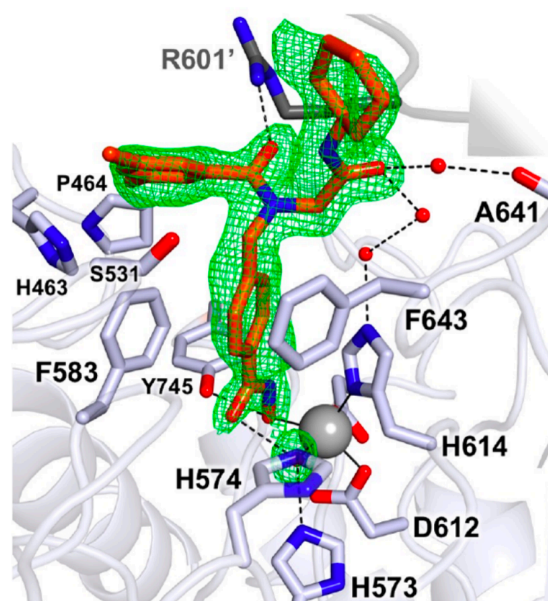
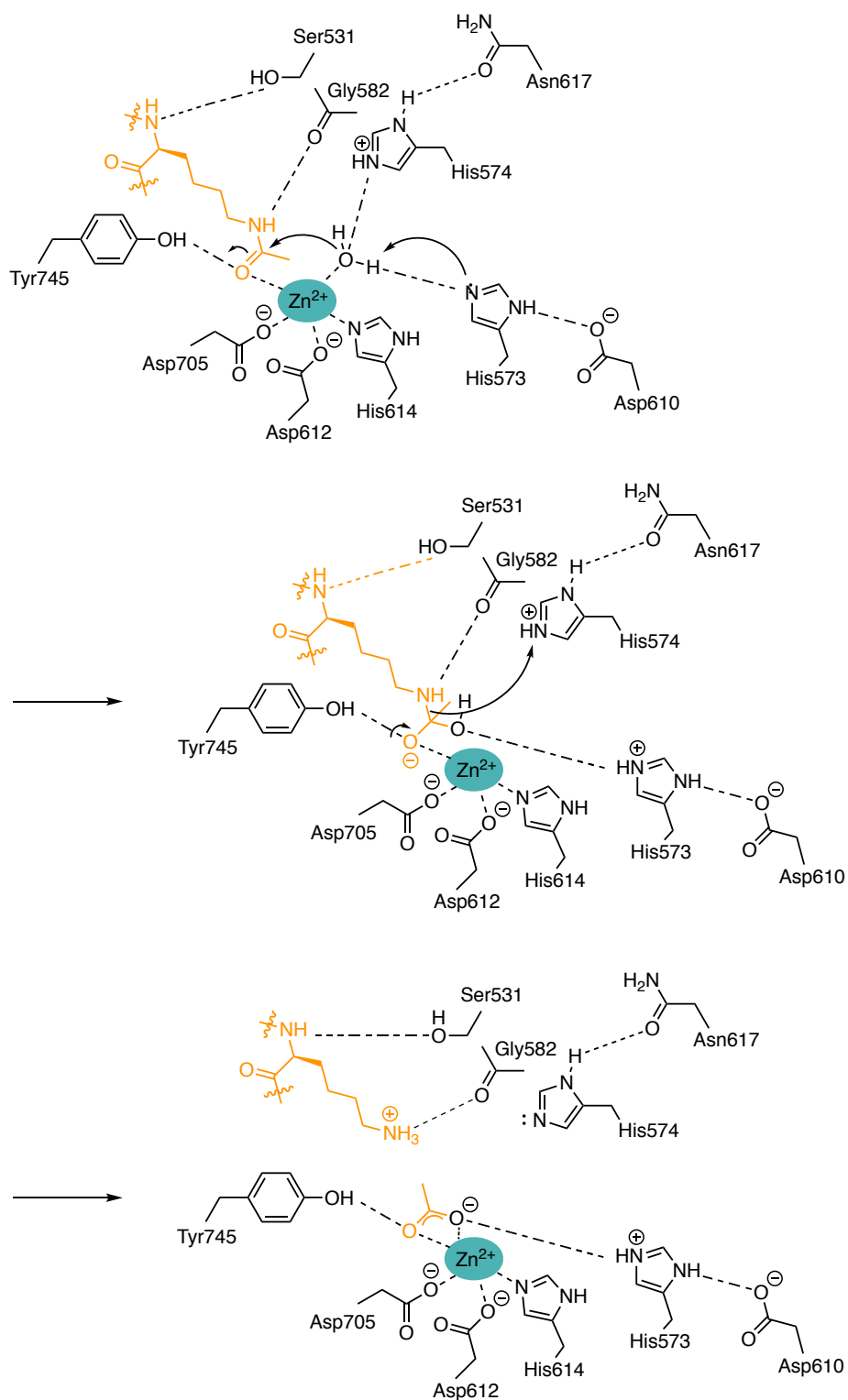


**Figure 1.14.** Polder omit map of a peptoid-based HDACi (orange; see chapter 3) in complex with zCD2 (PDB ID: 6DVL). The benzyl linker is sandwiched between two phenylalanine residues, F643 and F583. The picture was created by the Christianson group, University of Pennsylvania. Adapted and reprinted with permission from Porter NJ, Osko JD, Diedrich D, Kurz T, Hooker JM, Hansen FK, Christianson DW. 2018. Histone deacetylase 6-selective inhibitors and the influence of capping groups on hydroxamate-zinc denticity. *J Med Chem* **61**: 8054–8060. Copyright (2018) American Chemical Society.

Since the zinc-binding sites were found to be identical in both domains, Christianson and colleagues conclude that the catalytic functions are likely to follow the same mechanism (Osko & Christianson 2019). For CD2, the catalytic process (Scheme 1.3) was analysed by X-ray crystallography of zebrafish HDAC6 (zCD2) because the highly conserved active site

resembles its human counterpart (*hCD2*) with only minor, irrelevant differences outside the catalytic centre (Hai & Christianson 2016). Inspired by the natural substrate  $\alpha$ -tubulin, acetyllysine was used to trace the deacetylation process (Hai & Christianson 2016).



**Scheme 1.3.** Catalytic mechanism of HDAC6 zCD2 with acetyllysine depicted in orange. Adapted from Hai & Christianson 2016.



The catalytic mechanism leads to the removal of an acetyl group from the lysine substrate and begins with His573 deprotonating a water molecule in close proximity to the zinc ion. Upon deprotonation, the newly generated hydroxide binds to the carbonyl function of the acetyl group whose coordination to the zinc ion activates it towards nucleophilic attack. Thus, a tetrahedral intermediate arises near His574 and is stabilised by hydrogen bonds between the nitrogen of the substrate and the adjacent Gly582 as well as between the oxyanion, His573 and Tyr745. In the last step, regeneration of the carbonyl function induces the release of the formerly acetylated lysine which, in turn, accepts a proton from His574 to leave the acetate anion coordinated between the zinc ion, Tyr745, and His573 (Hai & Christianson 2016).

In addition to its catalytic domains, HDAC6 exerts some of its activity through the UBD. Zhai and co-workers used X-ray crystallography and biochemical experiments to reveal an active site containing three zinc ions that specifically gather unanchored ubiquitin C-terminal diglycine motifs from solvent-exposed sites of protein aggregates in order to initiate aggresome-mediated degradation (Ouyang et al. 2012). Additional crystal structures of the ZnF were provided by Arrowsmith and colleagues (Harding et al. 2017; de Freitas et al. 2018).

## 1.3 The 26S proteasome

### 1.3.1 Protein expression and cellular protein disposal systems

The viability of cells depends on the complex balance and functioning of various proteins. In eukaryotes, the synthesis of every protein starts in the nucleus where transcription factors control the transcription of a DNA-encoded gene into the corresponding mRNA molecule (Latchman 1997). The transcription process is executed by RNA-polymerases and followed by several post-transcriptional modifications, such as capping, polyadenylation, and splicing, that are necessary to remove dispensable residues in order to optimise the mRNA for the translation process in the cytosol (Latchman 1997). In presence of the ribosome, which recognises start and stop codons marking the relevant section, the genetic information transferred by the mRNA is then translated into a chain of amino acids. Acting as the protein primary structure, this peptide chain is subjected to multiple post-translational modifications which include the addition and alteration of functional groups. By forming intramolecular hydrogen bonds between NH and OH groups in the next step, the peptide adopts a locally-occurring three-dimensional shape which is known as the secondary structure, typically an  $\alpha$ -helix or a  $\beta$ -sheet (Kabsch & Sander 1983). Additional intramolecular interactions, e.g. hydrophobic or electrostatic interactions between amino acid residues and disulfide bridges, contribute to the formation of the tertiary structure that ultimately defines the protein's biological function (Konno et al. 2019). Proteins possessing several polypeptide chains or protein complexes may then assemble to form non-covalent quaternary structures (Sund & Weber 1966).

As the structures of larger proteins appear to be somewhat fragile and therefore prone to undergoing misfolding or aggregation, the essential process of protein folding is usually assisted by chaperonins and the ATP-dependent heat shock proteins Hsp70 and Hsp90 which act as chaperones (Kim et al. 2013). Apart from facilitating the formation of newly expressed proteins, chaperones ensure the proper refolding of proteins after the passage of cellular membranes. If overexpressed in response to oxidative stress, they are supposed to prevent the aggregation of hydrophobic protein sections exposed to the solvent (Kim et al. 2013).

In the case of protein damage, denaturation, deficient protein folding, or in the event that a protein is no longer required, polyubiquitin chains are attached to tag the protein for designated degradation (Lecker et al. 2006; Tanaka 2009). Requiring a network of ubiquitin-

related enzymes, this process involves E1 for activation, E2 for conjugation, and E3 for ligation (Lecker et al. 2006; Tanaka 2009). Once ubiquitinated, the proteins are subjected to digestion by the aggresome-autophagy pathway or, more significantly, the 26S proteasome as a part of the ubiquitin-proteasome system (UPS). Generally considered to be the most important non-lysosomal proteolytic pathway, the 26S proteasome manages the degradation of proteins into oligopeptides assembling up to 25 amino acids in length (Lecker et al. 2006). Throughout all tissues, the crucial degradation step of this process takes place in the 20S core particle (CP) of the proteasome, but depending on the circumstances, different types of proteasomes can be involved (Huber & Groll 2012). Among the three proteasomes yet found in humans, both the immunoproteasome (iCP) and the thymoproteasome (tCP) participate in immune responses, but for the latter, this action is limited to cortical thymic epithelial cells (Murata et al. 2018). The constitutive proteasome (cCP), on the other hand, is the most common UPS-related protease in vertebrates and thus found in most cells (Huber & Groll 2012; Murata et al. 2018).

### 1.3.2 Structure and catalytic mechanism

In 1995, Huber et al. reported on the X-ray crystal structure of the proteasome isolated from the archaeobacterium *Thermoplasma acidophilum* (Löwe et al. 1995). Over the following years, this work was complemented by X-ray structures of yeast, bacterial (*Mycobacterium tuberculosis*), and mammalian (rat, rabbit, mouse, bovine) proteasomes which were found to exhibit high homologies to the human 20S CPs (Huber et al. 2015; Groll et al. 1997; Hsu et al. 2017; Vimer et al. 2020; Huber et al. 2012; Unno et al. 2002). Having remained a challenge for a long time, the crystallisation of the human proteasome was not realised until 2015 when crystal structures of the human cCP alone and in complex with the FDA-approved inhibitor carfilzomib were finally solved (Harshbarger et al. 2015).

Adopting the form of a large, hollow, cylindrical multienzyme complex in the cytosols and nuclei of all

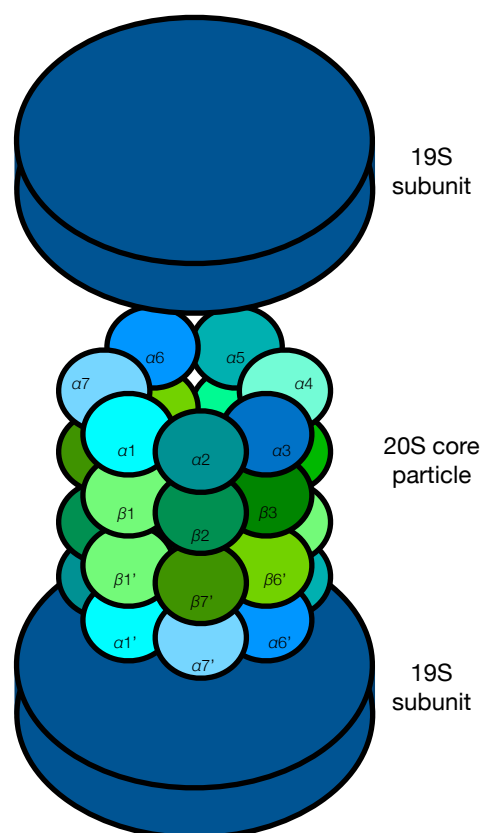
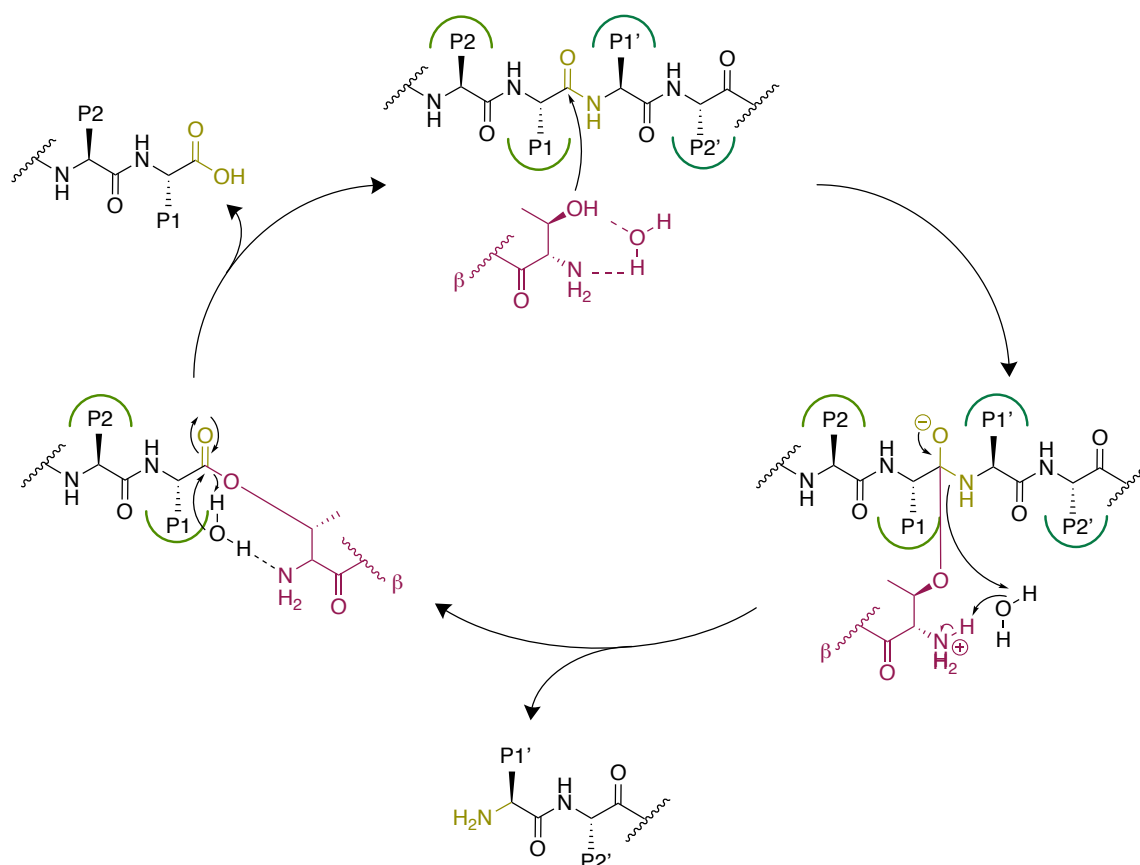


**Figure 1.15.** Structure of the subunits forming the 26S proteasome.

cells, the 26S proteasome adds up to a mass of 2500 kDa and features different subunits (Figure 1.15) that are named in accordance with their Svedberg sedimentation coefficients (Zhang et al. 2013; Groll & Huber 2004; Lecker et al. 2006). The protein degradation unit hosts the active sites and is situated in the 20S CP which, in turn, is capped by ATP-dependent 19S regulatory particles that are each built by an ATPase (Rpt)-containing base and a non-ATPase (Rpn)-containing lid (Lander et al. 2012; Rosenzweig et al. 2008). Located at either or both sides, the 19S regulatory particles enable the recognition of ubiquitinated proteins and manage their deubiquitination, unfolding, and selective access to the degradation chamber through a narrow gate (Lecker et al. 2006; Tanaka 2009). The 20S CP is formed by four layers of two identical  $\alpha$ -rings on the outside and two equally identical  $\beta$ -rings on the inside; each of which is further divided into seven subunits (Beck et al. 2012; Kisselev et al. 2012).



**Scheme 1.4.** Catalytic mechanism of the 20S CP adapted from Kisselev et al. 2012. The catalytically active Thr1 residue is highlighted in red; the cleavable amide bond of the protein substrate (black) is depicted in olive.

Sitting in the middle of the 20S CP, the  $\beta$ -subunits  $\beta 1$ ,  $\beta 2$  and  $\beta 5$  execute the proteolytic activity through Thr1 residues (Scheme 1.4; Beck et al. 2012). The nucleophilic hydroxy

group of Thr1 attacks the amide groups of proteins, whereupon the N-terminus accepts emerging protons shuttled by assembled water molecules (Beck et al. 2012; Kisselev et al. 2012).

Once transferred to the active site, the unfolded protein adopts an antiparallel  $\beta$ -sheet conformation, thus allowing for the protein side chains, which are generally referred to as P1–P4, to be accommodated in the active site's corresponding specificity pockets S1–S4 (Beck et al. 2012). Since the catalytically

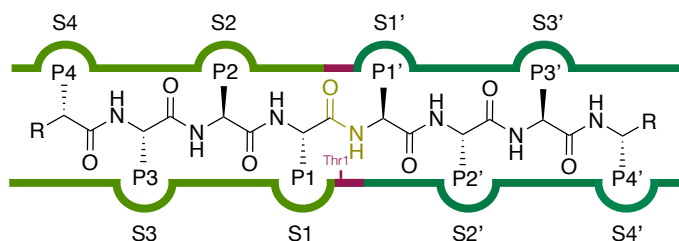


**Figure 1.16.** Structure of the 20S CP cleaving unit with specificity pockets S1–S4 and S1'–S4'. The catalytically active Thr1 residue is depicted in red.

active Thr1 is located behind the S1 pocket (Figure 1.16), an analysis of suitable P1 residues was conducted to illuminate the cleavage preferences of each  $\beta$ -subunit (Groll & Huber 2004). As a result, the  $\beta$ 1c subunits are classified to exert caspase-like (CL) activity due to their preferred breaking of peptide bonds after acidic side chains (Groll & Huber 2004). Associated with trypsin-like (TL) activity,  $\beta$ 2c subunits cleave a broad spectrum of basic residues as well as large, nonpolar groups, like leucine, tyrosine, or phenylalanine (Huber et al. 2015). The nature of the S1 pocket in  $\beta$ 5c subunits, in contrast, matches small, non-polar side chains and corresponds to chymotrypsin-like (ChTL) or small neutral amino acid preferring (SnAAP) activity (Huber & Groll 2012; Groll & Huber 2004; Beck et al. 2012).

On the whole, the 26S proteasome is equipped to process a variety of substrates. The peptide fragments and monomeric ubiquitin that remain after the degradation process are further digested by endopeptidases and aminopeptidases so as to recycle amino acids for reuse in the cell (Lecker et al. 2006).

### 1.3.2 Targeting of the 20S CP in cancer therapy

The 26S proteasome protects cells from apoptosis due to proteotoxic stress and is therefore especially crucial to fast-proliferating tumour cells (Manasanch & Orłowski 2017). By degrading particular proteins, it may moreover serve to regulate cellular mechanisms. One example of a protein controlled by the 26S proteasome is the nuclear factor kappa-B (NF- $\kappa$ B) which acts as a transcription factor involved in immune responses and tumourigenic events (Orłowski & Baldwin 2002; Manasanch & Orłowski 2017). Processed by the 26S proteasome, the degradation of the natural inhibitor I $\kappa$ B leads to the translocation of NF- $\kappa$ B

to the nucleus where it assumes its role in gene expression, thereby contributing to angiogenesis, proliferation, metastasis, and the suppression of apoptosis (Orlowski & Baldwin 2002; Manasanch & Orlowski 2017). In cancer therapy, targeting those processes has become a priority which can be accomplished by inhibiting the 26S proteasome with a special focus on the 20S CP.

As a protease, the 20S CP preferably interacts with peptides and indeed, this specification also predefines the nature of inhibitors which typically evolve from the field of small peptidomimetics (Huber & Groll 2012). Depending on the interaction with the active site, 20S CPi are generally classified as covalent or non-covalent inhibitors. The covalent occupation of the active site usually occurs after electrophilic reactions with the Thr1 residue near the S1 pocket and may be of a reversible or irreversible nature (Blackburn et al. 2012). Non-covalent inhibitors, in contrast, rely on high affinities between the P1–P4 residues and the corresponding binding pockets S1–S4 (Blackburn et al. 2012). Due to the highly conserved structures of the three different 20S CP types, e.g. the tCP, the iCP, and the cCP, selective addressing of a particular subunit of either proteasome is challenging and requires detailed structural knowledge and careful fine-tuning of each binding site (Huber et al. 2015). As a consequence of their capability to host and process the majority of peptides, the CL-like  $\beta 5$  subunits of the iCP and especially the cCP have become the primary proteasome-related targets in recent drug discovery.

Using crystallographic data of the 20S CP from yeast and inhibition assays in presence of the human counterpart, Groll and colleagues undertook comprehensive studies on substrate preferences and concluded that alanine may be a P1 residue with high selectivity for  $\beta 5c$  as its interactions with the adjacent Met45 differ from those in  $\beta 5i$  (Huber et al. 2015; Xin et al. 2016). Hydrophobic contacts of the larger, aromatic phenylalanine and additional hydrogen bonds of tyrosine in P1 did, in turn, appear to increase the affinity to both  $\beta 5$  subunits (Huber et al. 2015). Large, but non-aromatic, a P1 leucine featuring an *iso*-propyl group displayed a 17-fold preference for  $\beta 5c$  over  $\beta 5i$  and is therefore a common motif of cCP inhibitors, including all three FDA-approved 20S CPi (Huber et al. 2015). In absence of a defined S2 pocket, the nature of the P2 residue seemed to have no significant impact on the affinity to either of the  $\beta 5$  subunits, except for the stabilisation of larger, aromatic groups by the adjacent Cys48 residue of the iCP (Huber et al. 2015; Beck et al. 2012). In agreement with Blackburn et al. who suggested the neopentylamide group as an ideal  $\beta 5c$ -selective P3 residue (Figure 1.17), Groll and co-workers emphasise the high affinity of the equally hydrophobic and branched *iso*-propyl group to the S3 pocket (Blackburn et al. 2012; Huber

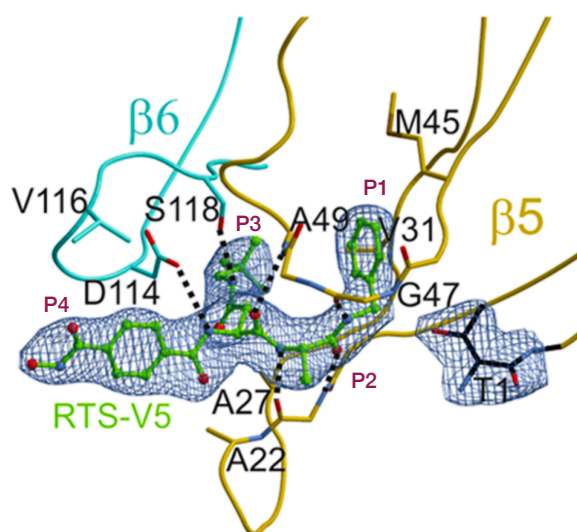


**Figure 1.17.** The dual HDAC/20S CP inhibitor RTS-V5 (green; see chapter 4) featuring a P3 neopentylamide group in complex with  $\beta 5c$  from yeast 20S CP (PDB ID: 6H39). The P2 and P4 residues are solvent-exposed. The picture was created by the Groll group, TU München. Adapted and reprinted with permission from Bhatia S, Krieger V, Groll M, Osko JD, Reßing N, Ahlert H, Borkhardt A, Kurz T, Christianson DW, Hauer J, Hansen FK. 2018. Discovery of the first-in-class dual histone deacetylase-proteasome inhibitor. *J Med Chem* **61**: 10299–10309. Copyright (2018) American Chemical Society.

in the active site (Huber & Groll 2012). Although this type of drug-target interaction is highly effective in terms of reducing proteasome activity, there are serious drawbacks associated with permanent proteasome inhibition in chemotherapy (Beck et al. 2012). The high affinity of the ligands to the 20S CP in healthy tissue results in poor distribution to the designated malignant targets (Huber & Groll 2012; Beck et al. 2012). This effect further entails a short

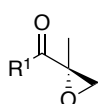


**Figure 1.18.** Structure of the irreversible covalent  $\alpha',\beta'$ -epoxyketone.

half-life, increased drug resistance due to upregulated proteasome expression and higher activity of alternative pathways (Huber & Groll 2012; Beck et al. 2012; Manasanch & Orłowski 2017). Permanent but selective inhibition of the  $\beta 5$  subunit is nevertheless considered desirable for chemotherapy as it appears to induce higher toxicity in tumour cells than in healthy tissue (Groen et al. 2019).

et al. 2015). An additional screening of different P4 groups in the  $\beta 5c$  binding site revealed a preference for bulky, aromatic groups, in spite of the ill-defined nature of the S4 pocket (Blackburn et al. 2010a). Based on the comparison of crystal structures of both human cCP and mouse iCP in complex with the site-specific, covalent inhibitors PR-957 and carfilzomib, respectively, Sacchetti and co-workers attributed the latter's selectivity for the iCP to its small alanine and morpholine residues in P3 and P4 (Harshbarger et al. 2015). Carfilzomib, featuring a P3 leucine and a P4 phenyl group, displays a higher affinity to the  $\beta 5c$  subunit (Harshbarger et al. 2015).

An example for potent, irreversible 20S CP inhibitors are  $\alpha',\beta'$ -epoxyketones (Figure 1.18) functioning as precursors to the formation of stable morpholine rings

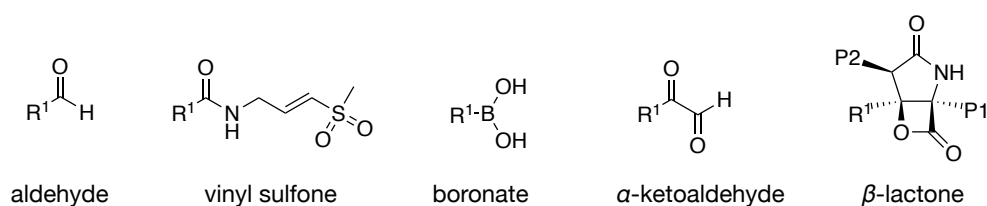


**Figure 1.19.** Electrophilic warheads of reversible covalent 20S CPI (Huber & Groll 2012).

Reversible covalent inhibitors typically comprise electrophilic warheads, such as aldehydes, vinyl sulfones, boronates,  $\alpha$ -ketoaldehydes, and  $\beta$ -lactones (Figure 1.19), which disassociate from the target in a time-dependent manner (Kisselev et al. 2012). Being non-permanent, this mode of inhibition allows for an increased chance of activity in the tumour tissue with a minimised risk of proteasome overexpression (Kisselev et al. 2012; Blackburn et al. 2010b).

Despite their high therapeutic potential, only three 20S CPI have yet been approved by the FDA (Figure 1.20). Two of those, bortezomib and ixazomib, are boronic acids belonging to the group of reversible covalent inhibitors. The third drug, the  $\alpha',\beta'$ -epoxyketone carfilzomib, is a second-generation 20S CPI derived from the natural compound epoxomicin and acts as a permanent inhibitor which is only recommended for patients who have received a minimum of two prior therapies including bortezomib (Groen et al. 2019). So far, clinical application of the three inhibitors is limited to haematological cancers, e.g. multiple myeloma for all three drugs and mantle cell lymphoma in the case of bortezomib, because promising *in vitro* activities against solid tumour cell lines did not correspond to improved outcomes in clinical trials (Roeten et al. 2018; Manasanch & Orlowski 2017). Apart from complications due to side-effects, several factors affecting the efficacy in solid tumours have been proposed. Unlike blood cancers in which both  $\beta 5c$  and  $\beta 5i$  represent valuable targets, solid tumours are presumed to mainly express the cCP which renders them susceptible to drug

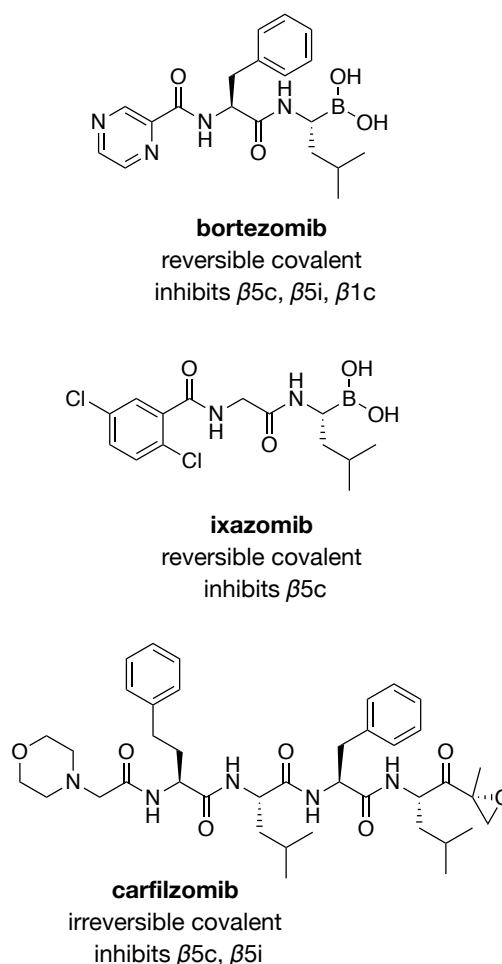


**Figure 1.20.** FDA-approved 20S CPI.

Unlike blood cancers in which both  $\beta 5c$  and  $\beta 5i$  represent valuable targets, solid tumours are presumed to mainly express the cCP which renders them susceptible to drug



resistance (Roeten et al. 2018). Interactions of the drug with healthy cells could moreover limit the dose reaching the malignant cells. In the long term, this complication could be overcome by developing new administration methods allowing for selective addressing of the tumour (Roeten et al. 2018), but meanwhile, the scope for tackling either resistance or distribution issues by dose increase is limited as increased off-target interactions may elicit severe side effects (Manasanch & Orlowski 2017; Beck et al. 2012). One example of such, the peripheral neuropathy, appears to be the most common adverse event associated with unintended inhibition of non-proteasome targets and affects a large majority of bortezomib-treated multiple myeloma patients (Groen et al. 2019; Huber & Groll 2012). Other frequently observed complications include neutropenia, thrombocytopenia, nausea, diarrhoea, and fatigue (Manasanch & Orlowski 2017). Interestingly, after application of the  $\beta$ 5c-preferential carfilzomib, the risk of peripheral neuropathy seemed to decrease while cardiovascular adverse effects became more likely (Groen et al. 2019).

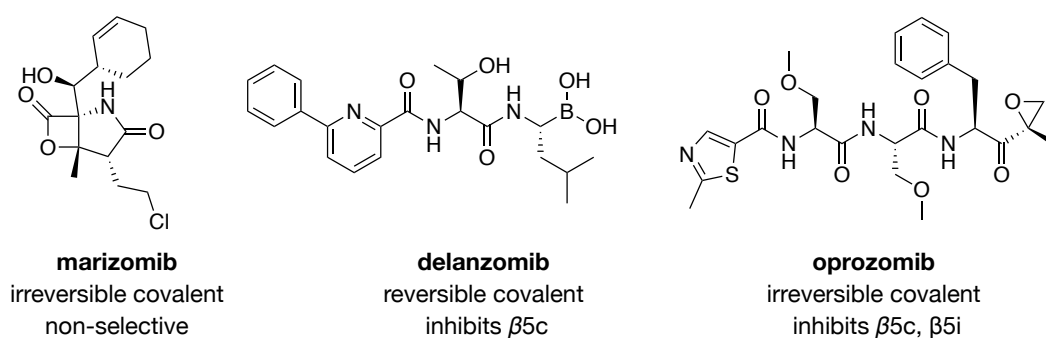


**Figure 1.21.** 20S CPI in phase II clinical trials.

In addition to the approved drugs, there are several second-generation 20S CPI under clinical investigation against haematological and solid cancers (Figure 1.21). These include the natural  $\beta$ -lactone marizomib acting as an irreversible pan-inhibitor of proteasome subunits, the  $\beta$ 5c-selective boronic acid delanzomib, and the  $\alpha',\beta'$ -epoxyketone oprozomib with selectivity for  $\beta$ 5c and  $\beta$ 5i. A growing toolbox of compounds offering further means to evaluate the effects of proteasome inhibition on preclinical stage contains the reversible covalent peptide aldehyde MG-132 and the non-covalent inhibitor ML-16 (Figure 1.22; Palombella et al. 1994; Blackburn et al. 2010b).

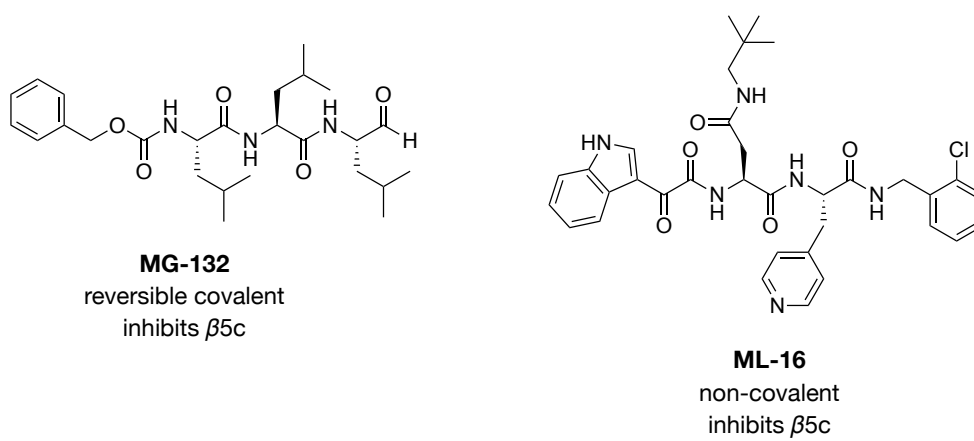


**Figure 1.22.** Tool 20S CPI for research purposes.

## 1.4 References

Adalbert R, Kaieda A, Antoniou C, Loreto A, Yang X, Gilley J, Hoshino T, Uga K, Makhija MT, Coleman MP. 2020. Novel HDAC6 inhibitors increase tubulin acetylation and rescue axonal transport of mitochondria in a model of Charcot–Marie–Tooth type 2F. *ACS Chem Neurosci* **11**: 258–267.

Aldana-Masangkay GI, Sakamoto KM. 2011. The role of HDAC6 in cancer. *J Biomed Biotechnol* **2011**: 875824.

Aramsangtienchai P, Spiegelman NA, He B, Miller SP, Dai L, Zhao Y, Lin H. 2016. HDAC8 catalyzes the hydrolysis of long chain fatty acyl lysine. *ACS Chem Biol* **11**: 2685–2692.

Bandolik JJ, Hamacher A, Schrenk C, Weishaupt R, Kassack MU. 2019. Class I-histone deacetylase (HDAC) inhibition is superior to pan-HDAC inhibition in modulating cisplatin potency in high grade serous ovarian cancer cell lines. *Int J Mol Sci* **20**: 3052.

Banerjee I, Miyake Y, Nobs SP, Schneider C, Horvath P, Kopf M, Matthias P, Helenius A, Yamauchi Y. 2014. Influenza A virus uses the aggresome processing machinery for host cell entry. *Science* **346**: 473–477.

Bannister AJ, Kouzarides T. 2011. Regulation of chromatin by histone modifications. *Cell Res* **21**: 381–395.

Beck P, Dubiella C, Groll M. 2012. Covalent and non-covalent reversible proteasome inhibition. *Biol Chem* **393**: 1101–1120.

Bergman JA, Woan K, Perez-Villarroel P, Villagra A, Sotomayor EM, Kozikowski AP. 2012. Selective histone deacetylase 6 inhibitors bearing substituted urea linkers inhibit melanoma cell growth. *J Med Chem* **55**: 9891–9899.

Bertran A, Khomiak D, Konopka A, Rejmak E, Bulska E, Seco J, Kaczmarek L, Tarragó T, Prades R. 2020. Design and synthesis of selective and blood-brain barrier-permeable hydroxamate-based gelatinase inhibitors. *Bioorg Chem* **94**: 103365.

Bertrand P. 2010. Inside HDAC with HDAC inhibitors. *Eur J Med Chem* **45**: 2095–2116.

Bhatia S, Krieger V, Groll M, Osko JD, Reßing N, Ahlert H, Borkhardt A, Kurz T, Christianson DW, Hauer J, Hansen FK. 2018. Discovery of the first-in-class dual histone deacetylase-proteasome inhibitor. *J Med Chem* **61**: 10299–10309.

Biel M, Wascholowski V, Giannis A. 2005. Epigenetics – an epicenter of gene regulation: Histones and histone-modifying enzymes. *Angew Chem Int Ed* **44**: 3186–3216.

Blackburn C, Barrett C, Blank JL, Bruzzese FJ, Bump N, Dick LR, Fleming P, Garcia K, Hales P, Hu Z, Jones M, Liu JX, Sappal DS, Sintchak MD, Tsu C, Gigstad KM. 2010a. Optimization of a series of dipeptides with a P3 threonine residue as non-covalent inhibitors of the chymotrypsin-like activity of the human 20S proteasome. *Bioorg Med Chem Lett* **20**: 6581–6586.

Blackburn C, Barrett C, Blank JL, Bruzzese FJ, Bump N, Dick LR, Fleming P, Garcia K, Hales P, Jones M, Liu JX, Nagayoshi M, Sappal DS, Sintchak MD, Tsu C, Xia C, Zhou X, Gigstad KM. 2012. Optimization of a series of dipeptides with a P3 b-neopentyl asparagine residue as non-covalent inhibitors of the chymotrypsin-like activity of human 20S proteasome. *Med Chem Commun* **3**: 710–719.

Blackburn C, Gigstad KM, Hales P, Garcia K, Jones M, Bruzzese FJ, Barrett C, Liu JX, Soucy TA, Sappal DS, Bump N, Olhava EJ, Fleming P, Dick LR, Tsu C, Sintchak MD, Blank JL. 2010b. Characterization of a new series of non-covalent proteasome inhibitors with exquisite potency and selectivity for the 20S  $\beta$ 5-subunit. *Biochem J* **430**: 461–476.

Bobrowska A, Paganetti P, Matthias P, Bates GP. 2011. Hdac6 knock-out increases tubulin acetylation but does not modify disease progression in the R6/2 mouse model of Huntington's disease. *PLOS ONE* **6**: e20696.

Bolger TA, Yao T-P. 2005. Intracellular trafficking of histone deacetylase 4 regulates neuronal cell death. *J Neurosci* **25**: 9544–9553.

Bottomley MJ, Lo Surdo P, Di Giovine P, Cirillo A, Scarpelli R, Ferrigno F, Jones P, Neddermann P, De Francesco R, Steinkühler C, Gallinari P, Carfi A. 2008. Structural and functional analysis of the human HDAC4 catalytic domain reveals a regulatory structural zinc-binding domain. *J Biol Chem* **283**: 26694–26704.

Boyault C, Sadoul K, Pabion M, Khochbin S. 2007. HDAC6, at the crossroads between cytoskeleton and cell signaling by acetylation and ubiquitination. *Oncogene* **26**: 5468–5476.

Bressi JC, Jennings AJ, Skene R, Wu Y, Melkus R, De Jong R, O'Connell S, Grimshaw CE, Navre M, Gangloff AR. 2010. Exploration of the HDAC2 foot pocket: Synthesis and SAR of substituted N-(2-aminophenyl)benzamides. *Bioorg Med Chem Lett* **20**: 3142–3145.

Brindisi M, Saraswati AP, Brogi S, Gemma S, Butini S, Campiani G. 2020. Old but gold: Tracking the new guise of histone deacetylase 6 (HDAC6) enzyme as a biomarker and therapeutic target in rare diseases. *J Med Chem* **63**: 23–39.

Bürli RW, Luckhurst CA, Aziz O, Matthews KL, Yates D, Lyons KA, Beconi M, McAllister G, Breccia P, Stott AJ, Penrose SD, Wall M, Lamers M, Leonard P, Müller I, Richardson CM, Jarvis R, Stones L, Hughes S, Wishart G, Haughan AF, O'Connell C, Mead T, McNeil H, Vann J, Mangette J, Maillard M, Beaumont V, Munoz-Sanjuan I, Dominguez C. 2013. Design, synthesis, and biological evaluation of potent and selective class IIa histone deacetylase (HDAC) inhibitors as a potential therapy for Huntington's disease. *J Med Chem* **56**: 9934–9954.

von Burstin J, Eser S, Paul MC, Seidler B, Brandl M, Messer M, von Werder A, Schmidt A, Mages J, Pagel P, Schnieke A, Schmid RM, Schneider G, Saur D. 2009. E-Cadherin regulates metastasis of pancreatic cancer *In vivo* and is suppressed by a SNAIL/HDAC1/HDAC2 repressor complex. *Gastroenterology* **137**: 361–371.

Butler KV, Kalin J, Brochier C, Vistoli G, Langley B, Kozikowski AP. 2010. Rational design and simple chemistry yield a superior, neuroprotective HDAC6 inhibitor, tubastatin A. *J Am Chem Soc* **132**: 10842–10846.

Calzada AA, Todoerti K, Donadoni L, Pellicoli A, Tuana G, Gatta R, Neri A, Finazzi G, Mantovani R, Rambaldi A, Introna M, Lombardi L, Golay J. 2012. The HDAC inhibitor Givinostat modulates the hematopoietic transcription factors NFE2 and C-MYB in JAK2V617F myeloproliferative neoplasm cells. *Exp Hematol* **40**: 634–645.

Chen B, Cepko CL. 2009. HDAC4 regulates neuronal survival in normal and diseased retinas. *Science* **323**: 256–259.

Chen S, Yin C, Lao T, Liang D, He D, Wang C, Sang N. 2015. AMPK-HDAC5 pathway facilitates nuclear accumulation of HIF-1 $\alpha$  and functional activation of HIF-1 by deacetylating Hsp70 in the cytosol. *Cell Cycle* **14**: 2520–2536.

Chun P. 2015. Histone deacetylase inhibitors in hematological malignancies and solid tumors. *Arch Pharm Res* **38**: 933–949.

Cohen TJ, Guo JL, Hurtado DE, Kwong LK, Mills IP, Trojanowski JQ, Lee VMY. 2011. The acetylation of tau inhibits its function and promotes pathological tau aggregation. *Nat Commun* **2**: 252.

Depetter Y, Geurs S, De Vreese R, Goethals S, Vandoorn E, Laevens A, Steenbrugge J, Meyer E, de Tullio P, Bracke M, D'hooghe M, De Wever O. 2019. Selective pharmacological inhibitors of HDAC6 reveal biochemical activity but functional tolerance in cancer models. *Int J Cancer* **145**: 735–747.

Deubzer HE, Schier MC, Oehme I, Lodrini M, Haendler B, Sommer A, Witt O. 2013. HDAC11 is a novel drug target in carcinomas. *Int J Cancer* **132**: 2200–2208.

Diedrich D, Hamacher A, Gertzen CGW, Alves Avelar LA, Reiss GJ, Kurz T, Gohlke H, Kassack MU, Hansen FK. 2016. Rational design and diversity-oriented synthesis of peptoid-based selective HDAC6 inhibitors. *Chem Commun* **52**: 3219–3222.

Ding H, Dolan PJ, Johnson GVW. 2008. Histone deacetylase 6 interacts with the microtubule-associated protein tau. *J Neurochem* **106**: 2119–2130.

Dokmanovic M, Clarke C, Marks PA. 2007. Histone deacetylase inhibitors: Overview and perspectives. *Mol Cancer Res* **5**: 981–989.

Dompierre JP, Godin JD, Charrin BC, Cordelières FP, King SJ, Humbert S, Saudou F. 2007. Histone deacetylase 6 inhibition compensates for the transport deficit in Huntington's disease by increasing tubulin acetylation. *J Neurosci* **27**: 3571–3583.

Emmett MJ, Lazar MA. 2019. Integrative regulation of physiology by histone deacetylase 3. *Nat Rev Mol Cell Biol* **20**: 102–115.

Finnin MS, Donigian JR, Cohen A, Richon VM, Rifkind RA, Marks PA, Breslow R, Pavletich NP. 1999. Structures of a histone deacetylase homologue bound to the TSA and SAHA inhibitors. *Nature* **401**: 188–193.

Fischer A, Sananbenesi F, Mungenast A, Tsai L-H. 2010. Targeting the correct HDAC(s) to treat cognitive disorders. *Trends Pharmacol Sci* **31**: 605–617.

Fischle W, Dequiedt F, Hendzel MJ, Guenther MG, Lazar MA, Voelter W, Verdin E. 2002. Enzymatic activity associated with class II HDACs is dependent on a multiprotein complex containing HDAC3 and SMRT/N-CoR. *Mol Cell* **9**: 45–57.

Francelle L, Outeiro TF, Rappold GA. 2020. Inhibition of HDAC6 activity protects dopaminergic neurons from alpha-synuclein toxicity. *Sci Rep* **10**: 6064.

de Freitas RF, Harding RJ, Franzoni I, Ravichandran M, Mann MK, Ouyang H, Lautens M, Santhakumar V, Arrowsmith CH, Schapira M. 2018. Identification and structure-activity relationship of HDAC6 zinc-finger ubiquitin binding domain inhibitors. *J Med Chem* **61**: 4517–4527.

Fujisawa T, Filippakopoulos P. 2017. Functions of bromodomain-containing proteins and their roles in homeostasis and cancer. *Nat Rev Mol Cell Biol* **18**: 246–262.

Gaisina IN, Tueckmantel W, Ugolkov A, Shen S, Hoffen J, Dubrovskiy O, Mazar A, Schoon RA, Billadeau D, Kozikowski AP. 2016. Identification of HDAC6-selective inhibitors of low cancer cell cytotoxicity. *ChemMedChem* **11**: 81–92.

Gaughan L, Logan IR, Cook S, Neal DE, Robson CN. 2002. Tip60 and histone deacetylase 1 regulate androgen receptor activity through changes to the acetylation status of the receptor. *J Biol Chem* **277**: 25904–25913.

Geng H, Harvey CT, Pittsenbarger J, Liu Q, Beer TM, Xue C, Qian DZ. 2011. HDAC4 protein regulates HIF1 protein lysine acetylation and cancer cell response to hypoxia. *J Biol Chem* **286**: 38095–38102.

Greer EL, Shi Y. 2012. Histone methylation: a dynamic mark in health, disease and inheritance. *Nat Rev Genet* **13**: 343–357.

Gregoretti IV, Lee Y-M, Goodson HV. 2004. Molecular evolution of the histone deacetylase family: functional implications of phylogenetic analysis. *J Mol Biol* **338**: 17–31.

Groen K, van de Donk NWCJ, Stege CAM, Zweegman S, Nijhof IS 2019. Carfilzomib for relapsed and refractory multiple myeloma. *Cancer Manag Res* **11**: 2663–2675.

Groll M, Ditzel L, Löwe J, Stock D, Bochtler M, Bartunik HD, Huber R. 1997. Structure of 20S proteasome from yeast at 2.4 Å resolution. *Nature* **386**: 463–471.

Groll M, Huber R. 2004. Inhibitors of the eukaryotic 20S proteasome core particle: a structural approach. *Biochim Biophys Acta* **1695**: 33–44.

Grozinger CM, Hassig CA, Schreiber SL. 1999. Three proteins define a class of human histone deacetylases related to yeast Hda1p. *Proc Natl Acad Sci* **96**: 4868–4873.

Guan J-S, Haggarty SJ, Giacometti E, Dannenberg J-H, Joseph N, Gao J, Nieland TJF, Zhou Y, Wang X, Mazitschek R, Bradner JE, DePinho RA, Jaenisch R, Tsai L-H. 2009. HDAC2 negatively regulates memory formation and synaptic plasticity. *Nature* **459**: 55–60.

Guo L, Han A, Bates DL, Cao J, Chen L. 2007. Crystal structure of a conserved N-terminal domain of histone deacetylase 4 reveals functional insights into glutamine-rich domains. *PNAS* **104**: 4297–4302.

Hai Y, Christianson DW. 2016. Histone deacetylase 6 structure and molecular basis of catalysis and inhibition. *Nat Chem Biol* **12**: 741–747.

Hai Y, Shinsky SA, Porter NJ, Christianson DW. 2017. Histone deacetylase 10 structure and molecular function as a polyamine deacetylase. *Nat Commun* **8**: 15368.

Harding RJ, de Freitas RF, Collins P, Franzoni I, Ravichandran M, Ouyang H, Juarez-Ornelas KA, Lautens M, Schapira M, von Delft F, Santhakumar V, Arrowsmith CH. 2017. Small molecule antagonists of the interaction between the histone deacetylase 6 zinc-finger domain and ubiquitin. *J Med Chem* **60**: 9090–9096.

Harshbarger W, Miller C, Diedrich C, Sacchettini J. 2015. Crystal structure of the human 20S proteasome in complex with carfilzomib. *Structure* **23**: 418–424.

Heimburg T, Kolbinger FR, Zeyen P, Ghazy E, Herp D, Schmidtkunz K, Melesina J, Shaik TB, Erdmann F, Schmidt M, Romier C, Robaa D, Witt O, Oehme I, Jung M, Sippl W. 2017. Structure-based design and biological characterization of selective histone deacetylase 8 (HDAC8) inhibitors with anti-neuroblastoma activity. *J Med Chem* **60**: 10188–10204.

Hideshima T, Richardson PG, Anderson KC. 2011. Mechanism of action of proteasome inhibitors and deacetylase inhibitors and the biological basis of synergy in multiple myeloma. *Mol Cancer Ther* **10**: 2034–2042.

Ho TCS, Chan AHY, Ganesan A. 2020. Thirty years of HDAC inhibitors: 2020 Insight and hindsight. *J Med Chem* **63**: 12460–12484.

Holdermann I, Meyer NH, Round A, Wild K, Sattler M, Sinning I. 2012. Chromodomains read the arginine code of post-translational targeting. *Nat Struct Mol Biol* **19**: 260–263.

Hook SS, Orian A, Cowley SM, Eisenmann RN. 2002. Histone deacetylase 6 binds polyubiquitin through its zinc finger (PAZ domain) and copurifies with deubiquitinating enzymes. *PNAS* **99**: 13425–13430.

Hsu H-C, Singh PK, Fan H, Wang R, Sukenick G, Nathan C, Lin G, Li H. 2017. Structural basis for the species-selective binding of N,C-capped dipeptides to the *Mycobacterium tuberculosis* proteasome. *Biochemistry* **56**: 324–333.

Hu E, Chen Z, Fredrickson T, Zhu Y, Kirkpatrick R, Zhang GF, Johanson K, Sung CM, Liu R, Winkler J. 2000. Cloning and characterization of a novel human class I histone deacetylase that functions as a transcription repressor. *J Biol Chem* **275**: 15254–15264.

Huang J, Wang L, Dahiya S, Beier UH, Han R, Samanta A, Bergman J, Sotomayor EM, Seto E, Kozikowski AP, Hancock WW. 2017. Histone/protein deacetylase 11 targeting promotes Foxp3+ Treg function. *Sci Rep* **7**: 8626.

Hubbert C, Guardiola A, Shao R, Kawaguchi Y, Ito A, Nixon A, Yoshida M, Wang X-F, Yao T-P. 2002. HDAC6 is a microtubule-associated deacetylase. *Nature* **417**: 455–458.



Huber EM, Basler M, Schwab R, Heinemeyer W, Kirk CJ, Groettrup M, Groll M. 2012. Immuno- and constitutive proteasome crystal structures reveal differences in substrate and inhibitor specificity. *Cell* **148**: 727–738.

Huber EM, de Bruin G, Heinemeyer W, Soriano GP, Overkleeft HS, Groll M. 2015. Systematic analyses of substrate preferences of 20S proteasomes using peptidic epoxyketone inhibitors. *J Am Chem Soc* **137**: 7835–7842.

Huber EM, Groll M. 2012. Inhibitors for the immuno- and constitutive proteasome: Current and future trends in drug development. *Angew Chem Int Ed* **51**: 8708–8720.

Ito K, Yamamura S, Essilfie-Quaye S, Cosio B, Ito M, Barnes PJ, Adcock IM. 2006. Histone deacetylase 2-mediated deacetylation of the glucocorticoid receptor enables NF- $\kappa$ B suppression. *J Exp Med* **203**: 7–13.

Jenke R, Reßing N, Hansen FK, Aigner A, Büch T. 2021. Anticancer therapy with HDAC inhibitors: Mechanism-based combination strategies and future perspectives. *Cancers* **13**: 634.

Jenuwein T, Allis CD. 2001. Translating the histone code. *Science* **293**: 1074–1080.

Jiang Y, Hsieh J. 2014. HDAC3 controls gap 2/mitosis progression in adult neural stem/progenitor cells by regulating CDK1 levels. *PNAS* **111**: 13541–13546.

Johnson CA, White DA, Lavender JS, O'Neill LP, Turner BM. 2002. Human class I histone deacetylase complexes show enhanced catalytic activity in the presence of ATP and co-immunoprecipitate with the ATP-dependent chaperone protein Hsp70. *J Biol Chem* **277**: 9590–9597.

Jones PA, Issa J-PJ, Baylin S. 2016. Targeting the cancer epigenome for therapy. *Nat Rev Genet* **17**: 630–641.

Joosten LAB, Leoni F, Meghji S, Mascagni P. 2011. Inhibition of HDAC activity by ITF2357 ameliorates joint inflammation and prevents cartilage and bone destruction in experimental arthritis. *Mol Med* **17**: 391–396.

Jung KH, Noh JH, Kim JK, Eun JW, Bae HJ, Xie HJ, Chang YG, Kim MG, Park H, Lee JY, Nam SW. 2012. HDAC2 overexpression confers oncogenic potential to human lung cancer cells by deregulating expression of apoptosis and cell cycle proteins. *J Cell Biochem* **113**: 2167–2177.

Jung M, Hoffmann K, Brosch G, Loidl P. 1997. Analogues of trichostatin A and trapoxin B as histone deacetylase inhibitors. *Bioorg Med Chem Lett* **7**: 1655–1658.

Kabsch W, Sander C. 1983. Dictionary of protein secondary structure: Pattern recognition of hydrogen-bonded and geometrical features. *Biopolymers* **22**: 2577–2637.

Kalin JH, Bergman JA. 2013. Development and therapeutic implications of selective histone deacetylase 6 inhibitors. *J Med Chem* **56**: 6297–6313.

Kang Y, Nian H, Rajendran P, Kim E, Dashwood WM, Pinto JT, Boardman LA, Thibodeau SN, Limburg PJ, Löhr CV, Bisson WH, Williams DE, Ho E, Dashwood RH. 2014. HDAC8 and STAT3 repress BMF gene activity in colon cancer cells. *Cell Death Dis* **5**: e1476.

Kawaguchi Y, Kovacs JJ, McLaurin A, Vance JM, Ito A, Yao T-P. 2003. The deacetylase HDAC6 regulates aggresome formation and cell viability in response to misfolded protein stress. *Cell* **115**: 727–738.

Kazantsev AG, Thompson LM. 2008. Therapeutic application of histone deacetylase inhibitors for central nervous system disorders. *Nat Rev Drug Discov* **7**: 854–868.

Kelly RDW, Chandru A, Watson PJ, Song Y, Blades M, Robertson NS, Jamieson AG, Schwabe JWR, Cowley SM. 2018. Histone deacetylase (HDAC) 1 and 2 complexes regulate both histone acetylation and crotonylation *in vivo*. *Sci Rep* **8**: 14690.

Kim YE, Hipp MS, Bracher A, Hayer-Hartl M, Hartl FU. 2013. Molecular chaperone functions in protein folding and proteostasis. *Annu Rev Biochem* **82**: 323–355.

Kisselev AF, van der Linden WA, Overkleeft HS. 2012. Proteasome inhibitors: An expanding army attacking a unique target. *Chem Biol* **19**: 99–115.

Koeneke E, Witt O, Oehme I. 2015. HDAC Family members intertwined in the regulation of autophagy: A druggable vulnerability in aggressive tumor entities. *Cells* **4**: 135–168.

Kong X, Lin Z, Liang D, Fath D, Sang N, Caro J. 2006. Histone deacetylase inhibitors induce VHL and ubiquitin-independent proteasomal degradation of hypoxia-inducible factor 1 $\alpha$ . *Mol Cell Biol* **26**: 2019–2028.

Konno S, Namiki T, Ishimori K. 2019. Quantitative description and classification of protein structures by a novel robust amino acid network: interaction selective network (ISN). *Sci Rep* **9**: 16654.

Kovacs JJ, Murphy PJM, Gaillard S, Zhao X, Wu J-T, Nicchitta CV, Yoshida M, Toft DO, Pratt WB, Yao T-P. 2005. HDAC6 regulates Hsp90 acetylation and chaperone-dependent activation of glucocorticoid receptor. *Mol Cell* **18**: 601–607.

Lahm A, Paolini C, Pallaoro M, Nardi MC, Jones P, Neddermann P, Sambucini S, Bottomley MJ, Lo Surdo P, Carfi A, Koch U, De Francesco R, Steinkühler C, Gallinari P. 2007. Unraveling the hidden catalytic activity of vertebrate class IIa histone deacetylases. *PNAS* **104**: 17335–17340.

Lander GC, Estrin E, Matyskiela ME, Bashore C, Nogales E, Martin A. 2012. Complete subunit architecture of the proteasome regulatory particle. *Nature* **482**: 186–191.

Latchman DS. 1997. Transcription factors: An overview. *Int J Biochem Cell Biol* **29**: 1305–1312.

Lecker SH, Goldberg AL, Mitch WE. 2006. Protein degradation by the ubiquitin–proteasome pathway in normal and disease states. *J Am Soc Nephrol* **17**: 1807–1819.

Lee J, Hong EC, Jeong H, Hwang JW, Kim H, Bae E-K, Ahn JK, Choi Y-L, Han J, Cha H-S, Koh E-M. 2015. A novel histone deacetylase 6-selective inhibitor suppresses synovial inflammation and joint destruction in a collagen antibody-induced arthritis mouse model. *Int J Rheum Dis* **18**: 514–523.

Lee J-H, Mahendran A, Yao Y, Ngo L, Venta-Perez G, Choy ML, Kim N, Ham W-S, Breslow R, Marks PA. 2013. Development of a histone deacetylase 6 inhibitor and its biological effects. *PNAS* **110**: 15704–15709.

de Lera AR, Ganesan A. 2016. Epigenetic polypharmacology: from combination therapy to multitargeted drugs. *Clin Epigenetics* **8**: 105.

Li KW, Wu J, Xing W, Simon JA. 1996. Total synthesis of the antitumor depsipeptide FR-901,228. *J Am Chem Soc* **118**: 7237–7238.

Li Y, Kao GD, Garcia BA, Shabanowitz J, Hunt DF, Qin J, Phelan C, Lazar MA. 2006. A novel histone deacetylase pathway regulates mitosis by modulating Aurora B kinase activity. *Genes Dev* **20**: 2566–2579.

Li Y, Seto E. 2016. HDACs and HDAC inhibitors in cancer development and therapy. *Cold Spring Harb Perspect Med* **6**: a026831.

Lin A, Giuliano CJ, Palladino A, John KM, Abramowicz C, Yuan ML, Sausville EL, Lukow DA, Liu L, Chait AR, Galluzzo ZC, Tucker C, Sheltzer JM. 2019. Off-target toxicity is a common mechanism of action of cancer drugs undergoing clinical trials. *Sci Transl Med* **11**: eaaw8412.

Lin H-S, Hu C-Y, Chan H-Y, Liew Y-Y, Huang H-P, Lepescheux L, Bastianelli E, Baron R, Rawadi G, Clément-Lacroix P. 2007. Anti-rheumatic activities of histone deacetylase (HDAC) inhibitors *in vivo* in collagen-induced arthritis in rodents. *Br J Pharmacol* **150**: 862–872.

Liu T, Wan Y, Xiao Y, Xia C, Duan G. 2020. Dual-target inhibitors based on HDACs: Novel antitumor agents for cancer therapy. *J Med Chem* **63**: 8977–9002.

Löwe J, Stock D, Jap B, Zwickl P, Baumeister W, Huber R. 1995. Crystal structure of the 20S proteasome from the archaeon *T. acidophilum* at 3.4 Å resolution. *Science* **268**: 533–539.

Luan Y, Li J, Bernatchez JA, Li R. 2019. Kinase and histone deacetylase hybrid inhibitors for cancer therapy. *J Med Chem* **62**: 3171–3183.

Luger K, Mäder AW, Richmond RK, Sargent DF, Richmond TJ. 1997. Crystal structure of the nucleosome core particle at 2.8 Å resolution. *Nature* **389**: 251–260.

Luo J, Su F, Chen D, Shiloh A, Gu W. 2000. Deacetylation of p53 modulates its effect on cell growth and apoptosis. *Nature* **408**: 377–381.

Manasanch EE, Orlowski RZ. 2017. Proteasome inhibitors in cancer therapy. *Nat Rev Clin Oncol* **14**: 417–433.

Margolis DM. 2011. Histone deacetylase inhibitors and HIV latency. *Curr Opin HIV AIDS* **6**: 25–29.

Marks PA, Breslow R. 2007. Dimethyl sulfoxide to vorinostat: Development of this histone deacetylase inhibitor as an anticancer drug. *Nat Biotechnol* **25**: 84–90.

McQuown SC, Barrett RM, Matheos DP, Post RJ, Rogge GA, Alenghat T, Mullican SE, Jones S, Rusche JR, Lazar MA, Wood MA. 2011. HDAC3 is a critical negative regulator of long-term memory formation. *J Neurosci* **31**: 764–774.

Methot JL, Chakravarty PK, Chenard M, Close J, Cruz JC, Dahlberg WK, Fleming J, Hamblett CL, Hamill JE, Harrington P, Harsch A, Heidebrecht R, Hughes B, Jung J, Kenific CM, Kral AM, Meinke PT, Middleton RE, Ozerova N, Sloman DL, Stanton MG, Szewczak AA, Tyagarajan S, Witter DJ, Secrist JB, Miller TA. 2008. Exploration of the internal cavity of histone deacetylase (HDAC) with selective HDAC1/HDAC2 inhibitors (SHI-1:2). *Bioorg Med Chem Lett* **18**: 973–978.

Michaelis UR. 2014. Mechanisms of endothelial cell migration. *Cell Mol Life Sci* **71**: 4131–4148.

Mielcarek M, Zielonka D, Carnemolla A, Marcinkowski JT, Guidez F. 2015. HDAC4 as a potential therapeutic target in neurodegenerative diseases: a summary of recent achievements. *Front Cell Neurosci* **9**: 42.

Millard CJ, Watson PJ, Celardo I, Gordiyenko Y, Cowley SM, Robinson CV, Fairall L, Schwabe JWR. 2013. Class I HDACs share a common mechanism of regulation by inositol phosphates. *Mol Cell* **51**: 57–67.

Miller KM, Tjeertes JV, Coates J, Legube G, Polo SE, Britton S, Jackson SP. 2010. Human HDAC1 and HDAC2 function in the DNA-damage response to promote DNA nonhomologous end-joining. *Nat Struct Mol Biol* **17**: 1144–1151.

Mrakovcic M, Kleinheinz J, Fröhlich LF. 2019. p53 at the crossroads between different types of HDAC inhibitor-mediated cancer cell death. *Int J Mol Sci* **20**: 2415.

Murata S, Takahama Y, Kasahara M, Tanaka K. 2018. The immunoproteasome and thymoproteasome: functions, evolution and human disease. *Nat Immunol* **19**: 923–931.

Nakajima H, Kim YB, Terano H, Yoshida M, Horinouchi S. 1998. FR901228, a potent antitumor antibiotic, is a novel histone deacetylase inhibitor. *Exp Cell Res* **241**: 126–133.

Nasu Y, Nishida K, Miyazawa S, Komiyama T, Kadota Y, Abe N, Yoshida A, Hirohata D, Ohtsuka A, Ozaki T. 2008. Trichostatin A, a histone deacetylase inhibitor, suppresses synovial inflammation and subsequent cartilage destruction in a collagen antibody-induced arthritis mouse model. *Osteoarthr Cartil* **16**: 723–732.

Nishida K, Komiyama T, Miyazawa S, Shen Z-N, Furumatsu T, Doi H, Yoshida A, Yamana J, Yamamura M, Ninomiya Y, Inoue H, Asahara H. 2004. Histone deacetylase inhibitor suppression of autoantibody-mediated arthritis in mice via regulation of p16<sup>INK4a</sup> and p21<sup>WAF1/Cip1</sup> expression. *Arthritis Rheum* **50**: 3365–3376.

Oehme I, Lodrini M, Brady NR, Witt O. 2013. Histone deacetylase 10-promoted autophagy as a druggable point of interference to improve the treatment response of advanced neuroblastomas. *Autophagy* **9**: 2163–2165.

Orlowski RZ, and Baldwin AS Jr. 2002. NF- $\kappa$ B as a therapeutic target in cancer. *Trends Mol Med* **8**: 285–389.

Osko JD, Christianson DW. 2019. Structural basis of catalysis and inhibition of HDAC6 CD1, the enigmatic catalytic domain of histone deacetylase 6. *Biochemistry* **58**: 4912–4924.

Osko JD, Christianson DW. 2020. Structural determinants of affinity and selectivity in the binding of inhibitors to histone deacetylase 6. *Bioorg Med Chem Lett* **30**: 127023.

Osko JD, Porter NJ, Reddy PAN, Xiao Y-C, Rokka J, Jung M, Hooker JM, Salvino JM, Christianson DW. 2020. Exploring structural determinants of inhibitor affinity and selectivity in complexes with histone deacetylase 6. *J Med Chem* **63**: 295–308.

Ouyang H, Ali YO, Ravichandran M, Dong A, Qiu W, MacKenzie F, Dhe-Paganon S, Arrowsmith CH, Zhai RG. 2012. Protein aggregates are recruited to aggresome by histone deacetylase 6 via unanchored ubiquitin C termini. *J Biol Chem* **287**: 2317–2327.

Owen DJ, Ornaghi P, Yang JC, Lowe N, Evans PR, Ballario P, Neuhaus D, Filetici P, Travers AA. 2000. The structural basis for the recognition of acetylated histone H4 by the bromodomain of histone acetyltransferase Gcn5p. *EMBO J* **19**: 6141–6149.

Ozaki K, Kishikawa F, Tanaka M, Sakamoto T, Tanimura S, Kohno M. 2008. Histone deacetylase inhibitors enhance the chemosensitivity of tumor cells with cross-resistance to a wide range of DNA-damaging drugs. *Cancer Sci* **99**: 376–384.

Palombella VJ, Rando OJ, Goldberg AL, Maniatis T. 1994. The ubiquitin-proteasome pathway is required for processing the NF- $\kappa$  B1 precursor protein and the activation of NF- $\kappa$  B. *Cell* **78**: 773–785.

Paris M, Porcelloni M, Binaschi M, Fattori D. 2008. Histone Deacetylase Inhibitors: From Bench to Clinic. *J Med Chem* **51**: 1505–1529.

Parra M, Verdin E. 2010. Regulatory signal transduction pathways for class IIa histone deacetylases. *Curr Opin Pharmacol* **10**: 454–460.

Porter NJ, Mahendran A, Breslow R, Christianson DW. 2017. Unusual zinc-binding mode of HDAC6-selective hydroxamate inhibitors. *PNAS* **114**: 13459–13464.

Porter NJ, Osko JD, Diedrich D, Kurz T, Hooker JM, Hansen FK, Christianson DW. 2018. Histone deacetylase 6-selective inhibitors and the influence of capping groups on hydroxamate-zinc denticity. *J Med Chem* **61**: 8054–8060.

Qian DZ, Kachhap SK, Collis SJ, Verheul HMW, Carducci MA, Atadja P, Pili R. 2006. Class II histone deacetylases are associated with VHL-independent regulation of hypoxia-inducible factor 1 $\alpha$ . *Cancer Res* **66**: 8814–8821.

Ragot A, Pietropaolo S, Vincent J, Delage P, Zhang H, Allinquant B, Leinekugel X, Fischer A, Cho YH. 2015. Genetic deletion of the histone deacetylase 6 exacerbates selected behavioral deficits in the R6/1 mouse model for Huntington's disease. *Brain Behav* **5**: e00361.

Reßing N, Sönnichsen M, JD Osko, Schöler A, Schliehe-Diecks J, Skerhut A, Borkhardt A, Hauer J, Kassack MU, Christianson DW, Bhatia S, Hansen FK. 2020. Multicomponent synthesis, binding mode, and structure-activity relationship of selective histone deacetylase 6 (HDAC6) inhibitors with bifurcated capping groups. *J Med Chem* **63**: 10339–10351.

Roche J, Bertrand P. 2016. Inside HDACs with more selective HDAC inhibitors. *Eur J Med Chem* **121**: 451–483.

Roeten MSF, Cloos J, Jansen G. 2018. Positioning of proteasome inhibitors in therapy of solid malignancies. *Cancer Chemother Pharmacol* **81**: 227–243.

Rosenzweig R, Osmulski PA, Gaczynska M, Glickman MH. 2008. The central unit within the 19S regulatory particle of the proteasome. *Nat Struct Mol Biol* **15**: 573–580.

Rossetto D, Avvakumov N, Côté J. 2012. Histone phosphorylation: a chromatin modification involved in diverse nuclear events. *Epigenetics* **7**: 1098–1108.

Rothbart SB, Strahl BD. 2014. Interpreting the language of histone and DNA modifications. *Biochim Biophys Acta, Gene Regul Mech* **1839**: 627–643.

Sandor V, Senderowicz A, Mertins S, Sackett D, Sausville E, Blagosklonny MV, Bates SE. 2000. P21-dependent G<sub>1</sub>arrest with downregulation of cyclin D1 and upregulation of cyclin E by the histone deacetylase inhibitor FR901228. *Br J Cancer* **83**: 817–825.

Santoro F, Botrugno OA, Dal Zuffo R, Pallavicini I, Matthews GM, Cluse L, Barozzi I, Senese S, Fornasari L, Moretti S, Altucci L, Pelicci PG, Chiocca S, Johnstone RW, Minucci S. 2013. A dual role for Hdac1: oncosuppressor in tumorigenesis, oncogene in tumor maintenance. *Blood* **121**: 3459–3468.

Schuetz A, Min J, Allali-Hassani A, Schapira M, Shuen M, Loppnau P, Mazitschek R, Kwiatkowski NP, Lewis TA, Maglathin RL, McLean TH, Bochkarev A, Plotnikov AN, Vedadi M, Arrowsmith CH. 2008. Human HDAC7 harbors a class IIa histone deacetylase-specific zinc binding motif and cryptic deacetylase activity. *J Biol Chem* **283**: 11355–11363.

Sellmer A, Stangl H, Beyer M, Grünstein E, Leonhardt M, Pongratz H, Eichhorn E, Elz S, Striegl B, Jenei-Lanzl Z, Dove S, Straub RH, Krämer OH, Mahboobi S. 2018. Marbostat-100 defines a new class of potent and selective antiinflammatory and antirheumatic histone deacetylase 6 inhibitors. *J Med Chem* **61**: 3454–3477.

Serrano-Gomez SJ, Maziveyi M, Alahari SK. 2016. Regulation of epithelial-mesenchymal transition through epigenetic and post-translational modifications. *Mol Cancer* **15**: 18.

Seto E, Yoshida M. 2014. Erasers of histone acetylation: The histone deacetylase enzymes. *Cold Spring Harb Perspect Biol* **6**: a018713.

Shen S, Kozikowski AP. 2016. Why hydroxamates may not be the best histone deacetylase inhibitors — What some may have forgotten or would rather forget? *ChemMedChem* **11**: 15–21.

Shen S, Kozikowski AP. 2020. A patent review of histone deacetylase 6 inhibitors in neurodegenerative diseases (2014-2019). *Expert Opin Ther Pat* **30**: 121–136.

Shi YG, Tsukada Y. 2013. The discovery of histone demethylases. *Cold Spring Harb Perspect Biol* **5**: a017947.

Simões-Pires C, Zwick V, Nurisso A, Schenker E, Carrupt P-A, Cuendet M. 2013. HDAC6 as a target for neurodegenerative diseases: what makes it different from the other HDACs? *Mol Neurodegener* **8**: 7.

Spivak AM, Planelles V. 2018. Novel latency reversal agents for HIV-1 cure. *Annu Rev Med* **69**: 421–436.

Stojanovic N, Hassan Z, Wirth M, Wenzel P, Beyer M, Schäfer C, Brand P, Kroemer A, Stauber RH, Schmid RM, Arit A, Sellmer A, Mahboobi S, Rad R, Reichert M, Saur D, Krämer OH, Schneider G. 2017. HDAC1 and HDAC2 integrate the expression of p53 mutants in pancreatic cancer. *Oncogene* **36**: 1804–1815.

Stoszko M, Ne E, Abner E, Mahmoud T. 2019. A broad drug arsenal to attack a strenuous latent HIV reservoir. *Curr Opin Virol* **38**: 37–53.

Strahl BD, Allis CD. 2000. The language of covalent histone modifications. *Nature* **403**: 41–45.

Strebl MG, Campbell AJ, Zhao W-N, Schroeder FA, Riley MM, Chindavong PS, Morin TM, Haggarty SJ, Wagner FF, Ritter T, Hooker JM. 2017. HDAC6 brain mapping with [<sup>18</sup>F]bavarostat enabled by a Ru-mediated deoxyfluorination. *ACS Cent Sci* **3**: 1006–1014.

Subramanian S, Bates SE, Wright JJ, Espinoza-Delgado I, Piekarczyk RL. 2010. Clinical toxicities of histone deacetylase inhibitors. *Pharmaceuticals* **3**: 2751–2767.

Sund H, Weber K. 1966. The quaternary structure of proteins. *Angew Chem Int Ed* **5**: 231–245.

Tanaka K. 2009. The proteasome: Overview of structure and functions. *Proc Jpn Acad Ser B* **85**: 12–36.



Tiffon C. 2018. The impact of nutrition and environmental epigenetics on human health and disease. *Int J Mol Sci* **19**: 3425.

Ueda H, Nakajima H, Hori Y, Fujita T, Nishimura M, Goto T, Okuhara M. 1994. FR901228, a novel antitumor bicyclic depsipeptide produced by *Chromobacterium violaceum* No. 968. I. Taxonomy, fermentation, isolation, physicochemical and biological properties, and antitumor activity. *J Antibiot (Tokyo)* **47**: 301–310.

Unno M, Mizushima T, Morimoto Y, Tomisugi Y, Tanaka K, Yasuoka N, Tsukihara T. 2002. The structure of the mammalian 20S Proteasome at 2.75 Å resolution. *Structure* **10**: 609–618.Å

Valenzuela-Fernández A, Cabrero JR, Serrador JM, Sánchez-Madrid F. 2008. HDAC6: a key regulator of cytoskeleton, cell migration and cell-cell interactions. *Trends Cell Biol* **18**: 291–297.

Vannini A, Volpari C, Filocamo G, Casavola EC, Brunetti M, Renzoni D, Chakravarty P, Paolini C, De Francesco R, Gallinari P, Steinkühler C, Di Marco S. 2004. Crystal structure of a eukaryotic zinc-dependent histone deacetylase, human HDAC8, complexed with a hydroxamic acid inhibitor. *PNAS* **101**: 15064–15069.

Van Veggel M, Westerman E, Hamberg P. 2018. Clinical pharmacokinetics and pharmacodynamics of panobinostat. *Clin Pharmacokinet* **57**: 21–29.

Verdin E, Dequiedt F, Kasler HG. 2003. Class II histone deacetylases: versatile regulators. *Trends Genet* **19**: 286–293.

Vigushin DM, Ali S, Pace PE, Mirsaidi N, Ito K, Adcock I, Coombes RC. 2001. Trichostatin A is a histone deacetylase inhibitor with potent antitumor activity against breast cancer *in vivo*. *Clin Cancer Res* **7**: 971–976.

Vimer S, Ben-Nissan G, Morgenstern D, Kumar-Deshmukh F, Polkinghorn C, Quintyn RS, Vasil'ev YV, Beckman JS, Elad N, Wysocki VH, Sharon M. 2020. Comparative structural analysis of 20S proteasome ortholog protein complexes by native mass spectrometry. *ACS Cent Sci* **6**: 573–588.

Vojinovic J, Damjanov N. 2011. HDAC Inhibition in rheumatoid arthritis and juvenile idiopathic arthritis. *Mol Med* **17**: 397–403.

Vojinovic J, Damjanov N, D'Urzo C, Furlan A, Susic G, Pasic S, Iagaru N, Stefan M, Dinarello CA. 2011. Safety and efficacy of an oral histone deacetylase inhibitor in systemic-onset juvenile idiopathic arthritis. *Arthritis Rheum* **63**: 1452–1458.

Waltregny D, Glénisson W, Tran SL, North BJ, Verdin E, Colige A, Castronovo V. 2005. Histone deacetylase HDAC8 associates with smooth muscle  $\alpha$ -actin and is essential for smooth muscle cell contractility. *FASEB J* **19**: 966–968.

Waltregny D, de Leval L, Glénisson W, Tran SL, North BJ, Bellahcène A, Weidle U, Verdin E, Castronovo V. 2004. Expression of histone deacetylase 8, a class I histone deacetylase, is restricted to cells showing smooth muscle differentiation in normal human tissues. *Am J Pathol* **165**: 553–564.

Wambua MK, Nalawansha DA, Negmeldin AT, Pflum MKH. 2014. Mutagenesis studies of the 14 Å internal cavity of histone deacetylase 1: Insights toward the acetate-escape hypothesis and selective inhibitor design. *J Med Chem* **57**: 642–650.

Wang C, Schroeder FA, Wey H-Y, Borra R, Wagner FF, Reis S, Kim SW, Holson EB, Haggarty SJ, Hooker JM. 2014. *In vivo* imaging of histone deacetylases (HDACs) in the central nervous system and major peripheral organs. *J Med Chem* **57**: 7999–8009.

Wang P, Wang Z, Liu J. 2020. Role of HDACs in normal and malignant hematopoiesis. *Mol Cancer* **19**: 5.

Wang W-H, Cheng L-C, Pan F-Y, Xue B, Wang D-Y, Chen Z, Li C-J. 2011. Intracellular trafficking of histone deacetylase 4 regulates long-term memory formation. *Anat Rec* **294**: 1025–1034.

Watson PJ, Fairall L, Santos GM, Schwabe JWR. 2012. Structure of HDAC3 bound to co-repressor and inositol tetrakisphosphate. *Nature* **481**: 335–341.

West AC, Johnstone RW. 2014. New and emerging HDAC inhibitors for cancer treatment. *J Clin Invest* **124**: 30–39.

Witt O, Deubzer HE, Milde T, Oehme I. 2009. HDAC family: What are the cancer relevant targets? *Canc Lett* **277**: 8–21.

Wolfson NA, Pitcairn CA, Fierke CA. 2013. HDAC8 substrates: histones and beyond. *Biopolymers* **99**: 112–126.

Wong JC, Hong R, Schreiber SL. 2003. Structural biasing elements for in-cell histone deacetylase paralog selectivity. *J Am Chem Soc* **125**: 5586–5587.

Wu M-Z, Tsai Y-P, Yang M-H, Huang C-H, Chang S-Y, Chang C-C, Teng S-C, K-J Wu. 2011. Interplay between HDAC3 and WDR5 is essential for hypoxia-induced epithelial-mesenchymal transition. *Mol Cell* **43**: 811–822.

Xiao H, Jiao J, Wang L, O'Brien S, Newick K, Wang L-CS, Falkensammer E, Liu Y, Han R, Kapoor V, Hansen FK, Kurz T, Hancock WW, Beier UH. 2016. HDAC5 controls the functions of Foxp3<sup>+</sup> T-regulatory and CD8<sup>+</sup> T cells. *Int J Cancer* **138**: 2477–2486.

Xin B-T, de Bruin G, Huber EM, Besse A, Florea BI, Filippov DV, van der Marel GA, Kisselev AF, van der Stelt M, Driessen C, Groll M, Overkleeft HS. 2016. Structure-based design of  $\beta$ 5c selective inhibitors of human constitutive proteasomes. *J Med Chem* **59**: 7177–7187.

Yamauchi Y, Boukari H, Banerjee I, Sbalzarini IF, Horvath P, Helenius A. 2011. Histone deacetylase 8 is required for centrosome cohesion and influenza A virus entry. *PLoS Pathog* **7**: e1002316.

Yan S, Wei X, Jian W, Qin Y, Liu J, Zhu S, Jiang F, Lou H, Zhang B. 2020. Pharmacological inhibition of HDAC6 attenuates NLRP3 inflammatory response and protects dopaminergic neurons in experimental models of parkinson's disease. *Front Aging Neurosci* **12**: 78.

Yano M, Yasuda M, Sakaki M, Nagata K, Fujino T, Arai E, Hasebe T, Miyazawa M, Miyazawa M, Ogane N, Hasegawa K, Narahara H. 2018. Association of histone deacetylase expression with histology and prognosis of ovarian cancer. *Oncol Lett* **15**: 3524–3531.

Zaikos TD, Painter MM, Sebastian Kettinger NT, Terry VH, Collins KL. 2018. Class 1-selective histone deacetylase (HDAC) inhibitors enhance HIV latency reversal while preserving the activity of HDAC isoforms necessary for maximal HIV gene expression. *J Virol* **92**: e02110–e02117.

Zhang J, Wu P, Hu Y. 2013. Clinical and marketed proteasome inhibitors for cancer treatment. *Curr Med Chem* **20**: 2537–2551.

Zhang L, Zhang J, Jiang Q, Zhang L, Song W. 2018. Zinc binding groups for histone deacetylase inhibitors. *J Enzyme Inhib Med Chem* **33**: 714–721.

Zhang X, Yuan Z, Zhang Y, Yong S, Salas-Burgos A, Koomen J, Olashaw N, Parsons JT, Yang X-J, Dent SR, Yao T-P, Lane WS, Seto E. 2007. HDAC6 modulates cell motility by altering the acetylation level of cortactin. *Mol Cell* **27**: 197–213.

Zhang X-H, Qin-Ma, Wu HP, Khamis MY, Li Y-H, Ma L-Y, Liu H-M. 2021. A Review of progress in histone deacetylase 6 inhibitors research: Structural specificity and functional diversity. *J Med Chem* **64**: 1362–1391.

# Chapter 2: Synthesis, binding mode and biological evaluation of selective HDAC6 inhibitors with bifurcated capping groups

***A modified version of the entire chapter (except for 2.1.1 and 2.1.2) has previously been published in:***

Reßing N, Sönnichsen M, Osko JD, Schöler A, Schliehe-Diecks J, Skerhut A, Borkhardt A, Hauer J, Kassack MU, Christianson DW, Bhatia S, Hansen FK. 2020. Multicomponent synthesis, binding mode, and structure-activity relationship of selective histone deacetylase 6 (HDAC6) inhibitors with bifurcated capping groups. *J Med Chem* **63**: 10339–10351. Adapted and reprinted with permission. Copyright (2020) American Chemical Society.

## 2.1 Introduction

### 2.1.1 LADME: Bioavailability of drugs

The achievement of sufficient bioavailability for potential drugs remains one of the major challenges in drug discovery. Depending on the route of administration, pharmacokinetic processes may significantly decrease the drug doses reaching the designated target and must therefore be considered throughout the entire development process. Pharmacokinetics describe all mechanisms that a drug encounters on its way through the organism, including the liberation of the drug from its formulation; the absorption into the blood circulation; the distribution to the tissues; metabolic modifications by liver enzymes or other proteins; and the elimination of metabolites and the drug itself. Those pharmacokinetic events mostly affect the therapeutically active doses of orally administered drugs and are generally referred to as **LADME** (**L**iberation, **A**bsorption, **D**istribution, **M**etabolism, **E**xcretion) but may also comprise the toxicity as an additional criterion (LADMET; van de Waterbeemd & Gifford 2003). In drug discovery, failure at either of those stages may slow down or even terminate the entire development process.

One sticking point in this context is the physicochemical profile of a drug candidate. If unsuitable, it is likely to impair the compound's ability to pass the gastrointestinal tract on the way to the bloodstream (van de Waterbeemd & Gifford 2003). Nowadays, this step can to some extent be facilitated by choosing appropriate formulation methods, but for some drugs,

oral delivery remains an issue. Through metabolic processes such as hydroxylations, methylations, and epoxidations happening in the intestinal system and the liver, additional dose loss may be caused by cytochrome P450 (CYP) monooxygenases which transform the drug into potentially toxic metabolites (Zanger & Schwab 2013). The overall dose decrease stemming from poor absorption and unfavourable metabolisation is known as the first-pass effect and could indeed be evaded by engaging alternative administration routes that address the mucosa or bloodstream directly; however, such methods bring the disadvantage of being particularly inconvenient for non-hospitalised patients (van de Waterbeemd & Gifford 2003). Finding ways to improve the bioavailability of orally administered pharmaceuticals therefore remains one of the key tasks in drug discovery.

One of the properties influencing a drug's availability at the target is the lipophilicity. The access into the blood circulation via the gastrointestinal tract as well as the transport to the cellular targets require the passage of membranes consisting of lipid bilayers that are impermeable for hydrophilic or polar molecules (Veber et al. 2002). A guideline helping to avoid such obstacles at early drug development stages is given by the Lipinski's *Rule of 5*. Based on the comparison of the physical properties of clinical candidates, the now well-established rules were first published in 1997 and have been refined ever since, including one study on specifications for lead structures (Lipinski et al. 1997; Oprea et al. 2001; Veber et al. 2002). The Rule of 5 state that the drug-likeness of orally administered drugs depends on sufficient absorption qualities which can be achieved by ensuring that the compounds comprise no more than five hydrogen bond donors and ten hydrogen bond acceptors, fewer than ten rotatable bonds, a molecular weight of less than 500 g/mol, a maximum polar surface area of 140 Å<sup>2</sup>, and a partition coefficient ( $\log P$ ) in the range between 0 and 5 (Lipinski et al. 1997). In this context, the  $\log P$  value describes the logarithmic ratio of drug concentrations in a two-layer mixture of 1-octanol and water. It indicates a good solubility in water for compounds characterised by a  $\log P < 0$  and a good lipophilicity for compounds with a  $\log P > 0$ . In the case of ionisable compounds, the distribution coefficient  $\log D$  is preferred to the partition coefficient. In addition to the ratio of compound present in the mixture of 1-octanol and water, the  $\log D$  value further considers the distribution of ionised and non-ionised species in each layer and therefore leads to more accurate results for acidic and basic drugs, such as carboxylic acids or amines (Tetko & Poda 2004).

With the exception of special drug classes, like antibiotics or antifungals, empirical studies on compounds developed by Merck and Pfizer revealed that an ideal drug candidate should not violate more than one rule of the Rule of 5 so as to maintain promising permeation and

absorption qualities (Lipinski et al. 1997; Lipinski 2000). In order to align the criteria with good target affinity, extensive SAR studies and the consideration of bioisosteric replacements of problematic residues are essential.

### 2.1.2 Bioisosterism

In medicinal chemistry, the concept of *bioisosterism* is frequently used to approach the optimisation of lead structures. In such cases, the basic structure of a compound is retained but specific groups affecting the physicochemical properties, the target affinity, or the metabolic stability are replaced by similar residues which are supposed to improve the compound's overall performance (Lima & Barreiro 2005; Patani & LaVoie 1996).

When first introduced by Langmuir in 1919, the concept of isosterism was closely modelled on the octet rule and described the similar behaviour of isoelectronic groups or molecules, for example  $O_2^-$ ,  $F^-$ ,  $Ne$ , and  $Na^+$ ; or  $CO$ ,  $CN^-$ , and  $N_2$  (Langmuir 1919; Patani & LaVoie 1996). Six years later, Grimm used the term *hydride displacement law* to characterise the phenomenon that addition of hydrides to main group elements results in their assuming the same physical properties as the following main group elements. Examples of such pseudoatoms are  $N = CH$ ,  $O = NH = CH_2$ , and  $OH = NH_2 = CH_3$  (Grimm 1925; Patani & LaVoie 1996). Building on this initial work, Erlenmeyer applied the term *isosterism* to elements, ions or molecules that share the same number of valence electrons, thus declaring all elements within the same main group of the periodic table as isosteres (Erlenmeyer & Leo 1932; Lima & Barreiro 2005). After successful applications of isosteric replacements in the early days of medicinal chemistry, Friedman presented his studies on bioisosterism in modified natural compounds in 1950 (Friedman 1951; Lima & Barreiro 2005). According to his findings, successful bioisosteric replacements may be achieved by considering the size, reactivity, and polarity of chemical groups. Electronic isosterism, in contrast, did not turn out to be a necessary requirement (Friedman 1951; Lima & Barreiro 2005). In 1979, Thornber extended this list by adding the shape, the electronic distribution, the solubility in lipids and water, the  $pK_a$ , and the hydrogen bonding capacities to the essential criteria. It was furthermore suggested to evaluate modifications of a compound in terms of their behaviour, e.g. their effect on specific interactions with receptors, structural requirements for maintaining a particular geometry, and the influence on pharmacokinetic properties and metabolic reactions (Thornber 1979; Patani & LaVoie 1996).

From today's point of view, this model is still valid and by now, numerous bioisosteric connections between functional groups have been identified. One important source offering

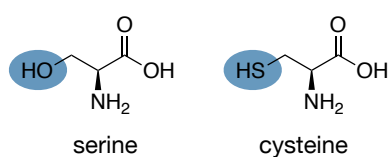


**Figure 2.1.** Structures of the natural isosteres serine and cysteine.

information on bioisosteres are natural compounds in which the concept is often realised. The amino acid serine, for instance, bears a hydroxyl group and is thus isosteric to cysteine with its thiol residue (Figure 2.1; Lima & Barreiro 2005). A striking example from the group of synthetic compounds is the bioisosteric relation of aniline ( $pK_b$  9.4) and phenol ( $pK_a$  10.0) which may be exchanged in order to benefit from their contrary acid-base properties, despite their similar size and isosteric nature (Lima & Barreiro 2005). In consideration of the variety of functional groups and organic residues, bioisosterism can be used as a versatile and valuable tool to refine a compound's characteristics.

information on bioisosteres are natural compounds in which the concept is often realised. The amino acid serine, for instance, bears a hydroxyl group and is thus isosteric to cysteine with its thiol residue (Figure 2.1; Lima & Barreiro 2005). A striking example from the group of synthetic compounds is the bioisosteric relation of aniline ( $pK_b$  9.4) and

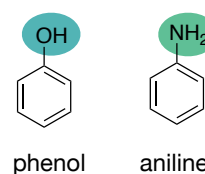
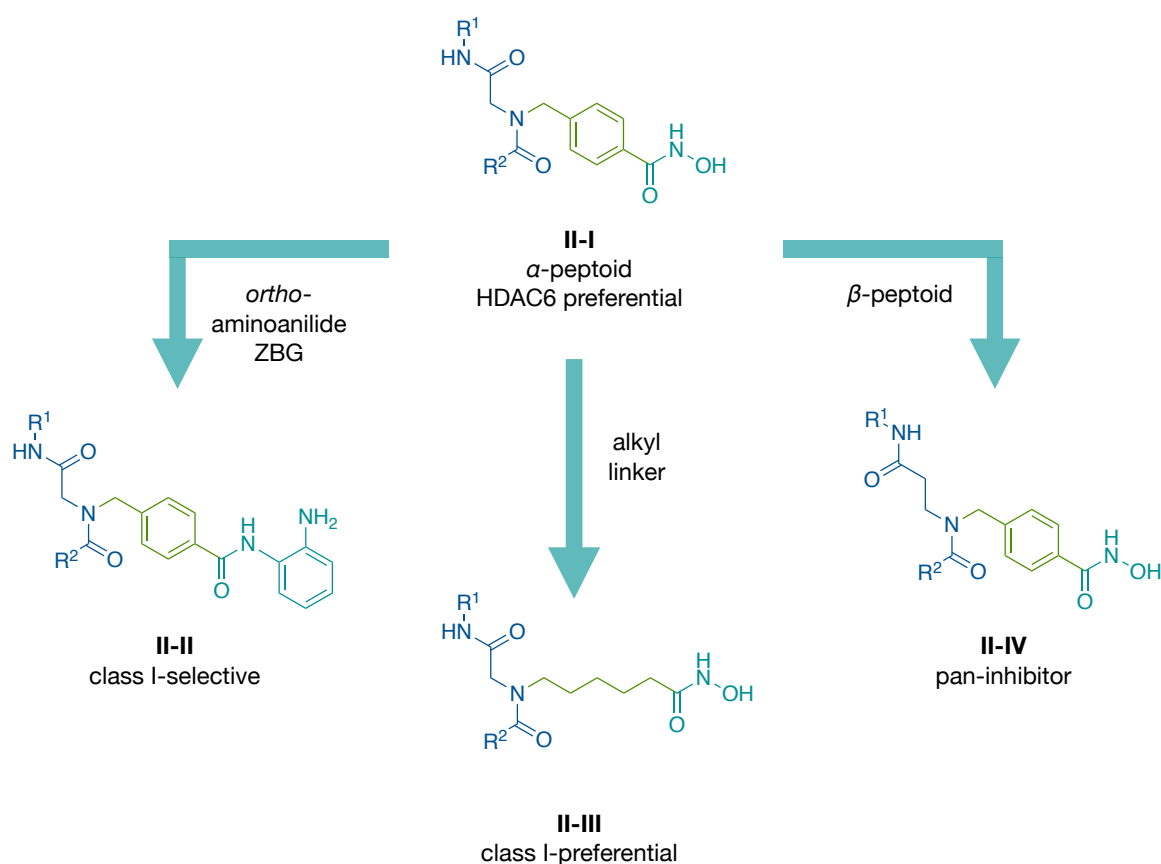


**Figure 2.2.** Phenol and aniline are bioisosteres.

### 2.1.3 Project outline

Motivated by the fact that the undeniable potential of HDACi in preclinical studies often collides with the occurrence of adverse effects due to unintentional class I HDAC inhibition, the search for isoform-selective inhibitors has been going on for more than a decade (Li & Seto 2016; Roche & Bertrand 2016). Meanwhile, HDAC6 has emerged as the most prominent target as it could open up new opportunities within and beyond the field of oncology (Kalin & Bergman 2013; Shen & Kozikowski 2020).

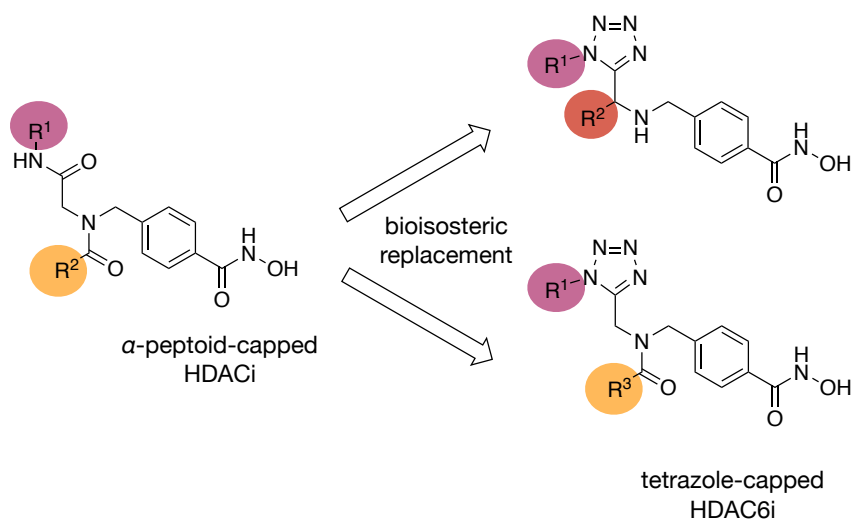
By undertaking extensive studies on different generations of peptoid-based HDACi over the last years, the Hansen group was able to demonstrate that isoform specificity can be achieved by making minor alterations to otherwise identical scaffolds (Scheme 2.1). Replacing the benzyl linker of the HDAC6-preferential compounds **II-I** by the alkyl chain present in compounds **II-III** significantly increased their affinity to class I isoforms (Diedrich et al. 2016; Krieger et al. 2017; Krieger et al. 2019). The combination of the benzyl linker of **II-I** and an *ortho*-aminoanilide ZBG afforded the compounds **II-II** with even higher class I selectivity (Krieger et al. 2019), whereas the elongation and increase of flexibility attempted in the hydroxamates **II-IV** favours non-selective inhibition (Reßing et al. 2019). Comparison of SAR data obtained for the compounds **II-I** further reveals that the substitution pattern of the aromatic residue  $R^2$  is crucial for steering the preference towards HDAC6 (Mackwitz et al. 2019; Mackwitz et al. 2021; Diedrich et al. 2018; Porter et al. 2018).



**Scheme 2.1.** Overview of HDACi developed by the Hansen group. Structural modifications of the peptoid scaffold were employed to generate compounds with different isoform specificity profiles.

In this work, a new generation of bifurcated HDAC6i was to be designed and synthesised. A structural novelty of the resulting compounds is the tetrazole motif which was introduced because previous studies indicated a correlation between reduced flexibility and HDAC6 selectivity (Scheme 2.2; Porter et al. 2018; Reßing et al. 2019). Usually, 1*H*-tetrazoles are considered to be similarly planar and acidic, but metabolically stable bioisosteres of carboxyl groups (Ballatore et al. 2013). In the present study, the substituted and thus non-acidic tetrazole moiety was chosen as a bioisosteric replacement for the amide group so as to increase the metabolic stability, rigidity, and the target affinity of the compounds (Kumari et al. 2021). Due to the availability of synthetic handles coming along with this modification, it was moreover possible to screen three different types of bifurcated capping groups. The library design therefore included variations on the position of the lower branch as well as modifications of the residues R<sup>1</sup> and R<sup>2</sup>.



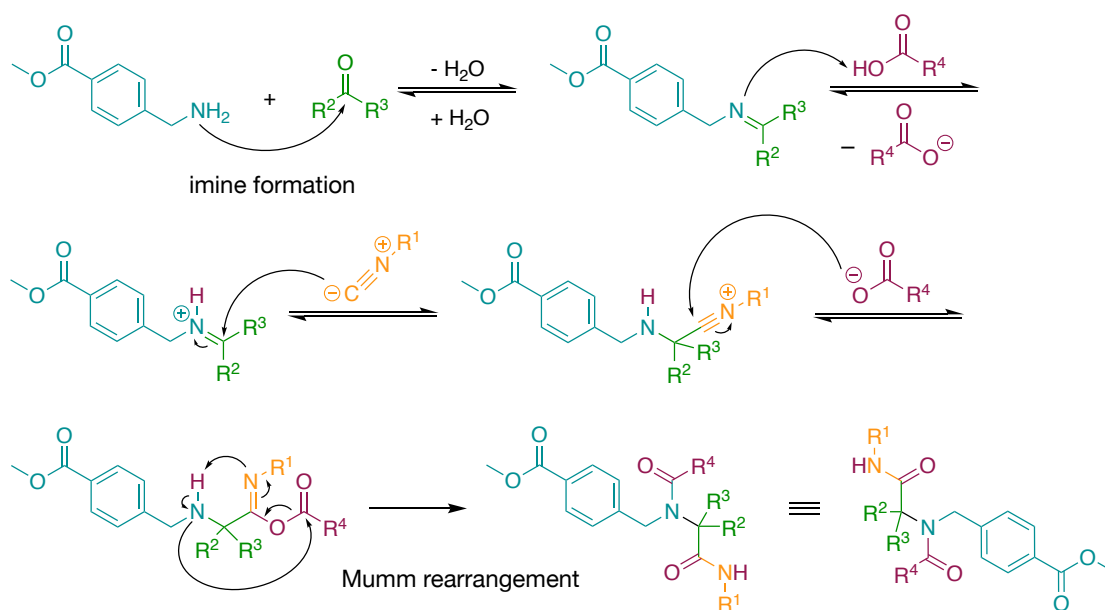


**Scheme 2.2.** Design of tetrazole-capped selective HDAC6i derived from  $\alpha$ -peptoid-based HDACi.

## 2.2 Results and discussion

### 2.2.1 Synthesis of tetrazole-capped HDAC inhibitors

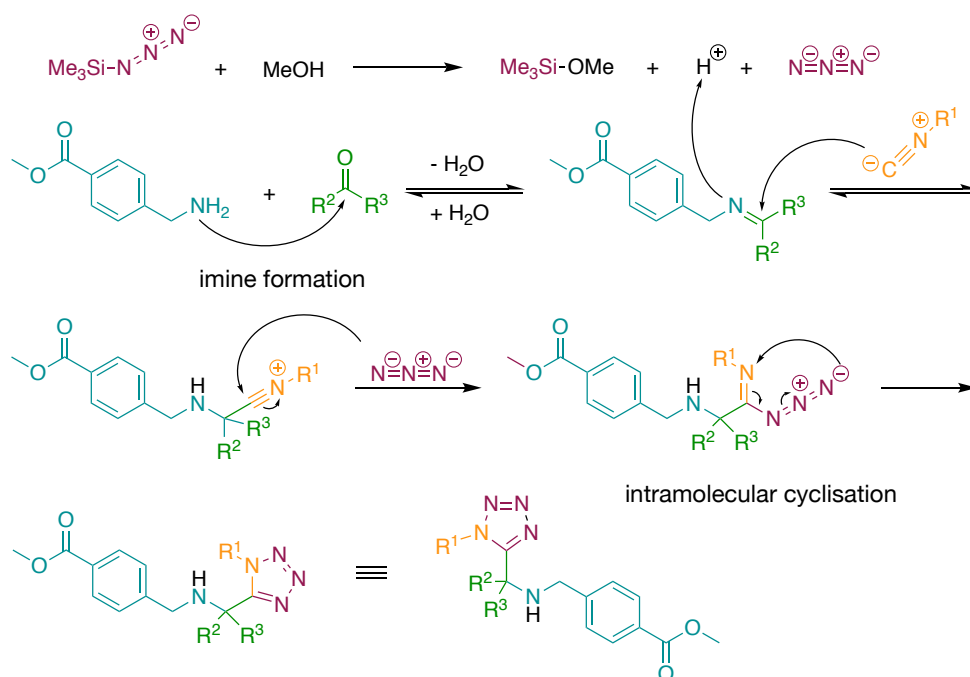
Prior to commencing library synthesis, three model compounds were synthesised by using the microwave-assisted Ugi-azide four-component reaction (UA4CR). A variation of the classic Ugi four-component reaction (U4CR) introduced by Ivar Karl Ugi, the UA4CR is a convenient multicomponent one-pot reaction (Ugi 1962; Ugi & Steinbrückner 1961). The U4CR generally starts from a mixture of an amine, a carboxylic acid, an isonitrile, and a carbonyl species. Most effective in polar solvents such as methanol or DMF, the U4CR affords versatile bisamide scaffolds via reversible condensation reactions followed by irreversible Mumm-rearrangements (Scheme 2.3).



**Scheme 2.3.** Mechanism of the U4CR and the following Mumm-rearrangement yielding HDACi precursors.

Replacing the carboxylic acid by an azide species, e.g. sodium azide or, more commonly, trimethylsilyl azide, yields 1,5-disubstituted tetrazole scaffolds through intramolecular cyclisations (Scheme 2.4) which are not succeeded by rearrangement reactions (Maleki & Sarvary 2015). The resulting products can usually be isolated by uncomplicated workups, like precipitation from the crude mixture or recrystallisation, so that the total amount of organic waste is kept at a minimum. Despite having been intended as one-pot protocols, it was suggested that preformation of the imine intermediate and subsequent addition of the

isonitrile and the respective carboxylic acid or azide component might have a beneficial impact on the Ugi reactions (Marcaccini & Torroba 2007). Increased yields can further be accomplished by driving the reaction equilibrium towards product formation. For this purpose, drying agents such as molecular sieves or magnesium sulfate may be added to remove water from the reaction mixture. Affording typically high yields and no byproducts but water, the U4CR offers a simple and reliable synthetic method with excellent atom economy.

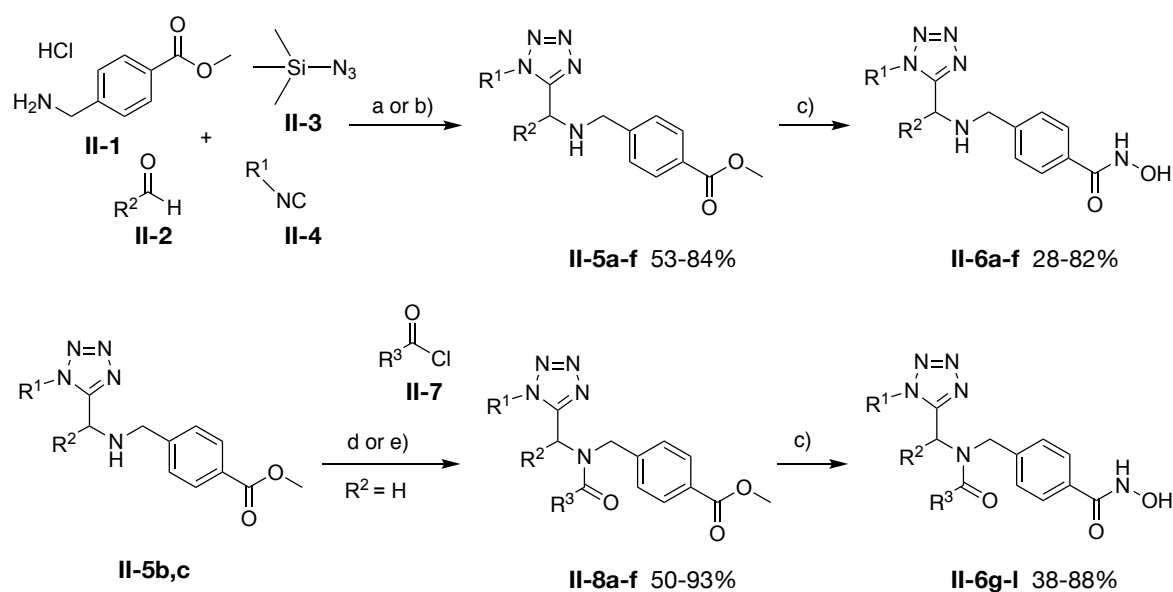


**Scheme 2.4.** Mechanism of the UA4CR yielding tetrazole-capped HDACi precursors. The protic solvent participates in generating the reactive azide species.

Due to its exothermic nature, the UA4CR usually finishes quickly after addition of the last component. The versatility of the reaction does, however, allow for a broad variety of substrates so that longer reaction times depending on the reactivities of the different components are not uncommon. A valuable method to significantly accelerate the reaction time is the usage of a microwave reactor. Previous projects in the Hansen group demonstrated that U4CR reactions that ran for several days at room temperature under atmospheric conditions could be performed in less than 2 h under microwave irradiation at 40 °C (Diedrich et al. 2016; Mackwitz et al. 2019). Apart from the higher temperature, this significant decrease in reaction time might be attributed to the lower amount of solvent and higher reagent concentrations in the microwave vessel which is able to tolerate high pressure.

In the first step, an optimised microwave protocol was used to form the imine intermediate

starting from the linker fragment, methyl 4-(aminomethyl)-benzoate hydrochloride (**II-1**), and paraformaldehyde as a formaldehyde source. The addition of trimethylsilyl azide was required to build the tetrazole ring while three different isonitriles were used to diversify the upper branch of the bifurcated capping group (**II-5a-c**; Scheme 2.5). The Ugi products thus obtained were isolated by aqueous workup and subsequently treated with a mixture of aqueous hydroxylamine and sodium hydroxide to generate the corresponding hydroxamates **II-6a-c** within 1–4 h at 0 °C. After precipitation from the aqueous crude mixtures and purification by recrystallisation, the prototypes **II-6a-c** were subjected to biochemical enzyme inhibition assays against HDACs 1 and 6. The results encouraged the discarding of the *tert*-butyl-derivative **II-6a** ( $IC_{50}$  HDAC1: 8.24  $\mu$ M; HDAC6: 0.330  $\mu$ M) in favour of the cyclohexyl- ( $IC_{50}$  HDAC1: 2.06  $\mu$ M; HDAC6: 0.120  $\mu$ M) and benzyl analogues ( $IC_{50}$  HDAC1: 2.45  $\mu$ M; HDAC6: 0.102  $\mu$ M) as the most promising compounds in terms of inhibitory activity and HDAC6 selectivity.



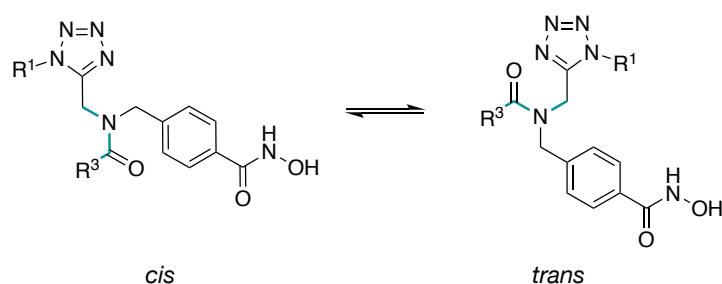
**Scheme 2.5.** Synthesis of tetrazole-capped HDAC6i. Reagents and conditions: a) Et<sub>3</sub>N, MeOH, MW, 45 °C, 150 W, 30 min (imine formation), then 2 h (UA4CR); b) Et<sub>3</sub>N, MeOH, rt, 3 days; c) NH<sub>2</sub>OH (50% solution in water), MeOH/DCM, 0 °C, 1–4 h; d) respective acyl chloride, Et<sub>3</sub>N, DCM, 0 °C to rt, 16 h; e) respective carboxylic acid, SOCl<sub>2</sub>, DCM, 0 °C, 30 min, then addition of **5** and Et<sub>3</sub>N, DCM, rt, 16 h.

From this starting point, a small library of branched inhibitors was created by varying the aldehyde component in the UA4CR (**II-5d-f**). An alternative scaffold was accessible by using *in situ*-generated or commercially available acyl chlorides for *N*-acylation of the formaldehyde-derived analogues **II-6b** and **II-6c** (**II-8a-f**; Scheme 2.5). The UA4CR affording compound **II-5e** was carried out using a microwave-assisted protocol; the esters **II-5d** and

**II-5f** were synthesised under ambient conditions over three days. Subsequent hydroxylaminolysis of all compounds yielded the desired hydroxamates which were obtained by precipitation from water (**II-6d-I**; Scheme 2.5). Recrystallisation of the final compounds sufficed to exceed purities of 95%.

## 2.2.2 Variable temperature NMR experiments

While all new HDACi were routinely characterised by nuclear magnetic resonance (NMR) experiments, it became apparent that some compounds formed rotamers by adopting different conformations in a temperature-dependent manner (Scheme 2.6). Hindered and thus decelerated rotation of amide substituents is a common phenomenon at very low temperatures and can be visualised by NMR spectra in which each rotamer appears with an individual set of signals. At higher temperatures, this effect typically diminishes as the additional energy facilitates the rotation around the amide bond up to the point of coalescence at which both rotamers melt into one signal. For compounds containing amide groups, coalescence often happens below room temperature and is therefore unnoticeable in NMR spectra recorded at 20 °C, but in the case of peptoids and HDACi based on this particular scaffold, the occurrence of *cis* and *trans* rotamers up to 50 °C and higher has regularly been reported (Laursen et al. 2013; Krieger et al. 2017; Reßing et al. 2019; Diedrich et al. 2016).



**Scheme 2.6.** Equilibrium of *cis* and *trans* rotamers of tetrazole-capped HDACi.

To investigate the point of coalescence of the HDACi presented in this study, compound **II-6j** was selected for <sup>1</sup>H NMR variable temperature experiments. The resulting spectra are overlapped in Figure 2.3 and show that the methylene groups align around 40–50 °C. The partially split peak of the two methyl groups around 2.20 ppm further suggests impeded rotation of the 3,5-dimethylphenyl group at 24 °C. With this information, it can be ruled out that the additional set of signals derives from byproducts or impurities.

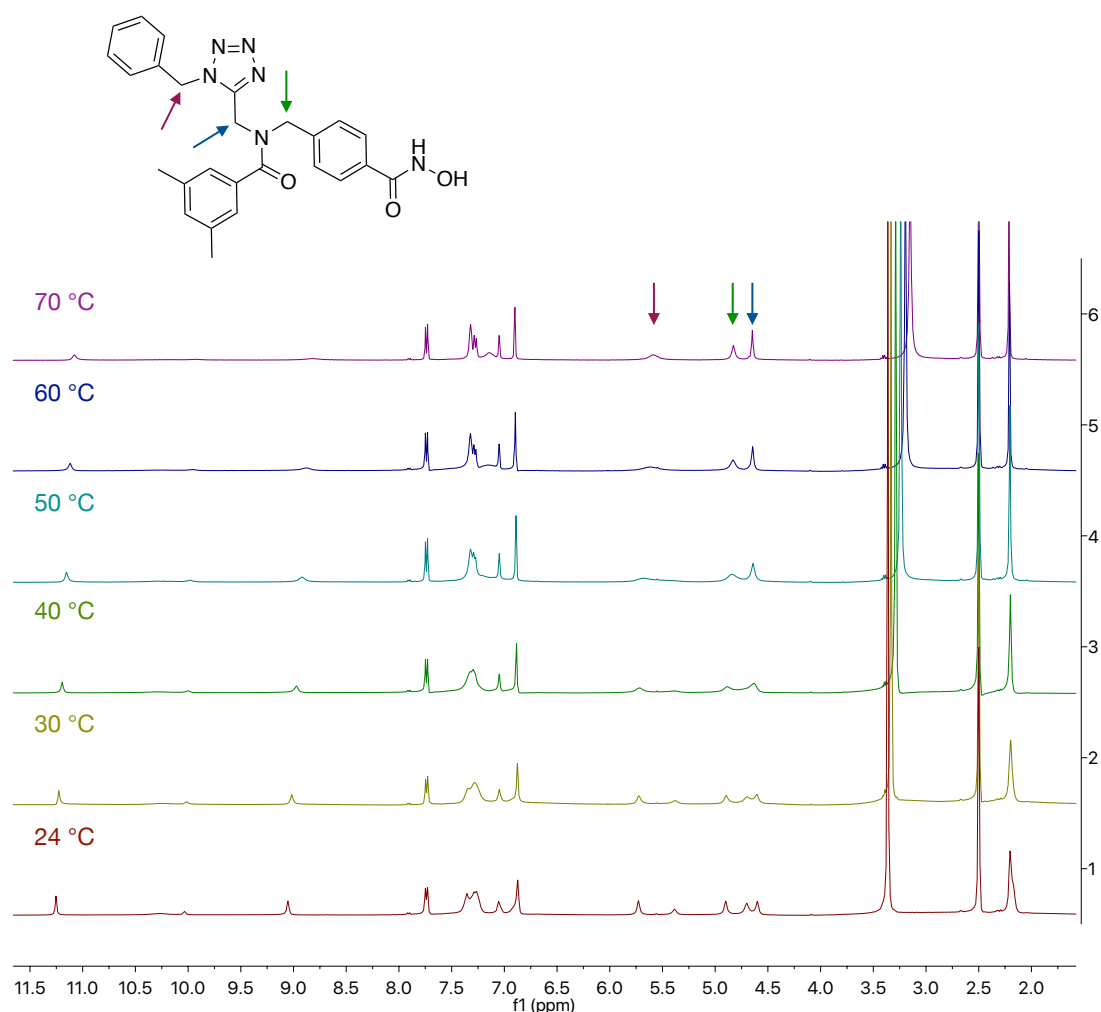


**Figure 2.3.** Variable temperature  $^1\text{H}$  NMR study of compound **II-6j**. The coloured arrows indicate the locations of the corresponding methylene groups in the spectra.

### 2.2.3 HDAC inhibition

**Biochemical assays.** Biochemical inhibition assays of all compounds against HDACs 1 and 6 revealed potent inhibitory activities and a clear preference for HDAC6 (Table 2.1) throughout the library.<sup>4</sup> It is striking that compounds **II-6d-f** (selectivity indices (SI): 17–34) exhibited similar selectivity profiles as compounds **II-6g-j** (SI: 11–49) but lower inhibitory activities ( $\text{IC}_{50}$  HDAC6: 0.098–0.121  $\mu\text{M}$ ). All *N*-acylated compounds except for the non-selective inhibitor **II-6k** ( $\text{IC}_{50}$  HDAC6: 0.317  $\mu\text{M}$ ) demonstrated potent HDAC6 inhibition in the low nanomolar concentration range ( $\text{IC}_{50}$  HDAC6: 0.030–0.083  $\mu\text{M}$ ). The comparison of compounds **II-6g** ( $\text{IC}_{50}$  HDAC6: 0.070  $\mu\text{M}$ , SI: 34) and **II-6h** ( $\text{IC}_{50}$  HDAC6: 0.062  $\mu\text{M}$ , SI: 49)

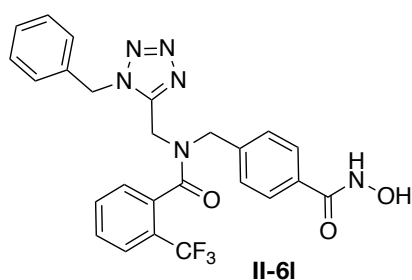
<sup>4</sup> Inhibition assays against HDACs 1–3 and HDAC6 were performed by Andrea Schöler in the group of Finn K. Hansen, Leipzig University.

**Table 2.1.** IC<sub>50</sub> of the tetrazole-capped HDACi **II-6a-f** against HDAC1 and HDAC6 in comparison with ricolinostat, nexturastat A, tubastatin A, and HPOB. Vorinostat was used as control.

Compound	R <sup>1</sup>	R <sup>2</sup>	R <sup>3</sup>	HDAC1 IC <sub>50</sub> [μM]	HDAC6 IC <sub>50</sub> [μM]	SI <sup>a</sup>
<b>II-6a</b>	<i>t</i> -Bu	H	-	8.24 ± 0.07	0.330 ± 0.007	25
<b>II-6b</b>	Bn	H	-	2.45 ± 0.22	0.102 ± 0.008	24
<b>II-6c</b>	<i>c</i> -Hexyl	H	-	2.06 ± 0.33	0.120 ± 0.005	17
<b>II-6d</b>	<i>c</i> -Hexyl	Ph	-	4.06 ± 0.02	0.119 ± 0.011	34
<b>II-6e</b>	Bn	Ph	-	3.37 ± 0.01	0.098 ± 0.014	34
<b>II-6f</b>	Bn	<i>n</i> -Bu	-	2.01 ± 0.01	0.121 ± 0.025	17
<b>II-6g</b>	<i>c</i> -Hexyl	H	Ph	2.37 ± 0.26	0.070 ± 0.003	34
<b>II-6h</b>	<i>c</i> -Hexyl	H	2-Me-Ph	3.03 ± 0.36	0.062 ± 0.003	49
<b>II-6i</b>	Bn	H	Ph	1.24 ± 0.06	0.032 ± 0.004	39
<b>II-6j</b>	Bn	H	3,5-Me-Ph	0.902 ± 0.165	0.083 ± 0.004	11
<b>II-6k</b>	Bn	H	4- <i>i</i> -Pr-Ph	1.78 ± 0.16	0.317 ± 0.064	6
<b>II-6l</b>	Bn	H	2-CF <sub>3</sub> -Ph	5.18 ± 0.31	0.030 ± 0.0002	173
Vorinostat	-	-	-	0.099 ± 0.005	0.041 ± 0.005	2
Ricolinostat <sup>b</sup>	-	-	-	0.188 ± 0.022	0.018 ± 0.003	11
Nexturastat A	-	-	-	0.504 ± 0.033	0.021 ± 0.0001	24
Tubastatin A <sup>c</sup>	-	-	-	2.49 ± 0.14	0.014 ± 0.0006	178
HPOB <sup>c</sup>	-	-	-	2.10 ± 0.23	0.085 ± 0.009	25

<sup>a</sup> Selectivity index (SI = IC<sub>50</sub> (HDAC1)/IC<sub>50</sub> (HDAC6)).  
<sup>b</sup> Data taken from: Reßing et al. 2019.  
<sup>c</sup> Data taken from: Mackwitz et al. 2018.

further indicates that residues in position 2 of the benzamide group lead to an increase in both HDAC6 selectivity and inhibition while the benzyl derivatives **II-6e** (IC<sub>50</sub> HDAC6: 0.098 μM, SI: 34) and **II-6i** (IC<sub>50</sub> HDAC6: 0.032 μM, SI: 39) are more potent and equally or slightly more selective than the cyclohexyl-capped compounds **II-6d** (IC<sub>50</sub> HDAC6: 0.119 μM, SI: 34) and **II-6g** (IC<sub>50</sub> HDAC6: 0.070 μM, SI: 34). In contrast to most derivatives which displayed only moderate selectivities for HDAC6 (SI: 5–49), compound **II-6l** featuring an *ortho*-trifluoromethyl residue stands out as a very potent and selective inhibitor (IC<sub>50</sub> HDAC6: 0.030 μM, SI: 173). Exceeding the HDAC6 selectivity of ricolinostat, HPOB, and nexturastat A, **II-6l** matched the selectivity index of the well-established HDAC6 tool compound tubastatin A (IC<sub>50</sub>: 0.014 μM, SI: 178). An additional screening of **II-6l** against



HDAC1 IC<sub>50</sub>: 5.18 ± 0.31 μM (SI<sup>1/6</sup>: 172)  
 HDAC2 IC<sub>50</sub>: 2.26 ± 0.11 μM (SI<sup>2/6</sup>: 75)  
 HDAC3 IC<sub>50</sub>: 8.48 ± 0.42 μM (SI<sup>3/6</sup>: 282)  
 HDAC4 IC<sub>50</sub>: 55.4 ± 7.23 μM (SI<sup>4/6</sup>: 1847)  
 HDAC6 IC<sub>50</sub>: 0.030 ± 0.0002 μM  
 HDAC8 IC<sub>50</sub>: 14.7 ± 1.04 μM (SI<sup>8/6</sup>: 490)

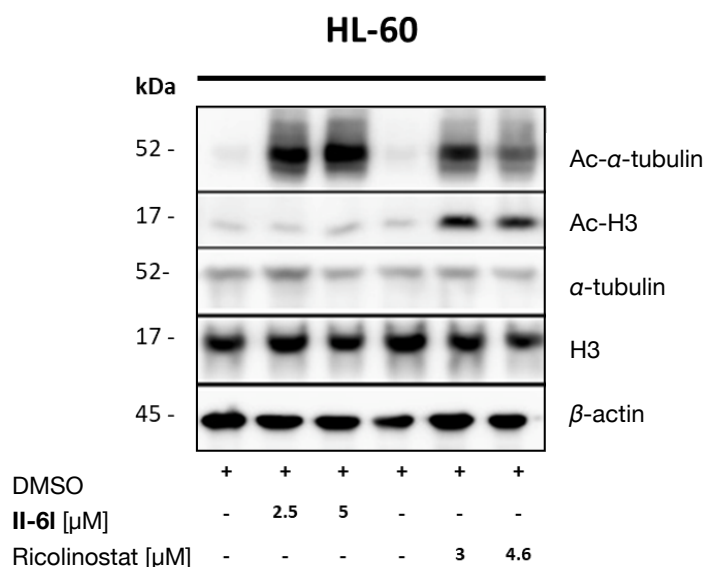
**Figure 2.4.** Structure and inhibitory activities of the hit compound **II-6I** against HDACs 1–4, 6, and 8.

HDAC2 (IC<sub>50</sub>: 2.26 μM, SI: 75), HDAC3 (IC<sub>50</sub>: 8.48 μM, SI: 282), and HDAC8 (IC<sub>50</sub>: 14.70 μM, SI: 490) confirmed the selectivity for HDAC6 over other class I isoforms (Figure 2.4). Chosen as an example of class IIa isoforms, no significant inhibition was measured after incubation with HDAC4 (IC<sub>50</sub>: 55.4 μM, SI: 1847).<sup>5</sup>

**Immunoblotting.** In order to examine the cellular properties of **II-6I**, the acute myeloid leukaemia (AML) cell line HL-60 was treated with different concentrations of **II-6I**, the clinical candidate ricolinostat, and DMSO as control. After incubation for 24 h, the cell lysates were immunoblotted with anti-acetyl-α-tubulin and acetyl-histone H3 antibodies to visualise the

activity of **II-6I** in the cellular environment (Figure 2.5).<sup>6</sup> The high acetylation levels of α-tubulin, which is a substrate of HDAC6, indicated potent HDAC6 inhibition by **II-6I** at both concentrations. The fact that **II-6I** treatment induced no acetylation of the class I substrate

**Figure 2.5.** Immunoblotting of HL-60 cells with acetyl-α-tubulin, acetyl-histone H3, total α-tubulin, total histone H3, and β-actin antibodies after treatment with different concentrations of **II-6I**. Ricolinostat and DMSO were used as controls. The picture was created by Melf Sönnichsen, HHU Düsseldorf. Reprinted with permission from Reßing et al. 2020. Copyright (2020) American Chemical Society.



<sup>5</sup> Inhibition assays against HDACs 4 and 8 were performed by Alexander Skerhut in the group of Matthias Kassack, HHU Düsseldorf.

<sup>6</sup> Immunoblotting was performed by Melf Sönnichsen in the group of Sanil Bhatia, HHU Düsseldorf.



Ac-histone H3 at either concentration further confirms the isoform selectivity of the compound.

#### 2.2.4 Co-crystal structure of **II-6I** and zebrafish HDAC6 CD2

X-ray crystallography using a co-crystal of **II-6I** and HDAC6 CD2 isolated from *Danio rerio* (zebrafish; zDC2) was performed by the collaborating Christianson group.<sup>7</sup> The crystal structure (Figure 2.6) revealed a bidentate binding mode between the hydroxamate group of **II-6I** and the zinc ion in the centre of the active site. The overall metal coordination was found to be pentacoordinate square pyramidal. Hydrogen bond interactions between the hydroxamate group and the surrounding Tyr745, His573, and His574 are in accordance with previous co-crystal structures of highly potent, but moderately selective peptoid-based HDACi (Porter et al. 2018). The high affinity of **II-6I** for HDAC6 is presumed to emanate from the structural match between the loop pockets and the bifurcated capping group of which the 2-trifluoromethyl phenyl group seems to occupy L1 while the *N*-(1-benzyl-1*H*-tetrazol-5-yl)methyl moiety resides in L2. Offering a hydrophobic binding site, the L1 pocket is a unique structural feature among HDACs that has already been mentioned in context with

the HDAC6 affinities of several peptoid-based inhibitors and the PET probe bavarostat (Porter et al. 2018). The simultaneous branching into both loop pockets, however, has only been observed for one other compound, the sterically complex dual HDACi/20S CPi RTS-V5, and is thus novel for sole HDACi (Bhatia et al. 2018). Another particularity of the binding

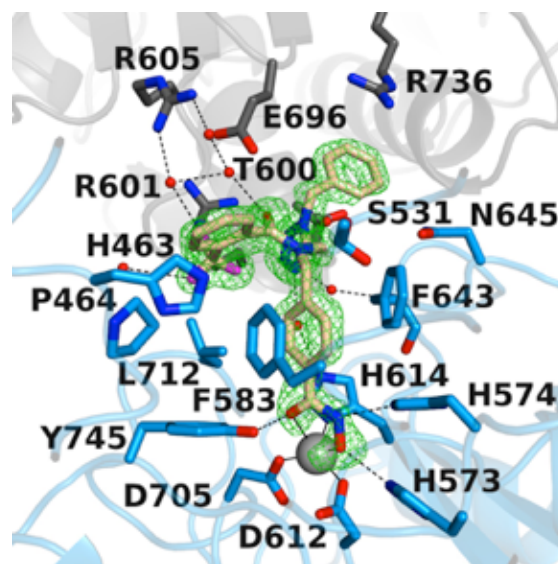


**Figure 2.6.** Polder omit map of zCD2 in complex with **II-6I** (PDB ID: 6PYE). Carbon atoms are coloured in light blue (zCD2 monomer A), dark grey (zCD2 symmetry mate), or wheat (inhibitor). Other atoms are highlighted as follows: nitrogen = dark blue, oxygen = red, fluorine = magenta. The zinc ion is illustrated as a grey sphere and solvent molecules are depicted as small red spheres. Metal coordination is indicated by solid black lines and hydrogen bond interactions are drawn as dashed black lines. The picture was created by the Christianson group, University of Pennsylvania. Reprinted with permission from Reßing et al. 2020. Copyright (2020) American Chemical Society.

<sup>7</sup> Crystal structure analysis was performed by Jeremy D. Osko in the group of David W. Christianson, University of Pennsylvania.

mode of **II-6I** in zCD2 is the observation that the compound turned out to be highly selective although neither of the cap group branches appears to undergo any direct interactions with the protein residues in the loop pockets, nor with the gatekeeper residue Ser531.

### 2.2.5 Biological evaluation of **II-6I**

**Metabolic stability.** Analyses of the microsomal stability of **II-6I** were performed by Bienta/Enamine Ltd.<sup>8</sup> Upon incubation with liver microsomes, the amount of remaining compound was measured in duplicates using LC-MS/MS methods in four time intervals within 40 min (Figure 2.7; Table 2.2). The results confirm pleasing microsomal stabilities towards human (HLM,  $Cl_{int}$ : 30  $\mu$ L/min/mg) and mouse liver enzymes (MLM,  $Cl_{int}$ : 26  $\mu$ L/min/mg; Table 2.2). In presence of either species, nearly 60% of the drug remained unaltered after 40 min of incubation. Given that the bioavailability after oral drug administration partly relies on the drug's ability to pass liver enzymes without being metabolised, these results are particularly encouraging in terms of the drug metabolism and pharmacokinetic qualities of **II-6I**.

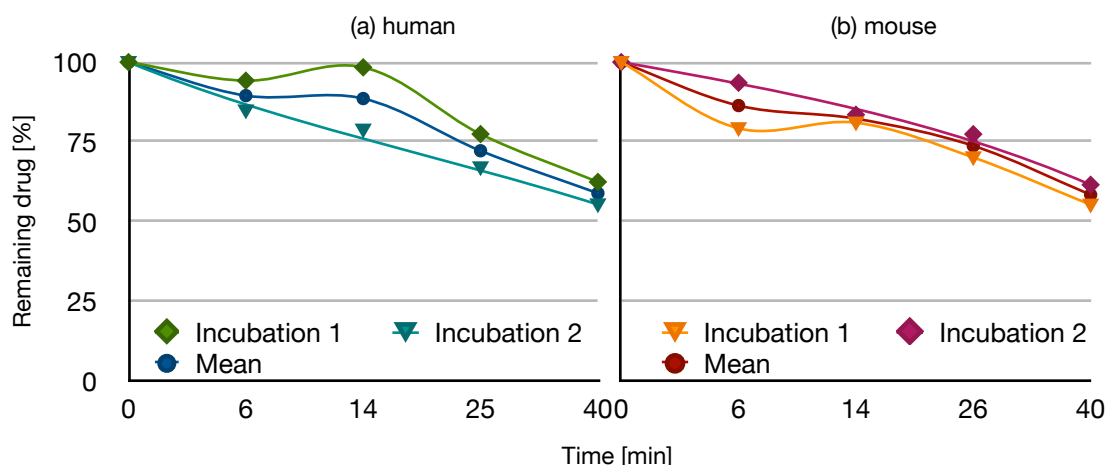


**Figure 2.7.** Microsomal stabilities of **II-6I** in presence of human (a) and mouse (b) liver microsomes.

<sup>8</sup> Bienta/Enamine Ltd., Kiev, Ukraine.

**Table 2.2.** Stability of **II-6I** in presence of human and mouse liver microsomes. Caffeine, propranolol, diclofenac, and imipramine were used as controls.

Entry	Human microsomal stability		Mouse microsomal stability	
	$t_{1/2}$ [min] <sup>a</sup>	$Cl_{int}$ [ $\mu$ L/min/mg] <sup>a</sup>	$t_{1/2}$ [min] <sup>a</sup>	$Cl_{int}$ [ $\mu$ L/min/mg] <sup>a</sup>
<b>II-6I</b>	56.6	30	64.1	26
Caffeine	1030 <sup>b</sup>	2 <sup>c</sup>	n.d.	n.d.
Propranolol	71.7	24	54.3	31
Diclofenac	6.8	248	n.d.	n.d.
Imipramine	n.d.	n.d.	8.4	202

<sup>a</sup> Half-time ( $t_{1/2}$ ) and clearance ( $Cl_{int}$ ) were determined in plot of  $\ln(\text{AUC})$  vs. time using linear regression analysis.

<sup>b</sup> Parameter should be considered as approximate due to the high stability of the compound.

**Antiproliferative effects.** In accordance with recent studies that indicated low cytotoxicity of selective HDAC6 inhibitors, treatment with compound **II-6I** had only little effect on selected leukaemia cell lines (Figure 2.8; Gaisina et al. 2016; Depetter et al. 2019).<sup>9</sup> The highest cytotoxicity was exerted on the SUP-B15 cell line with an  $IC_{50}$  of 22.5  $\mu$ M, but in most other cell lines,  $IC_{50}$  values were nearly twice as high.

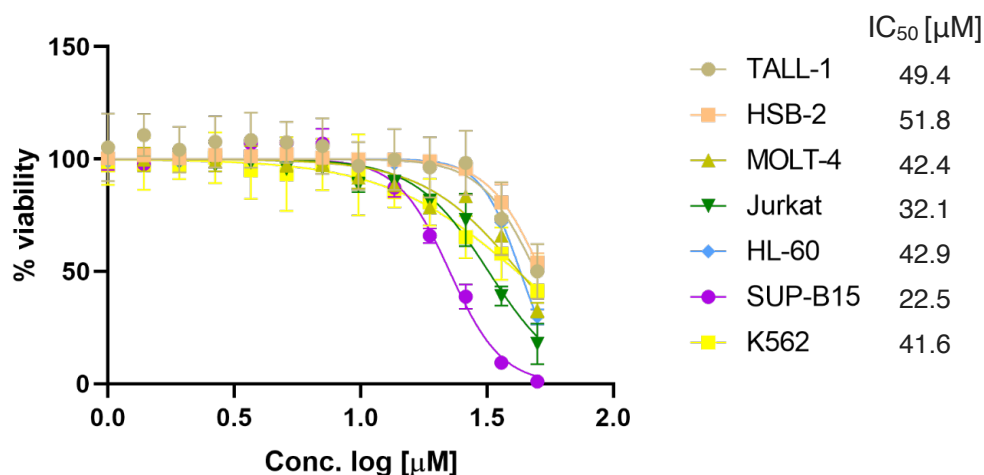


**Figure 2.8.** Cytotoxicity of compound **II-6I** against selected leukaemia cell lines. The diagram was created by Melf Sönnichsen, HHU Düsseldorf. Adapted and reprinted with permission from Reßing et al. 2020. Copyright (2020) American Chemical Society.

<sup>9</sup> Cytotoxicity screens were performed by Melf Sönnichsen in the group of Sanil Bhatia, HHU Düsseldorf.

The low cytotoxicity measured in this assay clearly limits the scope for single-agent applications of **II-6I** against oncological conditions. In a different experiment, however, **II-6I** exhibited potential as a combination drug by significantly enhancing the cytotoxicity of the established 20S CPi bortezomib (Figure 2.9). Using an annexin-propidium iodide (PI) apoptosis assay, the apoptosis induction in HL-60 cells after incubation with different concentrations of **II-6I** and bortezomib, either alone or in combination, was evaluated; the results are illustrated in Figure 2.9.<sup>10</sup> The diagram shows that the treatment with **II-6I** alone did not reduce the cell viability, which is consistent with the high IC<sub>50</sub> of 42.9 μM (Figure 2.8). If applied in combination, the compound significantly increased the percentage of late apoptotic cells compared to those that were subjected to bortezomib alone (Figure 2.9). After incubation with higher concentrations of both agents, this effect became even more striking, leading to nearly complete elimination of viable cells at 5 μM **II-6I** and 1.2 nM bortezomib. Together, those results allude to the ability of **II-6I** to block aggresome formation, thus enabling synergistic activities with 20S CPi (Hideshima et al. 2011).

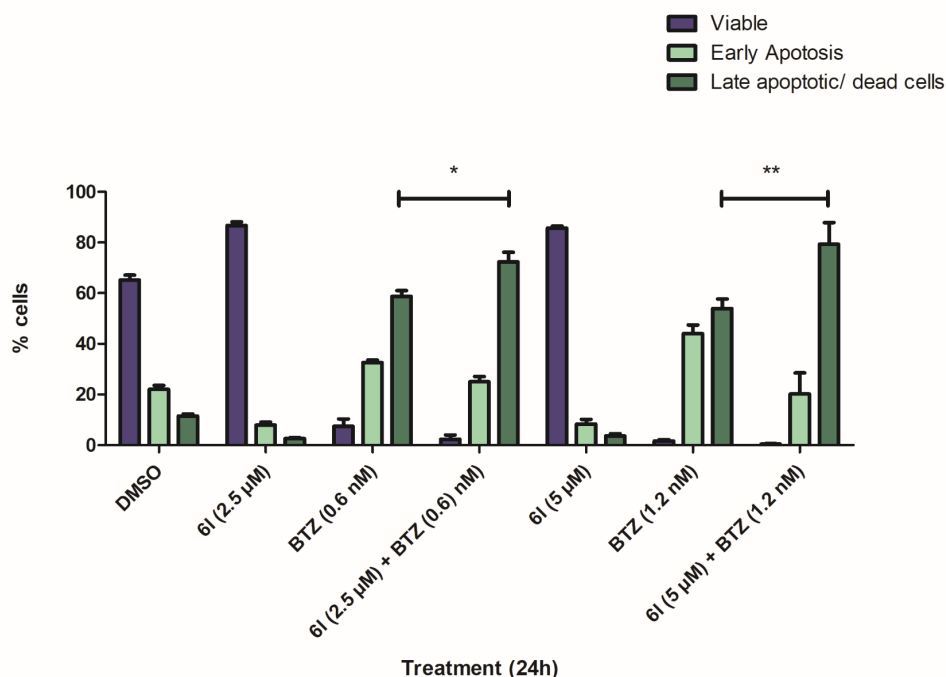


**Figure 2.9.** Annexin-PI staining of HL-60 cells after 24 h incubation with **II-6I**, bortezomib (BTZ) and combinations of both drugs at the indicated concentrations. The assays were performed in triplicates. The diagram was created by Melf Sönnichsen, HHU Düsseldorf. Adapted and reprinted with permission from Reßing et al. 2020. Copyright (2020) American Chemical Society.

<sup>10</sup> Annexin-PI assays were performed by Melf Sönnichsen in the group of Sanil Bhatia, HHU Düsseldorf.

## 2.3 Conclusions

A library of twelve potent tetrazole-capped HDAC6i based on three different scaffolds was successfully synthesised using a simple 2–3-step protocol that provided all compounds in good yields. Recrystallisation afforded all final compounds in purities of at least 95%.

The biological evaluation of the target compounds provided valuable SAR data and helped to identify **II-6I**, which features a benzyl residue and a trifluoromethyl substituent in the cap group, as a hit compound with remarkable selectivity for HDAC6 over HDACs 1–3 in the cellular environment of HL-60 cells. In biochemical assays, **II-6I** proved to be an equally potent and selective HDAC6i as the widely-used tool compound tubastatin A, thus exceeding the isoform selectivities of ricolinostat, nexturastat A, and HPOB. In those assays, no significant activity towards either class I isoform or the class IIa enzyme HDAC4 was detected. The molecular features responsible for the potent HDAC6 inhibition were disclosed by a co-crystal structure of zCD2 complexed with **II-6I**. Displaying a novel binding mode, the residues of the bifurcated capping group seemed to match the shape of both loop pockets so that L1 and L2 were simultaneously occupied.

Supposed to improve the metabolic stability of the new HDACi, the tetrazole group was chosen for the bioisosteric replacement of the more labile amide function featured in the previous peptoid libraries. In microsomal assays, **II-6I** pleasingly maintained good metabolic stability in presence of both human and mouse liver enzymes. In spite of its anticipated low cytotoxicity as a single-agent in a range of leukaemia cell lines, **II-6I** turned out to have beneficial effects on apoptosis induction in HL-60 cells treated with bortezomib. This effect indicates the successful activation of the synergism between the two targets and stresses the potential for selective HDAC6i in combination therapies.

Overall, **II-6I** may be considered an easily accessible, metabolically stable tool compound for potent and selective HDAC6 inhibition.

## 2.4 Experimental section

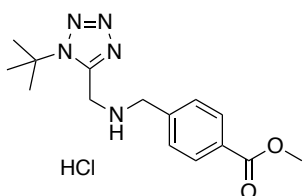
### 2.4.1 General information

Dry solvents, e.g. MeOH and DCM, were obtained from the MBraun MB SPS-800 solvent purification system. Except for DCM which was purified by distillation prior to use, all reagents and solvents were purchased from commercial sources and used without further purification. Thin layer chromatography (TLC) was carried out using Macherey-Nagel pre-coated aluminium foil sheets which were visualised using UV light (254 nm). Hydroxamic acids were stained using a 1% solution of iron(III) chloride in MeOH.  $^1\text{H}$  NMR and  $^{13}\text{C}$  NMR spectra were recorded at rt or, due to the occurrence of rotamers, at 60 °C using Bruker Avance III HD (400 MHz), and Varian/Agilent Mercury-plus (300 MHz & 400 MHz) spectrometers. Chemical shifts ( $\delta$ ) are quoted in parts per million (ppm). All spectra were standardised in accordance with the signals of the deuterated solvents (DMSO- $d_6$ :  $\delta_{\text{H}} = 2.50$  ppm,  $\delta_{\text{C}} = 39.5$  ppm;  $\text{CDCl}_3$ :  $\delta_{\text{H}} = 7.26$  ppm,  $\delta_{\text{C}} = 77.0$  ppm; MeOH- $d_4$ :  $\delta_{\text{H}} = 4.87$  ppm,  $\delta_{\text{C}} = 49.0$  ppm). Coupling constants ( $J$ ) are reported in Hertz (Hz). Mass spectra were measured by the Leipzig University Mass Spectrometry Service using electrospray ionisation (ESI) on Bruker Daltonics Impact II and Bruker Daltonics micrOTOF spectrometers. The uncorrected melting points were determined using a Barnstead Electrothermal 9100 apparatus. Analytical HPLC analysis were carried out using either a Gynkotec GINA 50 apparatus equipped with a Dionex P680A LPG pump, a Dionex UVD 340 U detector, and a China 50 autosampler; or a Thermo Fisher Scientific UltiMate 3000 system equipped with an UltiMate<sup>TM</sup> HPG-3400SD pump, an UltiMate<sup>TM</sup> 3000 Diode array detector, an UltiMate<sup>TM</sup> 3000 autosampler, and a TCC-3000SD standard thermostatted column compartment by Dionex. Both systems were operated using Macherey-Nagel NUCLEODUR 100-5  $\text{C}_{18}$  ec columns (250 mm x 4.6 mm). UV absorption was detected at 254 nm with a linear gradient of 5% B to 95% B within 23 min. Acidified HPLC-grade water (0.1% TFA; solvent A) and acidified HPLC-grade acetonitrile (0.1% TFA; solvent B) were used for elution at a flow rate of 1 mL/min. The purity of the final compounds was at least 95.0%.

## 2.4.2 Experimental procedures

**General procedure for the preparation of compounds II-5a-c.** Paraformaldehyde (75.0 mg, 2.5 mmol, 1.0 eq), methyl 4-(aminomethyl)benzoate hydrochloride (504 mg, 2.5 mmol, 1.0 eq), and Et<sub>3</sub>N (0.34 mL, 2.5 mmol, 1.0 eq) were dissolved in MeOH (2 mL) and subjected to microwave irradiation at 45 °C and 150 W under vigorous stirring for 30 min. The respective isonitrile (2.5 mmol, 1.0 eq) and trimethylsilyl azide (0.30 mL, 2.5 mmol, 1.0 eq) were added successively and the resulting mixture was again subjected to microwave irradiation at the same settings for 4 h before the solvent was removed under reduced pressure. The residue was dissolved in MeOH (1 mL) and Et<sub>2</sub>O (20 mL) to precipitate the triethylammonium chloride byproduct, which was removed by filtration. The filtrate was concentrated under reduced pressure to afford the crude product which was recrystallised from MeOH (1 mL), 37% HCl (0.2 mL), and chilled Et<sub>2</sub>O (20 mL). The resulting product was isolated by filtration and washed with chilled Et<sub>2</sub>O. If necessary, it was further purified by column chromatography.

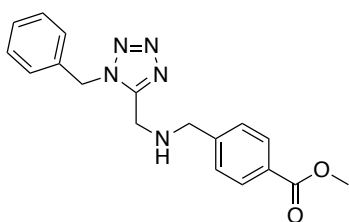
### Methyl 4-({[(1-*tert*-butyl-1*H*-1,2,3,4-tetrazol-5-yl)methyl]amino}methyl)benzoate hydrochloride (II-5a).



Synthesis using *tert*-butyl isonitrile (0.28 mL) and purification by column chromatography (DCM/MeOH 9:1 + 0.5% Et<sub>3</sub>N) followed by precipitation from MeOH (1 mL), 37% HCl (0.2 mL), and Et<sub>2</sub>O (20 mL) afforded **II-5a** as a white solid (400 mg, 1.32 mmol, 53%); mp 200–204 °C (decomp.); <sup>1</sup>H NMR (400 MHz, DMSO-*d*<sub>6</sub>):

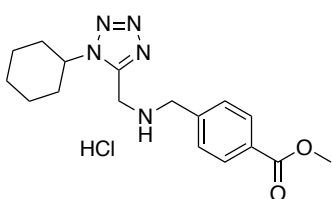
δ 10.37 (s, 2H, NH<sub>2</sub>), 8.09–7.98 (m, 2H, arom.), 7.80–7.67 (m, 2H, arom.), 4.85 (s, 2H, CH<sub>2</sub>), 4.45 (s, 2H, CH<sub>2</sub>), 3.87 (s, 3H, CH<sub>3</sub>), 1.67/1.52 (2 x s, 9H, *t*-Bu) ppm; <sup>13</sup>C NMR (101 MHz, DMSO-*d*<sub>6</sub>): δ 165.9, 148.4, 136.9, 130.6, 130.1, 129.3, 62.0, 52.3, 50.0, 41.2, 40.2, 28.9 ppm; HRMS (*m/z*): MNa<sup>+</sup> calcd for C<sub>15</sub>H<sub>21</sub>N<sub>5</sub>O<sub>2</sub> 326.1587, found 326.1580.

**Methyl 4-(((1-benzyl-1*H*-1,2,3,4-tetrazol-5-yl)methyl)amino)methyl)benzoate hydrochloride (II-5b).**



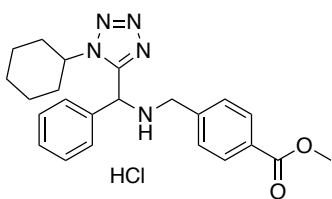
Synthesis using benzyl isocyanide (0.30 mL) afforded **II-5b** as an off-white solid (708 mg, 2.1 mmol, 84%); mp 155–160 °C (decomp.); <sup>1</sup>H NMR (300 MHz, DMSO-*d*<sub>6</sub>): δ 10.31 (s, 2H, NH<sub>2</sub>), 8.06–7.95 (m, 2H, arom.), 7.75–7.68 (m, 2H, arom.), 7.46–7.26 (m, 5H, arom.), 5.77 (s, 2H, CH<sub>2</sub>), 4.65 (s, 2H, CH<sub>2</sub>), 4.42 (s, 2H, CH<sub>2</sub>), 3.87 (s, 3H, CH<sub>3</sub>) ppm; <sup>13</sup>C NMR (101 MHz, DMSO-*d*<sub>6</sub>): δ 165.9, 149.1, 136.7, 133.9, 130.6, 130.1, 129.4, 128.9, 128.5, 128.4, 52.4, 50.6, 49.8, 38.0 ppm; HRMS (m/z): MH<sup>+</sup> calcd for C<sub>18</sub>H<sub>19</sub>N<sub>5</sub>O<sub>2</sub> 338.1612, found 338.1621.

**Methyl 4-(((1-cyclohexyl-1*H*-1,2,3,4-tetrazol-5-yl)methyl)amino)methyl)benzoate hydrochloride (II-5c).**



Synthesised using cyclohexyl isonitrile (0.30 mL). Purification by column chromatography (DCM/MeOH 9:1) followed by precipitation from MeOH (1 mL), 37% HCl (0.2 mL), and Et<sub>2</sub>O (20 mL) afforded **II-5c** as a white solid (458 mg, 1.39 mmol, 56%), mp 188–192 °C (decomp.); <sup>1</sup>H NMR (400 MHz, DMSO-*d*<sub>6</sub>): δ 10.44 (br s, 2H, NH<sub>2</sub>), 8.05–8.00 (m, 2H, arom.), 7.78–7.72 (m, 2H, arom.), 4.69 (s, 2H, CH<sub>2</sub>), 4.64–4.53 (m, 1H, CH), 4.43 (s, 2H, CH<sub>2</sub>), 3.87 (s, 3H, CH<sub>3</sub>), 2.11–2.03 (m, 2H, c-Hexyl), 1.88–1.64 (m, 5H, c-Hexyl), 1.49–1.17 (m, 3H, c-Hexyl) ppm; <sup>13</sup>C NMR (101 MHz, DMSO-*d*<sub>6</sub>): δ 165.9, 151.3, 148.2, 136.8, 130.7, 130.1, 129.3, 57.1, 56.5, 52.4, 49.8, 45.1, 38.1, 32.4, 24.6 ppm; HRMS (m/z): MH<sup>+</sup> calcd for C<sub>17</sub>H<sub>23</sub>N<sub>5</sub>O<sub>2</sub> 330.1925, found 330.1926.

**Methyl 4-(((1-cyclohexyl-1*H*-1,2,3,4-tetrazol-5-yl)(phenyl)methyl)amino)methyl)benzoate hydrochloride (II-5d).**

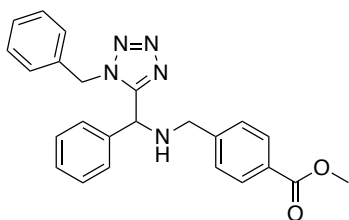


Methyl 4-(aminomethyl)benzoate hydrochloride (504 mg, 2.5 mmol, 1.0 eq), benzaldehyde (0.30 mL, 2.5 mmol, 1.0 eq), Et<sub>3</sub>N (0.34 mL, 2.5 mmol, 1.0 eq), and crushed molecular sieves 4 Å (200 mg) were suspended in dry MeOH (4 mL) and stirred at rt for 30 min before cyclohexyl isonitrile (0.30 mL, 2.5 mmol, 1.0 eq) and trimethylsilyl azide (0.30 mL, 2.5 mmol, 1.0 eq) were added



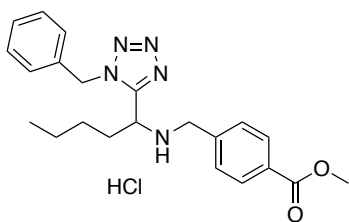
successively. After stirring at rt for 3 days, the molecular sieves were removed by filtration and washed with EtOAc (5 mL). The filtrate was concentrated under reduced pressure and redissolved in MeOH (1 mL) and Et<sub>2</sub>O (20 mL) to precipitate the triethylammonium chloride byproduct, which was removed by filtration. Acidification of the filtrate using 37% HCl (0.2 mL) did not induce crystallisation of the product. Instead, 1M NaOH was added to adjust pH 8 upon which the organic solvents were evaporated. The residue was then diluted with water (10 mL), extracted with EtOAc (3 x 50 mL), dried over MgSO<sub>4</sub>, and concentrated under reduced pressure to afford the crude product. Recrystallisation using EtOAc (1 mL) and petrol (20 mL) afforded **II-5d** as a white solid (853 mg, 2.10 mmol, 84%); mp 177 °C (decomp.); <sup>1</sup>H NMR (300 MHz, DMSO-*d*<sub>6</sub>): δ 11.30–10.51 (m, 2H, NH<sub>2</sub>), 8.05–7.93 (m, 2H, arom.), 7.74–7.62 (m, 4H, arom.), 7.58–7.43 (m, 3H, arom.), 6.50 (s, 1H, CH), 4.53–4.39 (m, 1H, CH), 4.34–4.02 (m, 2H, CH<sub>2</sub>), 3.86 (s, 3H, CH<sub>3</sub>), 2.20–0.80 (m, 10H, *c*-Hexyl) ppm; <sup>13</sup>C NMR (101 MHz, DMSO-*d*<sub>6</sub>): δ 165.9, 151.4, 130.6, 130.3, 129.9, 129.4, 129.3, 129.2, 57.2, 54.4, 52.3, 49.2, 32.4, 31.7, 24.6, 24.4, 24.3 ppm; HRMS (*m/z*): MNa<sup>+</sup> calcd for C<sub>23</sub>H<sub>27</sub>N<sub>5</sub>O<sub>2</sub> 428.2057, found 428.2065.

**Methyl 4-(((1-benzyl-1*H*-1,2,3,4-tetrazol-5-yl)(phenyl)methyl)amino)methyl)benzoate (II-5e).**



Methyl 4-(aminomethyl)benzoate hydrochloride (504 mg, 2.5 mmol, 1.0 eq), benzaldehyde (0.30 mL, 2.5 mmol, 1.0 eq), and Et<sub>3</sub>N (0.34 mL, 2.5 mmol, 1.0 eq) were dissolved in dry MeOH (1 mL) and subjected to microwave irradiation at 45 °C and 150 W under vigorous stirring for 2 h. Benzyl isonitrile (0.30 mL, 2.5 mmol, 1.0 eq) and trimethylsilyl azide (0.30 mL, 2.5 mmol, 1.0 eq) were added successively and the resulting mixture was again subjected to microwave irradiation at the same settings for 4 h. To allow for complete crystallisation, the reaction vessel was cooled to 0 °C for 2 h before the precipitate was isolated by filtration and washed with chilled MeOH (2 mL) and *n*-hexane (10 mL). **II-5e** was obtained as an off-white solid (813 mg, 1.97 mmol, 79%); mp 100 °C; <sup>1</sup>H NMR (400 MHz, CDCl<sub>3</sub>): δ 7.97–7.88 (m, 2H, arom.), 7.41–7.06 (m, 10H, arom.), 6.95–6.83 (m, 2H, arom.), 5.40/5.17 (2 x d, *J* = 15.4/15.4 Hz, 2H, CH<sub>2</sub>), 4.94 (s, 1H, NH), 3.93 (s, 3H, CH<sub>3</sub>), 3.71 (s, 2H, CH<sub>2</sub>) ppm; <sup>13</sup>C NMR (101 MHz, DMSO-*d*<sub>6</sub>): δ 166.2, 156.2, 145.5, 138.1, 134.5, 129.1, 128.6, 128.5, 128.2, 128.1, 128.0, 127.8, 127.7, 55.2, 52.1, 50.1 ppm; HRMS (*m/z*): MNa<sup>+</sup> calcd for C<sub>24</sub>H<sub>23</sub>N<sub>5</sub>O<sub>2</sub> 436.1744, found 436.1756.

**Methyl 4-([1-(1-benzyl-1*H*-1,2,3,4-tetrazol-5-yl)pentyl]amino)methyl)benzoate hydrochloride (**II-5f**).**

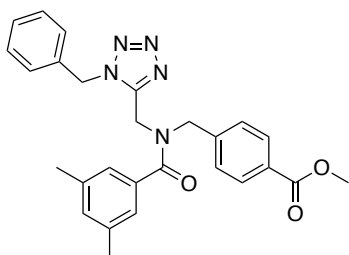


Methyl 4-(aminomethyl)benzoate hydrochloride (504 mg, 2.5 mmol, 1.0 eq), valeraldehyde (0.27 mL, 2.5 mmol, 1.0 eq), and Et<sub>3</sub>N (0.34 mL, 2.5 mmol, 1.0 eq) were dissolved in dry MeOH (4 mL) and stirred at rt for 30 min before benzyl isonitrile (0.30 mL, 2.5 mmol, 1.0 eq) and trimethylsilyl azide (0.30 mL, 2.5 mmol, 1.0 eq) were added successively. After stirring at rt for 3 days, the mixture was concentrated under reduced pressure and the residue was redissolved in EtOAc (1 mL) and petrol (20 mL) to precipitate the triethylammonium chloride byproduct, which was removed by filtration. The filtrate was acidified using 37% HCl (0.2 mL) to obtain the hydrochloride salt of the product which was allowed to crystallise at -18 °C for 16 h before it was isolated by filtration. The crude product thus obtained was recrystallised from MeOH (1 mL) and Et<sub>2</sub>O (20 mL) to afford **II-5f** as a grey solid (542 mg, 1.26 mmol, 50%); mp 189 °C (decomp.); <sup>1</sup>H NMR (300 MHz, DMSO-*d*<sub>6</sub>): δ 10.76–10.11 (m, 2H, NH<sub>2</sub>), 8.06–7.90 (m, 2H, arom.), 7.77–7.60 (m, 2H, arom.), 7.47–7.21 (m, 5H, arom.), 5.85 (d, *J* = 1.9 Hz, 2H, CH<sub>2</sub>), 5.02 (s, 1H, CH), 4.37/4.18 (2 x d, *J* = 13.2/13.0 Hz, 2H, CH<sub>2</sub>), 3.87 (s, 3H, CH<sub>3</sub>), 2.19–1.93 (m, 2H, CH<sub>2</sub>CH<sub>2</sub>CH<sub>2</sub>CH<sub>3</sub>), 1.26–0.74 (m, 4H, CH<sub>2</sub>CH<sub>2</sub>CH<sub>3</sub>), 0.61 (t, *J* = 7.3 Hz, 3H, CH<sub>3</sub>) ppm; <sup>13</sup>C NMR (101 MHz, DMSO-*d*<sub>6</sub>): δ 165.8, 151.7, 136.9, 134.2, 130.5, 129.9, 129.2, 128.8, 128.6, 128.1, 52.3, 50.4, 49.9, 47.8, 30.1, 26.2, 21.5, 13.4 ppm; HRMS (*m/z*): MH<sup>+</sup> calcd for C<sub>22</sub>H<sub>27</sub>N<sub>5</sub>O<sub>2</sub> 394.2238, found 394.2232.

**General procedure for the preparation of compounds II-8a and II-8b.** The respective carboxylic acid (0.70 mmol, 1.3 eq) was dissolved in dry DCM (5 mL) and cooled to 0 °C before thionyl chloride (0.08 mL, 1.1 mmol, 1.6 eq) was added dropwise. After 30 min of stirring at 0 °C, a solution of the respective ester or hydrochloride salt **II-5** (0.54 mmol, 1.0 eq) and Et<sub>3</sub>N (0.16 mL, 1.15 mmol, 2.1 eq) in dry DCM (2 mL) was added slowly and the resulting mixture was stirred at rt for 16 h. Afterwards, the mixture was diluted with DCM (100 mL) and washed with 10% aq. HCl (2x 10 mL), water (1 x 5 mL), sat. aq. NaHCO<sub>3</sub> (2 x 10 mL), water (1 x 5 mL), and brine (1 x 10 mL). The organic layer was separated, dried over MgSO<sub>4</sub>, and concentrated under reduced pressure. To remove excess acyl chloride, the residue was filtered over a layer of silica (*n*-hexane/EtOAc 3:1) which was subsequently

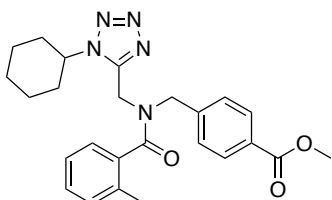
washed with DCM/MeOH (9:1) to elute the remaining product. The crude product thus obtained was recrystallised from EtOAc (2 mL) and *n*-hexane (20 mL).

**Methyl 4-({*N*-[(1-benzyl-1*H*-1,2,3,4-tetrazol-5-yl)methyl]-1-(3,5-dimethylphenyl)formamido}methyl)benzoate (**II-8a**).**



Synthesis using **II-5b** (202 mg) and 3,5-dimethyl-benzoic acid (105 mg) afforded **II-8a** as a colourless oil (126 mg, 0.27 mmol, 50%); <sup>1</sup>H NMR (300 MHz, CDCl<sub>3</sub>): δ 8.05–7.96 (m, 2H, arom.), 7.37–7.19 (m, 7H, arom.), 7.08–6.99 (m, 1H, arom.), 6.96–6.86 (m, 2H, arom.), 5.86 (s, 2H, CH<sub>2</sub>), 4.80–4.64 (m, 4H, 2 x CH<sub>2</sub>), 3.92 (s, 3H, OCH<sub>3</sub>), 2.39–2.35/2.29–2.21 (2 x m, 6H, 2 x CH<sub>3</sub>) ppm; <sup>13</sup>C NMR (101 MHz, CDCl<sub>3</sub>): δ 173.0, 166.7, 151.5, 140.8, 138.7, 138.3, 135.4, 134.2, 134.1, 132.2, 130.4, 130.1, 129.3, 129.3, 129.1, 129.0, 128.0, 127.9, 127.6, 127.5, 127.4, 124.5, 52.5, 52.4, 51.2, 36.0, 21.3 ppm; HRMS (m/z): MNa<sup>+</sup> calcd for C<sub>27</sub>H<sub>27</sub>N<sub>5</sub>O<sub>3</sub> 492.2006, found 492.2012.

**Methyl 4-({*N*-[(1-cyclohexyl-1*H*-1,2,3,4-tetrazol-5-yl)methyl]-1-(2-methylphenyl)formamido}methyl)benzoate (**II-8b**).**

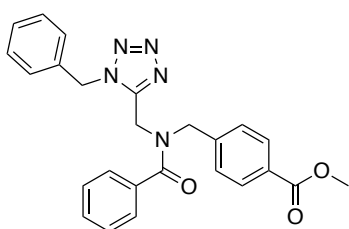


Synthesis using **II-5c** (177 mg) and 2-methylbenzoic acid (95.0 mg) afforded **II-8b** as a colourless oil (194 mg, 0.43 mmol, 80%); <sup>1</sup>H NMR (400 MHz, CDCl<sub>3</sub>): δ 8.06–7.96 (m, 2H, arom.), 7.33–7.16 (m, 6H, arom.), 5.02–4.29 (m, 5H, 2 x CH, 2 x CH<sub>2</sub>), 3.92 (s, 3H, OCH<sub>3</sub>), 2.08–1.89 (m, 3H, CH<sub>3</sub>), 2.08–1.89 (m, 5H, c-Hexyl), 1.81–1.71 (m, 1H, c-Hexyl), 1.57–1.23 (m, 4H, c-Hexyl) ppm; <sup>13</sup>C NMR (101 MHz, CDCl<sub>3</sub>): δ 172.5, 166.7, 150.4, 140.7, 134.8, 134.6, 131.0, 130.4, 130.3, 129.8, 128.9, 128.1, 127.8, 126.3, 125.8, 77.5, 77.2, 76.8, 58.4, 52.4, 52.0, 35.8, 32.7, 25.4, 25.0, 19.0 ppm; HRMS (m/z): MNa<sup>+</sup> calcd for C<sub>25</sub>H<sub>29</sub>N<sub>5</sub>O<sub>3</sub> 470.2163, found 470.2189.

**General procedure for the preparation of compounds II-8c-f.** The respective ester **II-5** (0.54 mmol, 1.0 eq) and Et<sub>3</sub>N (0.16 mL, 2.15 mmol, 2.1 eq) were dissolved in dry DCM (10 mL) and the respective acyl chloride (0.65 mmol, 1.2 eq) was added dropwise at 0 °C. The resulting solution was stirred at rt for 16 h. Upon completion of the reaction, the mixture

was diluted with DCM (100 mL) and washed with 10% aq. HCl (2 x 10 mL), water (1 x 5 mL), sat. aq. NaHCO<sub>3</sub> (2 x 10 mL), water (1 x 5 mL), and brine (1 x 10 mL). The organic layer was separated, dried over MgSO<sub>4</sub>, and concentrated under reduced pressure. The residue was purified by recrystallisation from EtOAc (2 mL) and petrol (20 mL) or by gradient column chromatography (EtOAc/petrol 3:1 to 1:1, followed by DCM/MeOH 9:1).

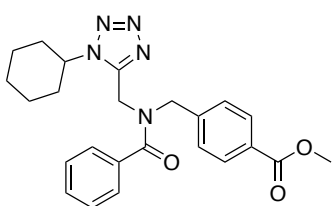
**Methyl 4-({N-[(1-benzyl-1H-1,2,3,4-tetrazol-5-yl)methyl]-1-phenylformamido}methyl)benzoate (II-8c).**



Synthesised using **II-5b** (202 mg) and benzoyl chloride (0.08 mL). Recrystallisation afforded **II-8c** as a white solid (202 mg, 0.46 mmol, 85%); mp 115–118 °C; <sup>1</sup>H NMR (300 MHz, CDCl<sub>3</sub>): δ 8.06–7.93 (m, 2H, arom.), 7.48–7.12 (m, 12H, arom.), 5.84 (s, 2H, CH<sub>2</sub>), 4.76 (s, 2H, CH<sub>2</sub>), 4.69 (s, 2H, CH<sub>2</sub>), 3.89 (s, 3H, CH<sub>3</sub>) ppm; <sup>13</sup>C NMR (101 MHz, CDCl<sub>3</sub>):

δ 172.7, 166.7, 151.5, 140.7, 134.3, 134.1, 133.6, 130.8, 130.5, 130.3, 130.2, 129.4, 129.0, 128.9, 127.7, 127.4, 127.0, 52.5, 52.4, 51.3, 36.3 ppm; HRMS (m/z): MNa<sup>+</sup> calcd for C<sub>25</sub>H<sub>23</sub>N<sub>5</sub>O<sub>3</sub> 464.1693, found 464.1696.

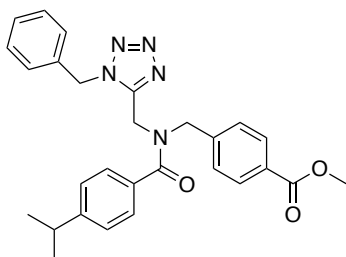
**Methyl 4-({N-[(1-cyclohexyl-1H-1,2,3,4-tetrazol-5-yl)methyl]-1-phenylformamido}methyl)benzoate (II-8d).**



Synthesised using **II-5c** (177 mg) and benzoyl chloride (0.08 mL). Filtration over a layer of silica using DCM/MeOH (9:1) as eluent and subsequent recrystallisation afforded **II-8d** as a white solid (153 mg, 0.35 mmol, 65%); mp 78–82 °C; <sup>1</sup>H NMR (400 MHz, CDCl<sub>3</sub>): δ 7.95–7.86 (m, 2H, arom.), 7.35–7.15 (m,

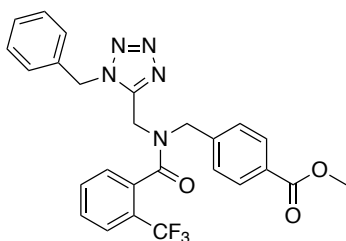
7H, arom.), 4.74–4.58 (m, 4H, 2 x CH<sub>2</sub>), 4.58–4.46 (m, 1H, CH), 3.78 (s, 3H, CH<sub>3</sub>), 1.96–1.53 (m, 7H, c-Hexyl); 1.43–1.07 (m, 3H, c-Hexyl) ppm; <sup>13</sup>C NMR (101 MHz, CDCl<sub>3</sub>): δ 172.4, 166.7, 150.4, 140.9, 134.6, 130.7, 130.5, 130.2, 129.0, 127.4, 126.9, 77.5, 77.2, 76.8, 58.3, 52.4, 36.3, 33.3, 27.1, 25.4, 25.0 ppm; HRMS (m/z): MH<sup>+</sup> calcd for C<sub>24</sub>H<sub>27</sub>N<sub>5</sub>O<sub>3</sub> 434.2187, found 434.2182.

**Methyl 4-((N-[(1-benzyl-1*H*-1,2,3,4-tetrazol-5-yl)methyl]-1-[4-(propan-2-yl)phenyl]formamido)methyl)benzoate (**II-8e**).**



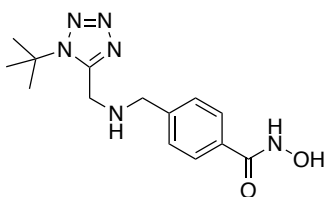
Synthesised using **II-5b** (202 mg) and 2-isopropyl-benzoyl chloride (118 mg). Filtration over a layer of silica using DCM/MeOH (9:1) as eluent and subsequent recrystallisation afforded **II-8e** as a yellow oil (145 mg, 0.30 mmol, 56%); mp 109 °C; <sup>1</sup>H NMR (400 MHz, CDCl<sub>3</sub>): δ 8.14–7.93 (m, 2H, arom.), 7.39–7.18 (m, 11H, arom.), 5.88 (s, 2H, CH<sub>2</sub>), 4.82 (s, 2H, CH<sub>2</sub>), 4.70 (s, 2H, CH<sub>2</sub>), 3.92 (s, 3H, CH<sub>3</sub>), 2.90 (p, *J* = 6.9 Hz, 1H, CH), 1.22 (d, *J* = 6.9 Hz, 6H, 2 x CH<sub>3</sub>) ppm; <sup>13</sup>C NMR (101 MHz, CDCl<sub>3</sub>): δ 172.8, 166.7, 152.0, 151.5, 140.9, 134.1, 131.6, 130.5, 130.1, 129.4, 129.0, 127.7, 127.4, 127.2, 126.9, 77.5, 77.2, 76.8, 52.6, 52.4, 51.3, 36.3, 34.2, 23.9 ppm; HRMS (*m/z*): MH<sup>+</sup> calcd for C<sub>28</sub>H<sub>29</sub>N<sub>5</sub>O<sub>3</sub> 484.2343, found 484.2339.

**Methyl 4-((N-[(1-benzyl-1*H*-1,2,3,4-tetrazol-5-yl)methyl]-1-[2-(trifluoromethyl)phenyl]formamido)methyl)benzoate (**II-8f**).**



Synthesised using **II-5b** (202 mg) and 2-(trifluoromethyl)benzoyl chloride (0.09 mL). Column chromatography afforded **II-8f** as a yellow oil (257 mg, 0.50 mmol, 93%); <sup>1</sup>H NMR (400 MHz, CDCl<sub>3</sub>): δ 7.98–7.87 (m, 2H, arom.), 7.69–7.63 (m, 1H, arom.), 7.56–7.45 (m, 2H, arom.), 7.35–7.19 (m, 8H, arom.), 5.89–5.61 (m, 2H, CH<sub>2</sub>), 5.04–4.89/4.61–4.34 (2 x m, 4H, 2 x CH<sub>2</sub>), 3.86/3.84 (2 x s, 3H, CH<sub>3</sub>) ppm; <sup>13</sup>C NMR (75 MHz, CDCl<sub>3</sub>): δ 169.9, 166.6, 150.7, 139.7, 134.0, 133.3, 133.2, 132.5, 130.4, 130.3, 130.1, 129.9, 129.5, 129.3, 129.0, 128.7, 127.9, 127.7, 127.4, 127.3, 127.2, 127.1, 127.1, 126.9, 125.4, 121.8, 52.4, 51.9, 51.3, 47.8, 35.3 ppm; HRMS (*m/z*): MH<sup>+</sup> calcd for C<sub>26</sub>H<sub>22</sub>F<sub>3</sub>N<sub>5</sub>O<sub>3</sub> 510.1748, found 510.1744.

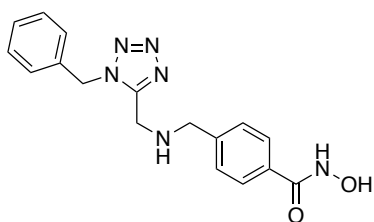
**4-(((1-*tert*-Butyl-1*H*-1,2,3,4-tetrazol-5-yl)methyl]amino)methyl)-*N*-hydroxybenzamide (II-6a).**



To a cooled solution (0 °C) of NaOH (149 mg, 3.73 mmol, 11 eq) in MeOH (4 mL) and DCM (1.5 mL) was added hydroxylamine (50% solution in water; 0.62 mL, 10.1 mmol, 30 eq) and the resulting mixture was stirred at 0 °C for 5 min before **II-5a** (114 mg, 0.34 mmol, 1.0 eq) was added. The mixture was stirred at 0 °C for 60 min and then at rt for another 60 min before TLC (DCM/MeOH 9:1) indicated full conversion upon which the solvents were evaporated. The residue was dissolved in water (10 mL) and the mixture was neutralised using 10% aq. HCl (pH 8). The collected organics obtained by extraction with EtOAc (5 x 30 mL) were dried over Na<sub>2</sub>SO<sub>4</sub> and the solvent was removed under reduced pressure. Recrystallisation of the residue from MeOH (0.5 mL) and Et<sub>2</sub>O (10 mL) afforded **II-6a** as a white solid (57.0 mg, 0.19 mmol, 55%); mp 154 °C (decomp.); *t<sub>R</sub>*: 5.72 min, purity: 95.5%; <sup>1</sup>H NMR (400 MHz, DMSO-*d*<sub>6</sub>): δ 11.20 (s, 1H, *NH*-OH), 9.00 (s, 1H, OH), 7.76–7.67 (m, 2H, arom.), 7.46–7.37 (m, 2H, arom.), 4.18 (s, 2H, CH<sub>2</sub>), 3.84 (s, 2H, CH<sub>2</sub>), 1.68/1.52 (2 x s, 9H, *t*-Bu) ppm; <sup>13</sup>C NMR (101 MHz, DMSO-*d*<sub>6</sub>): δ 164.0, 152.5, 131.6, 128.8, 126.9, 61.4, 51.4, 42.3, 29.0 ppm; HRMS (*m/z*): MH<sup>+</sup> calcd for C<sub>14</sub>H<sub>20</sub>N<sub>6</sub>O<sub>2</sub> 305.1721, found 305.1731.

**General procedure for the preparation of compounds II-6b-I.** To a cooled (0 °C) solution of NaOH in MeOH (4 mL) and DCM (1.5 mL) was added hydroxylamine (50% solution in water) and the mixture was stirred at 0 °C for 5 min before a solution of the respective ester **II-5** or **8** in DCM (1 mL) was added dropwise. The resulting mixture was stirred at 0 °C for 1–4 h until TLC (DCM/MeOH 9:1) indicated full conversion upon which the solvents were removed under reduced pressure. The residue was suspended in water (10 mL) and the mixture was neutralised using 10% aq. HCl (pH 8) to precipitate the crude product which was isolated by filtration and washed with water (5 x 4 mL). If HPLC proved insufficient purity < 95%, the solid thus obtained was further purified by recrystallisation from MeOH (0.5 mL) and Et<sub>2</sub>O (10 mL) or EtOAc (0.5 mL) and petrol (10 mL), respectively.

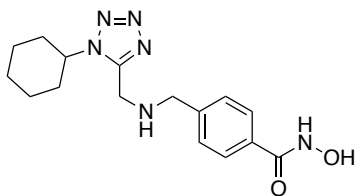
**4-([[(1-Benzyl-1*H*-1,2,3,4-tetrazol-5-yl)methyl]amino)methyl]-*N*-hydroxybenzamide (II-6b).**



Synthesised using **II-5b** (62.0 mg, 0.17 mmol 1.0 eq), hydroxylamine (50% solution in water; 0.33 mL, 5.39 mmol, 32 eq), and NaOH (75.0 mg, 1.88 mmol, 11 eq). Recrystallisation from MeOH and Et<sub>2</sub>O afforded **II-6b** as a white solid (47.0 mg, 0.14 mmol, 82%); mp 172 °C (decomp.); *t*<sub>R</sub>: 6.11 min, purity: 99.2%; <sup>1</sup>H NMR (400 MHz, DMSO-*d*<sub>6</sub>):

δ 11.26 (s, 1H, *NH*-OH), 9.05 (s, 1H, OH), 7.82–7.69 (m, 2H, arom.), 7.55–7.21 (m, 7H, arom.), 5.74 (s, 2H, CH<sub>2</sub>), 4.32 (s, 2H, CH<sub>2</sub>), 4.05 (s, 2H, CH<sub>2</sub>) ppm; <sup>13</sup>C NMR (101 MHz, DMSO-*d*<sub>6</sub>): δ 163.6, 149.4, 134.0, 133.2, 130.1, 128.9, 128.6, 128.3, 127.1, 50.6, 50.0, 38.2 ppm; HRMS (*m/z*): M<sup>-</sup> calcd for C<sub>17</sub>H<sub>18</sub>N<sub>6</sub>O<sub>2</sub> 337.1418, found 337.1430.

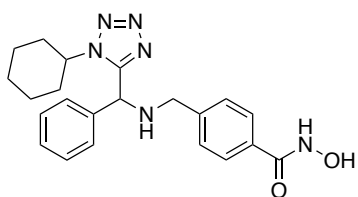
**4-([[(1-Cyclohexyl-1*H*-1,2,3,4-tetrazol-5-yl)methyl]amino)methyl]-*N*-hydroxybenzamide (II-6c).**



Synthesised using **II-5c** (116 mg, 0.34 mmol, 1.0 eq), hydroxylamine (50% solution in water; 0.62 mL, 10.1 mmol, 30 eq), and NaOH (149 mg, 3.73 mmol, 11 eq). Recrystallisation from MeOH and Et<sub>2</sub>O afforded **II-6c** as an off-white solid (53.0 mg, 0.16 mmol, 47%); mp 124 °C (decomp.); *t*<sub>R</sub>: 6.23 min, purity: 99.3%; <sup>1</sup>H NMR (400 MHz, DMSO-*d*<sub>6</sub>):

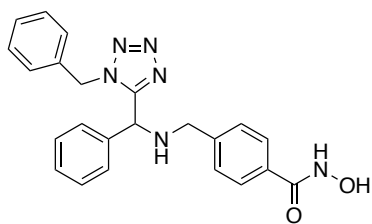
δ 11.17 (s, 1H, *NH*-OH), 9.00 (s, 1H, OH), 7.79–7.68 (m, 2H, arom.), 7.46–7.30 (m, 2H, arom.), 4.61–4.49 (m, 1H, CH), 4.00 (s, 2H, CH<sub>2</sub>), 3.73 (s, 2H, CH<sub>2</sub>), 2.05–1.60 (m, 7H, *c*-Hexyl), 1.48–1.20 (m, 3H, *c*-Hexyl) ppm; <sup>13</sup>C NMR (101 MHz, DMSO-*d*<sub>6</sub>): δ 164.0, 152.9, 143.4, 131.3, 127.9, 126.8, 56.7, 51.7, 40.4, 32.4, 24.8, 24.6 ppm; HRMS (*m/z*): MNa<sup>+</sup> calcd for C<sub>16</sub>H<sub>22</sub>N<sub>6</sub>O<sub>2</sub> 353.1696, found 353.1692.

**4-([[(1-Cyclohexyl-1*H*-1,2,3,4-tetrazol-5-yl)(phenyl)methyl]amino]methyl)-*N*-hydroxy benzamide (**II-6d**).**



Synthesis using **II-5d** (110 mg, 0.25 mmol, 1.0 eq), hydroxylamine (50% solution in water; 0.45 mL, 7.34 mmol, 30 eq), and NaOH (101 mg, 2.53 mmol, 10 eq) afforded **II-6d** as a red solid (81.0 mg, 0.18 mmol, 73%); mp 101 °C (decomp.);  $t_R$ : 6.98 min, purity: 97.0%;  $^1\text{H}$  NMR (300 MHz, DMSO- $d_6$ ):  $\delta$  11.39–10.83 (br s, 1H, *NH*-OH), 9.30–8.73 (br s, 1H, OH), 7.91–7.67 (m, 2H, arom.), 7.54–7.27 (m, 7H, arom.), 5.34 (d,  $J = 2.7$  Hz, 1H, Ph-*CH*), 4.65–4.47 (m, 1H, *c*-Hexyl-*CH*), 3.80–3.59 (m, 2H,  $\text{CH}_2$ ), 1.85–1.47 (m, 7H, *c*-Hexyl), 1.47–1.04 (m, 3H, *c*-Hexyl) ppm;  $^{13}\text{C}$  NMR (101 MHz, DMSO- $d_6$ ):  $\delta$  163.9, 155.1, 143.2, 138.5, 131.3, 129.2, 128.6, 128.0, 127.9, 127.7, 127.7, 126.8, 56.8, 55.3, 50.0, 32.34, 32.31, 24.7, 24.5 ppm; HRMS ( $m/z$ ):  $M^-$  calcd for  $\text{C}_{22}\text{H}_{26}\text{N}_6\text{O}_2$  405.2044, found 405.2041.

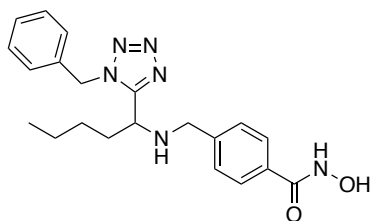
**4-([[(1-Benzyl-1*H*-1,2,3,4-tetrazol-5-yl)(phenyl)methyl]amino]methyl)-*N*-hydroxy benzamide (**II-6e**).**



Synthesised using **II-5e** (140 mg, 0.34 mmol, 1.0 eq), hydroxylamine (50% solution in water; 0.62 mL, 10.1 mmol, 30 eq), and NaOH (139 mg, 3.48 mmol, 10 eq). Recrystallisation from MeOH and Et<sub>2</sub>O afforded **II-6e** as a pale brown solid (114 mg, 0.28 mmol, 81%); mp 93 °C (decomp.);  $t_R$ : 6.79 min, purity: 98.9%;  $^1\text{H}$  NMR (300 MHz, DMSO- $d_6$ ):  $\delta$  11.18 (s, 1H, *NH*-OH), 8.94 (s, 1H, OH), 7.74–7.61 (m, 2H, arom.), 7.43–7.19 (m, 10H, arom.), 7.08–6.94 (m, 2H, arom.), 5.77–5.52 (m, 2H,  $\text{CH}_2$ ), 5.28 (s, 1H, CH), 3.63 (s, 2H,  $\text{CH}_2$ ) ppm;  $^{13}\text{C}$  NMR (101 MHz, DMSO- $d_6$ ):  $\delta$  164.1, 156.2, 143.0, 138.1, 134.5, 131.3, 129.3, 128.6, 128.5, 128.2, 128.0, 127.9, 127.8, 127.7, 126.8, 55.2, 50.09, 50.06 ppm; HRMS ( $m/z$ ):  $M^-$  calcd for  $\text{C}_{23}\text{H}_{22}\text{N}_6\text{O}_2$  413.1731, found 413.1746.



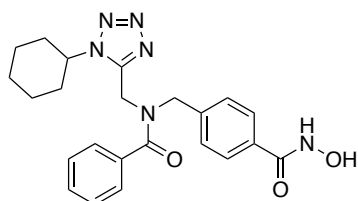
**4-([1-(1-Benzyl-1*H*-1,2,3,4-tetrazol-5-yl)pentyl]amino)methyl)-*N*-hydroxybenzamide (II-6f).**



Synthesised using **II-5f** (146 mg, 0.34 mmol, 1.0 eq), hydroxylamine (50% solution in water; 0.62 mL, 10.1 mmol, 30 eq), and NaOH (149 mg, 3.73 mmol, 11 eq). Recrystallisation from MeOH and Et<sub>2</sub>O afforded **II-6f** as an off-white solid (30.0 mg, 0.08 mmol, 28%); mp 130 °C (decomp.); *t<sub>R</sub>*: 6.94 min, purity: 99.0%; <sup>1</sup>H NMR (400 MHz,

DMSO-*d*<sub>6</sub>): δ 11.15 (s, 1H, *NH*-OH), 8.98 (s, 1H, OH), 7.70–7.59 (m, 2H, arom.), 7.39–7.23 (m, 5H, arom.), 7.18–7.13 (m, 2H, arom.), 5.79 (d, *J* = 15.6 Hz, 1H, CH<sub>2</sub>), 5.65 (d, *J* = 15.6 Hz, 1H, CH<sub>2</sub>), 4.09 (d, *J* = 7.1 Hz, 1H, CH), 3.62–3.42 (m, 2H, CH<sub>2</sub>), 2.91 (d, *J* = 6.8 Hz, 1H, NH), 1.81–1.51 (m, 2H, CH<sub>2</sub>CH<sub>2</sub>CH<sub>2</sub>CH<sub>3</sub>), 1.15–0.83 (m, 4H, CH<sub>2</sub>CH<sub>2</sub>CH<sub>3</sub>), 0.70 (t, *J* = 7.1 Hz, 3H, CH<sub>3</sub>) ppm; <sup>13</sup>C NMR (101 MHz, DMSO-*d*<sub>6</sub>): δ 164.0, 156.5, 143.3, 134.9, 131.2, 128.8, 128.2, 127.7, 127.5, 126.7, 51.7, 49.9, 49.8, 40.2, 39.7, 33.0, 27.5, 21.7, 13.7 ppm; HRMS (*m/z*): *M*<sup>-</sup> calcd for C<sub>21</sub>H<sub>26</sub>N<sub>6</sub>O<sub>2</sub> 393.2044, found 393.2053.

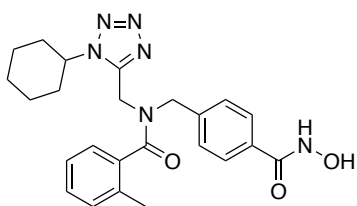
**4-([*N*-[(1-Cyclohexyl-1*H*-1,2,3,4-tetrazol-5-yl)methyl]-1-phenylformamido]methyl)-*N*-hydroxybenzamide (II-6g).**



Synthesis using **II-8d** (100 mg, 0.23 mmol, 1.0 eq), hydroxylamine (50% solution in water; 0.43 mL, 7.02 mmol, 31 eq), and NaOH (90.0 mg, 2.25 mmol, 9.8 eq) afforded **II-6g** as a white solid (71.0 mg, 0.16 mmol, 70%); mp 106 °C (decomp.); *t<sub>R</sub>*: 7.98 min, purity: 97.7%; <sup>1</sup>H NMR (300 MHz,

DMSO-*d*<sub>6</sub>): δ 11.23 (s, 1H, *NH*-OH), 9.03 (s, 1H, OH), 7.82–7.71 (m, 2H, arom.), 7.51–7.28 (m, 7H, arom.), 4.93–4.52 (m, 5H, 2 x CH<sub>2</sub>, CH), 1.95–1.07 (m, 10H, *c*-Hexyl) ppm; <sup>13</sup>C NMR (101 MHz, DMSO-*d*<sub>6</sub>): δ 171.3, 163.8, 151.4, 139.6, 135.1, 131.9, 130.0, 128.6, 127.3, 126.8, 126.4, 56.7, 52.5, 32.3, 24.6, 24.5 ppm; HRMS (*m/z*): *M*<sup>-</sup> calcd for C<sub>23</sub>H<sub>26</sub>N<sub>6</sub>O<sub>3</sub> 435.2139, found 435.2141.

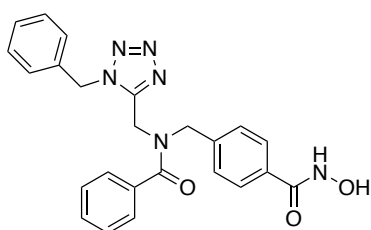
**4-({N-[(1-Cyclohexyl-1H-1,2,3,4-tetrazol-5-yl)methyl]-1-(2-methylphenyl)formamido}methyl)-N-hydroxybenzamide (II-6h).**



Synthesised using **II-8b** (105 mg, 0.23 mmol, 1.0 eq), hydroxylamine (50% solution in water; 0.43 mL, 7.02 mmol, 31 eq), and NaOH (90.0 mg, 2.25 mmol, 9.8 eq). Recrystallisation from EtOAc and petrol afforded **II-6h** as a pink solid (62.0 mg, 0.14 mmol, 60%); mp 117 °C (decomp.);

$t_R$ : 8.31 min, purity: 95.1%;  $^1H$  NMR (300 MHz, DMSO- $d_6$ ):  $\delta$  11.22 (s, 1H, NH-OH), 9.03 (s, 1H, OH), 7.83–7.66 (m, 2H, arom.), 7.51–7.06 (m, 6H, arom.), 4.90 (s, 1H, CH<sub>2</sub>), 4.68–4.52 (m, 3H, 2 x CH<sub>2</sub>), 2.18 (s, 3H, CH<sub>3</sub>), 2.07–1.08 (m, 10H, c-Hexyl) ppm;  $^{13}C$  NMR (101 MHz, DMSO- $d_6$ ):  $\delta$  171.2, 163.7, 151.4, 139.4, 135.2, 134.2, 132.0, 130.5, 130.4, 129.2, 127.7, 127.3, 127.2, 127.0, 125.8, 125.4, 56.7, 56.3, 52.0, 32.4, 31.9, 24.6, 24.5, 24.3, 18.5, 18.4 ppm; HRMS (m/z): M<sup>-</sup> calcd for C<sub>24</sub>H<sub>28</sub>N<sub>6</sub>O<sub>3</sub> 447.2150, found 447.2149.

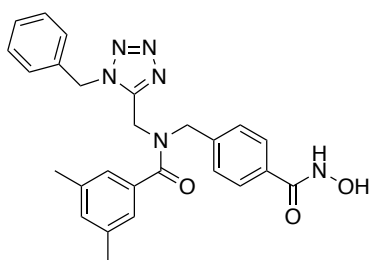
**4-({N-[(1-Benzyl-1H-1,2,3,4-tetrazol-5-yl)methyl]-1-phenylformamido}methyl)-N-hydroxybenzamide (II-6i).**



Synthesised using **II-8c** (150 mg, 0.34 mmol, 1.0 eq), hydroxylamine (50% solution in water; 0.62 mL, 10.1 mmol, 30 eq), and NaOH (139 mg, 3.48 mmol, 10 eq). Recrystallisation from MeOH and Et<sub>2</sub>O afforded **II-6i** as a white solid (93.0 mg, 0.21 mmol, 62%); mp 108 °C (decomp.);  $t_R$ : 7.84 min, purity: 97.7%;  $^1H$  NMR (300 MHz,

DMSO- $d_6$ ):  $\delta$  11.21 (s, 1H, NH-OH), 9.07 (s, 1H, OH), 7.80–7.71 (m, 2H), arom., 7.52–7.21 (m, 12H, arom.), 5.73 (s, 1H, CH<sub>2</sub>), 5.41 (s, 1H, CH<sub>2</sub>), 4.90 (s, 1H, CH<sub>2</sub>), 4.75–4.59 (m, 3H, 2 x CH<sub>2</sub>) ppm;  $^{13}C$  NMR (101 MHz, DMSO- $d_6$ ):  $\delta$  171.4, 163.7, 152.4, 139.4, 135.0, 134.5, 130.0, 128.9, 128.6, 128.3, 127.7, 127.3, 127.3, 126.8, 126.4, 52.5, 49.9, 37.9 ppm; HRMS (m/z): M<sup>-</sup> calcd for C<sub>24</sub>H<sub>22</sub>N<sub>6</sub>O<sub>3</sub> 441.1681, found 441.1687.

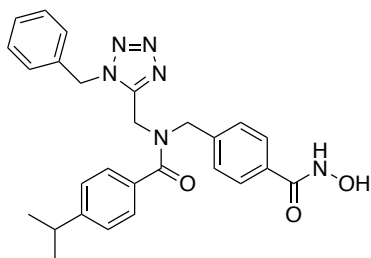
***N*-[(1-Benzyl-1*H*-1,2,3,4-tetrazol-5-yl)methyl]-*N*-[[4-(hydroxycarbamoyl)phenyl]methyl]-3,5-dimethylbenzamide (**II-6j**).**



Synthesised using **II-8a** (159 mg, 0.34 mmol, 1.0 eq), hydroxylamine (50% solution in water; 0.64 mL, 10.4 mmol, 31 eq), and NaOH (137 mg, 3.43 mmol, 10 eq). Recrystallisation from MeOH and Et<sub>2</sub>O afforded **II-6j** as an off-white solid (61.0 mg, 0.13 mmol, 38%); mp 98 °C (decomp.); t<sub>R</sub>: 8.38 min, purity: 96.6%; <sup>1</sup>H NMR (300 MHz,

DMSO-*d*<sub>6</sub>): δ 11.23 (s, 1H, *NH*-OH), 10.10 (d, *J* = 59.1 Hz, 1H, OH), 7.81–7.66 (m, 2H, arom.), 7.47–7.13 (m, 6H, arom.), 7.12–6.77 (m, 4H, arom.), 5.73 (s, 1H, CH<sub>2</sub>), 5.38 (s, 1H, CH<sub>2</sub>), 4.90 (s, 1H, CH<sub>2</sub>), 4.74–4.55 (m, 3H, 2 x CH<sub>2</sub>), 2.20 (s, 6H, 2 x CH<sub>3</sub>) ppm; <sup>13</sup>C NMR (101 MHz, DMSO-*d*<sub>6</sub>): δ 171.6, 163.8, 152.4, 139.6, 137.7, 134.9, 134.5, 131.9, 131.2, 128.8, 128.3, 127.6, 126.9, 124.0, 123.6, 52.3, 49.9, 40.2, 37.6, 20.7 ppm; HRMS (*m/z*): M<sup>-</sup> calcd for C<sub>26</sub>H<sub>26</sub>N<sub>6</sub>O<sub>3</sub> 469.1994, found 469.1996.

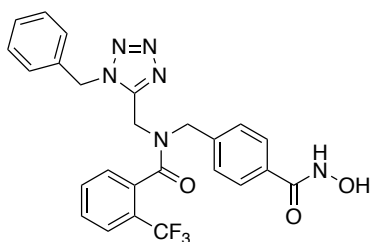
**4-({*N*-[(1-Benzyl-1*H*-1,2,3,4-tetrazol-5-yl)methyl]-1-[4(propan-2-yl)phenyl]formamido}methyl)-*N*-hydroxybenzamide (**II-6k**).**



Synthesis using **II-8e** (110 mg, 0.23 mmol, 1.0 eq), hydroxylamine (50% solution in water; 0.43 mL, 7.02 mmol, 31 eq), and NaOH (90.0 mg, 2.25 mmol, 9.8 eq) afforded **II-6k** as an off-white solid (98.0 mg, 0.20 mmol, 88%); mp 121 °C (decomp.); t<sub>R</sub>: 8.78 min, purity: 95.0%; <sup>1</sup>H NMR (400 MHz, DMSO-*d*<sub>6</sub>): δ 11.21 (s, 1H, *NH*-OH), 9.07 (s, 1H, OH), 7.94–7.61 (m, 2H, arom.), 7.44–7.06 (m, 11H, arom.),

5.80–5.34 (m, 2H, CH<sub>2</sub>), 4.96–4.59 (m, 3H, 2 x CH<sub>2</sub>), 4.09/3.77 (2 x s, 1H, CH<sub>2</sub>), 2.99–2.82 (m, 1H, CH), 1.18 (d, *J* = 6.9 Hz, 1H, 6H, 2 x CH<sub>3</sub>) ppm; <sup>13</sup>C NMR (101 MHz, DMSO-*d*<sub>6</sub>): δ 175.4, 166.1, 166.1, 163.1, 152.4, 150.5, 134.6, 132.5, 128.9, 128.3, 127.7, 127.7, 126.7, 126.7, 126.6, 126.4, 49.9, 40.2, 40.2, 33.3, 25.2, 23.6, 19.5 ppm; HRMS (*m/z*): MNa<sup>+</sup> calcd for C<sub>27</sub>H<sub>28</sub>N<sub>6</sub>O<sub>3</sub> 507.2115, found 507.2110.

**4-({*N*-[(1-Benzyl-1*H*-1,2,3,4-tetrazol-5-yl)methyl]-1-[2-(trifluoromethyl)phenyl]formamido)methyl-*N*-hydroxybenzamide (II-6I).**



Synthesis using **II-8f** (117 mg, 0.23 mmol, 1.0 eq), hydroxylamine (50% solution in water; 0.43 mL, 7.02 mmol, 31 eq), and NaOH (90.0 mg, 2.25 mmol, 9.8 eq) afforded **II-6I** as a pale brown solid (98.0 mg, 0.19 mmol, 83%); mp 103 °C (decomp.);  $t_R$ : 8.25 min, purity: 95.0%;  $^1H$  NMR (300 MHz, 60 °C, DMSO- $d_6$ ):  $\delta$  11.08 (s, 1H, *NH*-OH), 8.89

(s, 1H, OH), 7.95–6.79 (m, 13H, arom.), 5.73 (s, 1H, CH<sub>2</sub>), 5.39 (s, 1H, CH<sub>2</sub>), 4.93 (s, 1H, CH<sub>2</sub>), 4.66–4.22 (m, 3H, 2 x CH<sub>2</sub>) ppm;  $^{13}C$  NMR (101 MHz, 26 °C, DMSO- $d_6$ ):  $\delta$  168.8, 168.4, 163.8, 163.6, 151.9, 151.7, 139.5, 138.4, 134.4, 133.5, 133.4, 133.3, 133.3, 132.9, 132.7, 132.1, 131.8, 130.2, 130.1, 128.8, 128.34, 128.27, 128.0, 127.9, 127.34, 127.25, 127.21, 127.16, 127.0, 126.9, 126.83, 126.80, 125.7, 125.4, 125.2, 125.1, 124.9, 124.9, 122.21, 122.18, 52.2, 50.0, 49.7, 47.9, 42.3, 37.2 ppm; HRMS (*m/z*): MNa<sup>+</sup> calcd for C<sub>25</sub>H<sub>21</sub>F<sub>3</sub>N<sub>6</sub>O<sub>3</sub> 533.1519, found 533.1516.

## 2.5 References

Ballatore C, Huryn DM, Smith AB 3rd. 2013. Carboxylic acid (bio)isosteres in drug design. *ChemMedChem* **8**: 385–395.

Bhatia S, Krieger V, Groll M, Osko JD, Reßing N, Ahlert H, Borkhardt A, Kurz T, Christianson DW, Hauer J, Hansen FK. 2018. Discovery of the first-in-class dual histone deacetylase-proteasome inhibitor. *J Med Chem* **61**: 10299–10309.

Depetter Y, Geurs S, De Vreese R, Goethals S, Vandoorn E, Laevens A, Steenbrugge J, Meyer E, de Tullio P, Bracke M, D'hooghe M, De Wever O. 2019. Selective pharmacological inhibitors of HDAC6 reveal biochemical activity but functional tolerance in cancer models. *Int J Cancer* **145**: 735–774.

Diedrich D, Hamacher A, Gertzen CGW, Alves Avelar LA, Reiss GJ, Kurz T, Gohlke H, Kassack MU, Hansen FK. 2016. Rational design and diversity-oriented synthesis of peptoid-based selective HDAC6 inhibitors. *Chem Commun* **52**: 3219–3222.

Diedrich D, Stenzel K, Hesping E, Antonova-Koch Y, Woldearegai TG, Duffy S, Fisher G, Schöler A, Meister S, Kurz T, Avery VM, Winzeler EA, Held J, Andrews KT, Hansen FK. 2018. One-pot, multi-component synthesis and structure-activity relationships of peptoid-based histone deacetylase (HDAC) inhibitors targeting malaria parasites. *Eur J Med Chem* **158**: 801–813.

Erlenmeyer H, Leo M. 1932. Über Pseudoatome. *Helv Chim Acta* **15**: 1171–1186.

Friedman HL. 1951. Influence of isosteric replacements upon biological activity. *NASNRS* **206**: 295–358.

Gaisina IN, Tueckmantel W, Ugolkov A, Shen S, Hoffen J, Dubrovskiy O, Mazar A, Schoon RA, Billadeau D, Kozikowski AP. 2016. Identification of HDAC6-selective inhibitors of low cancer cell cytotoxicity. *ChemMedChem* **11**: 81–92.

Grimm HG. 1925. Structure and size of the non-metallic hydrides. *Z Electrochem* **31**: 474–480.

Hideshima T, Richardson PG, Anderson KG. 2011. Mechanism of action of proteasome inhibitors and deacetylase inhibitors and the biological basis of synergy in multiple myeloma. *Mol Cancer Ther* **10**: 2034–2042.

Kalin JH, Bergman JA. 2013. Development and therapeutic implications of selective histone deacetylase 6 inhibitors. *J Med Chem* **56**: 6297–6313.

Krieger V, Hamacher A, Cao F, Stenzel K, Gertzen CGW, Schäker-Hübner L, Kurz T, Gohlke H, Dekker FJ, Kassack MU, Hansen FK. 2019. Synthesis of peptoid-based class I selective histone deacetylase inhibitors with chemosensitizing properties. *J Med Chem* **62**: 11260–11279.

Krieger V, Hamacher A, Gertzen CGW, Senger J, Zwinderman MRH, Marek M, Romier C, Dekker FJ, Kurz T, Jung M, Gohlke H, Kassack MU, Hansen FK. 2017. Design, multicomponent synthesis, and anticancer activity of a focused histone deacetylase (HDAC) inhibitor library with peptoid-based cap groups. *J Med Chem* **60**: 5493–5506.

Kumari S, Carmona AV, Tiwari AK, Trippier PC. 2020. Amide bond bioisosteres: Strategies, synthesis, and successes. *J Med Chem* **63**: 12290–12358.

Langmuir I. 1919. Isomorphism, isosterism and covalence. *J Am Chem Soc* **41**: 1543–1559.

Laursen JS, Engel-Andreasen J, Fristrup P, Harris P, Olsen CA. 2013. Cis-trans amide bond rotamers in  $\beta$ -peptoids and peptoids: Evaluation of stereoelectronic effects in backbone and side chains. *J Am Chem Soc* **135**: 2835–2844.

Li Y, Seto E. 2016. HDACs and HDAC inhibitors in cancer development and therapy. *Cold Spring Harbor Perspect Med* **6**: a026831.

Lima LM, Barreiro EJ. 2005. Bioisosterism: A useful strategy for molecular modification and drug design. *Curr Med Chem* **12**: 23–49.

Lipinski CA. 2000. Drug-like properties and the causes of poor solubility and poor permeability. *J Pharmacol Toxicol Methods* **44**: 235–249.

Lipinski CA, Lombardo F, Dominy BW, Feeney PJ. 1997. Experimental and computational approaches to estimate solubility and permeability in drug discovery and development settings. *Adv Drug Deliv Rev* **23**: 3–25.

Mackwitz MKW, Hamacher A, Osko JD, Held J, Schöler A, Christianson DW, Kassack MU, Hansen FK. 2018. Multicomponent synthesis and binding mode of imidazo[1,2-*a*]pyridine-capped selective HDAC6 inhibitors. *Org Lett* **20**: 3255–3258.

Mackwitz MKW, Hesping E, Antonova-Koch Y, Diedrich D, Woldearegai TG, Skinner-Adams T, Clarke M, Schöler A, Limbach L, Kurz T, Winzeler EA, Held J, Andrews K, Hansen FK. 2019. Structure-activity and structure-toxicity relationships of peptoid-based histone deacetylase inhibitors with dual-stage antiplasmodial activity. *ChemMedChem* **14**: 912–926.

Mackwitz MK, Hesping E, Eribez K, Schöler A, Antonova-Koch Y, Held J, Winzeler EA, Andrews KT, Hansen FK. 2021. Investigation of the in vitro and in vivo efficacy of peptoid-based HDAC inhibitors with dual-stage antiplasmodial activity. *Eur J Med Chem* **211**: 113065.

Maleki A, Sarvary A. 2015. Synthesis of tetrazoles via isocyanide-based reactions. *RSC Adv* **5**: 60938–60955.

Marcaccini S, Torroba T. 2007. The use of the Ugi four-component condensation. *Nat Protoc* **2**: 632–639.

Oprea TI, Davis AM, Teague SJ, Leeson PD. 2001. Is there a difference between leads and drugs? A historical perspective. *J Chem Inf Comput Sci* **41**: 1308–1315.

Patani GA, LaVoie EJ. 1996. Bioisosterism: A rational approach in drug design. *Chem Rev* **96**: 3147–3176.

Porter NJ, Osko JD, Diedrich D, Kurz T, Hooker JM, Hansen FK, Christianson DW. 2018. Histone deacetylase 6-selective inhibitors and the influence of capping groups on hydroxamate-zinc denticity. *J Med Chem* **61**: 8054–8060.

Reßing N, Marquardt V, Gertzen CGW, Schöler A, Schramm A, Kurz T, Gohlke H, Aigner A, Remke M, Hansen FK. 2019. Design, synthesis and biological evaluation of  $\beta$ -peptoid-capped HDAC inhibitors with anti-neuroblastoma and anti-glioblastoma activity. *Med Chem Commun* **10**: 1109–1115.

Reßing N, Sönnichsen M, JD Osko, Schöler A, Schliehe-Diecks J, Skerhut A, Borkhardt A, Hauer J, Kassack MU, Christianson DW, Bhatia S, Hansen FK. 2020. Multicomponent synthesis, binding mode, and structure-activity relationship of selective histone deacetylase 6 (HDAC6) inhibitors with bifurcated capping groups. *J Med Chem* **63**: 10339–10351.

Roche J, Bertrand P. 2016. Inside HDACs with more selective HDAC inhibitors. *Eur J Med Chem* **121**: 451–483.

Shen S, Kozikowski AP. 2020. A patent review of histone deacetylase 6 inhibitors in neurodegenerative diseases (2014-2019). *Expert Opin Ther Pat* **30**: 121–136.

Tetko IV, Poda GI. 2004. Application of ALOGPS 2.1 to predict log *D* distribution coefficient for Pfizer proprietary compounds. *J Med Chem* **47**: 5601–5604.

Thornber CW. 1979. Isosterism and molecular modification in drug design. *Chem Soc Rev* **8**: 563–580.

Ugi I. 1962. The  $\alpha$ -addition of immonium ions and anions to isonitriles accompanied by secondary reactions. *Angew Chem Int Ed* **1**: 8–21.

Ugi I, Steinbrückner C. 1961. Reaktion von Isonitrilen mit Carbonylverbindungen, Aminen und Stickstoffwasserstoffsäure. *Chem Ber* **94**: 734–742.

Veber DF, Johnson SR, Cheng H-Y, Smith BR, Ward KW, Kopple KD. 2002. Molecular properties that influence the oral bioavailability of drug candidates. *J Med Chem* **45**: 2615–2623.

van de Waterbeemd H, Gifford E. 2003. ADMET in silico modelling: towards prediction paradise? *Nat Rev Drug Discov* **2**: 192–204.

Zanger UM, Schwab M. 2013. Cytochrome P450 enzymes in drug metabolism: Regulation of gene expression, enzyme activities, and impact of genetic variation. *Pharmacol Ther* **138**: 103–141.



# Chapter 3: Design, multicomponent synthesis and structure-activity relationships of fluorinated HDAC inhibitors

## 3.1 Introduction

### 3.1.1 Effects and benefits of drug fluorination

Even though rarely occurring in natural compounds, fluorine-substituents have become an important means to improve the bioavailability and pharmacokinetic properties of small molecule drugs. Having faced a tremendous upward trend in recent years, they are now present in 20–25% of all pharmaceuticals (Purser et al. 2008; Pan 2019).

The benefits of drug fluorination mostly stem from the element's small size and highly electronegative nature. In correlation with the number of incorporated fluorines, the high electron-withdrawing capabilities of fluorine substituents may significantly alter the  $pK_a$  of drugs in comparison to non-fluorinated analogues, for example by reducing the basicity of amines or by increasing the acidity of carboxylic acids (Purser et al. 2008; Müller et al. 2007). With regard to alterations in lipophilicity, there is no general conclusion to be drawn as the fluorine's impact on the polarity of a compound appears to be largely determined by its specific molecular environment (Purser et al. 2008; Meanwell 2018). Yet, fluorine introduction has been established as a valuable tool helping to improve the pharmacokinetic properties of orally administered drugs and is often used to minimise the risk of metabolic clearance at specific soft spots (Purser et al. 2008; Pan 2019; Müller et al. 2007). Nevertheless, Pan recently emphasised that fluorinated drugs are not generally insensitive to CYP-mediated metabolism (Pan 2019). In consequence, they are prone to releasing toxins, such as fluoride or hydrofluoric acid, and reactive metabolites, e.g. Michael acceptors or epoxides (Pan 2019). A particularly toxic species relevant in this context would be fluoroacetic acid which acts as an irreversible and thus fatal inhibitor of the citrat cycle (Johnson et al. 2020). Possibly emerging from various precursors, the eventual metabolic release of fluoroacetic acid must be carefully ruled out (Johnson et al. 2020). Referring to decomposition studies of dissolved drug candidates, Pan further stresses the necessity to evaluate the stability under

physiological conditions because unfavourable positioning of the fluorine, for example in benzylic, allylic, or  $\alpha$ -carbonyl positions, might have activating effects on the compound's reactivity (Pan 2019).

Despite the seemingly small sizes of both elements, the bioisosteric replacement of hydrogen by fluorine was found sufficient to alter the conformation of a drug (Müller et al. 2007). A comparison of the dimensions within a molecular context did, in fact, reveal that the length (1.35 Å), *van-der-Waals* (vdW) radius (1.47 Å), and vdW volume (13.31 Å<sup>3</sup>) of the C-F bond are more similar to a C=O bond (1.23 Å; 1.52 Å; 14.71 Å<sup>3</sup>) than to a C-H bond (1.09 Å; 1.20 Å; 7.34 Å<sup>3</sup>; Meanwell 2018). The replacement of a methyl group (21.6 Å<sup>3</sup>) by a trifluoromethyl group (39.8 Å<sup>3</sup>) appears to nearly double the vdW volume of the substituent which thus resembles an ethyl group (38.9 Å<sup>3</sup>) in respect of the steric demand (Meanwell 2018). A significant difference between the C-H bond and the C-F bond is the fact that the positive moiety of the latter is located at the carbon atom, thus allowing for the highly electronegative and non-polarisable fluorine to participate in strong electrostatic interactions but only weak hydrogen bonds with surrounding residues (Meanwell 2018; Purser et al. 2008; Müller et al. 2007). Depending on the nature of the drug targets, some of those unique characteristics could be used to optimise the binding modes and target affinities of drug candidates.

Another widely explored benefit of drug fluorination is the possibility of <sup>18</sup>F radiolabelling which may, in some cases, be applied to the synthesis of PET (positron emission tomography) tracers. Beside diagnostic measures that provide otherwise inaccessible information, PET-tracing offers insight into physiological mechanisms and may be used for biodistribution studies of early-stage drug candidates, thus facilitating the drug development process (Johnson et al. 2020; Purser et al. 2008).

### 3.1.2 Project outline

In 2016, the Hansen group published first results on preferential HDAC6 inhibition by peptoid-ligands obtained from the U4CR (Diedrich et al. 2016). Follow-up studies on co-crystals of selected peptoid-capped inhibitors and CD2 of *Danio rerio* HDAC6 revealed that the compounds adopt different binding modes than the highly HDAC6-selective PET probe [<sup>18</sup>F]bavarostat (Figure 3.1) which features a 2-F substituent in the otherwise identical linker moiety (Porter et al. 2018). Given that bavarostat and the non-selective HDACi [<sup>11</sup>C]martinostat, a PET probe in clinical phase I, share identical cap groups, it was concluded

that the remarkable HDAC6 selectivity of bavarostat is likely to stem from the unique binding mode of the fluorinated linker section (Wang et al. 2014; Porter et al. 2018).

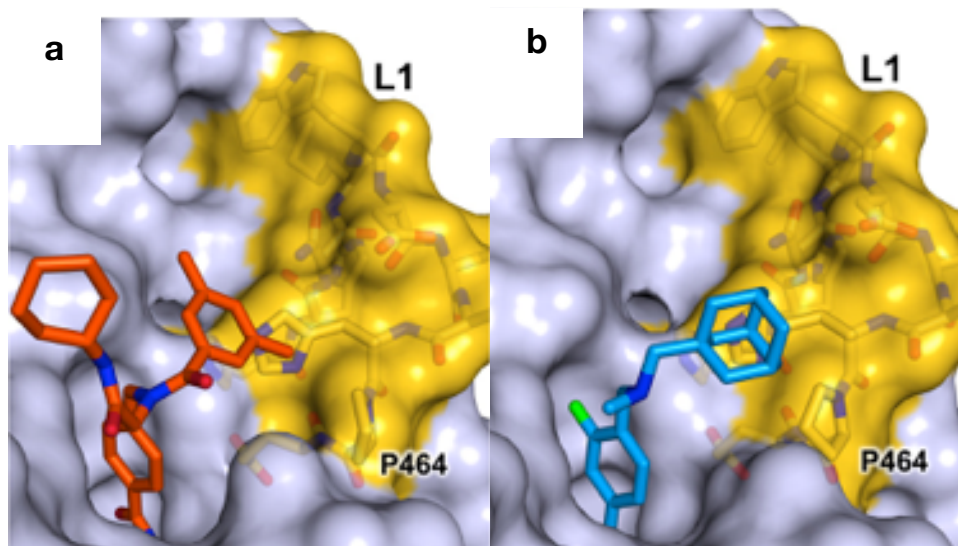
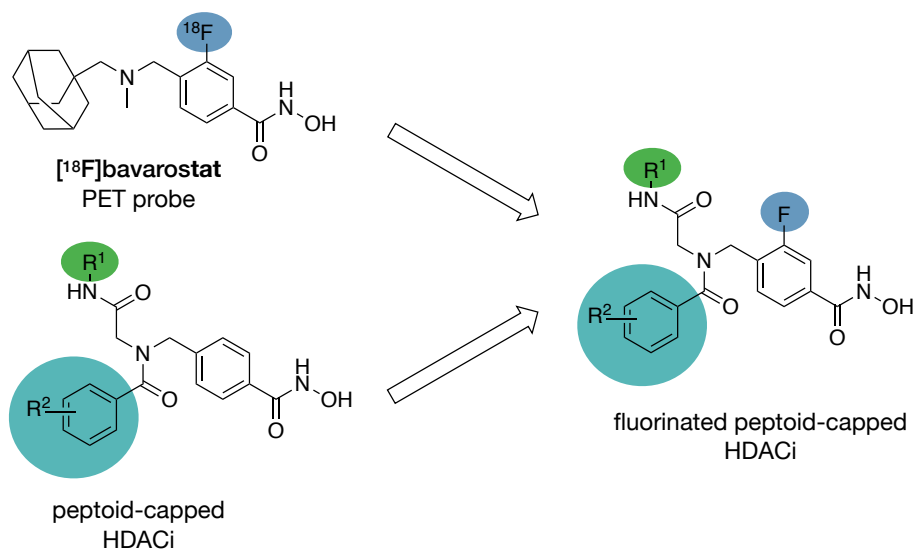


**Figure 3.1.** Co-crystal structures of a peptoid-capped HDACi (a; PDB ID: 6DVL) and bavarostat (b; PDB ID: 6DVO) in complex with zCD2. The L1 loop pocket is highlighted in orange. The pictures were created by the Christianson group, University of Pennsylvania. Adapted and reprinted with permission from Porter NJ, Osko JD, Diedrich D, Kurz T, Hooker JM, Hansen FK, Christianson DW. 2018. Histone deacetylase 6-selective inhibitors and the influence of capping groups on hydroxamate-zinc denticity. *J Med Chem* **61**: 8054–8060. Copyright (2018) American Chemical Society.

With the intention to determine whether the same type of linker fluorination would also enhance the HDAC6 inhibition of the peptoid-based inhibitors, a new set of compounds containing fluorinated analogues of the non-selective HDACi DDK115 and DDK137 as well as the HDAC6-preferential inhibitors **III-Ile** and **III-Ilf** was designed (Scheme 3.1; Porter et al. 2018; Mackwitz et al. 2019). Additional studies on tetrazole-capped HDACi derived from the same peptoid scaffold moreover led to the identification of the 2-trifluoromethyl substituent of the acyl moiety as a source of excellent selectivity (see chapter 2; Reßing et al. 2020). In order to further explore this effect by means of an SAR study, the library design was extended to encompass several analogues with residues of different shapes and sizes in the corresponding position.

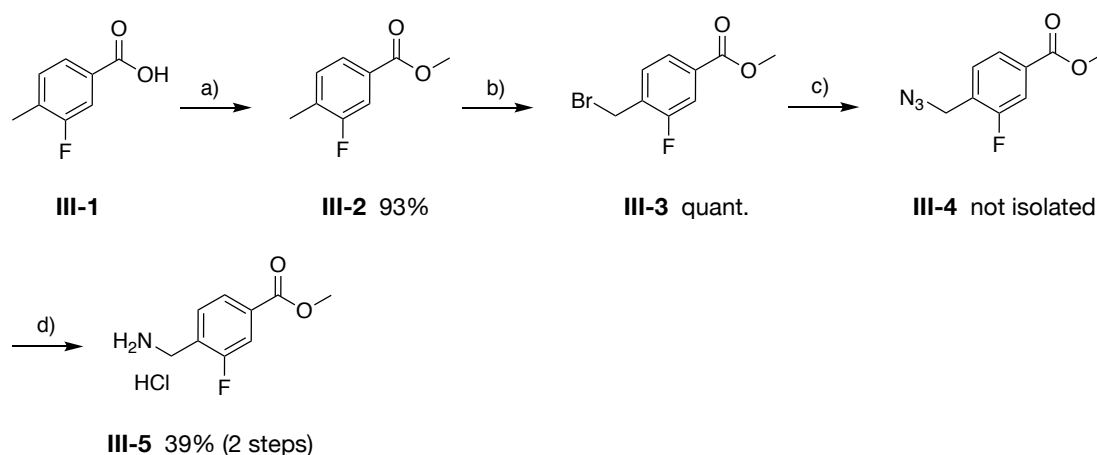


**Scheme 3.1.** Design of fluorinated peptoid-capped HDACi inspired by [<sup>18</sup>F]bavarostat and previous work from the Hansen group.

## 3.2 Results and discussion

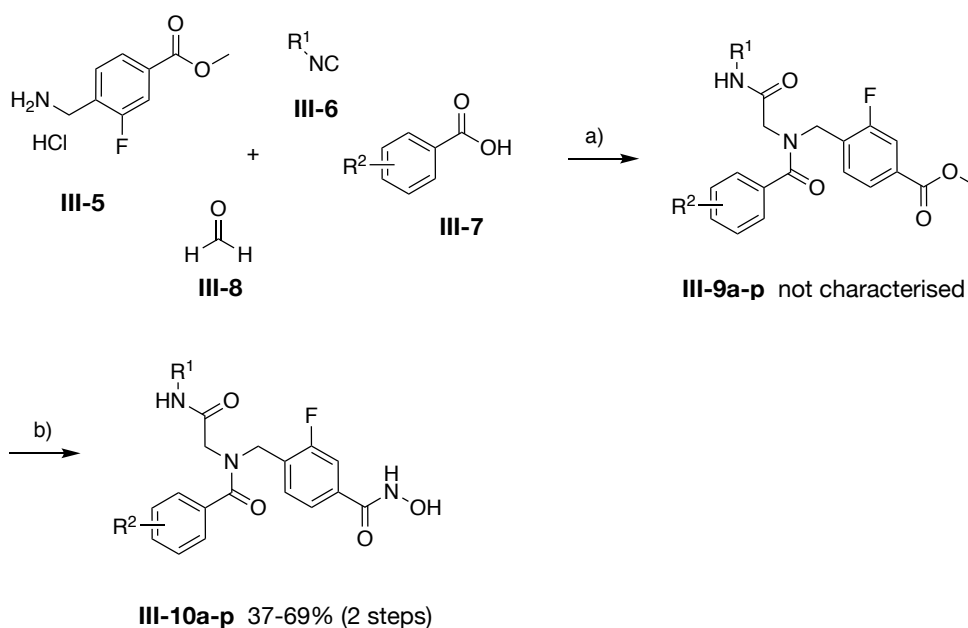
### 3.2.1 Synthesis of fluorinated HDACi

The synthesis of the 2-fluorobenzyl linker (Scheme 3.2) was accomplished in accordance with a literature protocol (Schmidt et al. 2017). Following the esterification of **III-1**, the Wohl-Ziegler bromination of **III-2** using *N*-bromosuccinimide (NBS) was performed to yield **III-3**. The reaction is usually carried out in presence of azobisisobutyronitrile (AIBN) which is supposed to act as a radical initiator for the homolysis of dibromine residues that are typically found in NBS. Thus, the reactive bromine species required for the reaction can be extracted from NBS through the following radical chain reaction (Incremona & Martin 1970). Obtained in quantitative yield, the bromine-derivative **III-3** was subsequently treated with sodium azide to yield the corresponding azide (**III-4**) as a crude product after aqueous workup. Due to the highly reactive nature of organic azides, compound **III-4** was not purified but directly subjected to treatment with triphenylphosphine in the following Staudinger reaction. Requiring hydrolysis to release the desired amine from the iminophosphorane intermediate, the reaction mixture was enriched with water. Aqueous workup of the crude product and precipitation using hydrochloric acid then afforded the fluorinated linker as the hydrochloride salt **III-5** in good purity but moderate yield of 39% after two steps.



**Scheme 3.2.** Synthesis of the fluorinated linker **III-5**. Reagents and conditions: a)  $\text{SOCl}_2$ , MeOH, 0 °C to rt, 16 h; b) NBS, AIBN, DCM, reflux, 16 h; c)  $\text{NaN}_3$ , DMF, 80 °C, 16 h; d)  $\text{PPh}_3$ , THF,  $\text{H}_2\text{O}$ , HCl, rt, 24 h.

The U4CR of **III-5**, the respective isonitriles **III-6**, the respective carboxylic acids **III-7**, and paraformaldehyde **III-8** afforded each peptoid **III-9** within less than 4 h of microwave irradiation. After purification by aqueous workup and recrystallisation, the resulting esters **III-9** were treated with a mixture of sodium hydroxide and aqueous hydroxylamine to yield the hydroxamic acids **III-10** after 15 min of stirring at 0 °C (Scheme 3.3). All final compounds were isolated by precipitation from the aqueous crude mixture and exceeded 95% purity without further purification.



**Scheme 3.3.** Synthesis of the fluorinated peptoid-capped HDACi **III-10a-p**. Reagents and conditions: a) Et<sub>3</sub>N, MS 4 Å, MeOH, MW, 45 °C, 150 W, 60–210 min; b) NH<sub>2</sub>OH (50% solution in water), NaOH, MeOH/DCM, 0 °C, 15 min.

### 3.2.2 HDAC inhibition

**Biochemical assays.** Biochemical assays were performed to evaluate the inhibitory activities of all final compounds against HDAC1 and HDAC6.<sup>11</sup> The resulting IC<sub>50</sub> values (Table 3.1) indicate that minor structural modifications suffice to steer between pan-inhibition and HDAC6 selectivity without affecting the overall high inhibitory activities against HDAC6 in the low nanomolar concentration range. In comparison to those compounds featuring a cyclohexyl group in position R<sup>1</sup> (**III-10c-f**; IC<sub>50</sub> HDAC6: 0.018–0.020 μM, SI: 43–75), it is apparent that the *tert*-butyl derivatives **III-10k-n** with identical substitution patterns at the R<sup>2</sup>

<sup>11</sup> HDAC inhibition assays were performed by Andrea Schöler in the group of Finn K. Hansen, Leipzig University.

moiety display more promising selectivity profiles (SI: 45–103) and similar potencies ( $IC_{50}$  HDAC6: 0.017–0.027  $\mu$ M). The selectivity profile of the voluminous and branched *iso*-propyl derivative **III-10p** (SI: 191) exceeded all other analogues as well as the control compound tubastatin A (SI: 178), in spite of the moderate  $IC_{50}$  against HDAC6 (0.042  $\mu$ M).

**Table 3.1.** Inhibition of HDAC1 and HDAC6 by compounds **III-10a-p** and the non-fluorinated peptoid-capped HDACi DDK115, DDK137, **III-Ile**, and **III-IIf**. Vorinostat was used as control.

Compound	R <sup>1</sup>	R <sup>2</sup>	HDAC1 $IC_{50}$ [ $\mu$ M]	HDAC6 $IC_{50}$ [ $\mu$ M]	SI <sup>a</sup>
<b>III-10a</b>	c-Hexyl	3,5-Me	0.310 $\pm$ 0.004	0.020 $\pm$ 0.002	16
<b>III-10b</b>	c-Hexyl	4-NMe <sub>2</sub>	0.066 $\pm$ 0.008	0.016 $\pm$ 0.004	4.1
<b>III-10c</b>	c-Hexyl	2-F	0.771 $\pm$ 0.006	0.018 $\pm$ 0.002	43
<b>III-10d</b>	c-Hexyl	2-Me	0.938 $\pm$ 0.013	0.018 $\pm$ 0.002	52
<b>III-10e</b>	c-Hexyl	2-OMe	1.50 $\pm$ 0.10	0.020 $\pm$ 0.004	75
<b>III-10f</b>	c-Hexyl	2-CF <sub>3</sub>	1.45 $\pm$ 0.05	0.027 $\pm$ 0.002	54
<b>III-10g</b>	Bn	3,5-Me	0.077 $\pm$ 0.003	0.013 $\pm$ 0.004	5.9
<b>III-10h</b>	Bn	4-NMe <sub>2</sub>	0.013 $\pm$ 0.001	0.010 $\pm$ 0.00004	1.3
<b>III-10i</b>	<i>t</i> -Bu	3,5-Me	0.573 $\pm$ 0.011	0.024 $\pm$ 0.002	24
<b>III-10j</b>	<i>t</i> -Bu	4-NMe <sub>2</sub>	0.158 $\pm$ 0.056	0.020 $\pm$ 0.006	7.9
<b>III-10k</b>	<i>t</i> -Bu	2-F	1.18 $\pm$ 0.05	0.026 $\pm$ 0.002	45
<b>III-10l</b>	<i>t</i> -Bu	2-Me	1.75 $\pm$ 0.13	0.027 $\pm$ 0.005	65
<b>III-10m</b>	<i>t</i> -Bu	2-OMe	1.75 $\pm$ 0.05	0.017 $\pm$ 0.0001	103
<b>III-10n</b>	<i>t</i> -Bu	2-CF <sub>3</sub>	2.33 $\pm$ 0.43	0.027 $\pm$ 0.005	86
<b>III-10o</b>	<i>t</i> -Bu	2-Cl	3.47 $\pm$ 0.14	0.021 $\pm$ 0.001	165
<b>III-10p</b>	<i>t</i> -Bu	2- <i>i</i> -Pr	8.01 $\pm$ 0.22	0.042 $\pm$ 0.006	191
DDK115	c-Hexyl	3,5-Me	0.249 $\pm$ 0.029	0.040 $\pm$ 0.008	6
DDK137	Bn	4-NMe <sub>2</sub>	0.005 $\pm$ 0.001	0.011 $\pm$ 0.003	0.5
<b>III-Ile<sup>b</sup></b>	<i>t</i> -Bu	2-Me	2.41 $\pm$ 0.086	0.051 $\pm$ 0.004	47
<b>III-IIf<sup>b</sup></b>	<i>t</i> -Bu	2-OMe	3.11 $\pm$ 0.308	0.038 $\pm$ 0.004	82
Vorinostat	-	-	0.099 $\pm$ 0.005	0.042 $\pm$ 0.005	2.4
Ricolinostat <sup>c</sup>	-	-	0.188 $\pm$ 0.022	0.018 $\pm$ 0.003	11
Tubastatin A <sup>d</sup>	-	-	2.49 $\pm$ 0.14	0.014 $\pm$ 0.0006	178
HPOB <sup>d</sup>	-	-	2.10 $\pm$ 0.23	0.085 $\pm$ 0.009	25

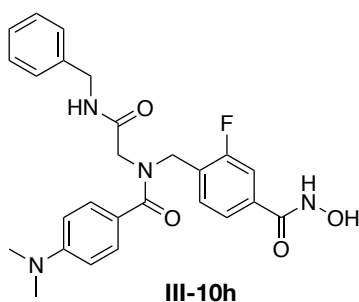
<sup>a</sup> Selectivity index (SI =  $IC_{50}$  (HDAC1)/ $IC_{50}$  (HDAC6)).

<sup>b</sup> Data taken from: Mackwitz et al. 2019.

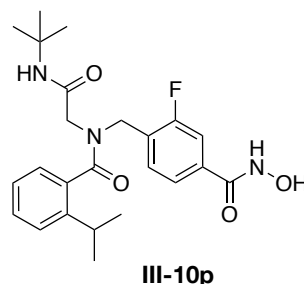
<sup>c</sup> Data taken from: Reßing et al. 2019.

<sup>d</sup> Data taken from: Mackwitz et al. 2018.

Hence, **III-10p** was singled out as the most selective inhibitor of this set. The equally bulky 2-chloro analogue **III-10o** was found to be twice as potent ( $IC_{50}$  HDAC6: 0.021  $\mu$ M) but less selective (SI: 165). Additional assays using HDAC2 and HDAC3 confirmed the low activity of **III-10p** against other class I isoforms ( $IC_{50}$  HDAC2: 4.48  $\pm$  0.79  $\mu$ M, SI: 107; HDAC3: 8.35  $\pm$  0.06  $\mu$ M, SI: 199; Figure 3.2).



HDAC1  $IC_{50}$ : 0.013  $\pm$  0.001  $\mu$ M (SI<sup>1/6</sup>: 1.3)  
 HDAC2  $IC_{50}$ : 0.014  $\pm$  0.0001  $\mu$ M (SI<sup>2/6</sup>: 1.4)  
 HDAC3  $IC_{50}$ : 0.021  $\pm$  0.002  $\mu$ M (SI<sup>3/6</sup>: 2.1)  
 HDAC6  $IC_{50}$ : 0.010  $\pm$  0.00004  $\mu$ M



HDAC1  $IC_{50}$ : 8.01  $\pm$  0.22  $\mu$ M (SI<sup>1/6</sup>: 191)  
 HDAC2  $IC_{50}$ : 4.48  $\pm$  0.79  $\mu$ M (SI<sup>2/6</sup>: 107)  
 HDAC3  $IC_{50}$ : 8.35  $\pm$  0.06  $\mu$ M (SI<sup>3/6</sup>: 199)  
 HDAC6  $IC_{50}$ : 0.042  $\pm$  0.006  $\mu$ M

**Figure 3.2.** Inhibition of HDACs 1–3 and 6 by **III-10h** and **III-10p**.

In accordance with previous SAR data (Diedrich et al. 2018; Mackwitz et al. 2019), all inhibitors featuring 3,5-dimethyl residues in the acyl ring (**III-10a**, **III-10g**, **III-10i**) exhibited only low to moderate HDAC6 selectivity (SI: 5.9–24) but high inhibitory qualities ranging from 0.013  $\mu$ M to 0.024  $\mu$ M against HDAC6. The two 4-dimethylamino derivatives **III-10b** and **III-10h** met the expectations by turning out to be strong but non-selective HDACi (SI: 1.4–7.9) of which **III-10h** proved to be the most potent inhibitor of both isoforms ( $IC_{50}$  HDAC1: 0.013  $\mu$ M; HDAC6: 0.010  $\mu$ M) and other class I enzymes ( $IC_{50}$  HDAC2: 0.014  $\pm$  0.0001  $\mu$ M, SI: 1.4; HDAC3: 0.021  $\pm$  0.002  $\mu$ M, SI: 2.1; Figure 3.2). The *tert*-butyl-capped analogue **III-10j** ( $IC_{50}$  HDAC1: 0.158  $\mu$ M; HDAC6: 0.020  $\mu$ M, SI: 7.9) exhibited similar inhibition qualities as ricolinostat.

In summary, those results indicate that the substitution pattern of the acyl ring is crucial in terms of isoform selectivity. Depending on the size of the residue, the sole occupation of position 2 of the aromatic ring promises a strong preference for HDAC6. The introduction of small residues in positions 3, 4, and 5, in turn, effectuates equal inhibition of HDAC1 and HDAC6 or a marginal preference for the latter. The HDAC6 selectivity achieved by appropriate R<sup>2</sup> residues may moreover be boosted by choosing the *tert*-butyl motif over a



cyclohexyl group in position R<sup>1</sup>. Overall, all new ligands, except for the most selective inhibitor **III-10p**, outmatched the HDAC6 inhibition of the control compound vorinostat and were equally potent as tubastatin A and ricolinostat.

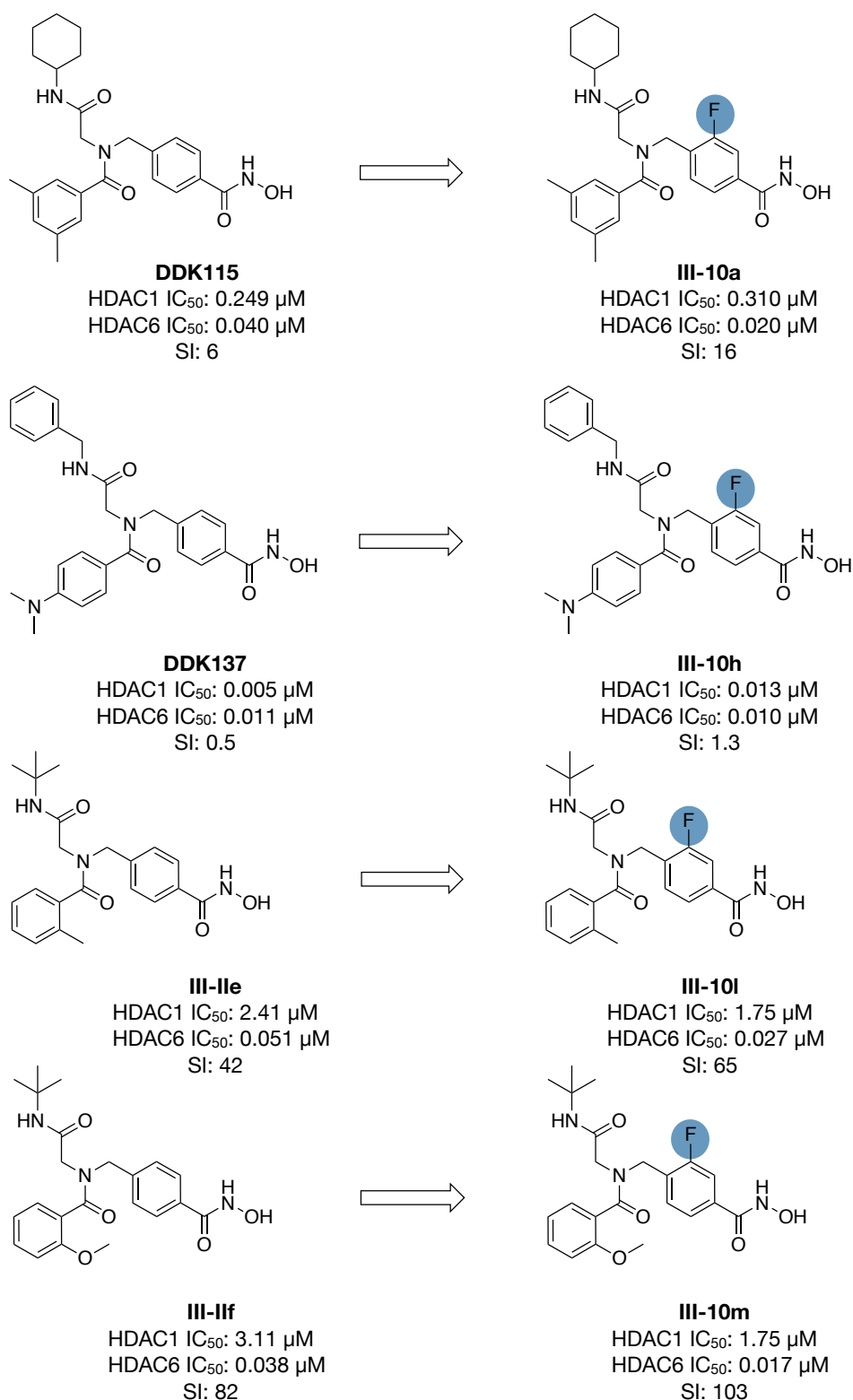


**Figure 3.3.** HDAC inhibition of non-fluorinated HDACi compared to their fluorinated analogues.

The comparison of the non-selective compounds **III-10a** and **III-10h** with their non-fluorinated analogues DDK115 and DDK137 (Figure 3.3) implies that linker fluorination results in decreased HDAC1 inhibition (DDK115 vs. **III-10a**: 0.249  $\mu$ M/0.310  $\mu$ M; DDK137 vs. **III-10h**: 0.005  $\mu$ M/0.013  $\mu$ M) accompanied by higher inhibitory activity against HDAC6 (DDK115 vs. **III-10a**: 0.040  $\mu$ M/0.020  $\mu$ M; DDK137 vs. **III-10h**: 0.011  $\mu$ M/0.010  $\mu$ M), thus almost tripling the selectivity for HDAC6 in both cases. In respect of the HDAC6-selective compounds **III-10e** and **III-10f**, linker fluorination increased the inhibitory activity towards HDAC1 (**III-10e** vs. **III-10i**: 2.41  $\mu$ M/1.75  $\mu$ M; **III-10f** vs. **III-10m**: 3.11  $\mu$ M/1.75  $\mu$ M) and nearly doubled the inhibition of HDAC6 (**III-10e** vs. **III-10i**: 0.051  $\mu$ M/0.027  $\mu$ M; **III-10f** vs. **III-10m**: 0.038  $\mu$ M/0.017  $\mu$ M), thus favouring significantly improved selectivity profiles (Figure 3.3). Considering this data, it can be assumed that linker fluorination has a distinct beneficial effect on HDAC6 inhibition.

**Western blotting.** The HDAC inhibition of the pan-inhibitor **III-10h** and the selective HDAC6i **III-10p** were assessed in the cellular environment of the AML cell line HL-60. After addition of different inhibitor concentrations or DMSO and ricolinostat as controls, the cells were incubated for 24 h. The effects were then analysed by western blotting using acetyl- $\alpha$ -tubulin and acetyl-histone H3 antibodies (Figure 3.4).<sup>12</sup> The results suggest that both ligands as well as ricolinostat favour the accumulation of acetyl- $\alpha$ -tubulin, thereby confirming the inhibition of the tubulin deacetylase HDAC6 starting from low concentrations. The high levels of acetyl-histone H3 further imply that **III-10h**-treatment at concentrations higher than 49 nM is sufficient to significantly impair the activity of class I HDACs that deacetylate histone H3. The fact that this effect is minimised after treatment with ricolinostat and unapparent after

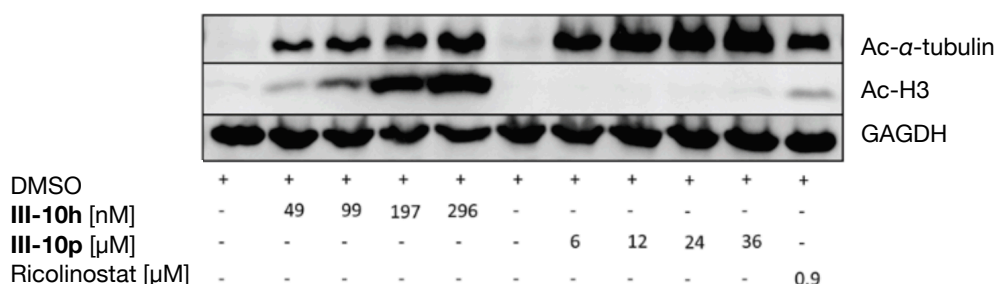


**Figure 3.4.** Western blotting of HL-60 cells with anti-acetyl- $\alpha$ -tubulin and acetyl-histone H3 antibodies after 24 h treatment at the indicated concentrations of **III-10h** and **III-10p**. Ricolinostat and DMSO were used as controls. The picture was kindly provided by Melf Sönnichsen, HHU Düsseldorf.

<sup>12</sup> Western blotting was performed by Melf Sönnichsen in the group of Sanil Bhatia, HHU Düsseldorf.

incubation with **III-10p** confirms the inactivity of **III-10p** towards class I isoforms. The comparison with ricolinostat further accentuates the excellent HDAC6 selectivity of **III-10p** in the cellular environment.

### 3.2.3 Biological evaluation

**Cytotoxic effects on leukaemia cell lines.** Each of the sixteen new inhibitors was screened against three selected leukaemia cell lines in order to elucidate their antiproliferative potential; the FDA-approved drug vorinostat, the HDAC6i HPOB, and the clinical candidate ricolinostat

**Table 3.2.** Cytotoxicities of compounds **III-10a-p** against selected leukaemia cell lines. Vorinostat, ricolinostat, and HPOB were used as controls.

Compound	R <sup>1</sup>	R <sup>2</sup>	HAL-01 IC <sub>50</sub> [μM]	HL-60 IC <sub>50</sub> [μM]	Jurkat IC <sub>50</sub> [μM]
<b>III-10a</b>	c-Hexyl	3,5-Me	3.10 ± 0.91	2.47 ± 2.05	3.91 ± 0.67
<b>III-10b</b>	c-Hexyl	4-NMe <sub>2</sub>	1.05 ± 0.28	0.494 ± 0.126	0.946 ± 0.087
<b>III-10c</b>	c-Hexyl	2-F	11.8 ± 5.14	6.79 ± 3.31	8.97 ± 1.73
<b>III-10d</b>	c-Hexyl	2-Me	9.93 ± 1.55	7.72 ± 3.45	9.47 ± 3.55
<b>III-10e</b>	c-Hexyl	2-OMe	> 25	12.3 ± 9.70	18.6 ± 9.01
<b>III-10f</b>	c-Hexyl	2-CF <sub>3</sub>	9.12 ± 4.44	2.00 ± 0.80	> 25
<b>III-10g</b>	Bn	3,5-Me	2.75 ± 1.92	9.15 ± 0.28	6.23 ± 1.62
<b>III-10h</b>	Bn	4-NMe <sub>2</sub>	0.375 ± 0.162	0.218 ± 0.122	0.285 ± 0.064
<b>III-10i</b>	<i>t</i> -Bu	3,5-Me	4.93 ± 2.60	4.84 ± 2.78	5.47 ± 0.86
<b>III-10j</b>	<i>t</i> -Bu	4-NMe <sub>2</sub>	2.47 ± 0.74	1.46 ± 0.77	1.74 ± 0.26
<b>III-10k</b>	<i>t</i> -Bu	2-F	22.2 ± 3.84	15.7 ± 6.87	19.0 ± 4.58
<b>III-10l</b>	<i>t</i> -Bu	2-Me	23.9 ± 1.54	13.6 ± 8.19	23.9 ± 1.49
<b>III-10m</b>	<i>t</i> -Bu	2-OMe	> 25	18.4 ± 9.34	24.5 ± 0.75
<b>III-10n</b>	<i>t</i> -Bu	2-CF <sub>3</sub>	> 25	18.6 ± 9.05	> 25
<b>III-10o</b>	<i>t</i> -Bu	2-Cl	22.9 ± 2.64	12.8 ± 8.66	21.6 ± 3.37
<b>III-10p</b>	<i>t</i> -Bu	2- <i>i</i> -Pr	> 25	12.2 ± 9.36	> 25
DDK137	Bn	4-NMe <sub>2</sub>	0.253 ± 0.064	0.232 ± 0.056	0.182 ± 0.030
Vorinostat	-	-	0.299 ± 0.045	0.223 ± 0.052	0.470 ± 0.023
Ricolinostat	-	-	2.04 ± 0.39	1.54 ± 0.16	2.42 ± 0.18
HPOB	-	-	13.9 ± 3.89	11.3 ± 7.22	16.1 ± 2.52

HAL-01: B-cell acute lymphoblastic leukaemia cell line; HL-60: human acute myeloid leukaemia cell line; Jurkat: human T-cell leukaemia cell line.

were used as controls (Table 3.2).<sup>13</sup> For selective HDAC6i, cytotoxicity levels are typically low and therefore it was not surprising that neither of the IC<sub>50</sub> values measured in presence of selective ligands lies below the micromolar concentration range (Depetter et al. 2019; Gaisina et al. 2016). Compound **III-10j** was found to resemble ricolinostat in terms of both HDAC inhibition and isoform selectivity and, accordingly, induced similar levels of cytotoxicity with IC<sub>50</sub> values ranging from 1.46 μM to 2.47 μM in all three cell lines. Two other compounds, **III-10c** and **III-10d**, exceeded the cytotoxic effects of HPOB throughout all screenings.

With regard to non-selective inhibitors, the most potent derivative **III-10h** nearly matched the bar set by the non-fluorinated analogue DDK137. In fact, it proved to be similarly active against the HL-60 cell line (IC<sub>50</sub> **III-10h**: 0.218 μM; DDK137: 0.232 μM) for which both compounds lie within the range of vorinostat (IC<sub>50</sub>: 0.223 μM). In Jurkat cells, **III-10h** turned out to be even more toxic than vorinostat but less effective than DDK137 (IC<sub>50</sub> **III-10h**: 0.285 μM; vorinostat: 0.470 μM; DDK137: 0.182 μM).

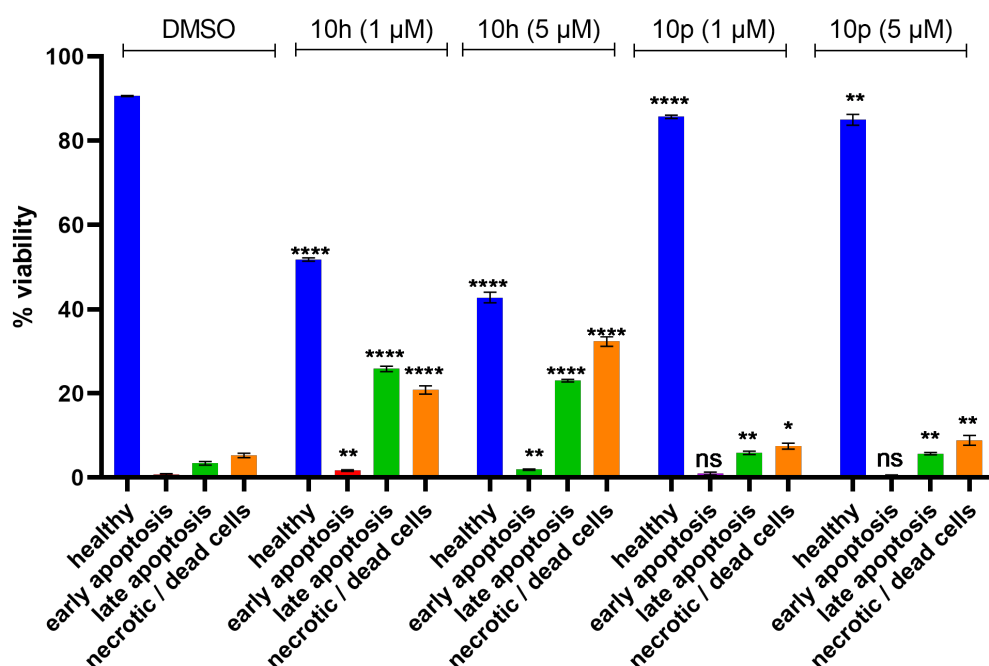


**Figure 3.5.** Annexin-PI assay of HL-60 cells after 24 h incubation with **III-10h** and **III-10p**, respectively, at the indicated concentrations. DMSO was used as control. The diagram was kindly provided by Melf Sönnichsen, HHU Düsseldorf.

An additional annexin-PI experiment (Figure 3.5) emphasised the observation that the highly selective **III-10p** bears no cytotoxic potential towards HL-60 cells, regardless of the

<sup>13</sup> Cytotoxicity screens were performed by Julian Schliehe-Diecks in the group of Sanil Bhatia, HHU Düsseldorf.

concentration. Incubation with **III-10h**, in contrast, increased the percentage of apoptotic and necrotic cells in comparison to the DMSO control.<sup>14</sup> Based on these results, compound **III-10h** was picked as the most promising candidate for additional biological experiments.

---

<sup>14</sup> Annexin-PI assays were performed by Melf Sönnichsen in the group of Sanil Bhatia, HHU Düsseldorf.

### 3.3 Conclusions

With the goal to investigate the effect of linker fluorination in comparison to non-fluorinated benzylic HDACi linkers, sixteen peptoid-capped HDACi were designed for this study. The established synthetic procedure via the U4CR was optimised to afford the desired hydroxamates in overall yields of 37–69% after an efficient 2-step protocol. None of the compounds required any purification to exceed purities of 95%.

In biochemical inhibition assays, all compounds turned out to be potent HDAC6i with  $IC_{50}$  values ranging between 0.010  $\mu$ M and 0.042  $\mu$ M. Additional, yet potent HDAC1 inhibition was only observed for the estimated pan-inhibitors. An SAR study on different acyl residues in position R<sup>2</sup> revealed that large and voluminous substituents in position 2 of the aromatic ring can be introduced to discriminate between HDAC1 and HDAC6. By employing a *tert*-butyl residue in position R<sup>1</sup> of the cap group, this effect can be increased and accordingly, the *iso*-propyl analogue **III-10p** stood out as the most selective HDAC6i. Exceeding the selectivity profile of tubastatin A, **III-10p** maintained its selectivity for HDAC6 in biochemical assays against HDAC2 and HDAC3 as well as in the cellular environment of HL-60 cells. Being accessible in good yield by simple synthetic methods, **III-10p** may serve useful as a highly HDAC6-selective tool compound with potential for drug combination studies on preclinical level.

The comparison of the fluorinated HDACi and their non-fluorinated analogues implies that linker fluorination enhances the inhibitory potential and selectivity for HDAC6, which, in turn, affects the inhibition of HDAC1. In cytotoxicity screenings using three leukaemia cell lines, this effect entailed a slight loss of antiproliferative potential for the pan-inhibitor **III-10h** compared to its non-fluorinated analogue DDK137. Nevertheless, **III-10h** was found to exhibit higher cytotoxic qualities than vorinostat and was thus chosen for more detailed biological evaluation in the future.

The results of this study suggest that fluorinated HDACi adopt different binding modes than their non-fluorinated parent compounds, but in absence of a co-crystal structure, such conclusions cannot be confirmed. The future work of this study therefore includes X-ray experiments on co-crystals of HDAC6 in complex with **III-10p**.

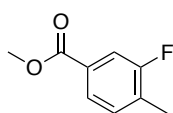
## 3.4 Experimental section

### 3.4.1 General information

Dry MeOH was obtained from the MBraun MB SPS-800 solvent purification system. Except for DCM which was purified by distillation prior to use, all reagents and solvents were purchased from commercial sources and used without further purification. TLC was carried out using Macherey-Nagel pre-coated aluminium foil sheets which were visualised using UV light (254 nm). Hydroxamic acids were stained using a 1% solution of iron(III) chloride in MeOH.  $^1\text{H}$  NMR and  $^{13}\text{C}$  NMR spectra were recorded at rt or, due to the occurrence of rotamers, at 60 °C using Bruker Avance III HD (400 MHz), and Varian/Agilent Mercury-plus (300 MHz & 400 MHz) spectrometers. Chemical shifts ( $\delta$ ) are quoted in parts per million (ppm). All spectra were standardised in accordance with the signals of the deuterated solvents (DMSO- $d_6$ :  $\delta_{\text{H}} = 2.50$  ppm,  $\delta_{\text{C}} = 39.5$  ppm;  $\text{CDCl}_3$ :  $\delta_{\text{H}} = 7.26$  ppm,  $\delta_{\text{C}} = 77.0$  ppm). Coupling constants ( $J$ ) are reported in Hertz (Hz). Mass spectra were measured by the Leipzig University Mass Spectrometry Service using electrospray ionisation (ESI) on Bruker Daltonics Impact II and Bruker Daltonics micrOTOF spectrometers. The uncorrected melting points were determined using a Barnstead Electrothermal 9100 apparatus. Analytical HPLC analysis were carried out using a Thermo Fisher Scientific UltiMate 3000 system equipped with an UltiMate<sup>TM</sup> HPG-3400SD pump, an UltiMate<sup>TM</sup> 3000 Diode array detector, an UltiMate<sup>TM</sup> 3000 autosampler, and a TCC-3000SD standard thermostatted column compartment by Dionex. The system was operated using a Macherey-Nagel NUCLEODUR 100-5  $\text{C}_{18}$  ec column (250 mm x 4.6 mm). UV absorption was detected at 254 nm with a linear gradient of 5% B to 95% B within 23 min. Acidified HPLC-grade water (0.1% TFA; solvent A) and acidified HPLC-grade acetonitrile (0.1% TFA; solvent B) were used for elution at a flow rate of 1 mL/min. The purity of the final compounds was at least 95.0%.

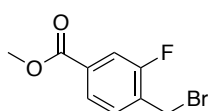
### 3.4.2 Experimental procedures

#### Methyl 3-fluoro-4-methylbenzoate (**III-2**).



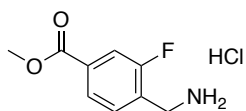
To a cooled (0 °C) solution of 3-fluoro-4-methylbenzoic acid (5.00 g, 32.5 mmol, 1.0 eq) in MeOH (150 mL) was added thionyl chloride (3.05 mL, 42.5 mmol, 1.3 eq) and the resulting mixture was stirred at rt for 16 h. Upon removal of the solvent under reduced pressure, the residue was dissolved in EtOAc (200 mL) and 10% HCl (50 mL) was added. The mixture was extracted with EtOAc (3 x 100 mL) and the combined organics were washed with sat. aq. NaHCO<sub>3</sub> (2 x 20 mL) and water (1 x 20 mL). Drying over MgSO<sub>4</sub> and evaporation of the solvent afforded **III-2** as a pale yellow liquid (5.10 g, 30.4 mmol, 93%). Spectroscopic data matched those reported in the literature (Jiang et al. 2008).

#### Methyl 4-(bromomethyl)-3-fluorobenzoate (**III-3**).



Synthesised according to the procedure reported in the literature (Schmidt et al. 2017). To a solution of **III-2** (4.91 g, 29.0 mmol, 1.0 eq) and NBS (7.83 g, 44.0 mmol, 1.5 eq) in DCM (150 mL) was added AIBN (476 mg, 2.90 mmol, 0.1 eq). The mixture was first refluxed for 10 h and then stirred at rt for another 16 h after which DCM (100 mL) was added. The resulting solution was washed with 1M NaOH (3 x 50 mL) and brine (2 x 50 mL) before it was dried over Na<sub>2</sub>SO<sub>4</sub>. Removal of the solvent under reduced pressure afforded the crude product **III-3** (quant.) as a colourless liquid that solidified upon storage at -18 °C. The crude product was used without further purification.

#### Methyl 4-(aminomethyl)-3-fluorobenzoate hydrochloride (**III-5**).



Synthesised according to the procedure reported in the literature (Schmidt et al. 2017). A solution of **III-3** (1.62 g, 6.50 mmol, 1.0 eq) and NaN<sub>3</sub> (510 mg, 7.80 mmol, 1.2 eq) in DMF (25 mL) was stirred at 80 °C for 12 h. After cooling to rt, brine (25 mL) was added and the resulting solution was extracted with a mixture of Et<sub>2</sub>O and cyclohexane (1:1; 3 x 100 mL). The combined organics were washed with brine (2 x 20 mL), dried over MgSO<sub>4</sub> and concentrated under reduced pressure to afford **III-4** as a pale yellow liquid. The crude azide thus obtained was subsequently dissolved in a mixture of THF (40 mL) and water (4 mL) to which triphenylphosphine (3.00 g, 11.4 mmol, 1.8 eq) was added in small portions. After



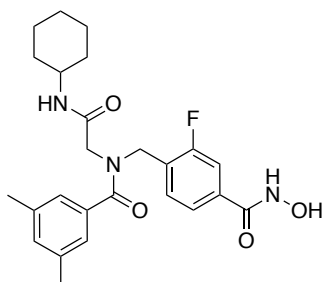
stirring at rt for 40 h, the solvent was evaporated. The residue was redissolved in DCM (200 mL) and extracted with 4M HCl (2 x 50 mL). The combined aqueous layers were then basified using 2M NaOH (pH 10) and extracted with DCM (3 x 100 mL). Drying of the combined organics over MgSO<sub>4</sub> and removal of the solvent under reduced pressure afforded the crude amine which was precipitated from MeOH (2 mL), 37% HCl (0.5 mL), and Et<sub>2</sub>O (20 mL) to afford the hydrochloride salt **III-5** as a white solid (553 mg, 2.50 mmol, 39% over 2 steps); mp 236–241 °C; <sup>1</sup>H NMR (400 MHz, DMSO-*d*<sub>6</sub>): δ 8.70 (s, 3H, NH<sub>3</sub><sup>+</sup>), 7.87–7.62 (m, 3H, arom.), 4.12 (q, *J* = 5.8 Hz, 2H, CH<sub>2</sub>), 3.88 (s, 3H, OCH<sub>3</sub>) ppm; <sup>13</sup>C NMR (101 MHz, DMSO-*d*<sub>6</sub>): δ 164.9, 161.2, 158.7, 132.0, 131.9, 131.7, 131.6, 126.6, 126.5, 125.2, 125.1, 115.9, 115.7, 52.6, 35.4 ppm; HRMS (*m/z*): MNa<sup>+</sup> calcd for C<sub>9</sub>H<sub>10</sub>FNO<sub>2</sub> 184.0768, found 184.0771.

**General procedure A.** The linker building block **III-5** (132 mg, 0.60 mmol, 1.2 eq), paraformaldehyde (18.0 mg, 0.60 mmol, 1.2 eq), and crushed molecular sieves 4 Å (50.0 mg) were suspended in MeOH (1.0 mL) and Et<sub>3</sub>N (0.08 mL, 0.60 mmol, 1.2 eq) was added. The mixture was subjected to microwave irradiation at 150 W and 45 °C for 20 min before the respective isonitrile (0.50 mmol, 1.0 eq) and the respective carboxylic acid (0.50 mmol, 1.0 eq) were added. The resulting mixture was again subjected to microwave irradiation at the same settings for 60 min after which the molecular sieves were removed by filtration and washed with DCM (10 mL). The filtrate was concentrated under reduced pressure and the residue was redissolved in DCM (100 mL), washed with 10% HCl (1 x 10 mL), water (1 x 10 mL), 1M NaOH (2 x 5 mL), and brine (1 x 10 mL). The organic layer was dried over MgSO<sub>4</sub> and the solvent was removed under reduced pressure to afford the crude product **III-9** which was recrystallised from EtOAc (1 mL) and petrol (20 mL). The ester thus obtained was allowed to dry before it was added to a mixture of NaOH (200 mg, 5.00 mmol, 10 eq) and hydroxylamine (50% solution in water; 0.95 mL, 15.5 mmol, 31 eq) in MeOH (4 mL) and DCM (1 mL). The resulting solution was stirred at 0 °C for approx. 15 min until TLC (DCM/MeOH 9:1) indicated full conversion upon which the solvents were evaporated and the residue was dissolved in water (10 mL). Dropwise addition of 10% HCl (pH 8) induced precipitation of the hydroxamic acid **III-10** which was then isolated by filtration and washed with 5% HCl (2 x 3 mL) and chilled water (3 x 5 mL), successively. For compounds derived from *tert*-butyl isocyanide, precipitation of the product was often incomplete so that the aqueous layer was further extracted with EtOAc (3 x 30 mL). The

combined organics were washed with brine (1 x 10 mL) and dried over  $\text{Na}_2\text{SO}_4$ . Removal of the solvent under reduced pressure yielded the remaining product.

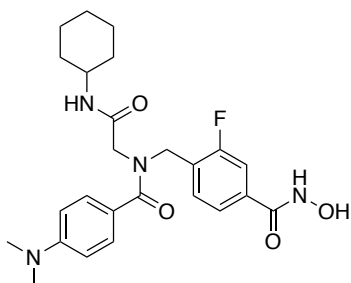
**General procedure B.** The linker building block **III-5** (109 mg, 0.50 mmol, 1.0 eq), paraformaldehyde (15.0 mg, 0.50 mmol, 1.0 eq), and crushed molecular sieves 4 Å (50.0 mg) were suspended in MeOH (1.0 mL) and  $\text{Et}_3\text{N}$  (0.08 mL, 0.60 mmol, 1.2 eq) was added. The mixture was subjected to microwave irradiation at 150 W and 45 °C for 30 min before the respective isonitrile (0.50 mmol, 1.0 eq) and 4-(dimethylamino)benzoic acid (83.0 mg, 0.50 mmol, 1.0 eq) were added. The resulting mixture was again subjected to microwave irradiation at the same settings for 3 h after which the molecular sieves were removed by filtration and washed with DCM (10 mL). The filtrate was concentrated under reduced pressure and the residue was redissolved in DCM (100 mL) and washed with 1M NaOH (2 x 5 mL), water (1 x 10 mL), and brine (1 x 10 mL). Drying over  $\text{MgSO}_4$  and evaporation of the solvent afforded the crude product **III-9** which was recrystallised from EtOAc (1 mL) and petrol (20 mL). The ester thus obtained was allowed to dry before it was added to a mixture of NaOH (200 mg, 5.00 mmol, 10 eq) and hydroxylamine (50% solution in water; 0.95 mL, 15.5 mmol, 31 eq) in MeOH (4 mL) and DCM (1 mL). The resulting solution was stirred at 0 °C for approx. 15 min until TLC (DCM/MeOH 9:1) indicated full conversion. The organic solvents were removed under reduced pressure and the residue was dissolved in water (10 mL). Dropwise addition of 10% HCl (pH 8) induced precipitation of the hydroxamic acid **III-10** which was then isolated by filtration and washed with chilled water (3 x 5 mL). For compound **III-10j** derived from *tert*-butyl isocyanide, precipitation of the product was incomplete so that the aqueous layer was extracted with EtOAc (3 x 30 mL). The combined organics were washed with brine (1 x 10 mL) and dried over  $\text{Na}_2\text{SO}_4$ . Removal of the solvent under reduced pressure yielded the remaining product.

**4-({N-[(Cyclohexylcarbamoyl)methyl]-1-(3,5-dimethylphenyl)formamido}methyl)-3-fluoro-N-hydroxybenzamide (III-10a).**



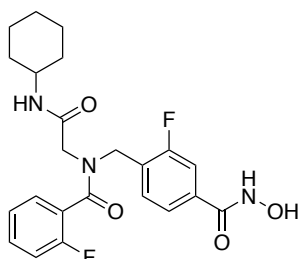
Synthesis according to general procedure A using 3,5-dimethylbenzoic acid (75.0 mg) and cyclohexyl isocyanide (0.06 mL) afforded **III-10a** as a white solid (86.0 mg, 0.18 mmol, 38%); mp 177 °C;  $t_R$ : 8.02 min, purity: 99.7%;  $^1H$  NMR (400 MHz, DMSO- $d_6$ , 20 °C):  $\delta$  7.75 (d,  $J$  = 8.2 Hz, 1H, NH), 7.63–7.31 (m, 3H, arom.), 7.10–6.93 (m, 3H, arom.), 4.68/4.52 (2 x s, 2H, CH<sub>2</sub>), 3.91/3.72 (2 x s, 2H, CH<sub>2</sub>), 3.52 (s, 1H, CH), 2.26/1.80 (2 x s, 6H, 2 x CH<sub>3</sub>), 1.74–0.97 (m, 10H, c-Hexyl) ppm;  $^{13}C$  NMR (101 MHz, DMSO- $d_6$ ):  $\delta$  171.6, 166.7, 162.4, 161.3, 158.9, 137.6, 135.9, 130.9, 129.8, 124.1, 122.9, 113.7, 113.4, 51.4, 47.7, 43.0, 32.4, 32.3, 25.2, 24.4, 20.8 ppm; HRMS (m/z): MNa<sup>+</sup> calcd for C<sub>25</sub>H<sub>30</sub>FN<sub>3</sub>O<sub>4</sub> 478.2113, found 478.2128.

**4-({N-[(Cyclohexylcarbamoyl)methyl]-1-[4-(dimethylamino)phenyl]formamido}methyl)-3-fluoro-N-hydroxybenzamide (III-10b).**



Synthesis according to general procedure B using cyclohexyl isocyanide (0.06 mL) afforded **III-10b** as a white solid (162 mg, 0.34 mmol, 69%); mp 123 °C;  $t_R$ : 6.38 min, purity: 98.1%;  $^1H$  NMR (400 MHz, DMSO- $d_6$ , 20 °C):  $\delta$  11.31 (s, 1H, NH-OH), 9.17 (s, 1H, OH), 7.81 (s, 1H, NH), 7.70–7.26 (m, 5H, arom.), 6.78–6.62 (m, 2H, arom.), 4.64 (s, 2H, CH<sub>2</sub>), 3.85 (s, 2H, CH<sub>2</sub>), 3.55 (d,  $J$  = 9.8 Hz, 1H, CH), 2.93 (s, 6H, 2 x CH<sub>3</sub>), 1.76–1.45 (m, 5H, c-Hexyl), 1.31–1.02 (m, 5H, c-Hexyl) ppm;  $^{13}C$  NMR (101 MHz, DMSO- $d_6$ ):  $\delta$  171.7, 166.9, 162.5, 161.2, 158.9, 151.3, 133.9, 129.8, 128.7, 127.5, 127.4, 123.0, 121.9, 113.7, 113.5, 111.0, 47.6, 32.3, 25.2, 24.5 ppm; HRMS (m/z): MNa<sup>+</sup> calcd for C<sub>25</sub>H<sub>31</sub>FN<sub>4</sub>O<sub>4</sub> 493.2222, found 493.2214.

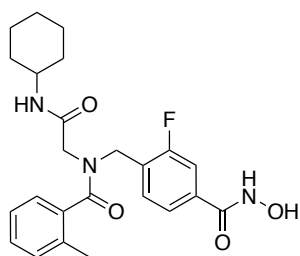
**4-({N-[(Cyclohexylcarbamoyl)methyl]-1-(2-fluorophenyl)formamido}methyl)-3-fluoro-N-hydroxybenzamide (III-10c).**



Synthesis according to general procedure A using 2-fluorobenzoic acid (70.0 mg) and cyclohexyl isocyanide (0.06 mL) afforded **III-10c** as a pink solid (85.0 mg, 0.19 mmol, 38%); mp 179 °C;  $t_R$ : 7.40 min, purity: 96.6%;  $^1H$  NMR (300 MHz, DMSO- $d_6$ , 20 °C):  $\delta$  11.30 (d,  $J$  = 4.7 Hz, 1H, NH-OH), 9.14 (s, 1H, OH), 7.77–7.16 (m, 8H, arom., NH), 4.73/4.50 (2 x s, 2H, CH<sub>2</sub>), 3.98/3.73 (2 x s, 2H, CH<sub>2</sub>), 3.47–3.40 (m, 1H, CH), 1.81–1.43 (m, 5H, c-Hexyl),

1.36–0.89 (m, 5H, c-Hexyl) ppm;  $^{13}C$  NMR (101 MHz, DMSO- $d_6$ ):  $\delta$  166.5, 166.0, 165.9, 162.6, 161.3, 161.1, 158.9, 158.8, 158.7, 156.5, 156.3, 133.9, 131.5, 131.4, 129.8, 129.7, 129.6, 128.72, 128.68, 128.4, 127.1, 126.9, 124.8, 124.7, 124.6, 124.0, 123.8, 122.9, 115.9, 115.7, 113.9, 113.6, 50.9, 47.62, 47.55, 47.1, 47.0, 43.2, 32.4, 32.1, 25.2, 25.1, 24.5, 24.3 ppm; HRMS (m/z): M<sup>-</sup> calcd for C<sub>23</sub>H<sub>25</sub>F<sub>2</sub>N<sub>3</sub>O<sub>4</sub> 444.1740, found 444.1741.

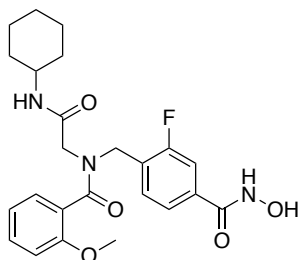
**4-({N-[(Cyclohexylcarbamoyl)methyl]-1-(2-methylphenyl)formamido}methyl)-3-fluoro-N-hydroxybenzamide (III-10d).**



Synthesis according to general procedure A using 2-methylbenzoic acid (68.0 mg) and cyclohexyl isocyanide (0.06 mL) afforded **III-10d** as a pink solid (84.0 mg, 0.19 mmol, 38%); mp 115 °C;  $t_R$ : 7.55 min, purity: 95.1%;  $^1H$  NMR (400 MHz, DMSO- $d_6$ , 60 °C):  $\delta$  11.12 (s, 1H, NH-OH), 8.99 (s, 1H, OH), 7.71–7.37 (m, 4H, arom., NH), 7.37–7.06 (m, 4H, arom.), 4.75/4.41 (2 x s, 2H, CH<sub>2</sub>), 4.01/3.64 (2 x s, 2H, CH<sub>2</sub>), 3.48 (d,  $J$  = 9.7 Hz, 1H, CH), 2.30/2.22 (2 x s, 3H, CH<sub>3</sub>),

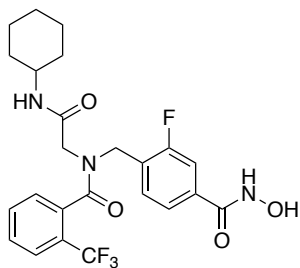
1.82–1.47 (m, 5H, c-Hexyl), 1.36–0.95 (m, 5H, c-Hexyl) ppm;  $^{13}C$  NMR (75 MHz, DMSO- $d_6$ ):  $\delta$  171.1, 166.2, 135.8, 134.3, 134.1, 130.3, 128.8, 125.7, 125.6, 123.0, 113.9, 113.6, 50.6, 47.7, 47.6, 42.5, 40.1, 32.4, 32.2, 25.2, 25.1, 24.5, 24.4, 18.5 ppm; HRMS (m/z): M<sup>-</sup> calcd for C<sub>24</sub>H<sub>28</sub>FN<sub>3</sub>O<sub>4</sub> 440.1991, found 440.1988.

**4-({N-[(Cyclohexylcarbamoyl)methyl]-1-(2-methoxyphenyl)formamido}methyl)-3-fluoro-N-hydroxybenzamide (III-10e).**



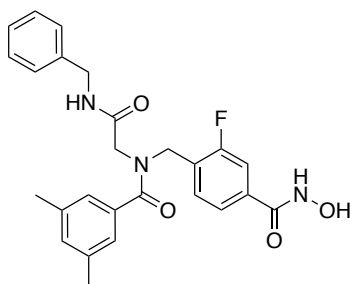
Synthesis according to general procedure A using 2-methoxybenzoic acid (76.0 mg) and cyclohexyl isocyanide (0.06 mL) afforded **III-10e** as a white solid (121 mg, 0.26 mmol, 53%); mp 130 °C;  $t_R$ : 7.33 min, purity: 95.1%;  $^1H$  NMR (400 MHz, DMSO- $d_6$ , 20 °C):  $\delta$  11.31 (d,  $J$  = 6.8 Hz, 1H,  $NH-OH$ ), 9.14 (s, 1H, OH), 7.69–6.92 (m, 8H, arom. NH), 4.95 (s, 1H,  $CH_2$ ), 4.46–3.99 (m, 2H,  $CH_2$ ), 3.83–3.57 (m, 4H,  $OCH_3$ ,  $CH_2$ ), 3.47–3.39 (m, 1H, CH), 1.80–1.43 (m, 5H, c-Hexyl), 1.32–0.90 (m, 5H, c-Hexyl) ppm;  $^{13}C$  NMR (75 MHz, DMSO- $d_6$ ):  $\delta$  169.2, 169.1, 166.3, 166.2, 162.7, 161.6, 158.3, 154.9, 154.5, 133.61, 130.57, 130.4, 129.0, 127.7, 125.3, 125.1, 123.0, 120.5, 113.7, 113.4, 111.4, 55.6, 55.3, 50.7, 47.5, 42.7, 32.4, 32.2, 25.1, 24.5, 24.4 ppm; HRMS (m/z):  $MH^+$  calcd for  $C_{24}H_{28}FN_3O_5$  458.2086, found 458.2066.

**4-({N-[(Cyclohexylcarbamoyl)methyl]-1-[2-(trifluoromethyl)phenyl]formamido}methyl)-3-fluoro-N-hydroxybenzamide (III-10f).**



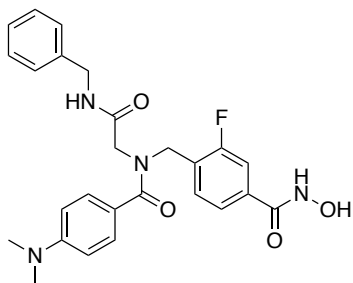
Synthesis according to general procedure A using 2-(trifluoromethyl)benzoic acid (95.0 mg) and cyclohexyl isocyanide (0.06 mL) afforded **III-10f** as a white solid (142 mg, 0.29 mmol, 57%); mp 107 °C;  $t_R$ : 7.84 min, purity: 95.0%;  $^1H$  NMR (400 MHz, DMSO- $d_6$ , 20 °C):  $\delta$  11.31 (d,  $J$  = 8.4 Hz, 1H,  $NH-OH$ ), 9.15 (s, 1H, OH), 7.95–7.23 (m, 8H, arom., NH), 5.27–5.07/4.60–4.24 (2 x m, 2H,  $CH_2$ ), 3.70–3.43 (m, 3H, CH,  $CH_2$ ), 1.81–1.43 (m, 5H, c-Hexyl), 1.36–0.91 (m, 5H, c-Hexyl) ppm;  $^{13}C$  NMR (101 MHz, DMSO- $d_6$ ):  $\delta$  168.6, 168.5, 166.0, 162.5, 161.4, 159.0, 158.7, 134.2, 134.1, 134.0, 132.7, 132.0, 131.5, 131.4, 130.5, 130.0, 129.8, 129.7, 128.8, 128.7, 127.6, 126.7, 126.54, 126.49, 126.45, 125.5, 125.2, 125.0, 124.9, 122.8, 122.3, 113.8, 113.6, 50.6, 47.7, 47.5, 47.0, 42.5, 32.4, 32.1, 25.2, 25.1, 24.5, 24.3 ppm; HRMS (m/z):  $M^-$  calcd for  $C_{24}H_{25}F_4N_3O_4$  494.1708, found 494.1718.

**4-({N-[(Benzylcarbamoyl)methyl]-1-(3,5-dimethylphenyl)formamido}methyl)-3-fluoro-N-hydroxybenzamide (III-10g).**



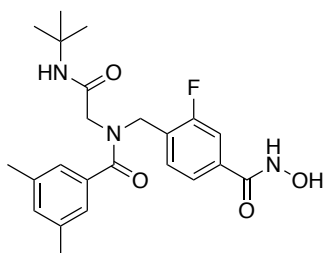
Synthesis according to general procedure A using 3,5-dimethylbenzoic acid (75.0 mg) and benzyl isocyanide (0.06 mL) afforded **III-10g** as a dark brown solid (85.0 mg, 0.18 mmol, 37%); mp 215 °C;  $t_R$ : 7.77 min, purity: 95.2%;  $^1H$  NMR (300 MHz, DMSO- $d_6$ , 20 °C):  $\delta$  11.31 (s, 1H, NH-OH), 9.14 (s, 1H, OH), 8.42 (s, 1H, NH), 7.75–6.92 (m, 11H, arom.), 4.71/4.59 (s, 2H, CH<sub>2</sub>), 4.36–4.23 (m, 2H, CH<sub>2</sub>), 4.02/3.87 (s, 2H, CH<sub>2</sub>), 2.24 (s, 6H, 2 x CH<sub>3</sub>) ppm;  $^{13}C$  NMR (101 MHz, DMSO- $d_6$ ):  $\delta$  171.6, 167.8, 139.4, 139.3, 139.1, 139.0, 137.6, 136.1, 135.8, 131.1, 130.9, 129.9, 129.8, 129.6, 129.51, 129.45, 128.3, 127.2, 126.9, 124.1, 123.1, 123.0, 113.9, 113.7, 51.5, 43.1, 42.2, 20.8 ppm; HRMS (m/z): M<sup>-</sup> calcd for C<sub>26</sub>H<sub>26</sub>FN<sub>3</sub>O<sub>4</sub> 462.1835, found 462.1839.

**4-({N-[(Benzylcarbamoyl)methyl]-1-[4-(dimethylamino)phenyl]formamido}methyl)-3-fluoro-N-hydroxybenzamide (III-10h).**



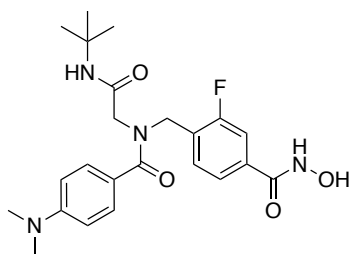
Synthesised according to general procedure B using benzyl isocyanide (0.06 mL). The reaction time for the ester formation was reduced to 60 min (imine formation: 20 min, U4CR: 40 min). **III-10h** was obtained as an off-white solid (162 mg, 0.34 mmol, 68%); mp 205 °C;  $t_R$ : 6.35 min, purity: 97.2%;  $^1H$  NMR (400 MHz, DMSO- $d_6$ , 20 °C):  $\delta$  11.31 (s, 1H, NH-OH), 9.16 (s, 1H, OH), 8.47 (t,  $J$  = 6.0 Hz, 1H, NH), 7.68–7.43 (m, 3H, arom.), 7.39–7.16 (m, 7H, arom.), 6.74–6.58 (m, 2H, arom.), 4.69 (s, 2H, CH<sub>2</sub>), 4.30 (d,  $J$  = 5.8 Hz, 2H, CH<sub>2</sub>), 3.96 (s, 2H, CH<sub>2</sub>), 2.93 (s, 6H, NMe<sub>2</sub>) ppm;  $^{13}C$  NMR (101 MHz, DMSO- $d_6$ ):  $\delta$  171.8, 168.2, 162.5, 158.7, 151.3, 139.2, 133.8, 128.6, 128.3, 127.2, 126.8, 123.0, 113.8, 110.9, 42.1 ppm; HRMS (m/z): MNa<sup>+</sup> calcd for C<sub>26</sub>H<sub>27</sub>FN<sub>4</sub>O<sub>4</sub> 501.1909, found 501.1910.

**4-({N-[(*tert*-Butylcarbamoyl)methyl]-1-(3,5-dimethylphenyl)formamido}methyl)-3-fluoro-*N*-hydroxybenzamide (**III-10i**).**



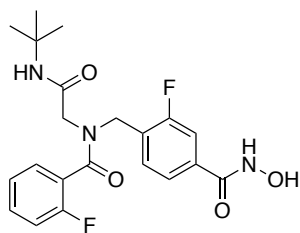
Synthesis according to general procedure A using 3,5-dimethylbenzoic acid (75.0 mg) and *tert*-butyl isocyanide (0.06 mL) afforded **III-10i** as a white solid (125 mg, 0.29 mmol, 58%); mp 162 °C;  $t_R$ : 7.72 min, purity: 97.9%;  $^1H$  NMR (400 MHz, DMSO- $d_6$ ):  $\delta$  11.31 (s, 1H, *NH*-OH), 9.14 (s, 1H, OH), 7.69–7.28 (m, 4H, arom., NH), 7.12–6.87 (m, 3H, arom.), 4.67/4.51 (2 x s, 2H, CH<sub>2</sub>), 3.88/3.69 (2 x s, 2H, CH<sub>2</sub>), 2.27 (s, 6H, 2 x CH<sub>3</sub>), 1.42/1.24/1.21 (s, 9H, *t*-Bu) ppm;  $^{13}C$  NMR (101 MHz, DMSO- $d_6$ ):  $\delta$  171.6, 166.6, 162.6, 161.3, 161.1, 158.9, 137.6, 137.5, 136.0, 133.8, 131.5, 131.4, 130.8, 129.9, 128.8, 128.7, 127.4, 127.3, 124.1, 123.5, 123.0, 113.8, 113.6, 51.6, 50.2, 43.1, 28.5, 28.4, 20.8 ppm; HRMS (*m/z*): *M*<sup>+</sup> calcd for C<sub>23</sub>H<sub>28</sub>FN<sub>3</sub>O<sub>4</sub> 428.1991, found 428.1992.

**4-({N-[(*tert*-Butylcarbamoyl)methyl]-1-[4-(dimethylamino)phenyl]formamido}methyl)-3-fluoro-*N*-hydroxybenzamide (**III-10j**).**



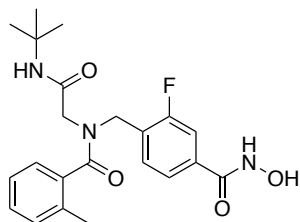
Synthesis according to general procedure B using *tert*-butyl isocyanide (0.06 mL) afforded **III-10j** as an off-white solid (85.0 mg, 0.19 mmol, 38%); mp 132 °C;  $t_R$ : 6.10 min, purity: 95.5%;  $^1H$  NMR (400 MHz, DMSO- $d_6$ , 20 °C):  $\delta$  11.22 (s, 1H, *NH*-OH), 9.14 (s, 1H, OH), 7.71–7.23 (m, 6H, arom., NH), 6.78–6.62 (m, 2H, arom.), 4.63 (s, 2H, CH<sub>2</sub>), 3.82 (s, 2H, CH<sub>2</sub>), 2.93 (s, 6H, NMe<sub>2</sub>), 1.22 (s, 9H, *t*-Bu) ppm;  $^{13}C$  NMR (101 MHz, DMSO- $d_6$ ):  $\delta$  171.7, 169.3, 167.3, 162.5, 161.3, 151.3, 133.7, 131.5, 131.4, 129.7, 128.8, 128.7, 127.7, 127.5, 123.0, 122.0, 113.8, 113.6, 111.0, 58.4, 50.3, 49.9, 28.43, 28.38 ppm; HRMS (*m/z*): *MNa*<sup>+</sup> calcd for C<sub>23</sub>H<sub>29</sub>FN<sub>4</sub>O<sub>4</sub> 467.2065, found 467.2071.

**4-({N-[(*tert*-Butylcarbamoyl)methyl]-1-(2-fluorophenyl)formamido}methyl)-3-fluoro-N-hydroxybenzamide (III-10k).**



Synthesis according to general procedure A using 2-fluorobenzoic acid (70.0 mg) and *tert*-butyl isocyanide (0.06 mL) afforded **III-10k** as an orange solid (133 mg, 0.32 mmol, 63%); mp 111 °C;  $t_R$ : 7.10 min, purity: 96.8%;  $^1H$  NMR (400 MHz, DMSO- $d_6$ , 20 °C):  $\delta$  9.21 (s, 1H, OH), 7.73–7.12 (m, 8H, arom. NH), 4.72/4.47 (s, 2H, CH<sub>2</sub>), 3.95/3.75 (2 x s, 2H, CH<sub>2</sub>), 1.44/1.24/1.17/1.14 (4 x s, 9H, *t*-Bu) ppm;  $^{13}C$  NMR (101 MHz, DMSO- $d_6$ ):  $\delta$  166.9, 166.4, 166.1, 162.5, 161.3, 161.2, 158.9, 158.7, 134.4, 134.0, 133.9, 131.5, 131.4, 129.9, 129.6, 128.8, 128.7, 128.5, 127.1, 126.9, 126.1, 124.8, 124.6, 124.0, 123.9, 122.9, 115.9, 115.7, 113.8, 113.6, 51.2, 50.2, 47.3, 46.9, 43.3, 28.5, 28.3, 27.9 ppm; HRMS (m/z):  $M^-$  calcd for C<sub>21</sub>H<sub>23</sub>F<sub>2</sub>N<sub>3</sub>O<sub>4</sub> 418.1584, found 418.1584.

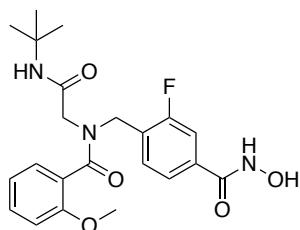
**4-({N-[(*tert*-Butylcarbamoyl)methyl]-1-(2-methylphenyl)formamido}methyl)-3-fluoro-N-hydroxybenzamide (III-10l).**



Synthesis according to general procedure A using 2-methylbenzoic acid (68.0 mg) and *tert*-butyl isocyanide (0.06 mL) afforded **III-10l** as an off-white solid (105 mg, 0.25 mmol, 50%); mp 109 °C;  $t_R$ : 7.24 min, purity: 96.4%;  $^1H$  NMR (300 MHz, DMSO- $d_6$ , 60 °C):  $\delta$  11.05 (s, 1H, *NH*-OH), 8.98 (s, 1H, OH), 7.70–7.12 (m, 8H, arom., NH), 4.74/4.41 (2 x s, 2H, CH<sub>2</sub>), 3.93/3.60 (2x s, 2H, CH<sub>2</sub>), 2.30/2.22 (2 x s, 3H, CH<sub>3</sub>), 1.47/1.27/1.18/1.17 (s, 9H, *t*-Bu) ppm;  $^{13}C$  NMR (101 MHz, DMSO- $d_6$ ):  $\delta$  171.2, 171.0, 166.5, 162.5, 162.3, 135.9, 134.3, 134.0, 133.94, 133.86, 132.0, 131.5, 131.4, 130.3, 129.8, 128.83, 128.78, 128.7, 127.4, 127.2, 125.7, 125.6, 125.5, 123.0, 113.9, 113.6, 51.0, 50.2, 46.7, 46.5, 42.7, 28.5, 28.3, 18.5 ppm; HRMS (m/z):  $M^-$  calcd for C<sub>22</sub>H<sub>26</sub>FN<sub>3</sub>O<sub>4</sub> 414.1835, found 414.1835.



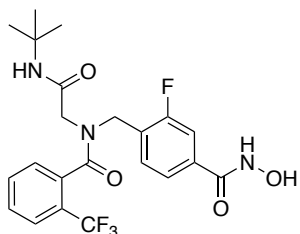
**4-({*N*-[(*tert*-Butylcarbamoyl)methyl]-1-(2-methoxyphenyl)formamido}methyl)-3-fluoro-*N*-hydroxybenzamide (III-10m).**



Synthesis according to general procedure A using 2-methoxybenzoic acid (76.0 mg) and *tert*-butyl isocyanide (0.06 mL) afforded **III-10m** as a white solid (83.0 mg, 0.19 mmol, 38%); mp 126 °C;  $t_R$ : 7.54 min, purity: 95.6%;  $^1H$  NMR (300 MHz, DMSO- $d_6$ , 60 °C):  $\delta$  9.46–8.85 (br s, 1H, OH), 7.71–6.80 (m, 8H, arom., NH), 4.42 (s, 1H, CH<sub>2</sub>), 4.01–3.40 (m, 6H, OCH<sub>3</sub>, 2 x CH<sub>2</sub>),

1.47–1.09 (m, 9H, *t*-Bu) ppm;  $^{13}C$  NMR (101 MHz, DMSO- $d_6$ ):  $\delta$  169.4, 169.3, 169.1, 166.7, 166.5, 162.6, 161.2, 158.7, 154.9, 154.7, 154.5, 134.0, 133.6, 133.5, 132.1, 131.5, 131.4, 130.7, 130.6, 130.4, 129.1, 129.0, 128.8, 128.7, 127.8, 127.7, 127.5, 127.4, 125.4, 125.1, 123.0, 122.8, 122.7, 120.6, 120.5, 113.7, 113.4, 111.5, 111.4, 55.6, 55.3, 51.0, 50.2, 47.7, 46.5, 42.6, 42.6, 28.5, 28.3 ppm; HRMS ( $m/z$ ):  $M^-$  calcd for C<sub>22</sub>H<sub>26</sub>FN<sub>3</sub>O<sub>5</sub> 430.1784, found 430.1784.

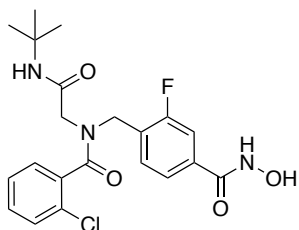
**4-({*N*-[(*tert*-Butylcarbamoyl)methyl]-1-[2-(trifluoromethyl)phenyl]formamido}methyl)-3-fluoro-*N*-hydroxybenzamide (III-10n).**



Synthesis according to general procedure A using 2-(trifluoromethyl)benzoic acid (95.0 mg) and *tert*-butyl isocyanide (0.06 mL) afforded **III-10n** as a yellow solid (103 mg, 0.22 mmol, 44%); mp 137 °C;  $t_R$ : 7.03 min, purity: 95.1%;  $^1H$  NMR (300 MHz, DMSO- $d_6$ , 60 °C):  $\delta$  10.91 (s, 1H, *NH*-OH), 9.00 (s, 1H, OH), 7.89–7.17 (m, 8H, arom., NH), 5.11/4.47 (2 x s, 2H, CH<sub>2</sub>),

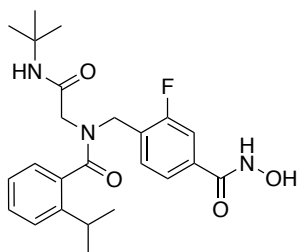
3.90/3.57 (2 x s, 2H, CH<sub>2</sub>), 1.46/1.26/1.18 (3 x s, 9H, *t*-Bu) ppm;  $^{13}C$  NMR (75 MHz, DMSO- $d_6$ ):  $\delta$  168.5, 166.4, 166.2, 162.5, 162.4, 161.8, 134.4, 134.32, 134.29, 134.1, 134.04, 133.99, 132.71, 132.68, 132.6, 132.06, 132.05, 132.0, 131.5, 131.4, 130.52, 130.45, 130.4, 129.8, 129.7, 128.8, 128.7, 127.73, 127.67, 127.6, 126.8, 126.6, 126.51, 126.49, 126.4, 125.2, 124.8, 122.9, 122.81, 122.79, 121.8, 113.91, 113.87, 113.6, 50.8, 50.3, 42.7, 42.6, 28.5, 28.3 ppm; HRMS ( $m/z$ ):  $M^-$  calcd for C<sub>22</sub>H<sub>23</sub>F<sub>4</sub>N<sub>3</sub>O<sub>4</sub> 468.1552, found 468.1548.

**4-({N-[(*tert*-Butylcarbamoyl)methyl]-1-(2-chlorophenyl)formamido}methyl)-3-fluoro-*N*-hydroxybenzamide (III-10o).**



Synthesis according to general procedure A using 2-chlorobenzoic acid (78.0 mg) and *tert*-butyl isocyanide (0.06 mL) afforded **III-10o** as a white solid (150 mg, 0.34 mmol, 69%); mp 145 °C;  $t_R$ : 7.27 min, purity: 98.6%;  $^1H$  NMR (400 MHz, DMSO- $d_6$ , 20 °C):  $\delta$  11.27 (s, 1H, *NH*-OH), 9.15 (s, 1H, OH), 7.71–7.24 (m, 8H, arom., NH), 5.27–5.05/4.73–4.22 (2 x m, 2H, CH<sub>2</sub>), 4.05–3.79/3.72–3.52 (2 x m, 2H, CH<sub>2</sub>), 1.24/1.14 (2 x s, 9H, *t*-Bu) ppm;  $^{13}C$  NMR (101 MHz, DMSO- $d_6$ ):  $\delta$  168.3, 168.0, 166.3, 166.1, 162.5, 161.3, 161.2, 158.8, 158.7, 135.30, 135.27, 134.3, 134.2, 133.9, 133.9, 131.5, 131.4, 130.7, 130.6, 130.1, 130.04, 129.97, 129.9, 129.6, 129.4, 129.4, 128.9, 128.8, 128.7, 128.3, 128.1, 127.4, 127.3, 127.0, 126.9, 50.8, 50.3, 47.3, 46.6, 42.9, 42.9, 28.5, 28.3 ppm; HRMS (*m/z*):  $M^-$  calcd for C<sub>21</sub>H<sub>23</sub>ClFN<sub>3</sub>O<sub>4</sub> 434.1288, found 434.1273.

**4-({N-[(*tert*-Butylcarbamoyl)methyl]-1-[2-(propan-2-yl)phenyl]formamido}methyl)-3-fluoro-*N*-hydroxybenzamide (III-10p).**



Synthesis according to general procedure A using 2-isopropylbenzoic acid (82.0 mg) and *tert*-butyl isocyanide (0.06 mL) afforded **III-10p** as a white solid (132 mg, 0.30 mmol, 60%); mp 130 °C;  $t_R$ : 7.96 min, purity: 96.4%;  $^1H$  NMR (400 MHz, DMSO- $d_6$ , 20 °C):  $\delta$  11.31 (s, 1H, *NH*-OH), 9.116 (s, 1H, OH), 7.68–7.09 (m, 8H, arom., NH), 4.98–4.82/4.64–4.08 (2 x m, 2H, CH<sub>2</sub>), 3.81–3.70/3.66–3.48 (2 x m, 2H, CH<sub>2</sub>), 3.12 (2 x p,  $J = 6.7/6.9$  Hz, 1H, *i*-Pr-CH), 1.38–1.04 (m, 15H, *i*-Pr, *t*-Bu) ppm;  $^{13}C$  NMR (101 MHz, DMSO- $d_6$ ):  $\delta$  171.1, 166.6, 166.5, 162.5, 161.4, 161.0, 159.0, 158.6, 145.1, 144.9, 135.0, 134.9, 134.0, 133.9, 131.5, 131.4, 129.6, 129.3, 129.2, 128.8, 128.7, 127.3, 127.2, 125.8, 125.7, 125.6, 125.5, 123.1, 123.0, 113.9, 113.7, 51.0, 50.3, 46.9, 42.3, 29.9, 29.8, 28.5, 28.3, 24.9, 24.2, 23.2, 22.8 ppm; HRMS (*m/z*):  $MNa^+$  calcd for C<sub>24</sub>H<sub>30</sub>FN<sub>3</sub>O<sub>4</sub> 466.2113, found 466.2128.

### 3.5 References

Depetter Y, Geurs S, De Vreese R, Goethals S, Vandoorn E, Laevens A, Steenbrugge J, Meyer E, de Tullio P, Bracke M, D'hooghe M, De Wever O. 2019. Selective pharmacological inhibitors of HDAC6 reveal biochemical activity but functional tolerance in cancer models. *Int J Cancer* **145**: 735–747.

Diedrich D, Hamacher A, Gertzen CGW, Alves Avelar LA, Reiss GJ, Kurz T, Gohlke H, Kassack MU, Hansen FK. 2016. Rational design and diversity-oriented synthesis of peptoid-based selective HDAC6 inhibitors. *Chem Commun* **52**: 3219–3222.

Gaisina IN, Tueckmantel W, Ugolkov A, Shen S, Hoffen J, Dubrovskiy O, Mazar A, Schoon RA, Billadeau D, Kozikowski AP. 2016. Identification of HDAC6-selective inhibitors of low cancer cell cytotoxicity. *ChemMedChem* **11**: 81–92.

Incremona JH, Martin JC. 1970. *N*-bromosuccinimide. Mechanisms of allylic bromination and related reactions. *J Am Chem Soc* **92**: 627–634.

Jiang X, Lee GT, Prasad K, Repič O. 2008. A practical synthesis of a diazepinylbenzoic acid, a retinoid X receptor antagonist. *Org Process Res Dev* **12**: 1137–1141.

Johnson BM, Shu Y-Z, Zhuo X, Meanwell NA. 2020. Metabolic and pharmaceutical aspects of fluorinated compounds. *J Med Chem* **63**: 6315–6386.

Mackwitz MKW, Hamacher A, Osko JD, Held J, Schöler A, Christianson DW, Kassack MU, Hansen FK. 2018. Multicomponent synthesis and binding mode of imidazo[1,2-*a*]pyridine-capped selective HDAC6 inhibitors. *Org Lett* **20**: 3255–3258.

Mackwitz MKW, Hesping E, Antonova-Koch Y, Diedrich D, Woldearegai TG, Skinner-Adams T, Clarke M, Schöler A, Limbach L, Kurz T, Winzeler EA, Held J, Andrews K, Hansen FK. 2019. Structure-activity and structure-toxicity relationships of peptoid-based histone deacetylase inhibitors with dual-stage antiplasmodial activity. *ChemMedChem* **14**: 912–926.

Meanwell NA. 2018. Fluorine and fluorinated motifs in the design and application of bioisosteres for drug design. *J Med Chem* **61**: 5822–5880.

Müller K, Faeh C, Diederich F. 2007. Fluorine in pharmaceuticals: Looking beyond intuition. *Science* **317**: 1881–1886.

Pan Y. 2019. The dark side of fluorine. *ACS Med Chem Lett* **10**: 1016–1019.

Porter NJ, Osko JD, Diedrich D, Kurz T, Hooker JM, Hansen FK, Christianson DW. 2018. Histone deacetylase 6-selective inhibitors and the influence of capping groups on hydroxamate-zinc denticity. *J Med Chem* **61**: 8054–8060.

Purser S, Moore PR, Swallow S, Gouverneur V. 2008. Fluorine in medicinal chemistry. *Chem Soc Rev* **37**: 320–330.

Reßing N, Marquardt V, Gertzen CGW, Schöler A, Schramm A, Kurz T, Gohlke H, Aigner A, Remke M, Hansen FK. 2019. Design, synthesis and biological evaluation of  $\beta$ -peptoid-capped HDAC inhibitors with anti-neuroblastoma and anti-glioblastoma activity. *Med Chem Commun* **10**: 1109–1115.

Reßing N, Sönnichsen M, Osko JD, Schöler A, Schliehe-Diecks J, Skerhut A, Borkhardt A, Hauer J, Kassack MU, Christianson DW, Bhatia S, Hansen FK. 2020. Multicomponent synthesis, binding mode, and structure-activity relationship of selective histone deacetylase 6 (HDAC6) inhibitors with bifurcated capping groups. *J Med Chem* **63**: 10339–10351.

Schmidt J, Rotter M, Weiser T, Wittmann S, Weizel L, Kaiser A, Heering J, Goebel T, Angioni C, Wurglics M, Paulke A, Geisslinger G, Kahnt A, Steinhilber D, Proschak E, Merk D. 2017. A dual modulator of Farnesoid X receptor and soluble epoxide hydrolase to counter nonalcoholic steatohepatitis. *J Med Chem* **60**: 7703–7724.

Wang C, Schroeder FA, Wey H-Y, Borra R, Wagner FF, Reis S, Kim SW, Holson EB, Haggarty SJ, Hooker JM. 2014. *In vivo* imaging of histone deacetylases (HDACs) in the central nervous system and major peripheral organs. *J Med Chem* **57**: 7999–8009.

# Chapter 4: Synthesis and biological evaluation of dual HDAC/20S CP inhibitors

## 4.1 Introduction

***A modified version of chapter 4.1 has previously been published in:***

Jenke R, Reßing N, Hansen FK, Aigner A, Büch T. 2021. Anticancer therapy with HDAC inhibitors: Mechanism-based combination strategies and future perspectives. *Cancers* **13**: 634.

### 4.1.1 Polypharmacy

The application of single-agent drugs is often complicated by the occurrence of side effects and emerging drug resistance (Anighoro et al. 2014). For complex diseases originating from multiple malfunctioning pathways, the efficacy of single-agent drugs directed at one particular biological target may also turn out to be insufficient (Anighoro et al. 2014). A common method to counteract those limitations is *polypharmacy*, the concurrent administration of several medications, which is particularly prevalent among patients suffering from complex or multiple independent disorders. In the latter case, the polypharmaceutical approach is indeed inevitable, but the necessity of differentiating between *appropriate polypharmacy*, covering the indispensable number of medications, and *inappropriate polypharmacy*, which describes the cumulation of too many unnecessary prescriptions due to ineffectiveness or therapeutic duplication, has been raised (Maher et al. 2014; Masnoon et al. 2017). Over the last decades, clinical observations as well as more detailed knowledge on disease progression have promoted the concept of polypharmacy as a therapeutic option for single diseases. This especially applies to epigenetic concepts as constant attempts at deciphering the histone code and the underlying interplay of histone-modifying enzymes contribute to the uncovering of new target combinations that may be addressed to manipulate specific pathways. Detailed reviews of the progress in this field were given by Tomaselli et al. and, more recently, Jenke et al. (Tomaselli et al. 2019; Jenke et al. 2021).

In polypharmacy, additive drugs are supposed to increase efficacy by targeting additional disease-related pathways, mitigate side effects, or reverse drug resistance by blocking the responsible mechanisms (Anighoro et al. 2014). Alternative approaches may aim at engaging the same or different biological targets entangled in the same pathway with one or more drugs that should be dissimilar in terms of resistance mechanisms and modes of action (Anighoro et al. 2014). Due to the multifactorial nature of tumourigenesis, the concept of polypharmacy is well-established in cancer therapy as it allows for the simultaneous interruption of different processes in order to arrest cell proliferation. Hence, standard regimens in oncology typically consist of several drugs employing different modes of action, for example antimetabolites, alkylating agents, intercalating agents, anthracyclines, and mitotic inhibitors.

While the effects of engaging multiple drug targets can to some extent be anticipated, it is noteworthy that drug-drug interactions, whether beneficial or harmful, largely depend on the somewhat unpredictable pharmacokinetic profiles and particularly the metabolic behaviour of the respective compounds (Scripture & Figg 2006). The desirable additive or synergistic effects of drug cocktails therefore come at the risk of inducing adverse effects through drug-drug interactions and off-target activities that may ultimately impair the patient's compliance and cooperation (Anighoro et al. 2014). In an attempt to quantify the frequency of adverse events linked to known drug-drug interactions, Jackson and Soldatos analysed clinical data collected from nearly 6.8 million patients that had been reported to the US Food and Drug Administration (FDA) Adverse Event Reporting System (FAERS) database between the years of 2000 and 2016 and concluded that the total sum adds up to more than 23% of all reported incidents (Soldatos & Jackson 2019). Keeping in mind that only a limited number of drug-drug interactions has yet been discovered, it is likely that the actual percentage lies even higher. With no doubt regarding the effectiveness of multi-targeted therapy in general, such complications caused by polymedications should clearly be tackled.

#### **4.1.2 Polypharmacology**

*Polypharmacology* is an emerging discipline and seeks to minimise the downsides of polypharmacy by designing single drugs that are capable of interacting with multiple targets. Although rather novel in the field of rational drug design, this idea might well have been inspired by the long-standing observation that the efficacies of some established market drugs emanate from additional and often serendipitous modes of action that were not considered during the initial development process (Morphy et al. 2004; Proschak et al. 2019).

In fact, Anighoro et al. point out that this is by no means a rare phenomenon but, on the contrary, a common characteristic among late clinical candidates which may even be considered a contributing factor to the drugs' success throughout the preclinical and clinical evaluation (Anighoro et al. 2014). By now, elaborate efforts to detect unexpected or harmful off-target activities have become an essential part of the drug development process but fail to provide a complete picture. For some drugs, the entirety of the biological involvements remains enigmatic to date (Anighoro et al. 2014). Careful profiling for other compounds yielded valuable information on synergistic or additional drug targets which could then be considered in the rational design process, thereby inspiring polypharmacological drug design (Proschak et al. 2019).

On the whole, the interest in polypharmacology has grown over the last years and Ramsay et al. calculated that nearly every fifth drug approved by the FDA between 2015 and 2017 could be classified as a multi-target agent (Ramsay et al. 2018). Notably, this number exceeds the percentage of newly approved drug combinations which added up to 10% (Ramsay et al. 2018). The overall trend towards multi-target ligands instead of combination drugs is further justified by the considerable reduction in cost and effort throughout the preclinical development and the following clinical investigation. Subjected to only one pharmacokinetic process, multi-target ligands further guarantee the simultaneous occupation of designated tissues, whereas the target-delivery of combination drugs might be deferred unless complicated dosing schedules are adhered to (Anighoro et al. 2014). Indeed, one clear drawback of addressing multiple targets by administering a single drug appears to be the balancing of the doses required in each target, but it was suggested that untypically low doses of dual ligands in synergistic targets suffice to elicit the desired efficacy (Proschak et al. 2019; Lötsch & Geisslinger 2011). Owing to fewer interactions with healthy tissue, such low drug doses are moreover presumed to bear a reduced risk of side effects (Proschak et al. 2019; Lötsch & Geisslinger 2011).

### 4.1.3 Multi-target drugs

In consideration of the highly distinguished shapes of biological targets, it is undeniable that designing selective drugs for multiple binding sites is a challenge. In 2019, Merk and colleagues classified the different types of multi-target ligands as *linked*, *fused*, or *merged pharmacophores* (Figure 4.1; Proschak et al. 2019). This model is in accordance with an earlier overview provided by Morphy et al. who further divided the linked pharmacophores into *cleavable* and *non-cleavable conjugates* (Morphy et al. 2004). The simple method of

*functional group interchange* suggested by de Lera & Ganesan appears to rarely come along with increased affinity to an additional target but may be successful if the groups in question are highly similar, such as carboxylic acids and hydroxamates (de Lera & Ganesan 2020). Choosing among the different types of multi-target ligands to address specific target combinations generally requires excellent knowledge on structural characteristics of each binding site. Careful design is moreover essential in order to meet the criteria for drug-likeness. In any case, it must be ensured that the level of drug promiscuity does not extend beyond the designated targets (Proschak et al. 2019).

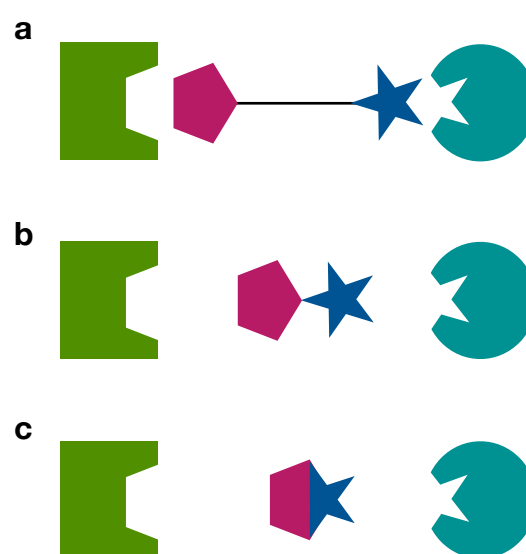


**Figure 4.1.** Structural concept of linked (a), fused (b) and merged (c) pharmacophores.

A typical characteristic of linked pharmacophores is their high molecular weight due to the incorporation of two complete drug scaffolds that are connected by a linker. The pharmacokinetic complications which usually arise as a consequence of bulky or heavy drugs can be circumvented by tying pharmacophores via cleavable linkers that enable the metabolic release of two independent drug molecules (Morphy et al. 2004; Proschak et al. 2019). Among others, some examples of cleavable linkers are esters, hydrazones, dipeptides, or disulfides (Morphy et al. 2004). While this method may be a simple way to address structurally unrelated and incompatible targets, it still requires a predictable point of cleavage as well as careful positioning of the linker which should not impede the interaction with the respective targets (Proschak et al. 2019).

In addition to combining small molecule drugs, the concept of linked pharmacophores is widely applied in the design of antibody-drug conjugates which enable targeted drug delivery into cancer cells through binding to tumour-specific antigens (Beck et al. 2017; Proschak et al. 2019). A related approach aims at designing peptide-drug conjugates carrying one or more toxophores which are supposed to selectively penetrate into tumours after binding to tumour-specific receptors on the cell surface (Böhme et al. 2016; Hoppenz et al. 2020; Vrettos et al. 2018). Indeed, another prominent example based on a similar principle are PROTACs (proteolysis targeting chimeras). On one end, PROTACs consist of tailored ligands



for specific proteins of interest (POIs) which are to be recruited for ubiquitination by E3 ubiquitin ligases. Those, in turn, are to be attracted by respective ligands located at the other end and upon successful ubiquitination, the tagged proteins are finally subjected to degradation by the cellular protein disposal systems (Sakamoto et al. 2001; Gu et al. 2018). In recent years, this method has proven effective for a variety of substrates and several degraders have yet been presented (Sakamoto et al. 2001; Yang et al. 2019; Li & Song 2020; Xiao & Zhang 2020).

Featuring two entire ligands, fused pharmacophores may be connected via the same non-cleavable or cleavable functional groups as linked pharmacophores but lack additional chain length (Proschak et al. 2019). Given the unavoidable high molecular weight and the fact that they are only suitable for solvent-exposed binding sites near the protein surface, this class of compounds may seem inelegant and the least desirable among multi-target drugs (Proschak et al. 2019). Depending on structural characteristics, however, the dissimilarity of designated targets may leave no other option than fusing pharmacophores and unsurprisingly, some examples in the field of epigenetic modifiers have already been realised (de Lera & Ganesan 2016; Proschak et al. 2019).

Merged pharmacophores, on the other hand, do not comprise a linker moiety but combine crucial structural features required for sufficient binding affinity to each target. Thus, they are particularly difficult to design (Proschak et al. 2019). The increased chance to create drug-like molecules complying with the Lipinski's Rule of 5 is the obvious benefit of this model; yet, the choice of targets is limited as they need to be highly compatible so as to tolerate indispensable residues that are intended to interact with the other target (Proschak et al. 2019). Even though merged pharmacophores are generally capable of reaching binding sites beyond the protein surface, it is still necessary to ensure that the incorporation of an additional moiety does not interfere with the ability to pass gatekeeper residues. A common method to avoid such collisions is the exploitation of wide, solvent-exposed areas. Such parts of a pharmacophore typically undergo no or little interaction with the surroundings in the binding pocket and might therefore be used to attach indispensable moieties of the other ligand.

#### 4.1.4 Multi-targeted HDAC inhibitors

Although challenging in terms of design, there are several FDA-approved drugs and clinical candidates built on the concept of merged pharmacophores (Proschak et al. 2019; de Lera & Ganesan 2020).

At this point, efforts on merged multi-target ligands featuring HDACi moieties display an overwhelming prevalence of dual HDAC/kinase inhibitors (de Lera & Ganesan 2020; Smalley et al. 2020; Tomaselli et al. 2020). As phosphotransferases, kinases generally operate the transport of phosphate groups from ATP to a range of respective substrates and the selective interruption of this process has long been deemed a valuable therapeutic goal (Luan et al. 2019). To date, more than forty kinase inhibitors have been approved to treat multiple forms of cancer (Luan et al. 2019; Pottier et al. 2020). Owing to the high number of client proteins, however, the eukaryotic kinase family consists of more than five hundred members in different subgroups of which some possess the ability to compensate for a lack of specific enzymes, e.g. after inhibition or downregulation, by means of redundancy or mutation (Anighoro et al. 2014). In cancer therapy, this effect is considered to drive resistance and after initial efforts towards selective kinase inhibitors, the trend has shifted to designing

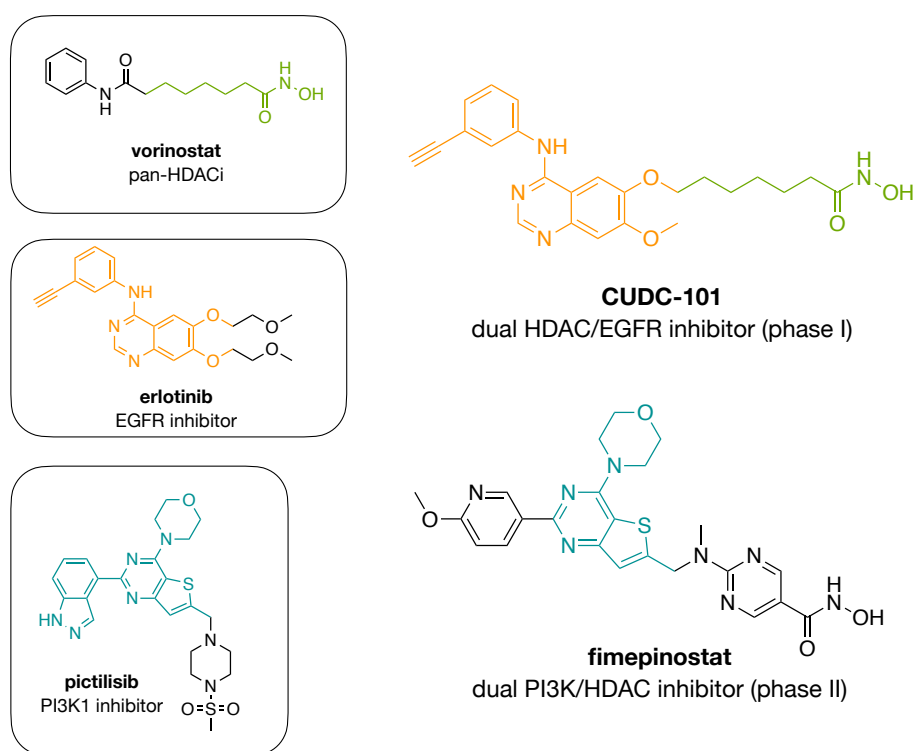


**Figure 4.2.** Dual HDAC/kinase inhibitors in clinical trials.

multi-kinase inhibitors or dual agents that address non-kinase targets as well (Anighoro et al. 2014; Ramsay et al. 2018). The relevance of combined kinase/HDAC inhibitors in this context primarily stems from the observation that HDACi may sensitise cancer cells to treatment with kinase inhibitors; however, complementary synergistic effects depending on both the specific target combination and the indication also seem possible (Luan et al. 2019; Greve et al. 2015; Nakagawa et al. 2013; Chen et al. 2013).

The structure of fimepinostat (Figure 4.2) matches the HDAC pharmacophore model with a hydroxamate ZBG, a pyrimidine-linker, and a cap group inspired the phosphoinositide 3-kinase (PI3K) inhibitor pictilisib (Qian et al. 2012; de Lera & Ganesan 2020). Thus functioning as an inhibitor of PI3K $\alpha$  and HDACs 1–3 and 10, the compound is currently undergoing phase II trials against lymphomas and solid tumours. Merging of the tyrosine kinase inhibitor erlotinib and an aliphatic HDAC linker bound to a hydroxamate ZBG yielded the dual EGFR/HDAC inhibitor CUDC-101 (Figure 4.2) which has since become a phase I candidate for the therapy of solid cancers (Lai et al. 2010; de Lera & Ganesan 2020; Tomaselli et al. 2020).

On preclinical level, research on dual kinase/HDAC inhibitors is quickly evolving and compounds addressing PI3Ks, receptor tyrosine kinases (RTKs), the proto-oncogene tyrosine-protein kinase Src (c-Src), cyclin-dependent kinases (CDKs), and janus kinases (JAKs) have yet been presented. The remarkable progress in this area has been extensively reviewed over the last years (de Lera & Ganesan 2016; Suraweera et al. 2018; Luan et al. 2019; Tomaselli et al. 2019; Smalley et al. 2020; de Lera & Ganesan 2020; Liu et al. 2020).

Outside the field of kinase inhibition, current approaches towards bifunctional HDACi engage a multitude of additional targets and one prominent example of an HDACi with dual activity is tinostamustine (Figure 4.3). Designed as a hybrid of the pan-HDACi vorinostat and the alkylating agent bendamustine, tinostamustine acts as a potent HDACi with DNA-alkylating properties and has entered phase I/II trials against lung cancer, brain tumours, and haematological malignancies. Other analogues based on nitrogen mustard drugs were designed by Yuan and co-workers and have been investigated on preclinical level (Xie et al. 2017; Xie et al. 2018; Liu et al. 2020). One of those, the chlorambucil/vorinostat hybrid vorambucil (Figure 4.3), outmatched its parent compounds in terms of both HDAC inhibition and antiproliferative potential in four cancer cell lines (Xie et al. 2017). Chlordinaline (Figure 4.3), on the other hand, features the *ortho*-aminoanilide-based HDAC binding site of tacedinaline attached to the chlorambucil scaffold and displays moderate but HDAC3-preferential inhibition and promising DNA-damaging properties *in vitro* (Xie et al. 2018).

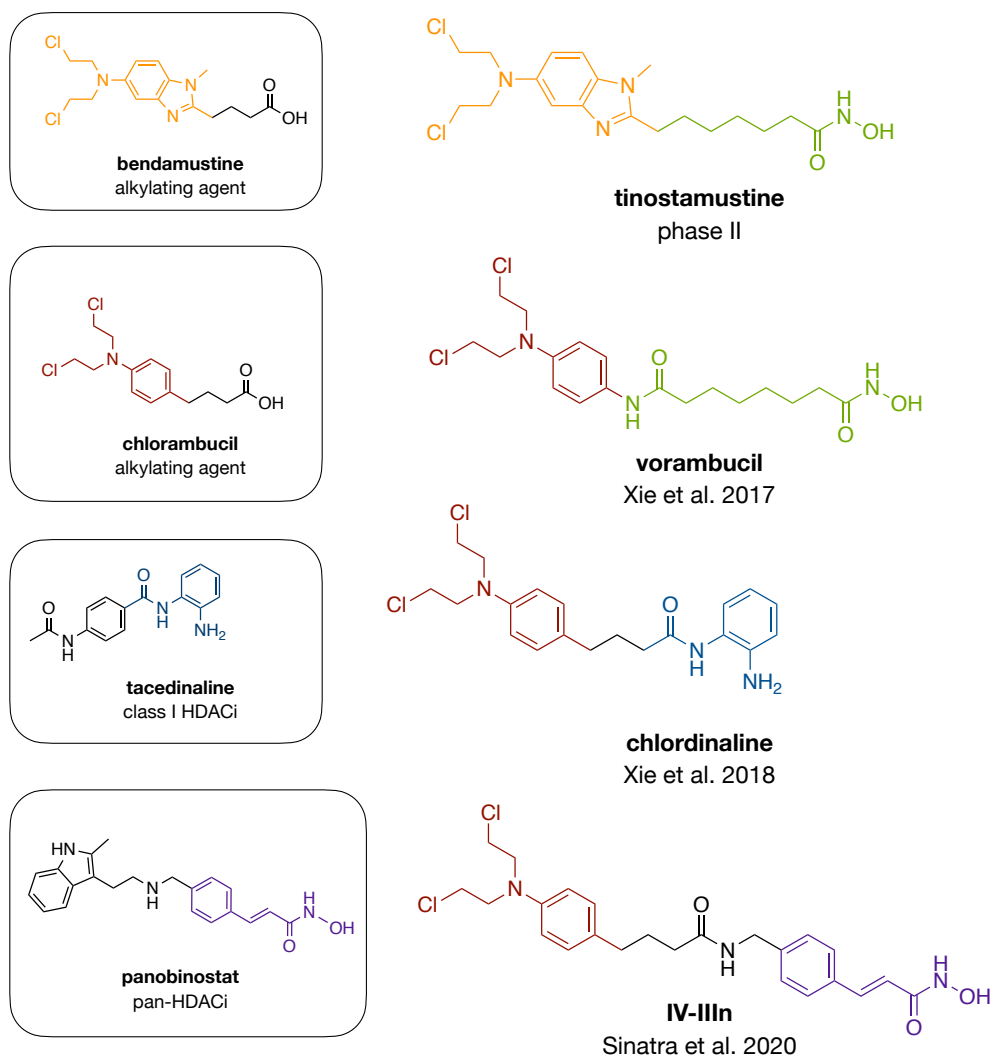


**Figure 4.3.** Preclinical and clinical DNA-damaging HDACi.

Seeking to employ modes of action other than dual inhibition, the Hansen group recently reported on their successful development of a solid phase-supported protocol yielding HDACi precursors that could be transformed into either tinostamustine-inspired alkylating agents (Figure 4.3) or PROTACs (Figure 4.4; Sinatra et al. 2020). Other PROTACs with the

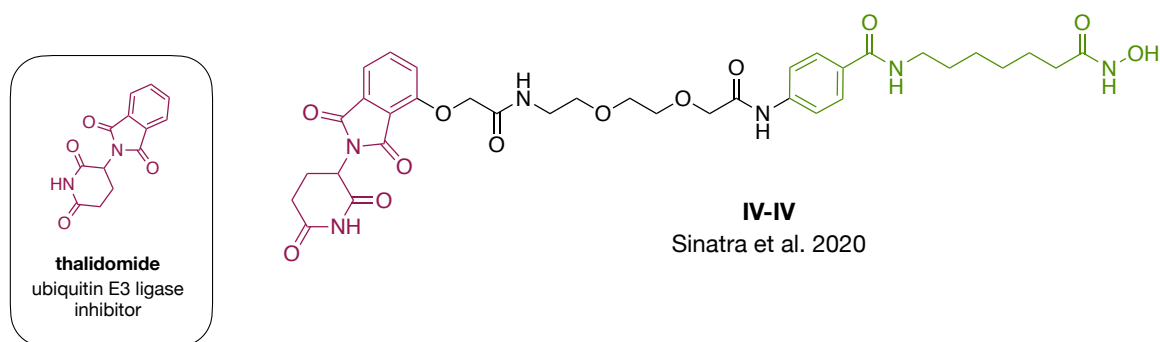


**Figure 4.4.** An HDAC degrader (PROTAC) inspired by vorinostat and thalidomide.

ability to degrade HDACs are summarised in recent articles by Xiao and Zhang and Smalley et al. (Xiao & Zhang 2020; Smalley et al. 2020).

With all aforementioned dual inhibitors being designed as such, there are also compounds whose actual dual activity emerged as a surprise. One example of such serendipity is the resminostat analogue domatinostat (Figure 4.5; Zhijun et al. 2016; de Lera & Ganesan 2020). Originally believed to impair the function of the epigenetic eraser lysine-specific demethylase 1 (LSD1) which participates in the CoREST complex formation alongside HDACs 1 and 2, the class I HDACi unexpectedly turned out to inhibit tubulin polymerisation as well and ongoing clinical trials in phases I and II investigate the resulting effect on haematological and gastrointestinal cancers (Morera et al. 2016; Wobser et al. 2019). Further research on dual LSD1/HDAC inhibitors yielded a vorinostat derivative with a tranylcypromine cap group (**IV-VIIa**; Figure 4.5) that effectively inhibited both targets (Duan et al. 2017). By merging the tranylcypromine group with entinostat, Kalin et al. developed the class I-selective HDAC/LSD1 inhibitor corin (Figure 4.5) which inhibited the CoREST complex and reduced tumour growth in a melanoma mouse xenograft model (Kalin et al. 2018).

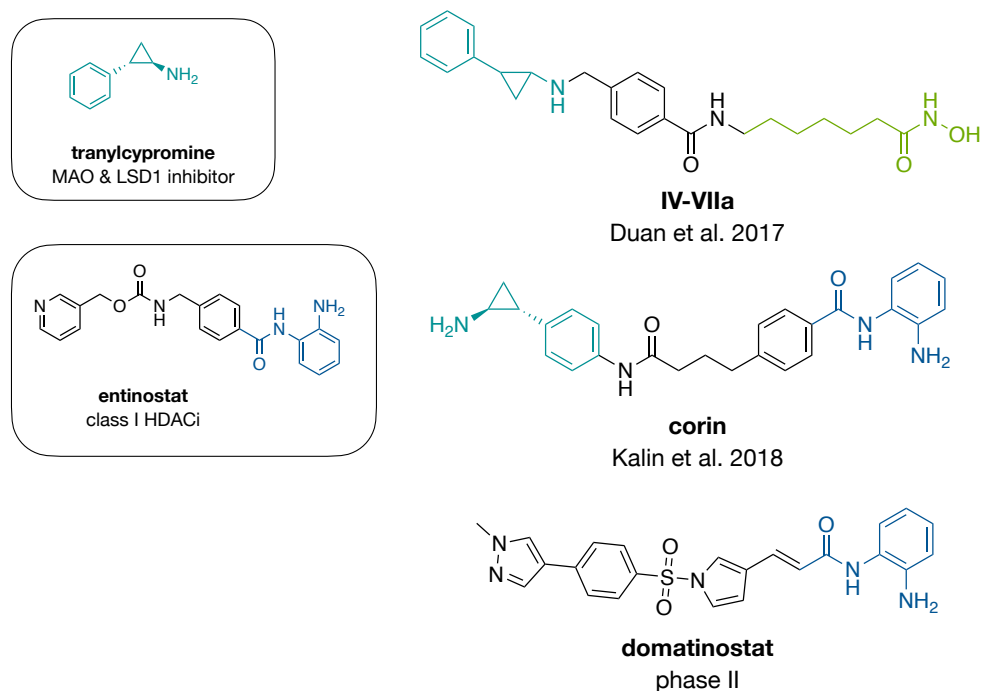


**Figure 4.5.** Preclinical and clinical dual HDAC/LSD1 inhibitors.

Beside the HDAC-involving synergisms elucidated in the clinic, dual HDAC inhibitors are proposed to be useful for a multitude of additional targets and several prototypes have yet been reported in the literature.

Through inhibiting HDACs, it is possible to maintain a relaxed chromatin structure which can be exploited to facilitate the access of DNA for topoisomerases (Liu et al. 2020). Responsible for uncoiling the DNA superhelix by breaking and ligating single strands (topoisomerases I) or double strands (topoisomerases II), topoisomerases are crucial for replication and transcription so that inhibition results in arrested cell proliferation (Liu et al. 2020). One class of compounds entertaining this mode of action are anthracyclines, such as daunorubicin and its analogue doxorubicin. Intending to combine the advantages of daunorubicin and the pan-HDACi vorinostat, Oyelere and co-workers introduced a small set of merged dual ligands among which **IV-VIIb** (Figure 4.6) was singled out as a hit compound with promising cytotoxicity against different solid tumour cell lines (Guerrant et al. 2012). In inhibition assays, compound **IV-VIIb** was observed to impair the activity of both HDACs and topoisomerase II at similar levels as vorinostat and daunorubicin, respectively (Guerrant et al. 2012). Following this work, alternative structures based on the camptothecin, acridine, and podophyllotoxin scaffolds were presented (Guerrant et al. 2012; Guerrant et al. 2013; Cincinelli et al. 2018; Seo 2015; Liu et al. 2020). Given that most attempts aim to benefit from the histone deacetylase qualities of class I HDACs, it is noteworthy that recent *in vitro* combination studies also suggested promising synergistic effects of anthracyclines and selective HDAC6i (Tu et al. 2018; Reßing et al. 2020).

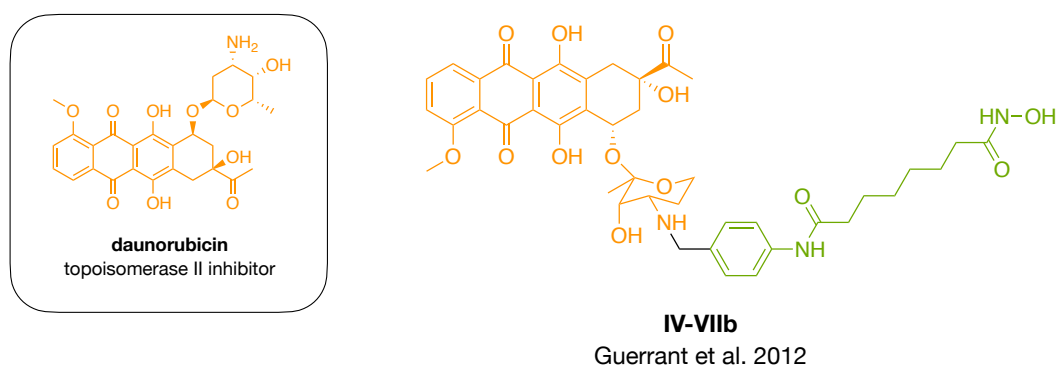


**Figure 4.6.** A dual HDAC/topoisomerase inhibitor.

Being part of the epigenetic network, HDACs function as erasers and happen to operate on molecular pathways and targets that are also served by the four bromo- and extra-terminal domain (BET) proteins (BRD2, BRD3, BRD4, BRDT) which recognise acetylated histones and are thus classified as epigenetic readers (Liu et al. 2020). With reference to their presumed association with super-enhancers that are suspected to boost cancer progression by assembling transcription factors near oncogenes, it was hypothesised that the most promising synergism concerns HDAC1, HDAC2, and particularly BRD4 which could be

inhibited to disturb the transcriptional machinery of super-enhancers (Liu et al. 2020; Atkinson et al. 2014; Tang et al. 2020). Since the first report on DUAL946 (Figure 4.7) by Atkinson and colleagues in 2014, several structures of dual BRD4/HDAC inhibitors have been disclosed (Atkinson et al. 2014; Zhang et al. 2016; Noguchi-Yachide et al. 2015; Liu et al. 2020; de Lera & Ganesan 2020). Most recently, He et al. merged the phenyl linker and hydroxamate ZBG of HDACi and the first BET inhibitor (+)-JQ1 into their hit compound **IV-XIIIa** (Figure 4.7) which demonstrated superior antitumour activity compared to its parent compounds in a capan-1 human pancreatic cancer xenograft model (He et al. 2020).

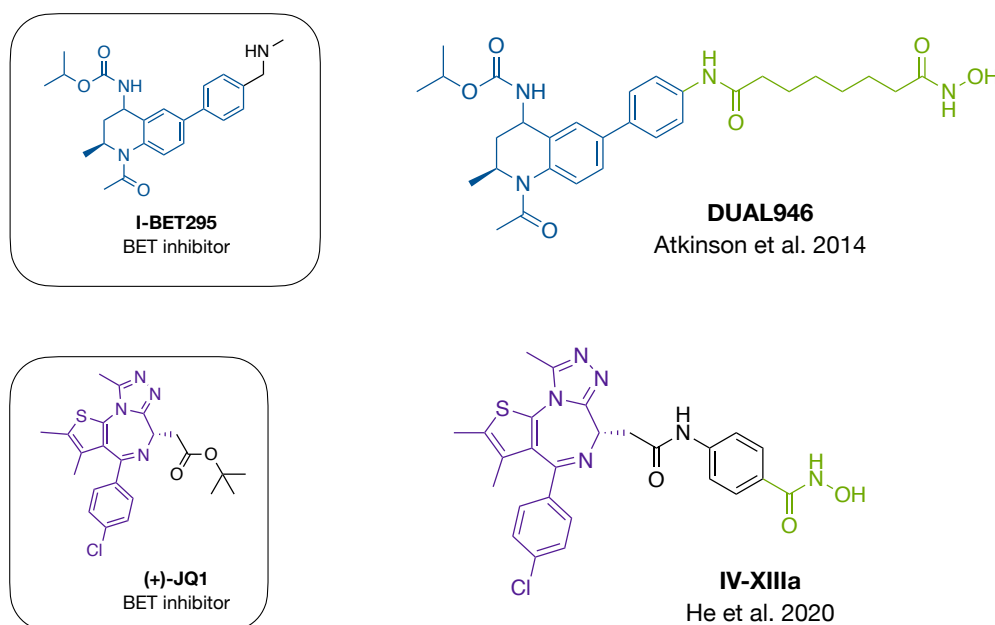


**Figure 4.7.** Dual HDAC/BET inhibitors.

Through its function as a chaperone assisting protein folding, Hsp90 is of particular importance for proliferating cells that rely on high protein expression. Interestingly, it has been observed that Hsp90 is activated by deacetylation and thus controlled by HDAC6 (Kovacs et al. 2005). The concurrent application of HDACi is therefore presumed to increase the effect of Hsp90 inhibitors and can furthermore be utilised to overcome acquired resistance (Pinzi et al. 2020). Considering that the pharmacophore models for HDAC6i and Hsp90 inhibitors show little similarity, the design of dual ligands appears to be challenging, but nevertheless, some examples were introduced over the last years (Pinzi et al. 2020). Replacing the phenyl cap group of vorinostat by the resorcinol moiety present in the phase II Hsp90 inhibitors luminespib and onalespib recently yielded compound **IV-XII** (Figure 4.8) which inhibited both targets and induced apoptosis in lung cancer cells (Ojha et al. 2018). Another group studying

the resorcinol scaffold chose to discard the indoline motif of onalespib in favour of a phenyl group and achieved similar effects (Figure 4.8; Mehndiratta et al. 2020). As expected, both compounds induced the upregulation of Hsp70 and the degradation of Hsp90 client proteins (Ojha et al. 2018; Mehndiratta et al. 2020).

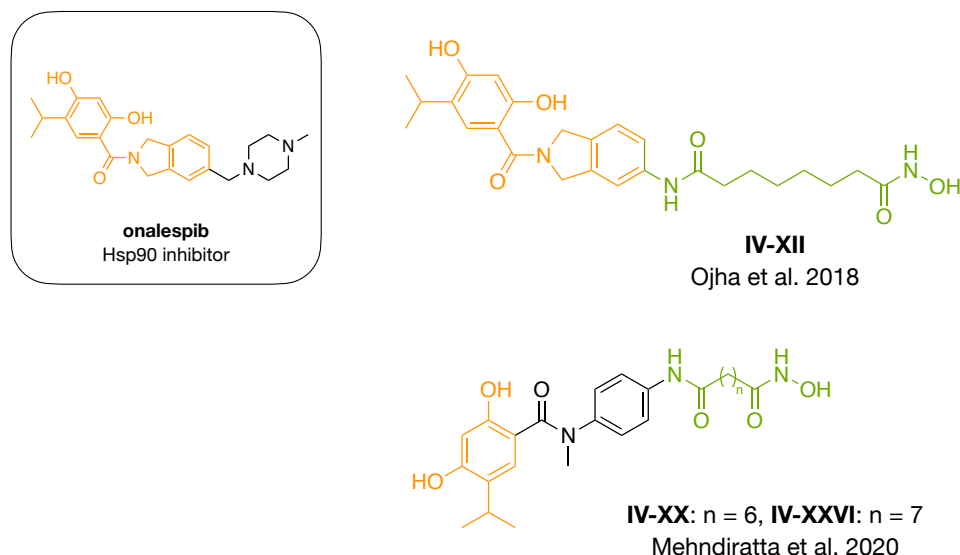


**Figure 4.8.** Dual HDAC/Hsp90 inhibitors.

#### 4.1.5 HDAC6 and the 20S CP as synergistic drug targets

The rapid and extensive proliferation of cancer cells goes along with high protein expression levels. At this rate, occasional errors during protein synthesis or the subsequent chaperone-aided folding process are likely to occur, whereas other, properly expressed proteins might become dispensable. In both cases, ubiquitin residues are attached as markers for designated proteasomal degradation which is supposed to prevent the formation of cytotoxic protein aggregates (Lecker et al. 2006). Despite its crucial function throughout all tissues, it has been suggested that malignant cells are more dependent on the 26S proteasome-mediated protein disposal than healthy cells (Hideshima et al. 2011; Adams 2004).

A malignancy exhibiting particular sensitivity towards proteasome inhibition is multiple myeloma (MM) whose progression seems to benefit from a dysregulation of the NF- $\kappa$ B pathway that requires proteasomal activation (Adams 2004). In 2003, clinical trials using the 20S CPi bortezomib in MM patients demonstrated improved outcomes and the subsequent FDA-approval was soon followed by the release of several second-generation drugs. Although initial studies implied that bortezomib may enhance the chemosensitivity to other



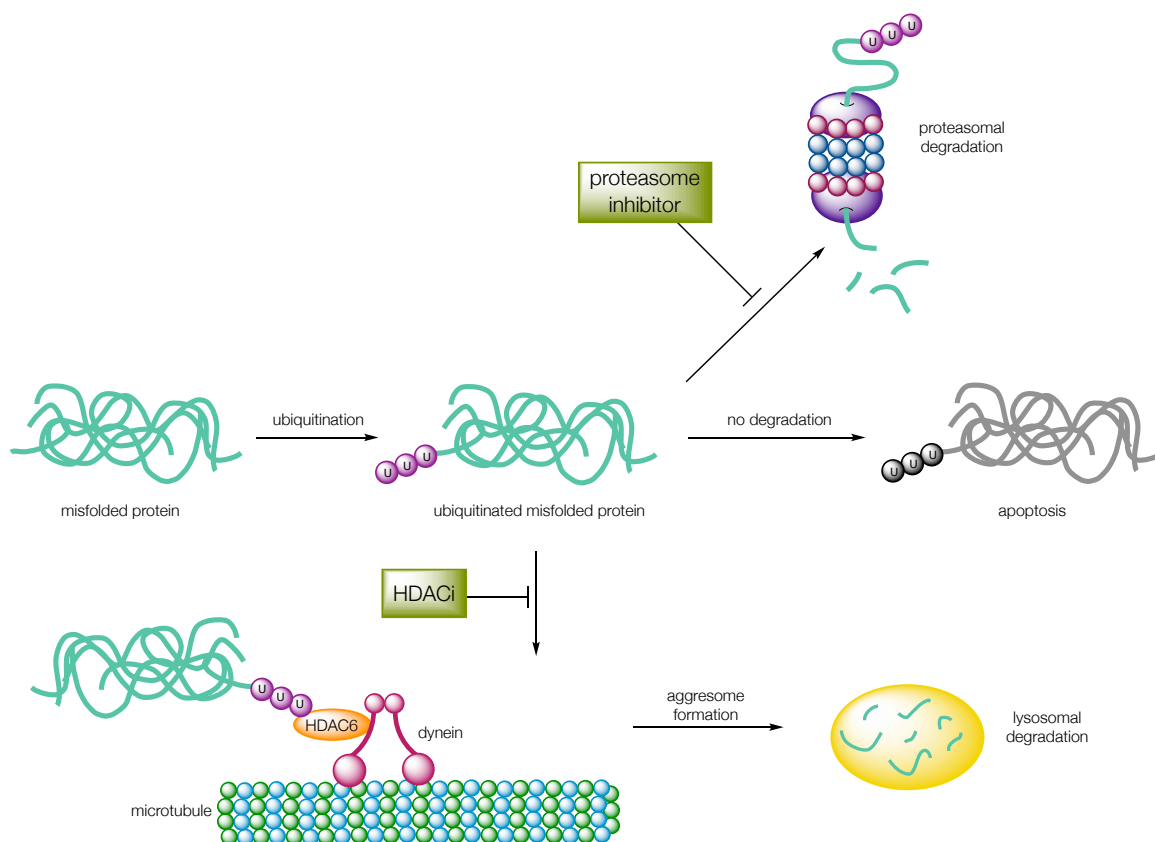
anticancer drugs by inhibiting the NF- $\kappa$ B pathway, it has since been observed that bortezomib-treatment itself induces drug resistance in many patients (Adams 2004). In addition to other cellular mechanisms including the upregulation of both chaperone and proteasome expression, the intrinsic or acquired bortezomib resistance is partly attributed to the activation of an alternative protein disposal system, the cytoplasmic aggresome-autophagy pathway (Manasanch & Orłowski 2017; Kawaguchi et al. 2003).

Early studies on this mechanism provided evidence that aggresome formation requires initiation by HDAC6 through the UBD-mediated transport of ubiquitinated proteins to dynein, which functions as a motor protein along the microtubule network (Kawaguchi et al. 2003; Hideshima et al. 2005). A deeper understanding of this mechanism was gained by Ouyang et al. who reported on the binding of the HDAC6 UBD to unconjugated C-terminal diglycine motifs of ubiquitin located at accessible sites on the surface of protein aggregates (Ouyang et al. 2012). Prior to this step, the polyubiquitinated protein aggregates seem to interact with the deubiquitinase ataxin-3 which generates the solvent-exposed, unanchored ubiquitin C-termini *in situ* to trigger the subsequent aggresomal clearance (Ouyang et al. 2012).

Based on those observations, Hideshima and co-workers hypothesised that the simultaneous application of bortezomib and a selective HDAC6i could reverse bortezomib resistance through inhibition of the two synergistic protein degradation pathways (Scheme 4.1; Hideshima et al. 2005). The group was able to confirm their assumption by demonstrating that the additional application of the HDAC6i tubacin in MM cells promoted the accumulation of polyubiquitinated proteins, thereby enhancing the cytotoxicity of bortezomib (Hideshima et al. 2005). Further research on this synergism indicated similar effects for other HDACi and 20S CPi and consequently, several combinations have been explored in clinical trials. In 2016, improved outcomes in relapsed and/or refractory MM patients resulted in the FDA approval of panobinostat in combination with bortezomib and dexamethasone (Richardson et al. 2016). Considering that panobinostat acts as a pan-inhibitor, some of its efficacy in this context may indeed be linked to class I HDAC inhibition rather than the protein disposal synergism.

Since its introduction into clinical trials, the HDAC6-preferential drug ricolinostat has been considered a potential candidate for initiating the protein degradation blockage in combination with 20S CPi. Accordingly, a phase I/II study using the HDAC6i in combination with bortezomib demonstrated promising efficacy, whereas application of ricolinostat in absence of a 20S CPi triggered no significant response (Vogl et al. 2017). The co-treatment

with ricolinostat moreover turned out to induce fewer and less severe adverse effects than



**Scheme 4.1.** Interplay of the 26S proteasome and HDAC6 as synergistic drug targets. Adapted from Hideshima et al. 2011.

the combination of bortezomib and panobinostat (Vogl et al. 2017).

The proposed mechanisms suggest that the synergism of the 20S CP and HDAC6 relies on interactions of the UBD rather than CD2. In preclinical studies, however, inhibition of the latter seemed sufficient to achieve the desired effects (Hideshima et al. 2005). Yet, the question whether UBD inhibitors could be more effective to this end has been raised and in recent years, several examples of HDAC6 UBDi were developed (Ouyang et al. 2012; Harding et al. 2017; de Freitas et al. 2018).

An additional substrate of HDAC6 contributing to the same synergism is the chaperone protein Hsp90. Typically responsible for ensuring the meticulous folding at later stages of the protein folding process, Hsp90 also regulates native proteins and prevents cells from proteotoxic stress (Karagöz & Rüdiger 2015). Beside its crucial activity in healthy cells, the chaperone function of Hsp90 is estimated to serve more than 200 client proteins in

malignant cells, such as kinases, transcription factors, and the tumour suppressor p23 (Karagöz & Rüdiger 2015; Anighoro et al. 2014). Another prominent protein depending on assistance by Hsp90 is tau which is presumed to play a pivotal role in neurological disorders (Karagöz & Rüdiger 2015).

Early studies on the interplay of HDACs and Hsp90 inspired the conclusion that the HDAC6-controlled acetylation state of Hsp90 may influence its interactions with client proteins and cochaperones so that the reduction of chaperone activity in presence of HDACi was attributed to the impaired deacetylase activity of HDAC6 (Bali et al. 2005; Kovacs et al. 2005; Boyault et al. 2007). Hence, inhibition of Hsp90 could amplify the cytotoxic effect of 20S CPi by promoting the aggregation of particular client proteins while other chaperone proteins serving different substrates would remain active (Pinzi et al. 2020).

#### 4.1.6 Project outline

Finding suitable and more selective ways to drug both HDAC6 and the 20S CP has long been a question of polypharmacy. Most recently, however, Zhou et al. designed a library of covalent dual HDACi/20S CPi (Figure 4.9) derived from the boronate-containing P1 moiety of bortezomib and the HDAC binding sites of entinostat and panobinostat (Zhou et al. 2020). To overcome HDAC1-conferred bortezomib resistance, the group also included class I-selective *ortho*-aminoanilides in their set. As a result, they identified ZY-2 as well as the hydroxamate ZY-13 as hit compounds which displayed excellent enzyme inhibition and cytotoxicity in MM cell lines (Zhou et al. 2020). With a focus on merged ligands, the work by Zhou et al. succeeded the presentation of a non-covalent HDACi/20S CPi developed by the Hansen group in 2018 (Bhatia et al. 2018).

Starting from the scaffold of the tool compound ML-16 (Blackburn et al. 2010a), Bhatia et al. removed both the pyridine and the chlorine residues and replaced the P4 group by a phenyl linker attached to a hydroxamate ZBG in order to create the first-in-class dual HDACi/20S CPi RTS-V5 (Figure 4.9; Bhatia et al. 2018). Comprehensive *in vitro* screenings of RTS-V5 indicated the high biological potential of the compound (Bhatia et al. 2018). Throughout a selection of eight leukaemia and MM cell lines, RTS-V5 displayed higher cytotoxicity than ricolinostat. After treatment of selected B-cell precursor acute lymphoblastic leukaemia (BCP-ALL) cell lines (SEM, SUP-B15, SUB-B15R), this effect was particularly significant, but additional screenings using BCP-ALL patient-derived blood samples yielded opposite results. In spite of being inferior to the highly potent bortezomib, RTS-V5 effectively inhibited the proteasome function in HL-60, SUP-B15R, and SEM cell lines. An annexin/PI assay

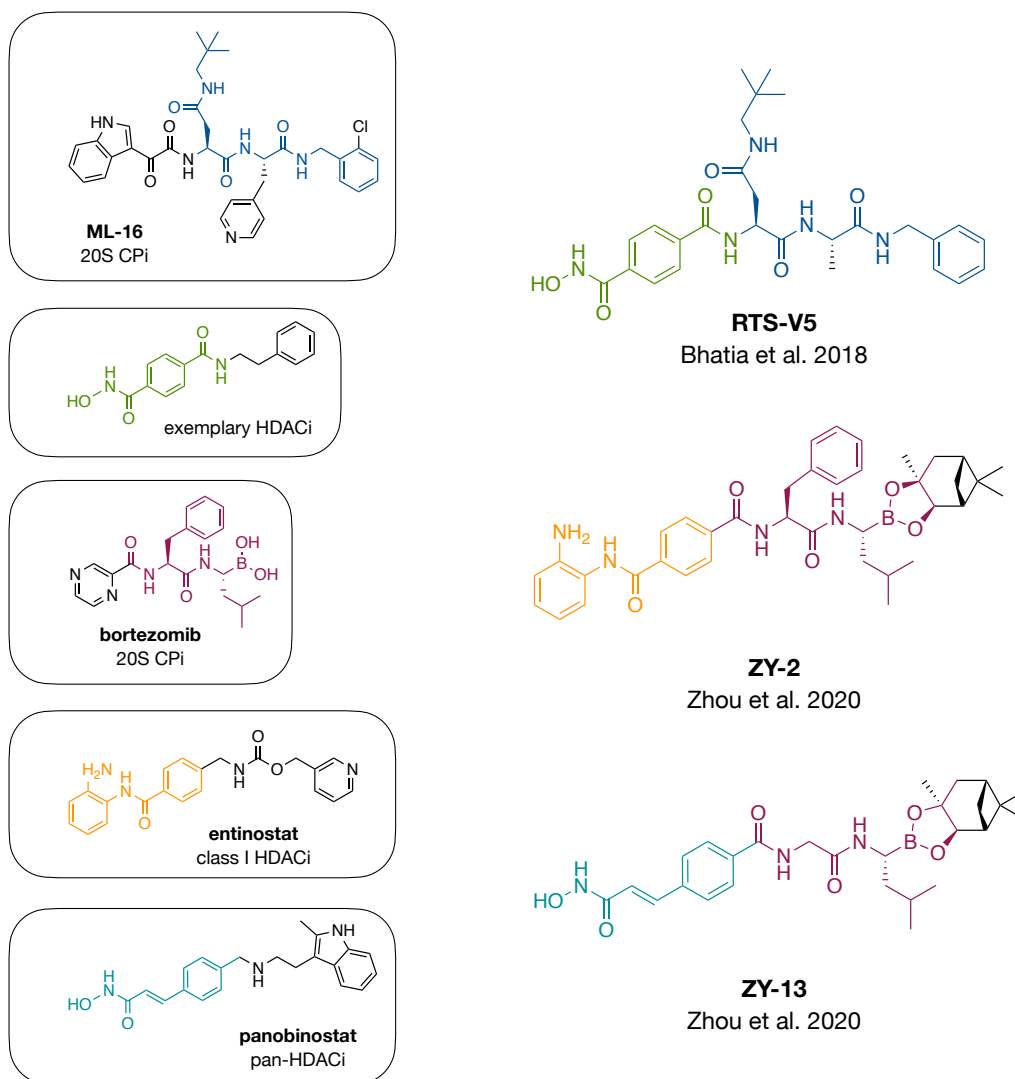
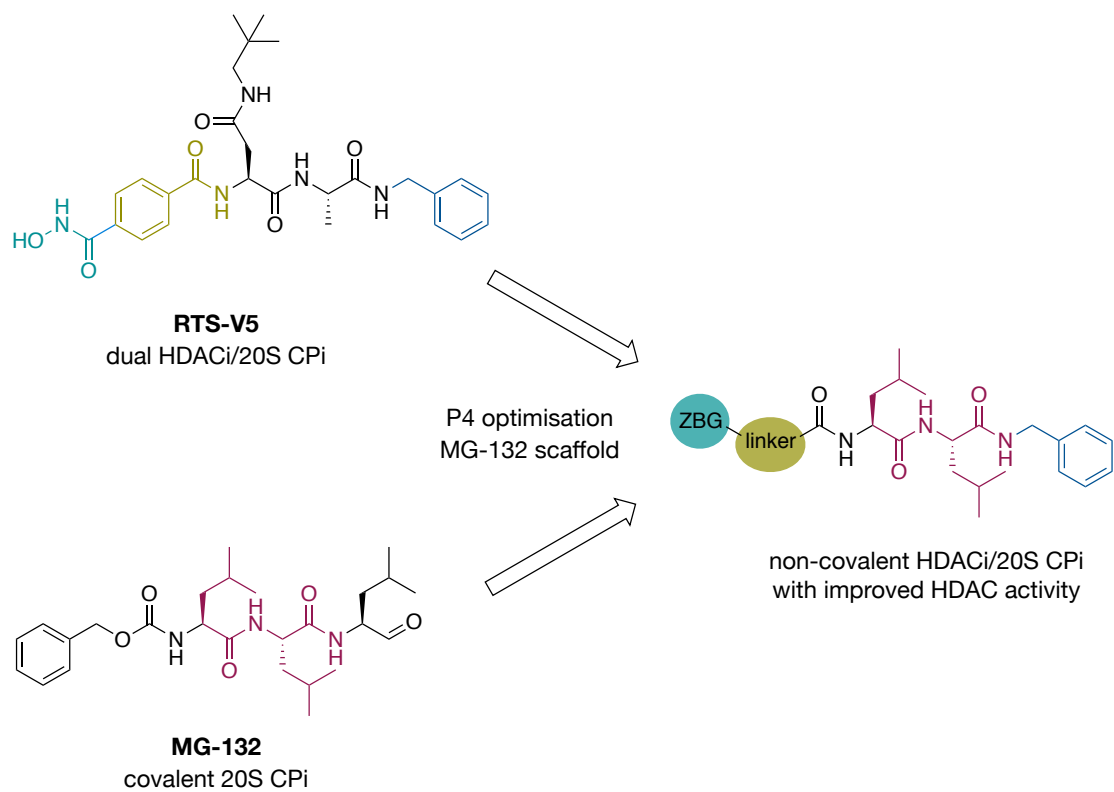


**Figure 4.9.** Dual HDACi/20S CPi.

using SEM cells furthermore revealed that the apoptosis induction levels of RTS-V5 matched those of ricolinostat. Unlike the 20S CPi bortezomib and MG-132, RTS-V5 was able to block aggresome formation in SEM cells at  $IC_{50}$  ( $0.89 \pm 0.01 \mu\text{M}$ ). To a lesser extent, the same effect was detected upon ricolinostat treatment ( $IC_{50}$ :  $1.61 \pm 0.02 \mu\text{M}$ ). Overall, the impact of RTS-V5 on the protein disposal synergism was apparent and pleasing. In terms of HDAC inhibition, however, the moderate inhibitory activity and HDAC6 selectivity are striking ( $IC_{50}$  HDAC1:  $2.31 \pm 0.04 \mu\text{M}$ ; HDAC6:  $0.413 \pm 0.038 \mu\text{M}$ , SI: 5.6). Aiming to improve the inhibition qualities, the design and synthesis of new RTS-V5 analogues with improved HDACi moieties was attempted in this study (Scheme 4.2).<sup>15</sup>

<sup>15</sup> HDAC inhibition assays were performed by Andrea Schöler in the group of Finn K. Hansen, Leipzig University. The data quoted here is not identical with the HDAC inhibition data reported in Bhatia et al. 2018 which was generated using a different substrate.



**Scheme 4.2.** Design of new dual HDACi/20S CPI derived from RTS-V5 and MG-132.

## 4.2 Results and discussion

### 4.2.1 1<sup>st</sup> Generation: Design and synthesis

In comparison to HDAC6i designed by the Hansen group and other researchers, the linker moiety of RTS-V5 appears rather short and lacks the established benzylic linker in favour of a phenyl group. The library design for the new ligands therefore focused on variations of the linker in order to fine-tune HDAC inhibition (Figure 4.10).

Supposed to improve the preference for HDAC6, analogue **IV-1a** was to comprise a benzyl linker. The effect of pan-inhibition was to be elucidated using **IV-1b** which features the phenylvinyl linker of panobinostat. Owing to matters of synthetic accessibility, the linker study was carried out using a non-covalent analogue of the MG-132 scaffold instead of RTS-V5 and therefore required the presumably non-selective phenyl linker derivative **IV-1c** inspired by RTS-V5 as a control. Through the introduction of a phenylvinyl linker and an *ortho*-aminoanilide ZBG, **IV-1d** was expected to exclusively address HDACs 1–3. A fifth analogue, **IV-1e**, was supposed to contain a benzylic linker attached to a urea group; the resulting selectivity profile of this motif was to be determined in the course of the study.

Realising the convergent synthesis of the different derivatives first required the formation of several building blocks (Scheme 4.3). In accordance with a literature protocol, 4-(2-methoxy-2-oxoethyl)benzoate was treated with one equivalent of potassium carbonate to achieve the selective hydrolysis at the aliphatic position (**IV-3**; Breslow et al. 2014). 4-Formylbenzoic acid (**IV-4**) and trimethyl phosphonoacetate were used to generate the olefinic linker **IV-5** via the Horner-Wadsworth-Emmons reaction. Obtained from commercial sources, 4-(methoxy-carbonyl)benzoic acid **IV-6** was attached to *O*-trityl-hydroxylamine by means of a HATU-mediated coupling

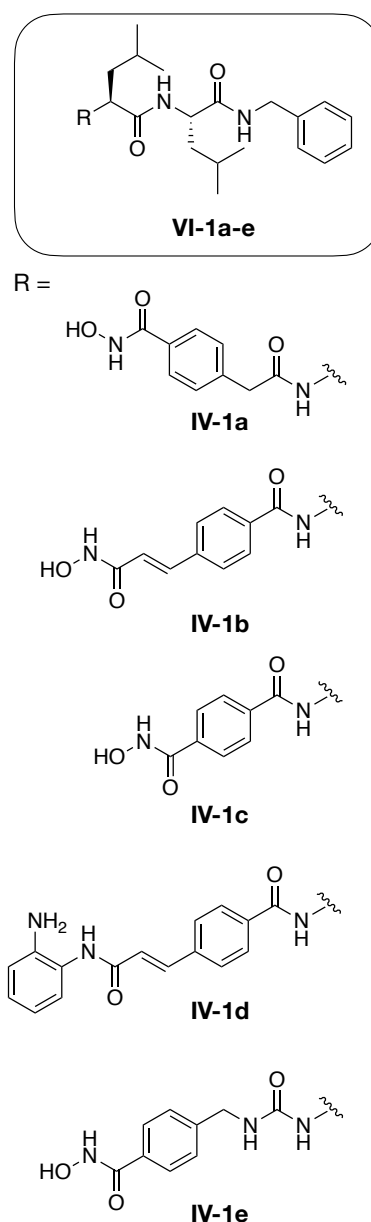
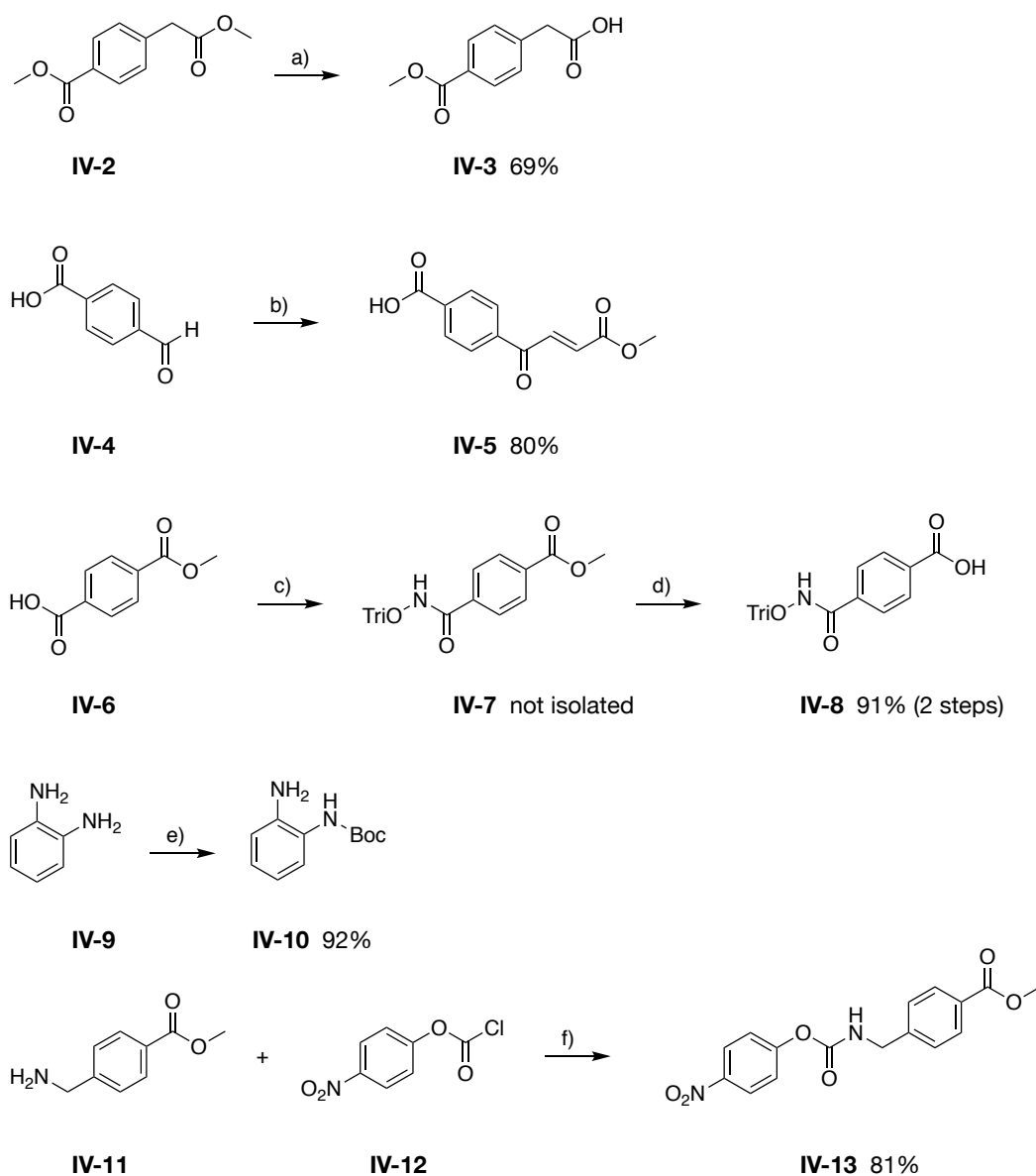


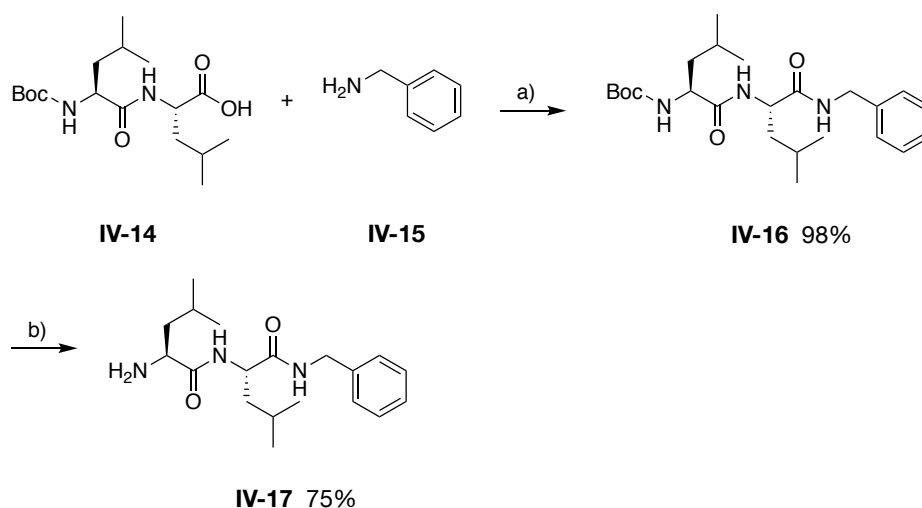
**Figure 4.10.** Linker and ZBG variations of the RTS-V5/ MG-132 hybrid scaffold.

reaction that afforded the linker fragment **IV-8**. The Boc-protection yielding **IV-10** was carried out using an excess of 1,2-phenyldiamine (**IV-9**) so as to avoid the formation of the double-protected derivative. Following a literature procedure, the final linker building block **IV-13** was prepared from 4-nitrophenyl chloroformate (**IV-12**; Stenzel et al. 2017). The resulting carbamate was supposed to serve as a precursor for urea-formation.



**Scheme 4.3.** Synthesis of linker building blocks. Reagents and conditions: a)  $K_2CO_3$ , MeOH/ $H_2O$ , 27 h; b)  $K_2CO_3$ , trimethyl phosphonoacetate, THF, rt, 16 h; c) *O*-tritylhydroxylamine, HATU, DIPEA, DMF, rt, 48 h; d) NaOH, THF/ $H_2O$ , rt, 24 h; e)  $Boc_2O$ , DCM, 0 °C to rt, 20 h; f)  $Et_3N$ , pyridine, DCM, 0 °C to rt, 3 h.

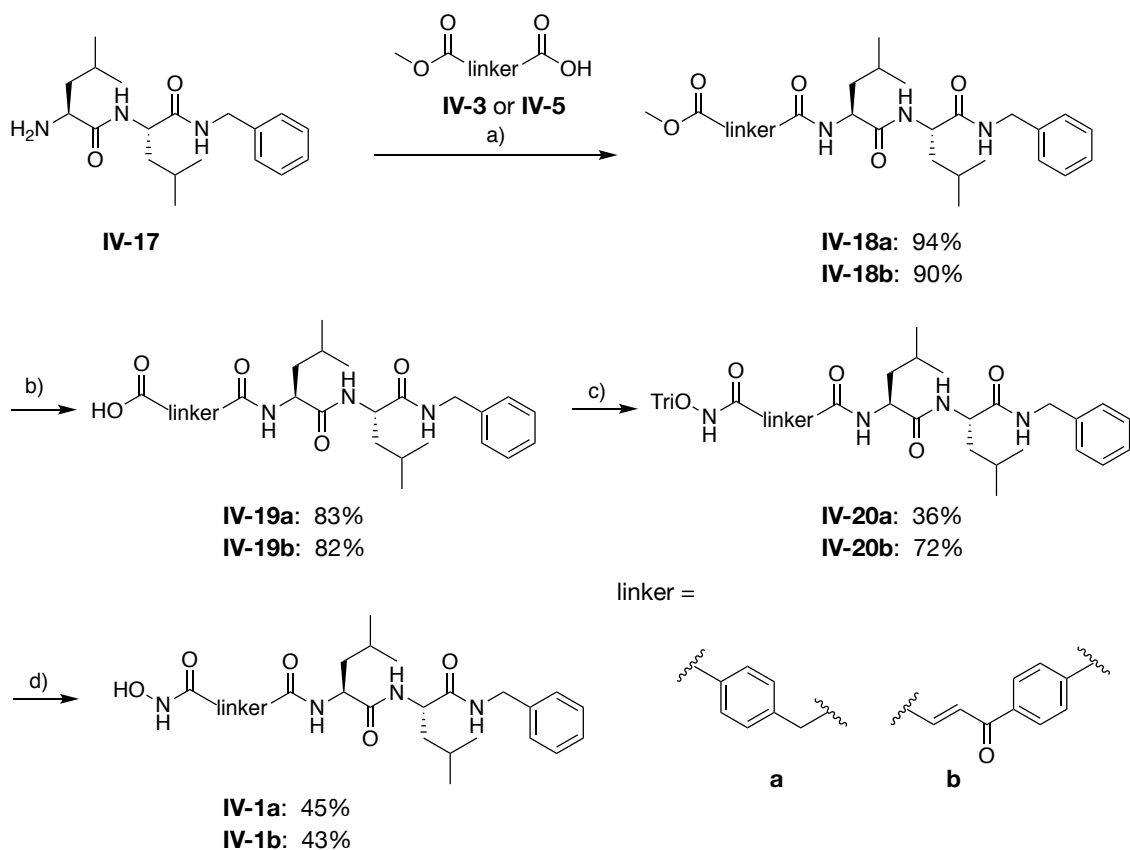
After complete preparation of all linker building blocks, the modified MG-132 scaffold was synthesised through isobutyl chloroformate-mediated coupling of the commercially available Boc-Leu-Leu-OH and benzylamine (Scheme 4.4). Subsequent Boc-removal under acidic conditions afforded the amine **IV-17**.



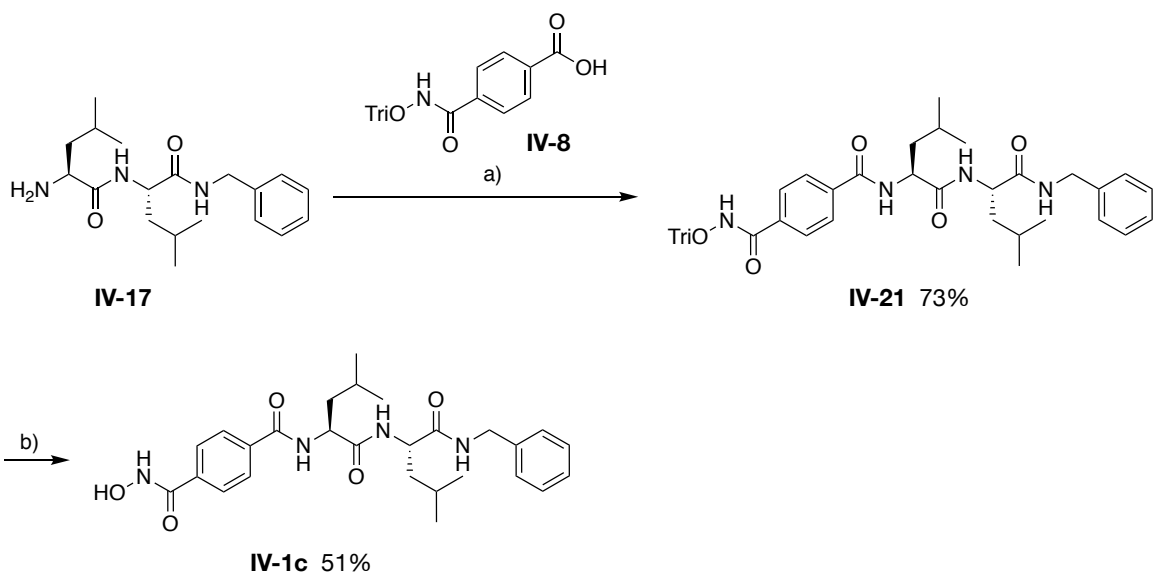
**Scheme 4.4.** Synthesis of the P1-3 scaffold **IV-17**. Reagents and conditions: a) Isobutyl chloroformate, NMM, THF, 0 °C to rt, 16 h; b) TFA, DCM, rt, 3 h.

First attempts to generate the desired hydroxamic acids from the corresponding esters failed for most compounds and yielded large amounts of the respective carboxylic acid byproducts, in spite of the optimised reaction conditions described in chapters 2 and 3. Alternative routes towards the formation of hydroxamic acids include the introduction of masked hydroxylamines, such as *O*-benzylhydroxylamine, *O*-THP-hydroxylamine, and *O*-tritylhydroxylamine, which are easily accessible via modified Gabriel reactions using *N*-hydroxyphthalimide and halogenated or electrophilic precursors for the desired amine residues (Martin et al. 2006). Once introduced, the protecting groups can be removed to release the hydroxamates by means of hydrogenolysis or acidic cleavage, respectively. The original RTS-V5 was prepared by Pd-catalysed hydrogenolysis of the benzyl-protected precursor, but for the MG-132 scaffold, this method turned out to be unreliable or, in the case of the olefine **IV-1b**, inapplicable. Instead, the trityl-protecting group was chosen as the most suitable alternative. Starting from **IV-17**, the respective linker fragments **IV-3**, **IV-5**, and **IV-8** were attached under HATU conditions (Schemes 4.5 & 4.6).



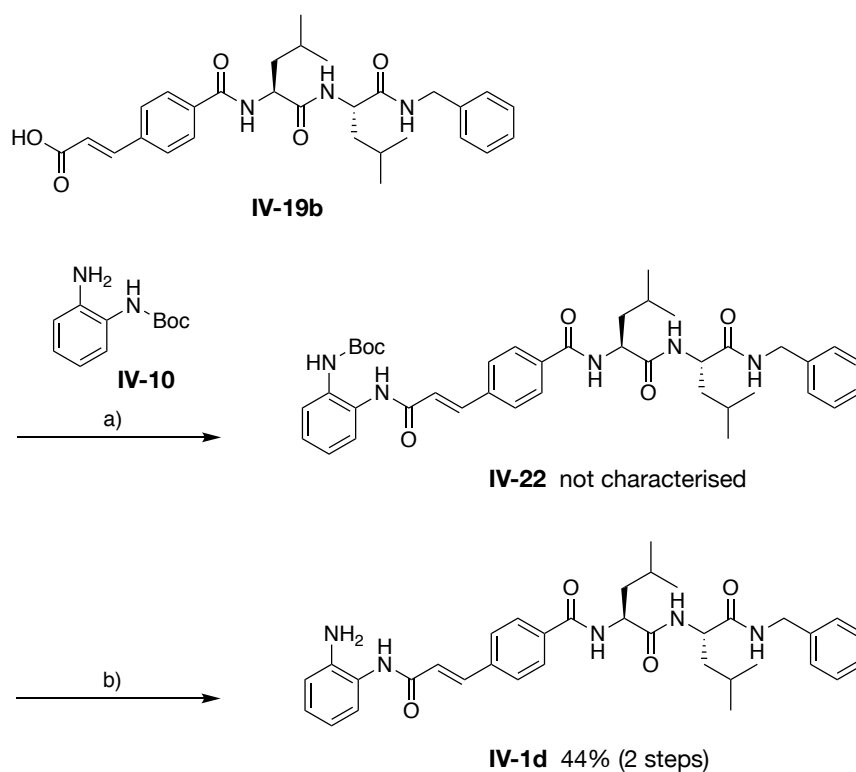


**Scheme 4.5.** Synthesis of compounds **IV-1a** and **IV-1b**. Reagents and conditions: a) HATU, DIPEA, DMF, rt, 18–24 h; b) NaOH, THF/H<sub>2</sub>O, rt, 24 h; c) O-tritylhydroxylamine, HATU, DIPEA, DMF, rt, 24–27 h; d) 1% TFA in DCM, rt, 15–20 min.



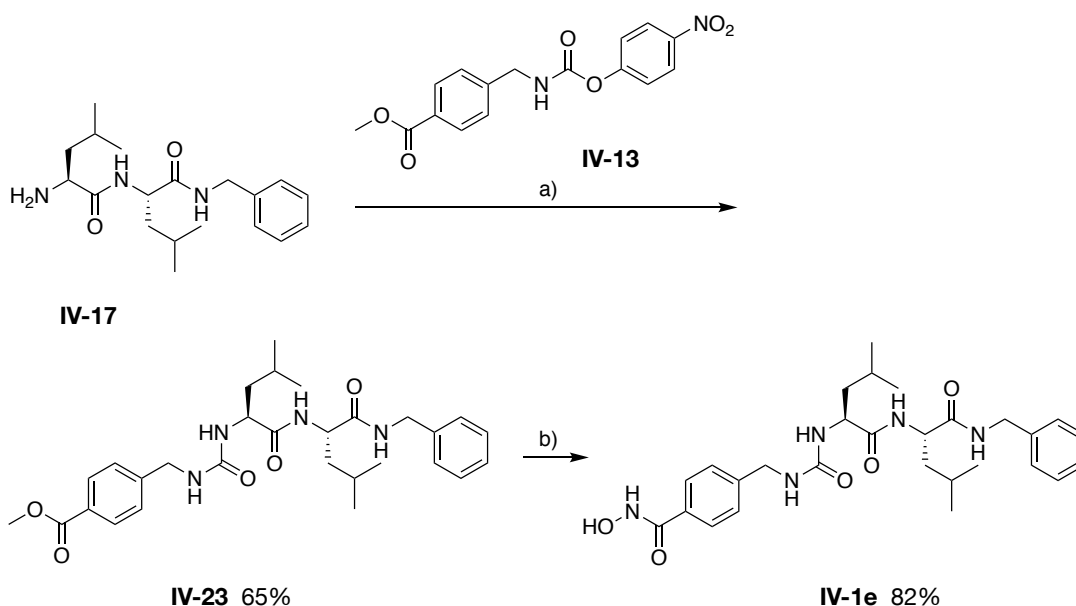
**Scheme 4.6.** Synthesis of compound **IV-1c**. Reagents and conditions: a) HATU, DIPEA, DMF, rt, 42 h; b) 1% TFA in DCM, rt, 10 min.

The esters **IV-18a** and **IV-18b** were hydrolysed using sodium hydroxide, whereupon the trityl-protecting group could be introduced via HATU-assisted coupling reactions yielding **IV-19a-b** (Scheme 4.5). The trityl-protected linker **IV-8** required for the formation of **IV-21** had been prepared beforehand (Schemes 4.3 & 4.6). Finally, all trityl-protected hydroxamic acids were released by treatment with 1% trifluoroacetic acid (TFA) in dichloromethane and isolated by precipitation from a neutralised aqueous solution (Schemes 4.5 & 4.6). It has been suggested to perform trityl-removal reactions in presence of triisopropylsilane (TIPS) or other silane-based scavengers that are supposed to bind the trityl carbocation byproduct, but due to the limited purification options for the poorly soluble and sensitive hydroxamates, no additives were used (Pearson et al. 1989).



**Scheme 4.7.** Synthesis of compound **IV-1d**. Reagents and conditions: a) HATU, DIPEA, DMF, rt, 24 h; b) TFA, DCM, rt, 3 h.

The *ortho*-aminoanilide **IV-1d** was synthesised by coupling **IV-19b** with **IV-10** and subsequent Boc-removal in presence of TFA (Scheme 4.7). The methyl ester **IV-23** was treated with a mixture of aqueous hydroxylamine and sodium hydroxide to generate the corresponding hydroxamic acid **IV-1e** which was also precipitated from water (Scheme 4.8). On the whole, all compounds were obtained in pleasing overall yields and exceeded purities of 95% after recrystallisation.



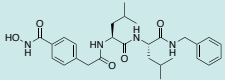
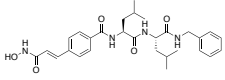
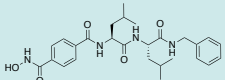
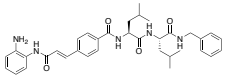
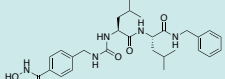
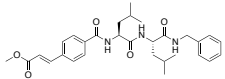
**Scheme 4.8.** Synthesis of compound **IV-1e**. Reagents and conditions: a) Et<sub>3</sub>N, THF, MW, 70 °C, 150 W, 2 h; b) NaOH, NH<sub>2</sub>OH (50% solution in water), MeOH/DCM, 0 °C, 2 h.

#### 4.2.2 1<sup>st</sup> Generation: Enzyme inhibition

**HDAC inhibition.** Biochemical assays using the MG-132 analogues (Table 4.1) implicated moderate HDAC6 inhibition for all compounds except **IV-1a** (IC<sub>50</sub> HDAC6: 0.539 μM).<sup>16</sup> As expected, **IV-1d** was inactive towards HDAC6 (IC<sub>50</sub>: < 10 μM) but surprisingly, it showed no significant inhibition of HDAC1 (IC<sub>50</sub>: 1.34 μM) either. RTS-V5 (IC<sub>50</sub> HDAC1: 2.31 μM; HDAC6: 0.413 μM) and **IV-1c** (IC<sub>50</sub> HDAC1: 1.91 μM; HDAC6: 0.361 μM) share identical linker motifs; by comparison, however, it becomes obvious that the MG-132-based scaffold is more suitable for inhibition of both HDACs while the selectivity profile (SI: 5.6 vs. 5.3) remains unaffected. The non-selective ligand **IV-1b** displayed promising inhibition of both HDAC1 (IC<sub>50</sub>: 0.099 μM) and HDAC6 (IC<sub>50</sub>: 0.138 μM) with the latter only being outmatched by the urea-derivative **IV-1e** (IC<sub>50</sub> HDAC6: 0.122 μM). Despite being equally selective (SI: 5.5 vs. 5.6), **IV-1e** tripled the HDAC6 inhibition of RTS-V5. Overall, three of the five compounds were superior to RTS-V5 in terms of HDAC inhibition; however, neither of the screened inhibitors matched the potential of the control drug vorinostat.

<sup>16</sup> HDAC and proteasome inhibition assays were performed by Andrea Schöler in the group of Finn K. Hansen, Leipzig University.

**Table 4.1.** Inhibitory activities of compounds **IV-1a-e** and **IV-18b** against HDAC1 and HDAC6. Vorinostat was used as control.

Compound	Structure	HDAC1 IC <sub>50</sub> [μM]	HDAC6 IC <sub>50</sub> [μM]	SI <sup>a</sup>
RTS-V5	-	2.31 ± 0.04	0.413 ± 0.038	5.6
<b>IV-1a</b>		3.31 ± 0.31	0.539 ± 0.169	6.1
<b>IV-1b</b>		0.099 ± 0.010	0.138 ± 0.014	0.7
<b>IV-1c</b>		1.91 ± 0.08	0.361 ± 0.016	5.3
<b>IV-1d</b>		1.34 ± 0.27	> 10	-
<b>IV-1e</b>		0.672 ± 0.043	0.122 ± 0.006	5.5
<b>IV-18b</b>		> 10	> 10	-
Vorinostat	-	0.118 ± 0.014	0.044 ± 0.011	2.7

<sup>a</sup> Selectivity index (SI = IC<sub>50</sub> (HDAC1)/IC<sub>50</sub> (HDAC6)).

**Proteasome inhibition.** The proteasome inhibition was quantified by measuring the remaining proteasomal activity of the 20S β5c subunit after incubation with different inhibitors at concentrations of 100 nM (Figure 4.11).<sup>16</sup> Inactive against HDAC isoforms, the ester **IV-18b** was used as a control in order to elucidate the proteasome inhibition of the scaffold in absence of a ZBG. As a result, **IV-18b** reduced the proteasome activity by 33%, whereas incubation with the 20S CPi MG-132 (6%) and bortezomib (2%) nearly eradicated the entire proteasomal function in comparison to the blank control. Incubation with RTS-V5 reduced the 20S β5c activity by 64% and was therefore potent but far less effective than the established 20S CPi. Ranging between remaining proteasomal functions of 81% and 94%, none of the MG-132-derived dual inhibitors reached the inhibitory quality of RTS-V5 after the same incubation time. Thus, the new generation of compounds must be considered ineffective in terms of proteasome inhibition. Interestingly, **IV-1c** (94%) had the lowest impact on 20S β5c function, despite being more similar to RTS-V5 than the other derivatives. Impairing the remaining proteasome activity by 19%, compound **IV-1e** stood out as the most effective new 20S CPi of this set.

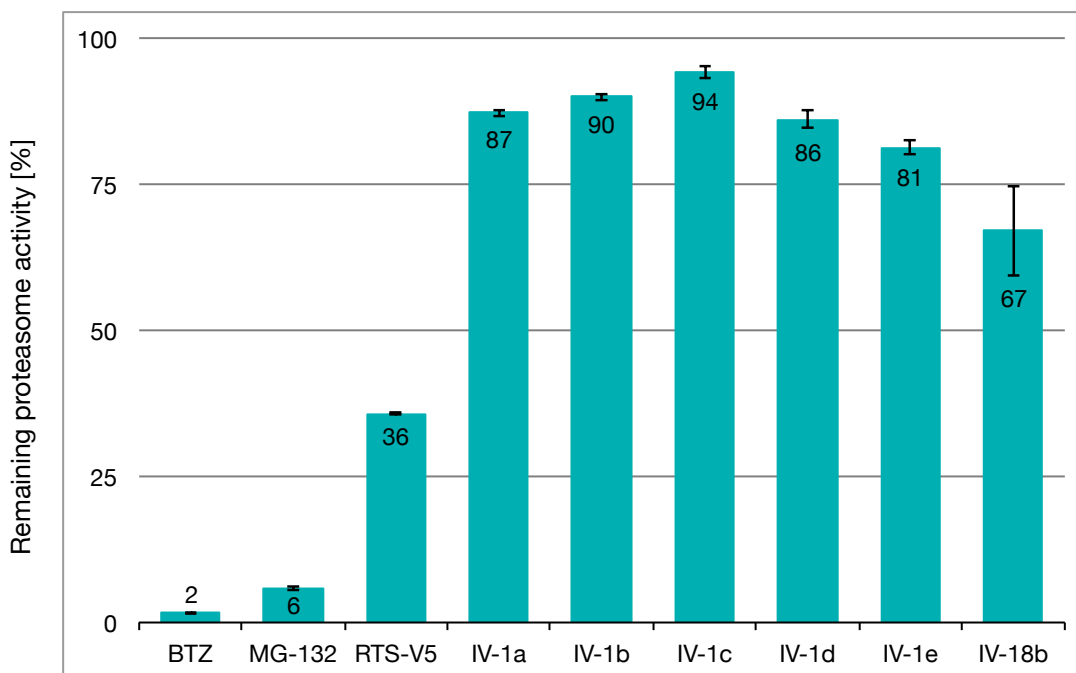


**Figure 4.11.** Remaining activity [%] of the  $\beta 5c$  subunit at  $C_{\text{inhibitor}} = 100$  nM. Bortezomib (BTZ), MG-132, and RTS-V5 were used as controls.

#### 4.2.3 1<sup>st</sup> Generation: Antiproliferative effects

Six different leukaemia cell lines were selected to investigate the antiproliferative effects of the MG-132-based dual inhibitors (Table 4.2); the 20S CPi bortezomib and MG-132 and the HDAC6i ricolinostat were used as controls.<sup>17</sup> Lacking a ZBG, the ester **IV-18b** happens to be inactive towards HDACs and was thus considered as a negative control in order to determine the cytotoxic potential of proteasome inhibition alone. Although none of the new compounds could compete with MG-132 and bortezomib, it is striking that **IV-1b** exhibited higher cytotoxicity than all other dual inhibitors and ricolinostat. The cytotoxicity of **IV-1b** also exceeded the  $IC_{50}$  values of the corresponding ester **IV-18b**, which had previously turned out to be the stronger proteasome inhibitor. The remarkable effect observed for **IV-1b** is thus likely to result from non-selective inhibition of several HDACs, including HDAC6 and the class I isoforms. Screened against the bortezomib-resistant HL-60R cell line, **IV-1b** ( $IC_{50}$ : 1.64  $\mu\text{M}$ ) appeared nearly as effective as MG-132 ( $IC_{50}$ : 1.31  $\mu\text{M}$ ), but in non-resistant HL-60 cells, the activities of MG-132 ( $IC_{50}$ : 0.219  $\mu\text{M}$ ) and **IV-1b** ( $IC_{50}$ : 1.97  $\mu\text{M}$ ) differed by a factor of nine. This observation is consistent with the recent suggestion that bortezomib-resistance may be driven by overexpression of HDAC1 (Zhou et al. 2020). The necessity to address class I

<sup>17</sup> Cytotoxicity screenings were performed by Melf Sönnichsen in the group of Sanil Bhatia, HHU Düsseldorf.

HDACs is further emphasised by the fact that the class I-selective dual inhibitor **IV-1d** succeeds **IV-1b** in terms of cytotoxicity, regardless of the poor inhibitory qualities against both the proteasome and HDAC1 in biochemical assays. Compound **IV-1e**, in turn, exhibited superior inhibition but had surprisingly little effect on either of the selected cell lines. With **IV-1a** and **IV-1c** turning out to be virtually inactive in this assay, there are no analogues with remarkable antiproliferative properties except **IV-1b**.

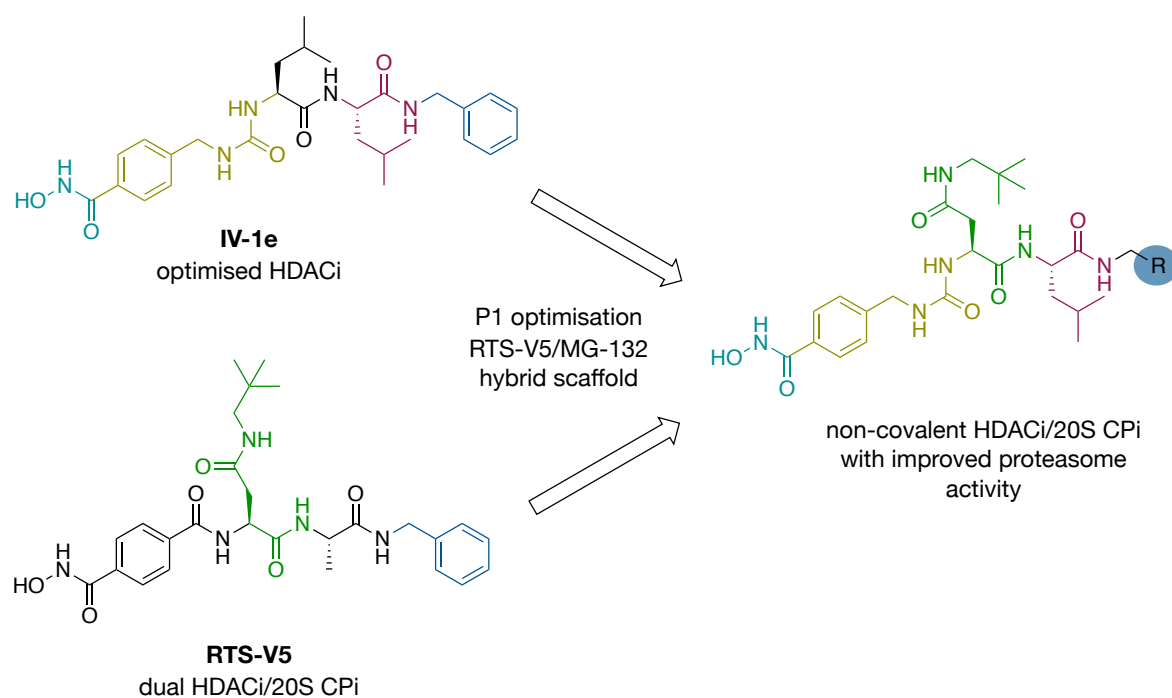
**Table 4.2.** Cytotoxicities of compounds **IV-1a-e** and **IV-18b** against selected leukaemia cell lines. Ricolinostat, bortezomib, and MG-132 were used as controls.

Compound	HL-60 IC <sub>50</sub> [μM]	HL-60R IC <sub>50</sub> [μM]	THP-1R IC <sub>50</sub> [μM]	SUP-B15 IC <sub>50</sub> [μM]	MV4-11 IC <sub>50</sub> [μM]	MOLM-13 IC <sub>50</sub> [μM]
<b>IV-1a</b>	> 25	20.2 ± 2.07	> 25	> 25	> 25	> 25
<b>IV-1b</b>	1.97 ± 0.09	1.64 ± 0.17	7.41 ± 0.56	1.32 ± 0.06	0.781 ± 0.050	1.44 ± 0.05
<b>IV-1c</b>	> 25	15.2 ± 0.64	> 25	13.2 ± 0.38	15.8 ± 0.34	20.9 ± 0.87
<b>IV-1d</b>	6.66 ± 0.63	15.4 ± 0.62	> 25	5.29 ± 0.27	5.58 ± 0.08	10.1 ± 0.44
<b>IV-1e</b>	7.91 ± 0.93	5.94 ± 0.88	> 25	7.59 ± 0.10	11.8 ± 0.91	19.8 ± 0.58
<b>IV-18b</b>	3.26 ± 0.77	> 25	> 25	2.36 ± 0.38	3.22 ± 0.16	6.59 ± 0.45
Ricolinostat	3.96 ± 0.24	4.63 ± 0.20	9.77 ± 0.23	2.31 ± 0.27	1.54 ± 0.06	3.00 ± 0.25
Bortezomib	0.0005 ± 0.00002	0.006 ± 0.0002	> 0.01	0.0004 ± 0.00001	0.0007 ± 0.00001	0.0009 ± 0.00004
MG-132	0.219 ± 0.021	1.31 ± 0.05	1.65 ± 0.005	0.157 ± 0.027	0.155 ± 0.014	0.215 ± 0.026

HL-60: human acute myeloid leukaemia cell line; HL-60R: bortezomib-resistant human acute myeloid leukaemia cell line; THP-1R: bortezomib-resistant monocytic leukaemia cell line; SUP-B15: human acute lymphoblastic leukaemia cell line; MV4-11: human acute myeloid leukaemia cell line; MOLM-13: human acute myeloid leukaemia cell line.

#### 4.2.4 1<sup>st</sup> Generation: Discussion

Both enzyme inhibition assays presented **IV-1e** as the most promising compound. In respect of cytotoxicity against HL-60 cells, compound **IV-1b** was the only analogue exhibiting sufficient potential. Considering the poor proteasome inhibition observed for **IV-1b**, the cytotoxic effects are most likely a result of potent and non-selective HDAC inhibition. In conclusion, it is obvious that the set of MG-132-derived analogues did not reach the potential of RTS-V5 due to insufficient 20S CP inhibition. It did, however, yield a linker moiety allowing for improved HDAC inhibition and low isoform selectivity as a possible means to overcome bortezomib-resistance (Zhou et al. 2020). From this starting point, the synthesis of a second generation of analogues combining structural features of RTS-V5 and **IV-1e** (Scheme 4.9) was attempted to improve the inhibition of the 20S β5c subunit.



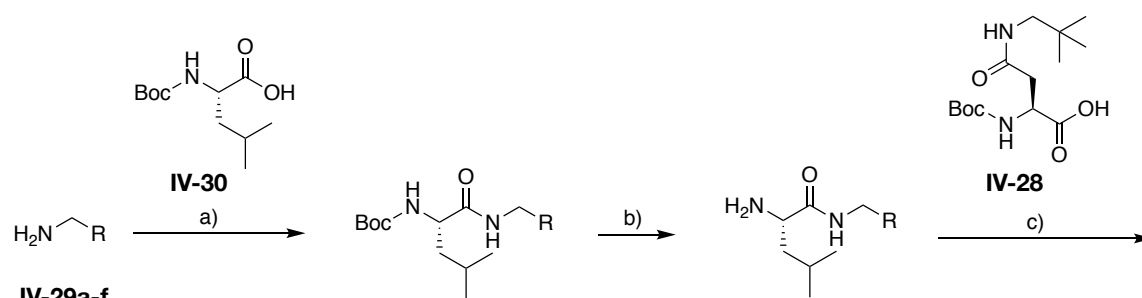
**Scheme 4.9.** Design of new dual HDACi/20S CPI inspired by RTS-V5 and compound **IV-1e** featuring an improved HDAC binding site.

#### 4.2.5 2<sup>nd</sup> Generation: Design and synthesis

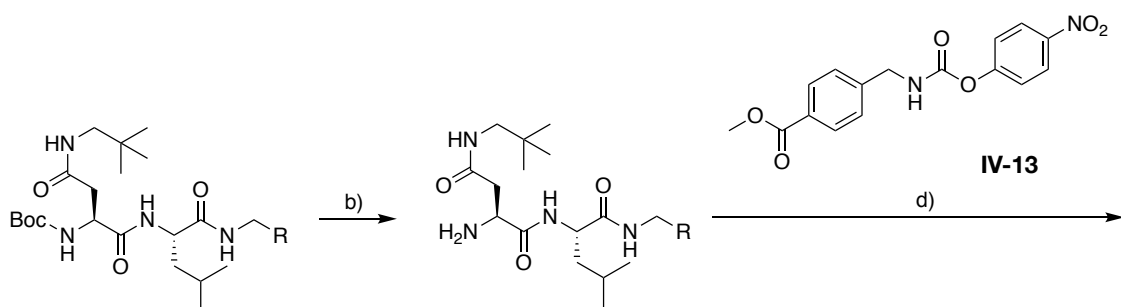
Merging the scaffolds of **IV-1e** and RTS-V5, the second generation of dual inhibitors was built around a neopentylamide group in P3 and the optimised urea-linker moiety in P4. In place of the alanine featured in RTS-V5, all analogues (Figure 4.12) were to comprise the MG-132-derived leucine group in position P2 as this residue is common in several established 20S CPI (Huber & Groll 2012). With the intention to explore steric characteristics and hydrophobic interactions with surrounding residues in the active site, different P1 groups were selected for an SAR study in which the non-covalent, aromatic nature of the previous P1 was to be retained. Designed as a control against previous dual agents, **IV-24a** featured the hitherto employed benzyl group in P1. Inspired by ML-16, two halogenated analogues carrying either a 2-fluorobenzyl (**IV-24b**) or a 2-chlorobenzyl (**IV-24c**) group were also included (Blackburn et al. 2010a). The *para*-methylbenzyl motif of **IV-24d** was chosen because earlier studies by Blackburn suggested increased target affinity for such compounds; an additional picolyl derivative (**IV-24e**) was supposed to help explore the effect of P1 hydrogen bond acceptors (Blackburn et al. 2010a; Blackburn et al. 2010b; Blackburn et al. 2012). **IV-24e** was moreover expected to tackle solubility issues that had emerged as a common drawback of this class of compounds. With reference to works by Blackburn and



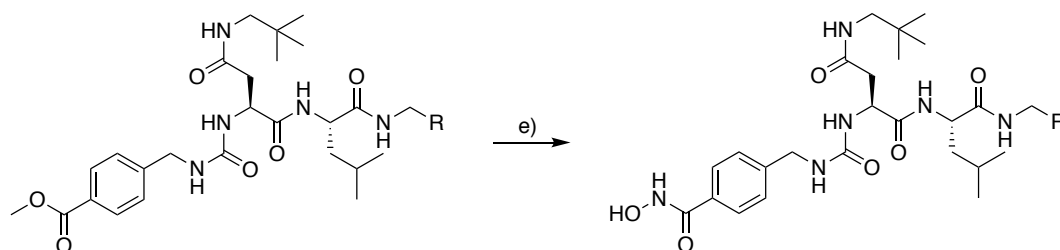




**IV-31a:** 76% **IV-31d:** 83% **IV-32a:** 83% **IV-32d:** 93%  
**IV-31b:** 73% **IV-31e:** 96% **IV-32b:** 75% **IV-32e:** 92%  
**IV-31c:** 78% **IV-31f:** 90% **IV-32c:** 98% **IV-32f:** 91%

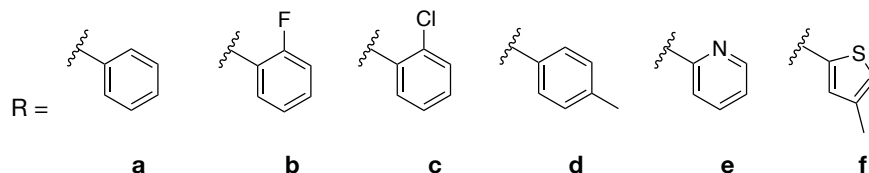


**IV-34a:** 93% **IV-34d:** 86%  
**IV-34b:** 77% **IV-34e:** 92%  
**IV-34c:** 97% **IV-34f:** 80%



**IV-35a:** 37% **IV-35d:** 36%  
**IV-35b:** 30% **IV-35e:** 21%  
**IV-35c:** 17% **IV-35f:** 10%

**IV-24a:** 52% **IV-24d:** 55%  
**IV-24b:** 50% **IV-24e:** 41%  
**IV-24c:** 59% **IV-24f:** 50%



**Scheme 4.11.** Synthesis of compounds **IV-24a-f**. Reagents and conditions: a) Isobutyl chloroformate, NMM, THF, 0 °C to rt, 16 h; b) TFA, DCM, rt, 3 h; c) HATU, DIPEA, DMF, rt, 48 h; d) Et<sub>3</sub>N, THF, MW, 70 °C, 150 W, 2 h; e) NaOH, NH<sub>2</sub>OH (50% solution in water), MeOH/DCM, 0 °C, 2–4 h.

group were obtained by HATU-mediated coupling reactions with **IV-28**. This reagent was chosen since prior scouting experiments using alternative coupling agents, like isobutyl chloroformate and 1-ethyl-3-(3-dimethylaminopropyl)carbodiimide (EDC), failed to provide similar products in sufficient yields. Upon successful amide formation, the Boc groups were directly removed under acidic conditions. The introduction of the aforementioned urea-linker precursor **IV-13** was achieved by microwave irradiation but did not exceed low to moderate yields of 10–37% for **IV-35a-f**. Except for **IV-35e** and **IV-35f** which could be isolated via column chromatography, this reaction generally afforded insoluble compounds that were isolated by filtration. The purification was accomplished by careful washing of the crude solids with 10% citric acid followed by saturated sodium bicarbonate solution and subsequent recrystallisation. HPLC analysis of the esters **IV-35a-f** was necessary because owing to the poor solubility and resulting lack of purification options, the final reaction step required highly pure starting materials. The hydroxylaminolysis was performed using sodium hydroxide and aqueous hydroxylamine. TLC control of the reaction mixture was carried out to ensure complete consumption of the starting material which, otherwise, could not have been separated from the final products.

Upon completion of the reaction, the hydroxamic acids **IV-24a-f** were precipitated from water. Small amounts of the corresponding carboxylic acids that emerged as byproducts in some reactions were removed by filtration over a thin layer of ISOLUTE PE-AX<sup>®</sup> (Riva et al. 2009). Subsequent recrystallisation finally afforded all six hydroxamates in purities of at least 95%.

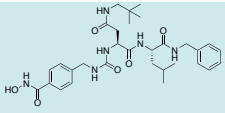
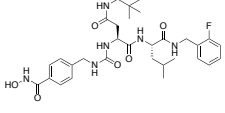
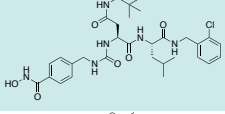
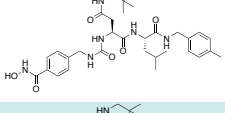
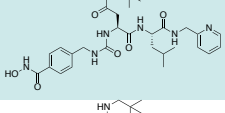
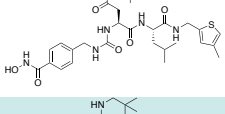
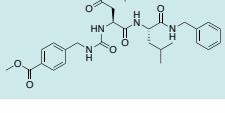
#### 4.2.6 2<sup>nd</sup> Generation: Enzyme inhibition

**HDAC inhibition.** In comparison to the MG-132 derivatives, it is apparent that the second set of RTS-V5 analogues is slightly more HDAC6-preferential, with selectivity indices ranging from 6.6 to 9.8 (Table 4.3).<sup>18</sup> The highest inhibition ( $IC_{50}$  HDAC6: 0.146  $\mu$ M) and the second highest HDAC6 selectivity (SI: 8.0) were measured for the P1 benzyl derivative **IV-24a** which was nearly as active as the two most potent MG-132 analogues, **IV-1b** ( $IC_{50}$  HDAC6: 0.099  $\mu$ M) and **IV-1e** ( $IC_{50}$  HDAC6: 0.122  $\mu$ M). The most selective compound **IV-24c** (SI: 9.8) exhibited the lowest inhibitory activities ( $IC_{50}$  HDAC1: 3.20  $\mu$ M; HDAC6  $IC_{50}$ : 0.328  $\mu$ M) but still exceeded the HDAC6 inhibition of RTS-V5 ( $IC_{50}$  HDAC1: 2.31  $\mu$ M; HDAC6: 0.413  $\mu$ M).

---

<sup>18</sup> HDAC and proteasome inhibition assays were performed by Andrea Schöler in the group of Finn K. Hansen, Leipzig University.

**Table 4.3.** Inhibitory activities of compounds **IV-24a-f** and **IV-35a** against HDAC1 and HDAC6. Vorinostat was used as control.

Compound	Structure	HDAC1 IC <sub>50</sub> [μM]	HDAC6 IC <sub>50</sub> [μM]	SI <sup>a</sup>
RTS-V5	-	2.31 ± 0.04	0.413 ± 0.038	5.6
IV-24a		1.17 ± 0.003	0.146 ± 0.029	8.0
IV-24b		1.97 ± 0.05	0.241 ± 0.046	8.2
IV-24c		3.20 ± 0.32	0.328 ± 0.037	9.8
IV-24d		2.31 ± 0.12	0.266 ± 0.021	8.7
IV-24e		1.58 ± 0.01	0.238 ± 0.036	6.6
IV-24f		1.39 ± 0.10	0.190 ± 0.009	7.3
IV-35a		> 10	> 10	-
Vorinostat	-	0.118 ± 0.014	0.044 ± 0.011	2.7

<sup>a</sup> Selectivity index (SI = IC<sub>50</sub> (HDAC1)/IC<sub>50</sub> (HDAC6)).

Failing to provide any new leads in the low nanomolar concentration range, the second generation of dual ligands displays overall higher HDAC inhibition than the first set of compounds. Considering that the structural alterations in this set merely concerned the P1 position lying opposite the designated HDAC binding site, it is striking that increasing P1 residue sizes entail decreased HDAC inhibition. This hints at unfavourable steric effects in the cap group region that may impair the occupation of the zinc-binding sites. Obviously affecting HDAC1 more than HDAC6, this phenomenon is consistent with the observation that the entry area of HDAC6 is more spacious than those of other isoforms (Hai & Christianson 2016).

**Proteasome inhibition.** The results of the proteasome inhibition assays are illustrated in Figure 4.13.<sup>18</sup> Having emerged as the weakest HDACi of the second set, compound **IV-24c** clearly induced the highest proteasome inhibition; the remaining enzyme activity of 42% nearly equals the inhibition measured for RTS-V5 (36%). This result complies with a study by Blackburn et al. who identified compound ML-16 featuring an identical 2-chlorobenzyl residue as a hit compound (Blackburn et al. 2010a). The methylthiophene derivative **IV-24f**, which displayed considerable HDAC inhibition, was slightly less active than **IV-24c** (47%), yet suppressing more than half of the proteasomal activity. Incubation with the other dual ligands reduced the 20S  $\beta$ 5c activity by only 6–32% and among those, the P1 benzyl derivative **IV-24a** and the picolyl analogue **IV-24e** turned out to be the least effective inhibitors. Regarding the halogenated derivatives, it is apparent that the replacement of the chlorine substituent by fluorine (**IV-24b**) accounts for a 34% loss in inhibition, with 76% enzyme activity remaining unaffected. Thus, it could be concluded that the existence of a hydrogen bond acceptor has no beneficial effect on proteasome inhibition, whereas a rather large substituent in position 2 of the benzyl group seems to increase the affinity to the S1 binding pocket. However, this assumption collides with the fact that the more potent RTS-V5 features an unsubstituted benzyl group and more clarity in this point would require the analysis of a chlorinated RTS-V5 analogue based on the original scaffold. In spite of both sites being presumably solvent-exposed, the inferior proteasome inhibition of **IV-24a**

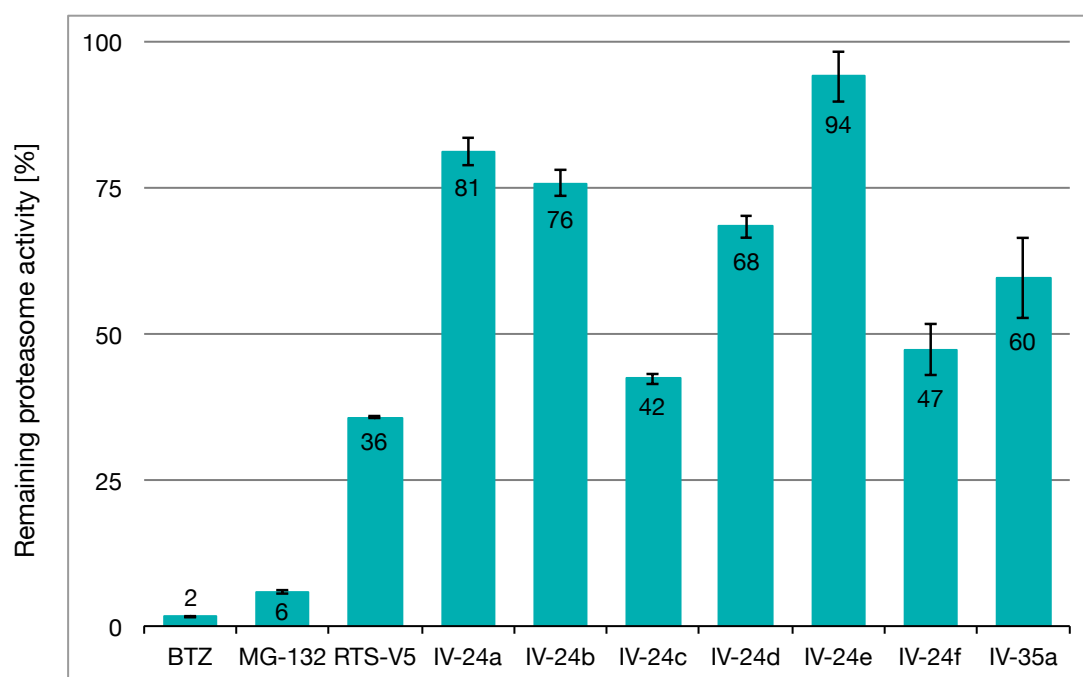


**Figure 4.13.** Remaining activity [%] of the  $\beta$ 5c subunit at  $C_{\text{inhibitor}} = 100$  nM. Bortezomib (BTZ), MG-132, and RTS-V5 were used as controls.

compared to RTS-V5 is likely to result from either the replacement of the P4 linker moiety or the exchange of the P2 residue, since the compounds are otherwise identical. The *para*-methyl substituent present in **IV-24d** appears to increase the inhibitory potential more than the fluorine residue of compound **IV-24b** and the superior inhibition by **IV-24f** suggests an overall beneficial effect of methyl groups opposite the peptide chain. Due to the different shapes of phenyl and thienyl residues and the lack of an unsubstituted thienyl derivative, however, such conclusions cannot be drawn with certainty.

**Table 4.4.** Cytotoxicities of compounds **IV-24a-f** and **IV-35a** against HL-60 and bortezomib-resistant HL-60R cell lines. Ricolinostat, bortezomib, MG-132, and RTS-V5 were used as controls.

Compound	HL-60 IC <sub>50</sub> [μM]	HL-60R IC <sub>50</sub> [μM]
<b>IV-24a</b>	10.3 ± 0.48	> 25
<b>IV-24b</b>	4.74 ± 0.27	> 25
<b>IV-24c</b>	5.47 ± 0.55	> 25
<b>IV-24d</b>	2.01 ± 0.20	> 25
<b>IV-24e</b>	> 25	> 25
<b>IV-24f</b>	4.40 ± 0.63	> 25
<b>IV-1b</b>	2.16 ± 0.41	1.40 ± 0.36
<b>IV-35a</b>	0.910 ± 0.089	> 25
RTS-V5	2.69 ± 0.12	> 25
Ricolinostat	5.73 ± 0.07	1.50 ± 0.02
Bortezomib	0.005 ± 0.0006	0.030 ± 0.009
MG-132	0.139 ± 0.026	1.20 ± 0.07

HL-60: human acute myeloid leukaemia cell line;  
HL-60R: bortezomib-resistant human acute myeloid leukaemia cell line.

#### 4.2.7 2<sup>nd</sup> Generation: Antiproliferative effects

The cytotoxic potential against leukaemia cells was first measured in HL-60 cells; ricolinostat, bortezomib, MG-132, and RTS-V5 were used as controls (Table 4.4). Comprising no ZBG, the benzyl analogue **IV-35a** (IC<sub>50</sub>: 0.910 μM) was selected to evaluate the antiproliferative potential of the 20S CPI scaffold alone and turned out to be almost threefold more active than the control RTS-V5 (IC<sub>50</sub>: 2.69 μM). In presence of a ZBG, however, the activity diminished by a factor of ten which makes the corresponding dual ligand **IV-24a** (IC<sub>50</sub>: 10.3 μM) the weakest compound beside the virtually inactive picolyl analogue **IV-24e** (IC<sub>50</sub>: > 25 μM). The only promising hydroxamate singled out from this set was **IV-24d** (IC<sub>50</sub>:

2.01 μM) which exerted higher activity than both RTS-V5 and **IV-1b** (IC<sub>50</sub>: 2.16 μM), the latter of which serving as a reference from the first generation. Albeit exhibiting lower antiproliferative potential on HL-60 cells, **IV-24f** (IC<sub>50</sub>: 4.40 μM) and **IV-24c** (IC<sub>50</sub>: 5.47 μM) were also picked for further experiments on different cell lines as they happened to be the most potent 20S CPI. Due to the low IC<sub>50</sub> of 4.74 μM, **IV-24b** was excluded from further assays. Probably resulting from the poor HDAC1 inhibition, none of the ML-16-derived dual agents had any effect on bortezomib-resistant HL-60 cells. Treatment with **IV-1b** (IC<sub>50</sub>:

1.40  $\mu\text{M}$ ), on the other hand, was even more effective than in regular HL-60 cells ( $\text{IC}_{50}$ : 2.16  $\mu\text{M}$ ).

**Table 4.5.** Cytotoxicities of compounds **IV-24c**, **IV-24d**, **IV-24f**, and **IV-1b** against four patient-derived AML cell lines and HAL-01. Ricolinostat, bortezomib, MG-132, and RTS-V5 were used as controls.

Compound	AML 981 $\text{IC}_{50}$ [ $\mu\text{M}$ ]	AML 579 $\text{IC}_{50}$ [ $\mu\text{M}$ ]	PA AML $\text{IC}_{50}$ [ $\mu\text{M}$ ]	393 $\text{IC}_{50}$ [ $\mu\text{M}$ ]	HAL-01 $\text{IC}_{50}$ [ $\mu\text{M}$ ]
<b>IV-24c</b>	10.4 $\pm$ 1.63	> 25	3.15 $\pm$ 0.39	24.1 $\pm$ 1.00	2.57 $\pm$ 0.09
<b>IV-24d</b>	11.4 $\pm$ 1.17	> 25	1.98 $\pm$ 0.07	> 25	1.41 $\pm$ 0.13
<b>IV-24f</b>	17.9 $\pm$ 1.32	> 25	5.89 $\pm$ 0.10	> 25	4.31 $\pm$ 0.55
<b>IV-1b</b>	5.09 $\pm$ 0.24	1.40 $\pm$ 0.08	8.00 $\pm$ 0.72	1.21 $\pm$ 0.08	1.82 $\pm$ 0.32
RTS-V5	10.7 $\pm$ 0.57	> 25	7.08 $\pm$ 0.54	> 25	2.02 $\pm$ 0.07
Ricolinostat	6.79 $\pm$ 0.24	1.50 $\pm$ 0.02	11.7 $\pm$ 0.26	2.21 $\pm$ 0.23	5.30 $\pm$ 0.29
Bortezomib	0.006 $\pm$ 0.0005	0.030 $\pm$ 0.007	0.002 $\pm$ 0.0001	0.007 $\pm$ 0.0003	0.006 $\pm$ 0.0006
MG-132	0.518 $\pm$ 0.030	1.20 $\pm$ 2.25	0.298 $\pm$ 0.005	0.432 $\pm$ 0.058	0.187 $\pm$ 0.024

AML 981, AML 579, PA AML, 393: patient-derived acute myeloid leukaemia cell lines; HAL-01: B-cell acute lymphoblastic leukaemia cell line.

In a second cytotoxicity assay against selected leukaemia cell lines (Table 4.5), **IV-1b** continued to be the most promising compound, thereby exceeding the  $\text{IC}_{50}$  values of ricolinostat throughout all cell lines. The activities of **IV-24c** and **IV-24d** lay within the range of RTS-V5. Screened against HAL-01 and patient-derived PA AML cells, **IV-24d** ( $\text{IC}_{50}$ : 1.41  $\mu\text{M}$ ; 1.98  $\mu\text{M}$ ) appeared even more potent than both RTS-V5 ( $\text{IC}_{50}$ : 2.02  $\mu\text{M}$ ; 7.08  $\mu\text{M}$ ) and **IV-1b** ( $\text{IC}_{50}$ : 1.82  $\mu\text{M}$ ; 8.00  $\mu\text{M}$ ). Compound **IV-24f**, in contrast, did not exhibit any striking activity. Noteworthy, none of the dual inhibitors matched the antiproliferative potential of MG-132 or bortezomib in either assay.<sup>19</sup>

#### 4.2.8 2<sup>nd</sup> Generation: Discussion

According to the available data, it is clear that the primary goal of improving the HDAC affinity in comparison to RTS-V5 was met by all compounds of both sets. The fact that the best HDACi (**IV-24a**) proved to be the weakest 20S CPi, whereas the most promising 20S CPi (**IV-24c**) acted as a poor HDACi suggests that an increase in inhibition of one target

<sup>19</sup> Both cytotoxicity assays were performed by Melf Sönnichsen in the group of Sanil Bhatia, HHU Düsseldorf.

counteracts the addressing of the other. As a consequence, none of the dual agents capable of improved HDAC inhibition emerged as a stronger 20S CPi than RTS-V5. Since the structural modifications in the second generation were limited to variations of the aromatic P1 residue on the proteasome binding site, it is likely that sterical hindrance in this area impaired the HDAC inhibition. This assumption concurs with the fact that the two compounds with the smallest P1 groups, the benzyl derivative **IV-24a** and the thienyl analogue **IV-24f**, were the strongest HDACi. As to the 20S CPi scaffold, it is obvious that the incorporation of the urea linker and the replacement of the P2 alanine by leucine reduced the proteasome inhibition for **IV-24a** by nearly one half compared to RTS-V5. The observation that the remaining proteasome activity of the ester **IV-35a** was only 24% lower than after incubation with RTS-V5 further implies that the loss of activity stems from the nature of the new linker moieties as well as the correlating final position of the hydroxamate group. Instead of P4, the positioning of the HDAC binding-site in a different solvent-exposed position, e.g. P2, could be attempted to circumvent the apparent complications due to incongruent pharmacophores.

Despite identical levels of low HDAC1 inhibition and a decrease in proteasome inhibition by nearly one half, **IV-24d** was found to be equally or even more potent against tumour cell lines than RTS-V5. A slight increase in both inhibition and selectivity for HDAC6 could thus have a boosting effect on cytotoxicity. If this phenomenon is a result of increased aggresome formation would need to be verified by additional assays. Although emerging as the only compound combining considerable inhibition of both HDAC6 and the 20S CP with significantly higher inhibition of HDAC1 than RTS-V5, **IV-24f** demonstrated the weakest antiproliferative potential. The fact that the pan-HDACi but poor 20S CPi **IV-1b** and the mere 20S CPi **IV-35a** expressed the highest anticancer activities could inspire the conclusion that occupation of either single target is more effective than addressing the synergism through simultaneous inhibition. However, it should be considered that the 20S CPi ligands are non-covalent by design and thus, it seems equally possible that the strong binding nature of the hydroxamate-zinc interaction suppresses sufficient 20S CP inhibition. Such unfavourable distribution between the two targets could limit the effectiveness of the proteasome-aggresome synergism and might be avoided by designing dual ligands with a reversible covalent warhead within the 20S CPi scaffold. With reference to the recent report by Fang and co-workers, it can be assumed that covalent 20S CPi would also enable higher proteasome inhibition on the same level as bortezomib (Zhou et al. 2020). Increasing the inhibitory potential towards class I HDACs could moreover help to tackle resistance

mechanisms that impair the efficacy of bortezomib and indeed, this effect would be complemented by the inherent cytotoxicity of class I HDACi (Zhou et al. 2020).



### 4.3 Conclusions

Building on the information gained with only one prototype compound, RTS-V5, two consecutive sets of dual HDACi/20S CPi were designed and synthesised. Data on target inhibition properties and antiproliferative potential were obtained for both libraries. On the whole, it seems that the optimisation options for the selected scaffold are rare because increasing affinity to one target generally extenuates the inhibition of the other. Despite occasional improvements in one discipline, there is thus no new compound outmatching RTS-V5 in all three measured criteria; HDAC inhibition, 20S CP inhibition, and cytotoxicity.

A crystal structure of HDAC6 in complex with **IV-24d** may shed light on the apparent question whether sterically complex P1 groups antagonise the binding to HDAC6. If this assumption does turn out to be relevant, it might certainly be worthwhile to explore the introduction of the HDAC binding site in a different position, for example P2. Since the already moderate 20S CP inhibition of RTS-V5 could not be surpassed by either of the new dual inhibitors, the replacement of the non-covalent proteasome binding unit by a more potent, reversible covalent warhead could serve as a suitable alternative. Given the rather strong nature of the hydroxamate zinc-binding motif, such covalent dual inhibitors might display a more balanced distribution between the two targets in a cellular context. In any case, it seems clear that future attempts at designing a third generation of dual inhibitors should not seek to engage the 20S CP and HDAC6, exclusively. Instead, a certain degree of class I HDAC inhibition with the potential to enhance the cytotoxicity achieved by exploiting the HDAC6/20S CP synergism should be considered. The remarkable antiproliferative potential of **IV-1b** in bortezomib-resistant HL60 cells moreover implies that HDAC1 inhibition could be helpful to tackle resistance issues.

In summary, this study succeeded in partly illuminating the influence of the individual structural features of the first-in-class prototype RTS-V5 on its reported *in vitro* activity. SAR analysis of variations in positions P1 and P4 yielded valuable results that could be narrowed down to identify promising starting points for future optimisation efforts.

## 4.4 Experimental section

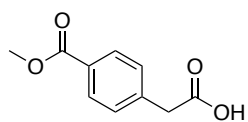
### 4.4.1 General information

Dry THF was obtained from the MBraun MB SPS-800 solvent purification system. Except for DCM, which was purified by distillation prior to use, all reagents and solvents were purchased from commercial sources and used without further purification. TLC was carried out using Macherey-Nagel pre-coated aluminium foil sheets which were visualised using UV light (254 nm). Hydroxamic acids were stained using a 1% solution of iron(III) chloride in MeOH.  $^1\text{H}$  NMR and  $^{13}\text{C}$  NMR spectra were recorded at rt using a Bruker Avance III HD (400 MHz) and Varian/Agilent Mercury-plus (300 MHz & 400 MHz) spectrometers. Chemical shifts ( $\delta$ ) are quoted in parts per million (ppm). All spectra were standardised in accordance with the signals of the deuterated solvents (DMSO- $d_6$ :  $\delta_{\text{H}} = 2.50$  ppm,  $\delta_{\text{C}} = 39.5$  ppm;  $\text{CDCl}_3$ :  $\delta_{\text{H}} = 7.26$  ppm,  $\delta_{\text{C}} = 77.0$  ppm; MeOH- $d_4$ :  $\delta_{\text{H}} = 4.87$  ppm,  $\delta_{\text{C}} = 49.0$  ppm). Coupling constants ( $J$ ) are reported in Hertz (Hz). Mass spectra were measured by the Leipzig University Mass Spectrometry Service using electrospray ionisation (ESI) on Bruker Daltonics Impact II and Bruker Daltonics micrOTOF spectrometers. The uncorrected melting points were determined using a Barnstead Electrothermal 9100 apparatus. Analytical HPLC analysis were carried out using a Thermo Fisher Scientific UltiMate 3000 system equipped with an UltiMate<sup>TM</sup> HPG-3400SD pump, an UltiMate<sup>TM</sup> 3000 Diode array detector, an UltiMate<sup>TM</sup> 3000 autosampler, and a TCC-3000SD standard thermostatted column compartment by Dionex. The system was operated using a Macherey-Nagel NUCLEODUR 100-5  $\text{C}_{18}$  ec column (250 mm x 4.6 mm). UV absorption was detected at 254 nm with a linear gradient of 5% B to 95% B within 23 min. Acidified HPLC-grade water (0.1% TFA; solvent A) and acidified HPLC-grade acetonitrile (0.1% TFA; solvent B) were used for elution at a flow rate of 1 mL/min. The purity of the final compounds was at least 95.0%.

#### 4.4.2 Experimental procedures

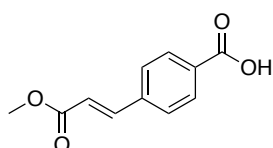
##### Building block synthesis

##### 2-[4-(Methoxycarbonyl)phenyl]acetic acid (**IV-3**).



Synthesised according to the procedure reported in the literature (Breslow et al. 2014). To a solution of methyl 4-(2-methoxy-2-oxoethyl)benzoate (1.18 g, 5.68 mmol, 1.0 eq) in MeOH (15 mL) and water (15 mL) was added  $K_2CO_3$  (784 mg, 5.68 mmol, 1.0 eq) and the resulting mixture was stirred at rt for 27 h. Upon completion of the reaction, the solvents were evaporated under reduced pressure and the residue was dissolved in sat. aq.  $NaHCO_3$  (5 mL). Addition of 10% HCl (pH 3–4) induced precipitation of the product which was then isolated by filtration and washed with water (3 x 5 mL). **IV-3** was obtained as a white solid (769 mg, 3.90 mmol, 69%); mp 107–111 °C;  $^1H$  NMR (400 MHz,  $CDCl_3$ ):  $\delta$  8.05–7.97 (m, 2H, arom.), 7.41–7.34 (m, 2H, arom.), 3.91 (s, 3H,  $CH_3$ ), 3.72 (s, 2H,  $CH_2$ ) ppm;  $^{13}C$  NMR (101 MHz,  $CDCl_3$ ):  $\delta$  176.8, 167.0, 138.4, 130.1, 129.6, 129.4, 52.3, 41.1 ppm; HRMS (m/z):  $MNa^+$  calcd for  $C_{10}H_{10}O_4$  217.0471, found 217.0472.

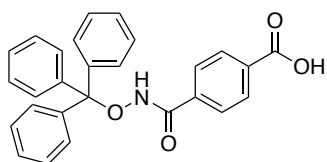
##### 4-[(1E)-3-Methoxy-3-oxoprop-1-en-1-yl]benzoic acid (**IV-5**).



$K_2CO_3$  (920 mg, 6.66 mmol, 2.0 eq) and trimethyl phosphonoacetate (727 mg, 3.99 mmol, 1.2 eq) were added to a solution of 4-formylbenzoic acid (500 mg, 3.33 mmol, 1.0 eq) in THF (35 mL) and the resulting suspension was stirred at rt for 16 h. The solvent was removed under reduced pressure and the remaining solid was washed with sat. aq.  $NaHCO_3$  (30 mL) and water (3 x 10 mL) before it was allowed to dry. The aqueous filtrate was washed with EtOAc (1 x 15 mL) and the organic layer was discarded. The remaining aqueous layer was acidified using 10% HCl (pH 2) and then extracted with EtOAc (4 x 50 mL). The collected organics were washed with brine (1 x 15 mL), dried over  $MgSO_4$ , and concentrated under reduced pressure. The residue and the water-insoluble solid obtained from the crude mixture were then combined and recrystallised from EtOAc (2 mL) and petrol (20 mL) to yield the desired product **IV-5** as a white solid (551 mg, 2.67 mmol, 80%); mp 225–229 °C;  $^1H$  NMR (400 MHz,  $DMSO-d_6$ ):  $\delta$  13.13 (br s, 1H, OH), 7.99–7.90 (m, 2H, arom.), 7.87–7.80 (m, 2H, arom.), 7.71 (d,  $J = 16.1$  Hz, 1H, Ar-CH=CH), 6.76 (d,  $J = 16.1$  Hz, 1H, Ar-CH=CH), 3.74 (s, 3H,  $CH_3$ ) ppm;  $^{13}C$  NMR (101 MHz,  $DMSO-d_6$ ):  $\delta$  166.8, 166.4, 143.2, 138.1, 132.1,

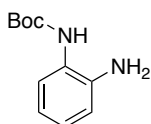
129.7, 128.4, 120.1, 51.6 ppm; HRMS (m/z): MH<sup>+</sup> calcd for C<sub>11</sub>H<sub>10</sub>O<sub>4</sub> 207.0652, found 207.0676. Spectroscopic data matched those reported in the literature (Zhu et al. 2011).

#### 4-[(Triphenylmethoxy)carbamoyl]benzoic acid (**IV-8**).



To a solution of 4-(methoxycarbonyl)benzoic acid (2.00 g, 11.1 mmol, 1.0 eq), *O*-tritylhydroxylamine (3.06 g, 11.1 mmol, 1.0 eq), and HATU (4.22 g, 11.1 mmol, 1.0 eq) in DMF (35 mL) was added DIPEA (2.00 mL, 11.5 mmol, 1.0 eq) and the resulting mixture was stirred at rt for 48 h. After removal of the solvent under reduced pressure, the residue was dissolved in DCM (100 mL) and washed with sat. aq. NaHCO<sub>3</sub> (2 x 15 mL), water (1 x 15 mL), and brine (1x 15 mL). The organic layer was dried over MgSO<sub>4</sub> and the solvent was evaporated. The residue was recrystallised from EtOAc (2 mL) and petrol (30 mL) to yield methyl 4-((trityloxy)carbamoyl)benzoate (**IV-7**) as a white solid which was subsequently dissolved in a mixture of THF (80 mL) and water (10 mL) to which NaOH (3.00 g, 75.0 mmol, 6.8 eq) was added. The resulting mixture was stirred at rt for 24 h and then concentrated under reduced pressure. The residue was suspended in water (10 mL) and 10% HCl was added dropwise (pH 7) to precipitate the desired product which was then isolated by filtration and washed with water (3 x 10 mL). **IV-8** was obtained as a white solid (4.23 g, 9.98 mmol, 91% over 2 steps); mp 193 °C (decomp.); <sup>1</sup>H NMR (400 MHz, DMSO-*d*<sub>6</sub>): δ 11.09 (s, 1H, OH), 8.01–7.81 (m, 2H, arom.), 7.56–7.16 (m, 17H, arom.), 7.14–7.04 (m, 1H, NH) ppm; <sup>13</sup>C NMR (75 MHz, CDCl<sub>3</sub>): δ 166.8, 142.4, 136.5, 129.1, 127.8, 127.5, 126.6 ppm; HRMS (m/z): MNa<sup>+</sup> calcd for C<sub>27</sub>H<sub>21</sub>NO<sub>4</sub> 446.1363, found 446.1363.

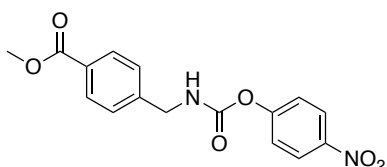
#### *tert*-Butyl *N*-(2-aminophenyl)carbamate (**IV-10**).



Synthesised according to the procedure reported in the literature (Krieger 2017). A solution of 1,2-phenylenediamine (3.30 g, 30 mmol, 5.0 eq) in DCM (10 mL) was cooled to 0 °C and a solution of di-*tert*-butyl dicarbonate (1.30 g, 6.0 mmol, 1.0 eq) in DCM (15 mL) was added. The mixture was stirred at rt for 20 h and then concentrated under reduced pressure. The residue was purified by flash column chromatography (EtOAc/petrol 3:1) to afford **IV-10** as a brown solid (1.15 g, 5.53 mmol, 92%); mp 112–115 °C; <sup>1</sup>H NMR (400 MHz, CDCl<sub>3</sub>): δ 7.29–7.26 (m, 1H, arom.), 7.02–6.96 (m, 1H, arom.), 6.82–6.74 (m, 2H, arom.), 6.24 (s, 1H, NH), 3.85–3.62 (m, 2H,

NH<sub>2</sub>), 1.55–1.47 (m, 9H, *t*-Bu) ppm; <sup>13</sup>C NMR (101 MHz, CDCl<sub>3</sub>): δ 154.0, 140.1, 126.3, 124.9, 124.8, 119.8, 117.7, 80.7, 28.5 ppm; HRMS (m/z): MH<sup>+</sup> calcd for C<sub>11</sub>H<sub>16</sub>N<sub>2</sub>O<sub>2</sub> 209.1285, found 209.1292.

#### Methyl 4-({[(4-nitrophenoxy)carbonyl]amino}methyl)benzoate (**IV-13**).



Synthesised according to the procedure reported in the literature (Stenzel et al. 2017). A solution of methyl 4-(aminomethyl)benzoate hydrochloride (1.04 g, 5.17 mmol, 1.0 eq), Et<sub>3</sub>N (0.72 mL, 5.17 mmol, 1.0 eq), and pyridine (0.58 mL, 7.2 mmol, 1.4 eq) in DCM (40 mL) was cooled to 0 °C and 4-nitrophenyl chloroformate (1.04 g, 5.17 mmol, 1.0 eq) was added. The resulting mixture was stirred at rt for 3 h before it was diluted with DCM (200 mL) and washed with 10% citric acid (3 x 10 mL) and water (2 x 10 mL). The organic layer was dried over MgSO<sub>4</sub> and the solvent was evaporated to afford **IV-13** as a white solid (1.38 g, 4.17 mmol, 81%) which was used without further purification.

#### General procedures

**General procedure A for the preparation of amides using isobutyl chloroformate.** A solution of the respective carboxylic acid (1.0 eq) and NMM (1.1 eq) in dry THF was cooled to 0 °C and isobutyl chloroformate (1.1 eq) was slowly added. The mixture was stirred at 0 °C for 20 min before the respective amine (1.0 eq) was added dropwise. The resulting suspension was stirred at rt for 16 h. Upon completion of the reaction, the precipitate was removed by filtration and extracted with EtOAc (20 mL) before it was discarded. The filtrate was concentrated under reduced pressure to afford the desired product.

**General procedure B for the preparation of amides using HATU.** The respective amine (1.0 eq), HATU (1.0 eq), and the respective carboxylic acid (1.0 eq) were dissolved in DMF (10 mL/mmol) and DIPEA (1.0–3.4 eq) was added. The resulting mixture was stirred at rt for 18–48 h before the solvent was evaporated. The residue was dissolved in DCM (100 mL) and the mixture was washed with 10% HCl (2 x 20 mL), water (1 x 10 mL), sat. aq. NaHCO<sub>3</sub> (3x 20 mL), water (1 x 10 mL), and brine (1 x 20 mL). For compounds featuring trityl residues, 10% citric acid (2 x 10 mL) was used instead of HCl. The collected organics were dried

over  $\text{MgSO}_4$  and concentrated under reduced pressure. The residue was recrystallised from either EtOAc (2 mL) and petrol (20 mL) or MeOH (2 mL) and  $\text{Et}_2\text{O}$  (20 mL).

**General procedure C for the removal of Boc protecting groups.** The Boc-protected amine (1.0 eq) was dissolved in a mixture of DCM and TFA (4:1) and the mixture was stirred at rt for 3 h. Afterwards, it was basified using sat. aq.  $\text{Na}_2\text{CO}_3$  (pH 9) and extracted with DCM (3 x 50 mL). The combined organics were washed with sat. aq.  $\text{NaHCO}_3$  (20 mL) and brine (20 mL) and dried over  $\text{MgSO}_4$ . Subsequent removal of the solvent under reduced pressure afforded the desired product.

**General procedure D for ester hydrolysis.** NaOH (4.1 eq) was added to a solution of the respective ester (1.0 eq) in a mixture of THF, MeOH, and water (10:1:1) and the resulting solution was stirred at rt for 24 h. Upon completion of the reaction, the solvents were removed under reduced pressure and the residue was suspended in sat. aq.  $\text{NaHCO}_3$  (10 mL). To induce precipitation of the carboxylic acid, 10% HCl was added dropwise (pH 3–4). The product was isolated by filtration and washed with water (3 x 10 mL).

**General procedure E for the removal of trityl protecting groups.** The respective trityl-protected hydroxamate (1.0 eq) was dissolved in DCM (10 mL) and TFA (0.1 mL) was added. The resulting mixture was stirred at rt for 10–20 min until TLC (DCM/MeOH 9:1) indicated full conversion. The mixture was basified using 1M NaOH (pH 10) and the organic solvent was evaporated. The remaining aqueous layer was neutralised using 10% HCl (pH 7–8) to induce precipitation of the deprotected hydroxamate which was removed by filtration and washed with water (3 x 5 mL), petrol (5 mL), and chilled  $\text{Et}_2\text{O}$  (5 mL). The crude product thus obtained was recrystallised from MeOH (1 mL) and  $\text{Et}_2\text{O}$  (10 mL).

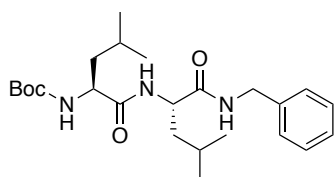
**General procedure F for the preparation of urea derivatives. IV-13** (344 mg, 1.04 mmol, 1.04 eq) was added to a solution of the respective amine (1.00 mmol, 1.0 eq) and  $\text{Et}_3\text{N}$  (0.14 mL, 1.00 mmol, 1.0 eq) in dry THF (5 mL) and the resulting mixture was subjected to microwave irradiation at 70 °C and 150 W under vigorous stirring for 6 h. The reaction mixture was diluted with DCM (50 mL) and the precipitate was isolated by filtration and

successively washed with sat. aq. NaHCO<sub>3</sub> (2 x 5 mL), water (1 x 5 mL), 10% citric acid (3 x 5 mL), and water (2 x 5 mL).

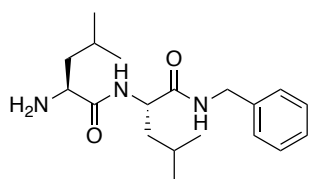
**General procedure G for the preparation of hydroxamates.** To a solution of NaOH (10 eq) in MeOH (4 mL) and DCM (1 mL) at 0 °C was added hydroxylamine (50% solution in water; 30 eq) and the resulting mixture was stirred for 5 min before the respective ester (1.0 eq) was added. The solution was stirred at 0 °C for 1–4 h until TLC (DCM/MeOH 9:1) indicated full conversion. The solvents were removed under reduced pressure and the residue was suspended in water (10 mL). Addition of 10% HCl (pH 8–9) induced the precipitation of the hydroxamate which was then removed by filtration and washed with water (3 x 5 mL).

#### Preparation of compounds IV-1a-e

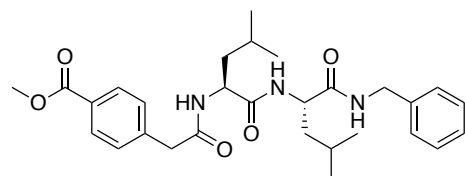
##### *tert*-Butyl *N*-[[*(1S)*-1-[[*(1S)*-1-(benzylcarbamoyl)-3-methylbutyl]carbamoyl]-3-methylbutyl]carbamate (**IV-16**).



Synthesised according to general procedure A using Boc-Leu-Leu-OH (2.06 g, 6.0 mmol), NMM (0.72 mL, 6.6 mmol), isobutyl chloroformate (0.84 mL, 6.6 mmol), and benzylamine (0.66 mL, 6.0 mmol) in THF (18 mL). Filtration of the crude product over a layer of silica (EtOAc/petrol 1:1 + 0.1% Et<sub>3</sub>N as eluent) and evaporation of the solvent afforded **IV-16** as a white solid (2.54 g, 5.85 mmol, 98%); mp 110–114 °C; <sup>1</sup>H NMR (400 MHz, CDCl<sub>3</sub>): δ 7.37–7.21 (m, 5H, arom.), 6.78 (s, 1H, NH), 6.50 (d, *J* = 8.1 Hz, 1H, NH), 5.03–4.82 (m, 1H, CH), 4.54–4.37 (m, 3H, CH<sub>2</sub>, CH), 4.12–3.88 (m, 1H, Boc-NH), 1.84–1.56 (m, 6H, 2 x *i*-Pr-CH, 2 x CH<sub>2</sub>), 1.42 (s, 9H, Boc), 1.03–0.86 (m, 12H, 2 x *i*-Pr) ppm; <sup>13</sup>C NMR (75 MHz, CDCl<sub>3</sub>): δ 172.8, 171.8, 156.0, 138.2, 128.7, 127.8, 127.6, 127.6, 127.5, 80.6, 51.9, 43.6, 40.8, 28.4, 24.9, 23.2, 23.0, 19.2 ppm; HRMS (*m/z*): *M*<sup>+</sup> calcd for C<sub>24</sub>H<sub>39</sub>N<sub>3</sub>O<sub>4</sub> 432.2868, found 432.2889.

**(2S)-2-[(2S)-2-Amino-4-methylpentanamido]-N-benzyl-4-methylpentanamide (IV-17).**

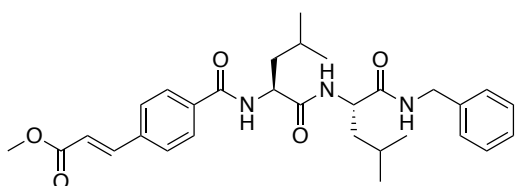
Synthesis according to general procedure C using **IV-16** (2.47 g, 5.70 mmol), TFA (15 mL), and DCM (60 mL) afforded **IV-17** as a yellow oil (1.44 g, 4.26 mmol, 75%);  $^1\text{H}$  NMR (400 MHz,  $\text{DMSO-}d_6$ ):  $\delta$  8.66–8.54 (m, 1H, NH), 8.41 (d,  $J = 8.4$  Hz, 1H, NH), 7.35–7.16 (m, 5H, arom.), 6.61–6.23 (br s, 2H,  $\text{NH}_2$ ), 4.45–4.13 (m, 3H,  $\text{CH}_2$ , CH), 3.78–3.52 (m, 1H, CH), 1.79–1.26 (m, 6H, 2 x *i*-Pr-CH, 2 x  $\text{CH}_2$ ), 0.95–0.71 (m, 12H, 2 x *i*-Pr) ppm;  $^{13}\text{C}$  NMR (101 MHz,  $\text{DMSO-}d_6$ ):  $\delta$  171.6, 171.2, 139.3, 128.2, 127.0, 126.7, 69.8, 51.7, 51.1, 42.0, 41.8, 41.2, 40.2, 39.9, 39.7, 39.5, 39.3, 39.1, 38.9, 24.2, 23.7, 22.9, 22.9, 21.9, 21.8 ppm; HRMS ( $m/z$ ):  $M^-$  calcd for  $\text{C}_{19}\text{H}_{31}\text{N}_3\text{O}_2$  332.2344, found 332.2334.

**Methyl 4-(((1S)-1-(((1S)-1-(benzylcarbamoyl)-3-methylbutyl)carbamoyl)-3-methylbutyl)carbamoyl)methyl)benzoate (IV-18a).**

Synthesis according to general procedure B using **IV-17** (500 mg, 1.50 mmol), **IV-3** (291 mg, 1.50 mmol), HATU (570 mg, 1.50 mmol), and DIPEA (0.30 mL, 1.72 mmol, 1.1 eq) in DMF (15 mL) within 18 h and recrystallisation from EtOAc and petrol afforded **IV-18a** as an off-white solid (720 mg, 1.41 mmol, 94%); mp 165–168 °C;  $^1\text{H}$  NMR (400 MHz,  $\text{CDCl}_3$ ):  $\delta$  8.08–7.90 (m, 2H, arom.), 7.31–7.17 (m, 7H, arom.,  $\text{CDCl}_3$ ), 6.83–6.58 (m, 2H, 2 x NH), 6.19 (d,  $J = 8.0$  Hz, 1H, NH), 4.52–4.41 (m, 2H, 2 x CH), 4.39–4.34 (m, 2H,  $\text{CH}_2$ ), 3.91 (s, 3H,  $\text{CH}_3$ ), 3.54 (s, 2H,  $\text{CH}_2$ ), 1.58–1.36 (m, 6H, 2 x *i*-Pr-CH, 2 x  $\text{CH}_2$ ), 0.97–0.72 (m, 12H, 2 x *i*-Pr) ppm;  $^{13}\text{C}$  NMR (101 MHz,  $\text{CDCl}_3$ ):  $\delta$  172.2, 172.1, 170.3, 166.9, 140.5, 138.2, 130.1, 130.0, 129.3, 129.0, 128.6, 127.7, 127.5, 127.4, 77.5, 77.2, 76.9, 54.7, 52.2, 52.0, 51.9, 43.4, 43.1, 42.8, 41.7, 41.1, 25.0, 25.0, 22.8, 22.8, 23.6, 18.8, 17.5, 12.4 ppm; HRMS ( $m/z$ ):  $M^-$  calcd for  $\text{C}_{29}\text{H}_{39}\text{N}_3\text{O}_5$  508.2817, found 508.2834.



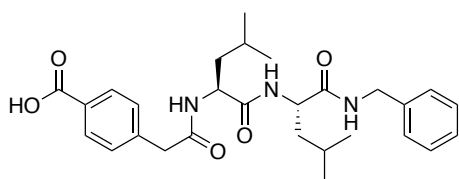
**Methyl (2E)-3-(4-[[[(1S)-1-[[[(1S)-1-(benzylcarbamoyl)-3-methylbutyl]carbamoyl]-3-methylbutyl]carbamoyl]phenyl]prop-2-enoate (IV-18b).**



Synthesis according to general procedure B using **IV-17** (500 mg, 1.50 mmol), **IV-5** (310 mg, 1.50 mmol), HATU (570 mg, 1.50 mmol), and DIPEA (0.30 mL, 1.72 mmol, 1.1 eq) in DMF (15 mL) within 24 h and recrystallisation from

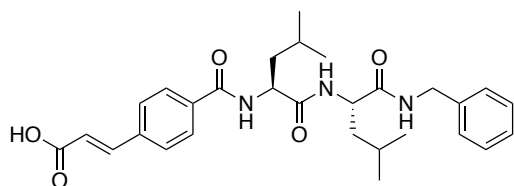
MeOH and Et<sub>2</sub>O afforded **IV-18b** as a white solid (707 mg, 1.36 mmol, 90%); mp 163–166 °C; <sup>1</sup>H NMR (400 MHz, CDCl<sub>3</sub>): δ 7.76–7.69 (m, 2H, arom.), 7.63 (d, *J* = 16.0 Hz, 1H, Ar-CH=CH), 7.46–7.40 (m, 2H, arom.), 7.36–7.11 (m, 7H, arom., 2 x NH), 7.06 (t, *J* = 5.9 Hz, 1H, NH), 6.42 (d, *J* = 16.0 Hz, 1H, Ar-CH=CH), 4.90–4.80 (m, 1H, CH), 4.62–4.51 (m, 1H, CH), 4.38 (d, *J* = 5.8 Hz, 2H, CH<sub>2</sub>), 3.82 (s, 3H, CH<sub>3</sub>), 1.81–1.39 (m, 6H, 2 x *i*-Pr-CH, 2 x CH<sub>2</sub>, H<sub>2</sub>O), 0.95–0.80 (m, 12H, 2 x *i*-Pr) ppm; <sup>13</sup>C NMR (101 MHz, CDCl<sub>3</sub>): δ 172.4, 172.0, 167.1, 166.7, 143.5, 138.17, 137.6, 135.2, 128.8, 128.1, 128.0, 127.6, 127.5, 119.9, 77.5, 77.2, 76.8, 53.9, 52.3, 52.2, 52.0, 43.5, 41.6, 41.2, 25.1, 25.0, 22.9, 22.8, 22.6, 22.5, 18.8, 17.5 ppm; HRMS (*m/z*): MNa<sup>+</sup> calcd for C<sub>30</sub>H<sub>39</sub>N<sub>3</sub>O<sub>5</sub> 544.2782, found 544.2788.

**4-[[[(1S)-1-[[[(1S)-1-(Benzylcarbamoyl)-3-methylbutyl]carbamoyl]-3-methylbutyl]carbamoyl]methyl]benzoic acid (IV-19a).**

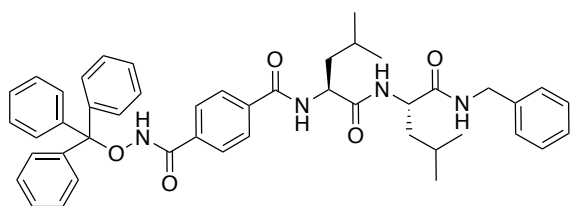


Synthesis according to general procedure D using **IV-18a** (668 mg, 1.31 mmol) and NaOH (216 mg, 5.40 mmol) in THF (60 mL), MeOH (6 mL), and water (6 mL) afforded **IV-19a** as a white solid (537 mg, 1.08 mmol, 83%); mp 197 °C (decomp.); <sup>1</sup>H NMR

(400 MHz, DMSO-*d*<sub>6</sub>): δ 12.83 (s, 1H, OH), 8.46–8.28 (m, 2H, 2 x NH), 8.05–7.96 (m, 1H, NH), 7.90–7.81 (m, 2H, arom.), 7.42–7.09 (m, 7H, arom.), 4.41–4.13 (m, 4H, 2 x CH, CH<sub>2</sub>), 3.56 (d, *J* = 2.9 Hz, 2H, CH<sub>2</sub>), 1.64–1.35 (m, 6H, 2 x *i*-Pr-CH, 2 x CH<sub>2</sub>), 0.94–0.74 (m, 12H, 2 x *i*-Pr) ppm; <sup>13</sup>C NMR (101 MHz, DMSO-*d*<sub>6</sub>): δ 171.8, 171.8, 169.5, 167.2, 141.7, 139.3, 129.2, 129.1, 128.8, 128.2, 127.0, 126.7, 51.2, 51.1, 42.0, 41.9, 40.8, 40.7, 24.2, 24.2, 23.0, 22.9, 21.6, 21.6 ppm; HRMS (*m/z*): M<sup>-</sup> calcd for C<sub>28</sub>H<sub>37</sub>N<sub>3</sub>O<sub>5</sub> 494.2660, found 494.2675.

**(2E)-3-(4-[[[(1S)-1-[[[(1S)-1-(Benzylcarbamoyl)-3-methylbutyl]carbamoyl]-3-methylbutyl]carbamoyl]phenyl]prop-2-enoic acid (IV-19b).**

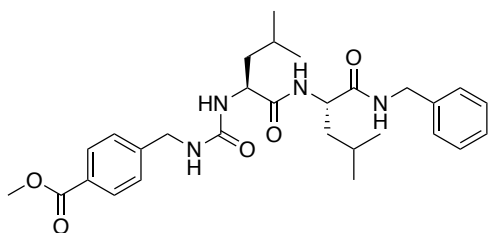
Synthesised according to general procedure D using **IV-18b** (686 mg, 1.31 mmol) and NaOH (216 mg, 5.40 mmol) in THF (60 mL), MeOH (6 mL), and water (6 mL). Due to incomplete precipitation, the acidified aqueous layer was extracted with EtOAc (2 x 20 mL). The combined organics were washed with brine (1 x 10 mL) and dried over MgSO<sub>4</sub>. Removal of the solvent under reduced pressure yielded **IV-19b** as a colourless oil (545 mg, 1.07 mmol, 82%); mp 191 °C (decomp.); <sup>1</sup>H NMR (400 MHz, MeOH-*d*<sub>4</sub>): δ 8.72 (dd, *J* = 4.5, 1.4 Hz, 1H, NH), 8.45–8.37 (m, 1H, NH), 8.07–8.03 (m, 1H, NH), 7.87–7.83 (m, 1H, arom.), 7.75–7.58 (m, 4H, arom., Ar-CH=CH), 7.33–7.11 (m, 5H, arom.), 6.59 (dd, *J* = 16.0, 9.4 Hz, 1H, Ar-CH=CH), 4.66–4.60 (m, 1H, CH), 4.51–4.42 (m, 1H, CH), 4.38 (d, *J* = 2.9 Hz, 2H, CH<sub>2</sub>), 1.85–1.54 (m, 6H, 2 x *i*-Pr-CH, 2 x CH<sub>2</sub>), 1.09–0.85 (m, 12H, 2 x *i*-Pr-CH) ppm; <sup>13</sup>C NMR (75 MHz, MeOH-*d*<sub>4</sub>): δ 174.9, 174.5, 169.9, 169.7, 144.8, 139.8, 139.1, 136.5, 131.3, 129.5, 129.4, 129.2, 129.2, 128.5, 128.2, 128.1, 121.5, 72.1, 54.1, 53.3, 45.4, 44.0, 41.9, 41.5, 29.9, 29.4, 26.1, 25.9, 23.4, 22.1, 22.0, 19.3 ppm; HRMS (*m/z*): MNa<sup>+</sup> calcd for C<sub>29</sub>H<sub>37</sub>N<sub>3</sub>O<sub>5</sub> 530.2625, found 530.2625.

**N<sup>1</sup>-[[[(1S)-1-[[[(1S)-1-(Benzylcarbamoyl)-3-methylbutyl]carbamoyl]-3-methylbutyl]-N<sup>4</sup>-(triphenylmethoxy)benzene-1,4-dicarboxamide (IV-21).**

Synthesised according to general procedure B using **IV-17** (500 mg, 1.50 mmol), **IV-8** (635 mg, 1.50 mmol), HATU (570 mg, 1.50 mmol), and DIPEA (0.30 mL, 1.72 mmol, 1.1 eq) in DMF (15 mL) within 42 h and recrystallised from EtOAc and petrol. Insoluble remains of the crude product were isolated by filtration and washed with 5% citric acid (2 x 5 mL), water (10 mL), sat. aq. NaHCO<sub>3</sub> (2 x 10 mL), and water (10 mL). Spectroscopic data for both the insoluble and the soluble fractions were identical. **IV-21** was obtained as an off-white solid (810 mg, 1.10 mmol, 73%); mp 108 °C (decomp.); <sup>1</sup>H NMR (400 MHz, DMSO-*d*<sub>6</sub>): δ 11.07 (s, 1H, NH), 8.55 (s, 1H, NH), 8.37–8.25 (m, 1H, NH), 8.05–7.91 (m, 2H, arom.), 7.85–7.72 (m, 2H, arom.), 7.53–7.13 (m, 20H, arom.), 4.57–4.19 (m, 4H, 2 x CH, CH<sub>2</sub>), 1.74–1.41 (m, 6H, 2 x *i*-Pr-CH, 2 x CH<sub>2</sub>), 0.99–0.74 (m, 12H, 2 x *i*-Pr) ppm; <sup>13</sup>C NMR (101 MHz, DMSO-*d*<sub>6</sub>): δ 171.9,

165.8, 142.4, 139.3, 129.2, 128.2, 127.8, 127.5, 127.3, 127.0, 126.7, 118.3, 54.9, 52.2, 51.2, 42.0, 40.8, 24.4, 24.2, 23.1, 23.0, 21.7, 21.4 ppm; HRMS (m/z): M<sup>-</sup> calcd for C<sub>46</sub>H<sub>50</sub>N<sub>4</sub>O<sub>5</sub> 737.3708, found 737.3706.

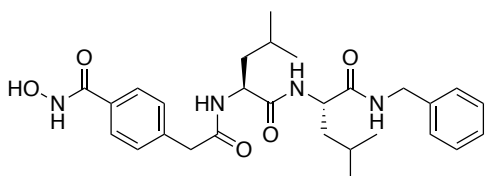
**Methyl 4-[[[[(1S)-1-[[[(1S)-1-(benzylcarbamoyl)-3-methylbutyl]carbamoyl]-3-methylbutyl]carbamoyl]amino)methyl]benzoate (IV-23).**



A solution of methyl 4-(aminomethyl)benzoate hydrochloride (300 mg, 1.80 mmol, 1.2 eq), Et<sub>3</sub>N (0.16 mL, 1.14 mmol, 0.8 eq), and pyridine (0.16 mL, 2.00 mmol, 1.3 eq) in DCM (40 mL) was cooled to 0 °C and 4-nitrophenyl chloroformate (300 mg, 1.80 mmol, 1.2 eq) was added. The

mixture was stirred at 0 °C for 3 h before it was diluted with DCM (100 mL) and washed with 10% citric acid (2 x 10 mL), water (1 x 10 mL), and brine (1 x 10 mL). The organic layer was dried over MgSO<sub>4</sub> and the solvent was removed under reduced pressure. The residue (**IV-13**) was dissolved in dry THF (2 mL) and added to a mixture of **IV-17** (500 mg, 1.50 mmol, 1.0 eq) and Et<sub>3</sub>N (2.0 mL, 14.3 mmol, 9.6 eq) in dry THF (2 mL). The resulting solution was then subjected to microwave irradiation at 150 W and 70 °C under vigorous stirring for 2 h. After evaporation of the solvent, the residue was dissolved in DCM (150 mL) and washed with sat. aq. NaHCO<sub>3</sub> (2 x 10 mL), 10% citric acid (2 x 10 mL), and water (2 x 20 mL). The organic layer was dried over MgSO<sub>4</sub> and concentrated under reduced pressure. The residue was recrystallised from EtOAc (2 mL) and petrol (20 mL) to yield **IV-23** as a yellow solid (510 mg, 0.97 mmol, 65%); mp 197–201 °C; <sup>1</sup>H NMR (300 MHz, DMSO-*d*<sub>6</sub>): δ 8.36 (t, *J* = 5.8 Hz, 1H, NH), 8.17–8.06 (m, 1H, arom.), 7.99–7.81 (m, 2H, arom.), 7.44–7.16 (m, 6H, arom.), 6.96–6.86 (m, 1H, NH), 6.67–6.51 (m, 1H, NH), 6.27–6.19 (m, 1H, NH), 4.40–4.08 (m, 6H, 2 x CH, 2 x CH<sub>2</sub>), 3.84 (d, *J* = 3.2 Hz, 3H, OCH<sub>3</sub>), 1.64–1.30 (m, 6H, 2 x *i*-Pr-CH, 2 x CH<sub>2</sub>), 0.94–0.77 (m, 12H, 2 x *i*-Pr) ppm; <sup>13</sup>C NMR (101 MHz, CDCl<sub>3</sub>): δ 173.7, 173.1, 166.9, 163.1, 158.0, 145.3, 138.2, 130.1, 129.7, 128.7, 128.5, 128.4, 127.5, 127.3, 127.0, 126.9, 126.8, 126.2, 115.8, 77.5, 52.3, 52.1, 43.6, 43.5, 43.1, 41.2, 25.2, 24.9, 23.4, 23.3, 22.6, 22.4 ppm; HRMS (m/z): MNa<sup>+</sup> calcd for C<sub>29</sub>H<sub>40</sub>N<sub>4</sub>O<sub>5</sub> 547.2891, found 547.2894.

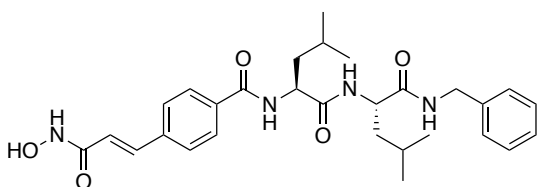
**4-([[(1S)-1-([[(1S)-1-(Benzylcarbamoyl)-3-methylbutyl]carbamoyl]-3-methylbutyl]-carbamoyl)methyl]-N-hydroxybenzamide (IV-1a).**



Synthesised according to general procedure B using **IV-19a** (100 mg, 0.20 mmol), *O*-tritylhydroxylamine (56.0 mg, 0.20 mmol), HATU (85.0 mg, 0.22 mmol, 1.1 eq), and DIPEA (0.07 mL, 0.40 mmol, 2.0 eq) in DMF (3.0 mL) within 27 h.

Subsequent purification via flash column chromatography (DCM/MeOH 9:1 + 1% Et<sub>3</sub>N) afforded the trityl-protected product **IV-20a** as a yellow oil (54.0 mg, 0.07 mmol, 36%) which was directly treated according to general procedure E. Due to incomplete precipitation of the hydroxamate, the neutralised aqueous layer was extracted with EtOAc (3 x 20 mL). The combined organics were washed with brine (1 x 5 mL), dried over Na<sub>2</sub>SO<sub>4</sub>, and concentrated under reduced pressure. The precipitate and the extract were combined and recrystallised from hot MeOH to afford **IV-1a** as a white solid (16.0 mg, 0.03 mmol, 45%); mp 135 °C (decomp.); *t*<sub>R</sub>: 7.41 min, purity: 95.1%; <sup>1</sup>H NMR (400 MHz, DMSO-*d*<sub>6</sub>): δ 11.16 (s, 1H, OH), 8.98 (s, 1H, *NH*-OH), 8.40–8.22 (m, 2H, arom.), 7.96 (d, *J* = 8.2 Hz, 1H, *NH*), 7.68–7.63 (m, 1H, *NH*), 7.33–7.18 (m, 8H, arom., *NH*), 4.35–4.27 (m, 2H, 2 x CH), 4.24 (d, *J* = 5.9 Hz, 2H, CH<sub>2</sub>), 3.54–3.47 (m, 2H, CH<sub>2</sub>), 1.59–1.41 (m, 6H, 2 x *i*-Pr-CH, 2 x CH<sub>2</sub>), 0.89–0.75 (m, 12H, 2 x *i*-Pr) ppm; <sup>13</sup>C NMR (101 MHz, DMSO-*d*<sub>6</sub>): δ 171.8, 169.7, 164.1, 139.3, 128.9, 128.2, 127.1, 127.0, 126.7, 51.1, 51.0, 42.0, 41.9, 40.8, 40.7, 40.2, 39.9, 39.7, 39.5, 39.3, 39.1, 38.9, 24.2, 23.0, 23.0, 21.6 ppm; HRMS (*m/z*): *MH*<sup>+</sup> calcd for C<sub>28</sub>H<sub>38</sub>N<sub>4</sub>O<sub>5</sub> 511.2915, found 511.2914.

**(2S)-N-Benzyl-2-[(2S)-2-([4-[(1E)-2-(hydroxycarbamoyl)eth-1-en-1-yl]phenyl]formamido)-4-methylpentanamido]-4-methylpentanamide (IV-1b).**

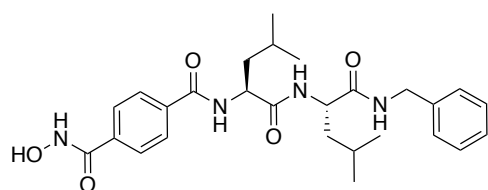


Synthesised according to general procedure B using **IV-19b** (200 mg, 0.39 mmol), *O*-tritylhydroxylamine (106 mg, 0.39 mmol), HATU (148 mg, 0.39 mmol), and DIPEA (0.23 mL, 1.32 mmol, 3.4 eq) in DMF (2.0 mL) within

24 h. Subsequent purification via flash column chromatography (EtOAc/petrol 1:1 + 0.1% Et<sub>3</sub>N; then DCM/MeOH 9:1 + 0.1% Et<sub>3</sub>N) followed by recrystallisation from EtOAc (0.5 mL) and petrol (5 mL) afforded the trityl-protected product **IV-20a** as a white solid (216 mg, 0.28 mmol, 72%) of which 69.0 mg (0.09 mmol) were directly treated according to general

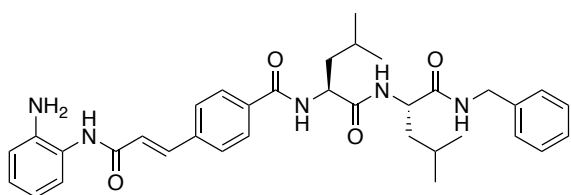
procedure E. **IV-1b** was obtained as a pale brown solid (20.0 mg, 0.04 mmol, 43%); mp 158 °C (decomp.);  $t_R$ : 8.18 min, purity: 98.2%;  $^1\text{H}$  NMR (400 MHz,  $\text{DMSO-}d_6$ ):  $\delta$  10.80 (s, 1H, OH), 9.10 (s, 1H, *NH*-OH), 8.52 (d,  $J = 8.0$  Hz, 1H, NH), 8.34 (t,  $J = 5.9$  Hz, 1H, NH), 7.97 (d,  $J = 8.3$  Hz, 1H, NH), 7.92–7.85 (m, 2H, arom.), 7.69–7.60 (m, 1H, arom.), 7.49 (d,  $J = 15.9$  Hz, 1H, Ar-CH=CH), 7.41–7.13 (m, 6H, arom.), 6.56 (d,  $J = 15.8$  Hz, 1H, Ar-CH=CH), 4.56–4.43 (m, 1H, CH), 4.38–4.20 (m, 3H, CH,  $\text{CH}_2$ ), 1.74–1.44 (m, 6H, 2 x *i*-Pr-CH, 2 x  $\text{CH}_2$ ), 0.99–0.75 (m, 12H, 2 x *i*-Pr) ppm;  $^{13}\text{C}$  NMR (75 MHz,  $\text{DMSO-}d_6$ ):  $\delta$  172.0, 171.9, 165.9, 162.4, 139.3, 137.6, 137.4, 134.5, 128.9, 128.2, 128.1, 127.6, 127.2, 127.0, 126.7, 120.8, 52.1, 51.1, 42.0, 40.8, 40.4, 40.1, 39.8, 39.5, 39.2, 39.0, 38.7, 24.4, 24.2, 23.1, 23.0, 21.7, 21.4 ppm; HRMS ( $m/z$ ):  $\text{MH}^+$  calcd for  $\text{C}_{29}\text{H}_{38}\text{N}_4\text{O}_5$  523.2915, found 523.2918.

***N*<sup>1</sup>-[[(1*S*)-1-[[[(1*S*)-1-(Benzylcarbamoyl)-3-methylbutyl]carbamoyl]-3-methylbutyl]-*N*<sup>4</sup>-hydroxybenzene-1,4-dicarboxamide (**IV-1c**).**



Synthesis according to general procedure E using **IV-21** (70.0 mg, 0.09 mmol) afforded **IV-1c** as a white solid (23.0 mg, 0.05 mmol, 51%); mp 246 °C (decomp.);  $t_R$ : 7.55 min, purity: 95.3%;  $^1\text{H}$  NMR (400 MHz,  $\text{DMSO-}d_6$ ):  $\delta$  11.34 (s, 1H, OH), 9.12 (s, 1H, *NH*-OH), 8.58 (d,  $J = 7.9$  Hz, 1H, NH), 8.34 (t,  $J = 6.0$  Hz, 1H, NH), 7.98 (d,  $J = 8.3$  Hz, 1H, NH), 7.95–7.88 (m, 2H, arom.), 7.85–7.79 (m, 2H, arom.), 7.34–7.14 (m, 5H, arom.), 4.55–4.46 (m, 1H, CH), 4.38–4.29 (m, 1H, CH), 4.29–4.19 (m, 2H,  $\text{CH}_2$ ), 1.73–1.44 (m, 6H, 2 x *i*-Pr-CH, 2 x  $\text{CH}_2$ ), 0.94–0.77 (m, 12H, 2 x *i*-Pr) ppm;  $^{13}\text{C}$  NMR (101 MHz,  $\text{DMSO-}d_6$ ):  $\delta$  171.91, 171.87, 165.9, 163.5, 139.3, 136.4, 135.2, 128.2, 127.8, 127.6, 127.0, 126.8, 126.7, 52.1, 51.2, 42.0, 40.8, 40.2, 39.9, 39.7, 39.5, 39.3, 39.1, 38.9, 24.5, 24.3, 23.1, 23.0, 21.7, 21.4 ppm; HRMS ( $m/z$ ):  $\text{MNa}^+$  calcd for  $\text{C}_{27}\text{H}_{36}\text{N}_4\text{O}_5$  519.2578, found 519.2575.

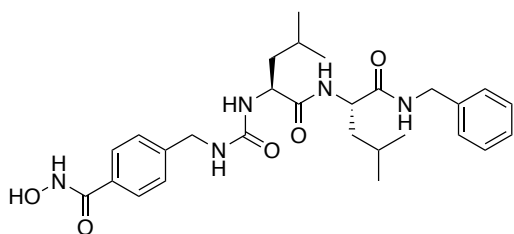
**(2S)-2-[(2S)-2-({4-[(1E)-2-[(2-Aminophenyl)carbamoyl]eth-1-en-1-yl]phenyl}formamido)-4-methylpentanamido]-N-benzyl-4-methylpentanamide (IV-1d).**



Synthesised according to general procedure B using **IV-19b** (200 mg, 0.39 mmol), **IV-10** (81.0 mg, 0.39 mmol), HATU (148 mg, 0.39 mmol), and DIPEA (0.23 mL, 1.32 mmol, 3.4 eq) in DMF (15 mL) within

24 h. Subsequent recrystallisation from EtOAc and petrol afforded the Boc-protected product **IV-22** as a pale-yellow solid which was directly treated according to general procedure C using TFA (4 mL) and DCM (16 mL). Recrystallisation from EtOAc (1 mL) and petrol (10 mL) afforded **IV-1d** as a fluorescent yellow solid (103 mg, 0.17 mmol, 44% over 2 steps); mp 235 °C (decomp.);  $t_R$ : 7.64 min, purity: 98.7%;  $^1H$  NMR (400 MHz, DMSO- $d_6$ ):  $\delta$  9.44 (s, 1H, NH), 8.56–8.48 (m, 1H, NH), 8.37–8.28 (m, 1H, NH), 8.02–7.90 (m, 2H, arom.), 7.73–7.68 (m, 1H, arom.), 7.59 (d,  $J$  = 15.9 Hz, 1H, Ar-CH=CH), 7.39–7.18 (m, 5H, arom.), 7.00 (d,  $J$  = 15.8 Hz, 1H, Ar-CH=CH), 6.95–6.90 (m, 1H, arom.), 6.78–6.74 (m, 1H, arom.), 6.63–6.53 (m, 1H, arom.), 5.02–4.82 (m, 2H, NH<sub>2</sub>), 4.53–4.21 (m, 4H, 2 x CH, CH<sub>2</sub>), 1.76–1.40 (m, 6H, 2 x *i*-Pr-CH, 2 x CH<sub>2</sub>), 0.97–0.80 (m, 12H, 2 x *i*-Pr) ppm;  $^{13}C$  NMR (101 MHz, DMSO- $d_6$ ):  $\delta$  172.0, 171.9, 166.0, 163.2, 141.6, 139.3, 138.5, 137.6, 134.7, 128.5, 128.2, 127.4, 127.0, 126.7, 125.9, 124.7, 124.1, 124.0, 123.4, 116.3, 116.1, 116.0, 52.1, 51.1, 42.0, 40.8, 40.2, 24.5, 24.3, 23.1, 23.0, 21.7, 21.4 ppm; HRMS ( $m/z$ ): MNa<sup>+</sup> calcd for C<sub>35</sub>H<sub>43</sub>N<sub>5</sub>O<sub>4</sub> 620.3207, found 620.3230.

**4-[[[[(1S)-1-[[[(1S)-1-(Benzylcarbamoyl)-3-methylbutyl]carbamoyl]-3-methylbutyl]-carbamoyl]amino)methyl]-N-hydroxybenzamide (IV-1e).**



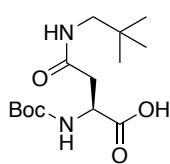
Synthesis according to general procedure G using **IV-23** (180 mg, 0.34 mmol, 1.0 eq), NaOH (137 mg, 3.4 mmol, 10 eq) and hydroxylamine (50% solution in water; 0.62 mL, 10.1 mmol, 30 eq) within 2 h afforded **IV-1e** as an off-white solid (146 mg, 0.27 mmol, 82%); mp 173 °C

decomp.  $t_R$ : 7.34 min, purity: 95.2%;  $^1H$  NMR (300 MHz, DMSO- $d_6$ ):  $\delta$  11.16 (s, 1H, OH), 8.98 (s, 1H, NH-OH), 8.35 (t,  $J$  = 6.0 Hz, 1H, NH), 8.08–7.89 (m, 1H, NH), 7.75–7.64 (m, 2H, arom.), 7.44–7.12 (m, 7H, arom.), 6.55 (t,  $J$  = 6.1 Hz, 1H, NH), 6.28–6.13 (m, 1H, NH), 4.43–4.05 (m, 6H, 2 x CH, 2 x CH<sub>2</sub>), 1.65–1.27 (m, 6H, 2 x *i*-Pr-CH, 2 x CH<sub>2</sub>), 0.93–0.67 (m, 12H,

2 x *i*-Pr ppm;  $^{13}\text{C}$  NMR (101 MHz, DMSO- $d_6$ ):  $\delta$  173.3, 172.9, 172.7, 172.0, 171.8, 164.1, 158.1, 157.8, 144.1, 139.4, 139.3, 131.0, 129.2, 128.2, 127.01, 126.99, 126.8, 126.7, 51.9, 51.0, 42.5, 42.0, 41.7, 40.8, 24.3, 24.2, 23.2, 23.1, 23.0, 22.6, 22.4, 22.0, 21.9, 21.6, 20.9 ppm; HRMS ( $m/z$ ):  $\text{MNa}^+$  calcd for  $\text{C}_{28}\text{H}_{39}\text{N}_5\text{O}_5$  548.2843, found 548.2856.

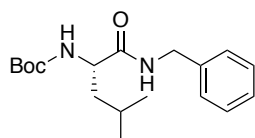
### Preparation of compounds **IV-24a-f**

#### (2S)-2-[[*tert*-Butoxy]carbonyl]amino]-3-[(2,2-dimethylpropyl)carbamoyl]-propanoic acid (**IV-28**).



Synthesis according to general procedure A using Boc-Asp-OBn-OH (4.53 g, 14.0 mmol), NMM (1.70 mL, 1.54 mmol), isobutyl chloroformate (2.00 mL, 15.4 mmol), and neopentylamine (1.64 mL, 14.0 mmol) in THF (40 mL) afforded benzyl (2S)-2-[[*tert*-butoxy]carbonyl]amino]-3-[(2,2-dimethylpropyl)carbamoyl]propanoate (**IV-27**) as a white solid (quant). Based on the procedure reported in the literature (Blackburn et al. 2010a), the crude product was directly dissolved in MeOH (30 mL) and 5% Pd/C (300 mg, 0.15 mmol, 0.01 eq) was added. The resulting suspension was stirred in  $\text{H}_2$  atmosphere (1 bar) at rt for 4 h after which the catalyst was removed by filtration over a layer of Celite<sup>®</sup> which was subsequently washed with EtOAc (50 mL). Removal of the solvent under reduced pressure afforded the desired product **IV-28** as a white solid (4.16 g, 13.8 mmol, 98% over 2 steps);  $^1\text{H}$  NMR (400 MHz, DMSO- $d_6$ ):  $\delta$  7.71 (t,  $J$  = 6.3 Hz, 1H,  $\text{CH}_2\text{-NH}$ ), 6.85 (d,  $J$  = 8.4 Hz, CH-NH), 4.30–4.22 (m, 1H, CH), 2.96–2.79 (m, 2H, *t*-Bu- $\text{CH}_2$ ), 2.63–2.42 (m, 2H,  $\text{CH}_2\text{-CH}$ ), 1.36 (s, 1H, 9H, Boc), 0.82 (s, 1H, *t*-Bu) ppm.

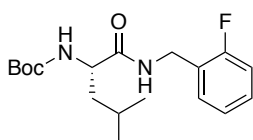
#### *tert*-Butyl *N*-[(1S)-1-(benzylcarbamoyl)-3-methylbutyl]carbamate (**IV-31a**).



Synthesised according to general procedure A using Boc-Leu-OH (1.74 g, 7.52 mmol), isobutyl chloroformate (1.08 mL, 8.30 mmol), NMM (0.91 mL, 8.19 mmol), and benzylamine (0.82 mL, 7.52) in dry THF (20 mL). Recrystallisation from EtOAc (1 mL) and petrol (20 mL) afforded **IV-31a** as a white solid (1.84 g, 5.75 mmol, 76%); mp 78–82;  $^\circ\text{C}$   $^1\text{H}$  NMR (400 MHz,  $\text{CDCl}_3$ ):  $\delta$  7.39–7.19 (m, 5H, arom.), 6.47 (s, 1H, NH), 4.87 (s, 1H, NH), 4.50–4.39 (m, 2H,  $\text{CH}_2$ ), 4.11 (s, 1H, CH), 1.74–1.61 (m, 3H, *i*-Pr-CH,  $\text{CH}_2$ ), 1.41 (s, 9H, Boc), 1.01–0.85 (m, 6H, *i*-Pr) ppm;  $^{13}\text{C}$  NMR (101 MHz,  $\text{CDCl}_3$ ):  $\delta$  172.5, 138.2, 128.8, 127.8, 127.6,

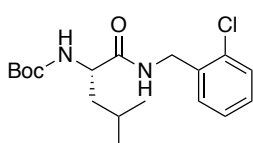
77.5, 53.4, 43.6, 41.2, 28.4, 24.9, 23.1, 22.2, 19.2 ppm; HRMS (m/z): MH<sup>+</sup> calcd for C<sub>18</sub>H<sub>28</sub>N<sub>2</sub>O<sub>3</sub> 321.2173, found 321.2148.

**tert-Butyl N-[(1S)-1-[(2-fluorophenyl)methyl]carbamoyl]-3-methylbutyl]carbamate (IV-31b).**



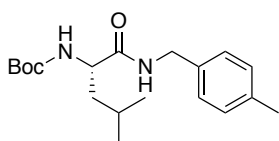
Synthesised according to general procedure A using Boc-Leu-OH (1.74 g, 7.52 mmol), isobutyl chloroformate (1.08 mL 8.30 mmol), NMM (0.91 mL, 8.19 mmol), and 2-fluorobenzylamine (0.85 mL, 7.52 mmol) in dry THF (20 mL). Recrystallisation from EtOAc (1 mL) and petrol (20 mL) afforded **IV-31b** as a white solid (1.86 g, 5.49 mmol, 73%); mp 96–98 °C; <sup>1</sup>H NMR (300 MHz, CDCl<sub>3</sub>): δ 7.36–7.19 (m, 2H, arom.), 7.14–7.00 (m, 2H, arom.), 6.50 (s, 1H, NH), 4.83 (s, 1H, NH), 4.54–4.41 (m, 2H, CH<sub>2</sub>), 4.10 (s, 1H, CH), 1.74–1.58 (m, 3H, CH<sub>2</sub>, *i*-Pr-CH) 1.41 (s, 9H, Boc), 1.00–0.84 (m, 6H, *i*-Pr) ppm; <sup>13</sup>C NMR (101 MHz, CDCl<sub>3</sub>): δ 172.8, 162.2, 159.8, 155.9, 130.0, 129.33, 129.25, 125.3, 125.1, 124.4, 124.3, 115.5, 115.3, 80.3, 63.8, 53.6, 53.2, 41.2, 37.5, 28.4, 24.9, 23.0, 22.1 ppm; HRMS (m/z): MNa<sup>+</sup> calcd for C<sub>18</sub>H<sub>27</sub>FN<sub>2</sub>O<sub>3</sub> 361.1898, found 361.1896.

**tert-Butyl N-[(1S)-1-[(2-chlorophenyl)methyl]carbamoyl]-3-methylbutyl]carbamate (IV-31c).**



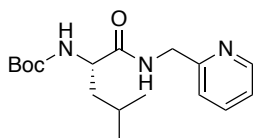
Synthesised according to general procedure A using Boc-Leu-OH (1.74 g, 7.52 mmol), isobutyl chloroformate (1.08 mL 8.30 mmol), NMM (0.91 mL, 8.19 mmol), and 2-chlorobenzylamine (0.91 mL, 7.52 mmol) in dry THF (20 mL). Recrystallisation from MeOH (1 mL) and Et<sub>2</sub>O (20 mL) afforded **IV-31c** as white crystals (2.09 g, 5.88 mmol, 78%); mp 102–105 °C; <sup>1</sup>H NMR (400 MHz, CDCl<sub>3</sub>): δ 7.37–7.30 (m, 2H, arom.), 7.23–7.15 (m, 2H, arom.), 6.74 (s, 1H, NH), 4.95 (d, *J* = 8.2 Hz, 1H, NH), 4.50 (d, *J* = 5.9 Hz, 2H, CH<sub>2</sub>), 4.19–4.06 (m, 1H, CH), 1.73–1.61 (m, 2H, *i*-Pr –CH, CH<sub>2</sub>), 1.52–1.45 (m, 1H, CH<sub>2</sub>), 1.40 (s, 9H, Boc), 0.91 (t, *J* = 6.0 Hz, 6H, *i*-Pr) ppm; <sup>13</sup>C NMR (101 MHz, CDCl<sub>3</sub>): δ 172.7, 155.9, 135.6, 133.6, 129.9, 129.6, 128.9, 127.2, 80.3, 53.3, 41.5, 41.1, 28.4, 24.9, 23.0, 22.2 ppm; HRMS (m/z): MNa<sup>+</sup> calcd for C<sub>18</sub>H<sub>27</sub>ClN<sub>2</sub>O<sub>3</sub> 377.1602, found 377.1615.



**tert-Butyl N-[(1S)-3-methyl-1-[[4-methylphenyl)methyl]carbamoyl]butyl]carbamate (IV-31d).**

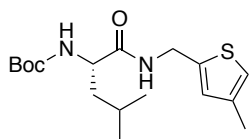
Synthesised according to general procedure A using Boc-Leu-OH (1.74 g, 7.52 mmol), isobutyl chloroformate (1.08 mL, 8.30 mmol), NMM (0.91 mL, 8.19 mmol), and 4-methylbenzylamine (0.95 mL, 7.52 mmol) in dry THF (20 mL). Recrystallisation from EtOAc (1 mL)

and petrol (20 mL) afforded **IV-31d** as a white solid (2.09 g, 6.25 mmol, 83%); mp 83–85 °C; <sup>1</sup>H NMR (400 MHz, CDCl<sub>3</sub>): δ 7.19–7.07 (m, 4H, arom.), 6.39 (s, 1H, NH), 4.86 (s, 1H, NH), 4.44–4.31 (m, 2H, CH<sub>2</sub>), 4.10 (s, 1H, CH), 2.33 (s, 3H, CH<sub>3</sub>), 1.76–1.60 (m, 3H, *i*-Pr-CH, CH<sub>2</sub>), 1.41 (s, 9H, Boc), 0.99–0.86 (m, 6H, *i*-Pr) ppm; <sup>13</sup>C NMR (101 MHz, CDCl<sub>3</sub>): δ 172.5, 155.9, 137.3, 135.1, 129.5, 127.8, 53.3, 43.4, 41.3, 28.4, 24.9, 23.1, 21.2, 19.2 ppm; HRMS (m/z): MNa<sup>+</sup> calcd for C<sub>19</sub>H<sub>30</sub>N<sub>2</sub>O<sub>3</sub> 357.2149, found 357.2166.

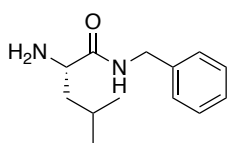
**tert-Butyl N-[(1S)-3-methyl-1-[[pyridin-2-yl)methyl]carbamoyl]butyl]carbamate (IV-31e).**

Synthesised according to general procedure A using Boc-Leu-OH (1.74 g, 7.52 mmol), isobutyl chloroformate (1.08 mL, 8.30 mmol), NMM (0.91 mL, 8.19 mmol), and 2-picolylamine (0.85 mL, 7.52 mmol) in dry THF (20 mL). The crude product was redissolved in EtOAc

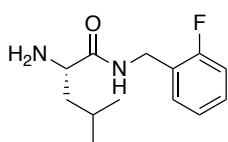
(100 mL), washed with sat. aq. NaHCO<sub>3</sub> (2 x 10 mL) and brine (1 x 10 mL), dried over MgSO<sub>4</sub>, and concentrated under reduced pressure. Drying *in vacuo* afforded **IV-31e** as an orange oil which solidified upon storage (2.31 g, 7.18 mmol, 96%); mp 62–64 °C; <sup>1</sup>H NMR (300 MHz, CDCl<sub>3</sub>): δ 8.56–8.49 (m, 1H, NH), 7.69–7.59 (m, 1H, arom.), 7.26–7.14 (m, 3H, arom.), 4.95 (s, 1H, NH), 4.56 (dd, *J* = 5.2, 1.5 Hz, 2H, CH<sub>2</sub>), 4.20 (s, 1H, CH), 1.81–1.65 (m, 3H, *i*-Pr-CH, CH<sub>2</sub>), 1.43 (s, 9H, Boc), 1.01–0.87 (m, 6H, *i*-Pr) ppm; <sup>13</sup>C NMR (101 MHz, CDCl<sub>3</sub>): δ 172.8, 156.5, 155.8, 149.2, 136.9, 122.5, 122.0, 80.1, 53.4, 44.6, 41.7, 28.4, 24.9, 23.1, 22.1, 19.2 ppm; HRMS (m/z): MNa<sup>+</sup> calcd for C<sub>17</sub>H<sub>27</sub>N<sub>3</sub>O<sub>3</sub> 344.1945, found 344.1956.

**tert-Butyl N-[(1S)-3-methyl-1-[[4-methylthiophen-2-yl)methyl]carbamoyl]butyl]-carbamate (IV-31f).**

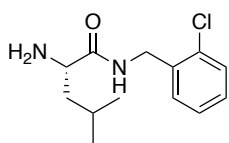
Synthesis according to general procedure A using Boc-Leu-OH (1.58 g, 2.50 mmol), isobutyl chloroformate (0.36 mL 2.77 mmol), NMM (0.30 mL, 2.70 mmol), and (4-methylthiophen-2-yl)methanamine (318 mg, 2.50 mmol) in dry THF (20 mL) afforded **IV-31f** as a yellow oil (766 mg, 2.25 mmol, 90%);  $^1\text{H}$  NMR (300 MHz,  $\text{CDCl}_3$ ):  $\delta$  6.79–6.65 (m, 3H, NH, arom.), 4.98 (d,  $J = 8.3$  Hz, 1H, CH), 4.55–4.41 (m, 2H,  $\text{CH}_2$ ), 4.12 (s, 1H, NH), 2.18 (d,  $J = 1.0$  Hz, 3H,  $\text{CH}_3$ ), 1.72–1.60 (m, 2H, *i*-Pr-CH,  $\text{CH}_2$ ), 1.52–1.42 (m, 1H,  $\text{CH}_2$ ), 1.40 (s, 9H, Boc), 0.95–0.88 (m, 6H, *i*-Pr) ppm;  $^{13}\text{C}$  NMR (101 MHz,  $\text{CDCl}_3$ ):  $\delta$  172.3, 155.9, 148.8, 140.6, 137.6, 128.4, 120.3, 75.9, 63.8, 53.6, 53.2, 41.2, 38.5, 28.4, 28.2, 27.8, 24.9, 23.1, 22.1, 19.2, 18.9, 15.8 ppm; HRMS ( $m/z$ ):  $\text{MH}^+$  calcd for  $\text{C}_{17}\text{H}_{28}\text{N}_2\text{O}_3\text{S}$  341.1893, found 341.1891.

**(2S)-2-Amino-N-benzyl-4-methylpentanamide (IV-32a).**

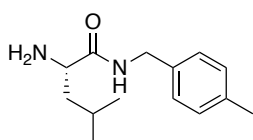
Synthesis according to general procedure C using **IV-31a** (1.60 g, 5.00 mmol), TFA (20 mL), and DCM (60 mL) afforded **IV-32a** as a yellow oil (912 mg, 4.14 mmol, 83%);  $^1\text{H}$  NMR (300 MHz,  $\text{CDCl}_3$ ):  $\delta$  7.65 (s, 1H, NH), 7.40–7.22 (m, 5H, arom.), 4.43 (d,  $J = 5.9$  Hz, 2H,  $\text{CH}_2$ ), 3.49 (dd,  $J = 9.8, 3.6$  Hz, 1H, CH), 1.83–1.68 (m, 2H,  $\text{CH}_2$ , *i*-Pr-CH), 1.49–1.33 (m, 1H,  $\text{CH}_2$ ), 1.01–0.85 (m, 6H, *i*-Pr) ppm;  $^{13}\text{C}$  NMR (75 MHz,  $\text{CDCl}_3$ ):  $\delta$  175.1, 138.6, 128.8, 127.9, 127.6, 127.5, 53.6, 44.0, 43.3, 25.0, 23.5, 21.6 ppm; HRMS ( $m/z$ ):  $\text{MH}^+$  calcd for  $\text{C}_{13}\text{H}_{20}\text{N}_2\text{O}$  221.1648, found 221.1652.

**(2S)-2-Amino-N-[(2-fluorophenyl)methyl]-4-methylpentanamide (IV-32b).**

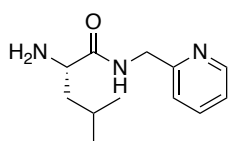
Synthesis according to general procedure C using **IV-31b** (1.69 g, 5.00 mmol), TFA (20 mL), and DCM (60 mL) afforded **IV-32b** as a yellow oil (816 mg, 3.74 mmol, 75%);  $^1\text{H}$  NMR (300 MHz,  $\text{CDCl}_3$ ):  $\delta$  7.66 (s, 1H, NH), 7.36–7.21 (m, 2H, arom.), 7.12–6.99 (m, 2H, arom.), 4.49 (d,  $J = 6.1$  Hz, 2H,  $\text{CH}_2$ ), 3.42 (dd,  $J = 9.8, 3.6$  Hz, 1H, CH), 1.81–1.65 (m, 2H,  $\text{CH}_2$ , *i*-Pr-CH), 1.41–1.30 (m, 1H,  $\text{CH}_2$ ), 0.99–0.88 (m, 6H, *i*-Pr) ppm;  $^{13}\text{C}$  NMR (101 MHz,  $\text{CDCl}_3$ ):  $\delta$  175.6, 162.2, 159.8, 130.1, 130.0, 129.2, 129.1, 125.6, 125.4, 124.3, 124.2, 115.4, 115.2, 53.5, 44.0, 37.0, 24.9, 23.4, 21.4 ppm; HRMS ( $m/z$ ):  $\text{MNa}^+$  calcd for  $\text{C}_{13}\text{H}_{19}\text{FN}_2\text{O}$  239.1554, found 239.1550.

**(2S)-2-Amino-N-[(2-chlorophenyl)methyl]-4-methylpentanamide (IV-32c).**

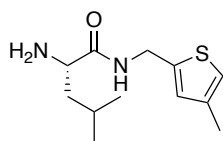
Synthesis according to general procedure C using **IV-31c** (1.77 g, 5.00 mmol), TFA (20 mL), and DCM (60 mL) afforded **IV-32c** as a colourless oil (1.26 g, 4.90 mmol, 98%);  $^1\text{H}$  NMR (400 MHz,  $\text{CDCl}_3$ ):  $\delta$  7.77 (t,  $J = 6.1$  Hz, 1H, NH), 7.39–7.32 (m, 2H, arom.), 7.24–7.17 (m, 2H, arom.), 4.52 (dd,  $J = 6.1, 1.5$  Hz, 2H,  $\text{CH}_2$ ), 3.50–3.43 (m, 1H, CH), 1.78–1.67 (m, 2H, *i*-Pr-CH), 1.43–1.34 (m, 1H,  $\text{CH}_2$ ), 0.98–0.89 (m, 6H, *i*-Pr) ppm;  $^{13}\text{C}$  NMR (75 MHz,  $\text{CDCl}_3$ ):  $\delta$  175.4, 133.8, 130.1, 129.6, 128.9, 127.2, 53.7, 44.1, 41.2, 25.0, 23.5, 21.5 ppm; HRMS ( $m/z$ ):  $\text{MH}^+$  calcd for  $\text{C}_{13}\text{H}_{19}\text{ClN}_2\text{O}_6$  255.1259, found 255.1261.

**(2S)-2-Amino-4-methyl-N-[(4-methylphenyl)methyl]pentanamide (IV-32d).**

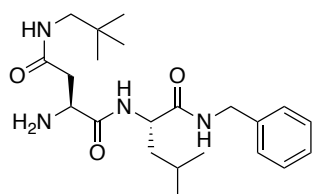
Synthesis according to general procedure C using **IV-31d** (1.67 g, 5.00 mmol), TFA (20 mL), and DCM (60 mL) afforded **IV-32d** as a yellow oil (1.09 g, 4.66 mmol, 93%);  $^1\text{H}$  NMR (400 MHz,  $\text{CDCl}_3$ ):  $\delta$  7.57 (s, 1H, NH), 7.22–7.06 (m, 4H, arom.), 4.38 (d,  $J = 5.8$  Hz, 2H,  $\text{CH}_2$ ), 3.45 (dd,  $J = 9.7, 3.5$  Hz, 1H, CH), 2.33 (s, 3H,  $\text{CH}_3$ ), 1.77–1.65 (m, 2H,  $\text{CH}_2$ , *i*-Pr-CH), 1.44–1.32 (m, 1H,  $\text{CH}_2$ ), 0.99–0.86 (m, 6H, *i*-Pr) ppm;  $^{13}\text{C}$  NMR (75 MHz,  $\text{CDCl}_3$ ):  $\delta$  175.3, 137.1, 135.6, 129.4, 127.8, 53.6, 44.1, 43.0, 36.6, 25.0, 23.5, 21.5, 21.2, 19.2 ppm; HRMS ( $m/z$ ):  $\text{MNa}^+$  calcd for  $\text{C}_{15}\text{H}_{21}\text{N}_5\text{O}_2$  326.1587, found 326.1580.

**(2S)-2-Amino-4-methyl-N-[(pyridin-2-yl)methyl]pentanamide (IV-32e).**

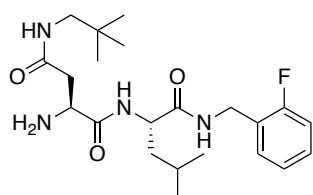
Synthesis according to general procedure C using **IV-31e** (1.61 g, 5.00 mmol), TFA (20 mL), and DCM (60 mL) afforded **IV-32e** as a pale-brown oil (1.01 g, 4.58 mmol, 92%);  $^1\text{H}$  NMR (400 MHz,  $\text{CDCl}_3$ ):  $\delta$  8.61–8.47 (m, 1H, arom.), 8.15 (s, 1H, NH), 7.70–7.59 (m, 1H, arom.), 7.30–7.13 (m, 2H, arom.), 4.52 (dd,  $J = 28.2, 5.4$  Hz, 2H,  $\text{CH}_2$ ), 3.49 (dd,  $J = 9.7, 3.6$  Hz, 1H, CH), 1.80–1.66 (m, 2H,  $\text{CH}_2$ , *i*-Pr-CH), 1.50–1.35 (m, 1H,  $\text{CH}_2$ ), 1.00–0.84 (m, 6H, *i*-Pr) ppm;  $^{13}\text{C}$  NMR (75 MHz,  $\text{CDCl}_3$ ):  $\delta$  175.7, 157.1, 149.3, 136.9, 122.4, 122.1, 53.7, 44.5, 44.2, 28.1, 25.0, 23.5, 21.5, 19.2 ppm; HRMS ( $m/z$ ):  $\text{MH}^+$  calcd for  $\text{C}_{12}\text{H}_{19}\text{N}_3\text{O}$  222.1601, found 222.1590.

**(2S)-2-Amino-4-methyl-N-[(4-methylthiophen-2-yl)methyl]pentanamide (IV-32f).**

Synthesis according to general procedure C using **IV-31f** (766 mg, 2.25 mmol), TFA (15 mL), and DCM (60 mL) afforded **IV-32f** as a brown oil (490 mg, 2.04 mmol, 91%);  $^1\text{H}$  NMR (400 MHz,  $\text{CDCl}_3$ ):  $\delta$  7.64 (s, 1H, NH), 6.80–6.74 (m, 2H, arom.), 4.54 (d,  $J = 5.8$  Hz, 2H,  $\text{CH}_2$ ), 3.45 (dd,  $J = 9.6, 3.7$  Hz, 1H, CH), 2.21 (s, 3H,  $\text{CH}_3$ ), 1.78–1.67 (m, 2H, *i*-Pr-CH,  $\text{CH}_2$ ), 1.44–1.33 (m, 1H,  $\text{CH}_2$ ), 0.97–0.88 (m, 6H, *i*-Pr) ppm;  $^{13}\text{C}$  NMR (75 MHz,  $\text{CDCl}_3$ ):  $\delta$  175.0, 141.2, 140.9, 137.7, 128.3, 120.2, 53.6, 43.9, 38.2, 25.0, 23.5, 21.6, 19.2, 15.8 ppm; HRMS ( $m/z$ ):  $\text{MH}^+$  calcd for  $\text{C}_{12}\text{H}_{20}\text{N}_2\text{OS}$  241.1369, found 241.1366.

**(2S)-2-Amino-N-[(1S)-1-(benzylcarbamoyl)-3-methylbutyl]-N'-(2,2-dimethylpropyl)-butanediamide (IV-34a).**

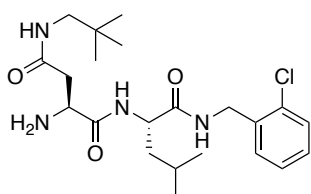
Synthesis according to general procedure B using **IV-32a** (400 mg, 1.81 mmol), **IV-28** (548 mg, 1.81 mmol), HATU (689 mg, 1.81 mmol), and DIPEA (0.32 mL, 1.84 mmol, 1.0 eq) in DMF (15 mL) within 48 h afforded the Boc-protected intermediate **IV-33a** as an off-white solid which was directly treated according to general procedure C using TFA (15 mL) and DCM (60 mL). **IV-34a** was obtained as a yellow solid (678 mg, 1.68 mmol, 93% over 2 steps); mp 92–96 °C;  $^1\text{H}$  NMR (400 MHz,  $\text{CDCl}_3$ ):  $\delta$  7.92 (d,  $J = 8.3$  Hz, 1H, NH), 7.35–7.23 (m, 5H, arom.), 7.05 (t,  $J = 5.7$  Hz, 1H, NH), 6.48–6.32 (m, 1H, NH), 4.52–4.34 (m, 3H, CH,  $\text{CH}_2$ ), 3.76–3.67 (m, 1H, CH), 3.00 (d,  $J = 6.3$  Hz, 2H,  $\text{CH}_2$ ), 2.68–2.49 (m, 2H,  $\text{CH}_2$ ), 2.44 (br s, 2H,  $\text{NH}_2$ ), 1.83–1.56 (m, 3H, *i*-Pr-CH,  $\text{CH}_2$ ), 0.98–0.86 (m, 15H, *t*-Bu, *i*-Pr) ppm;  $^{13}\text{C}$  NMR (101 MHz,  $\text{CDCl}_3$ ):  $\delta$  174.2, 172.0, 171.0, 138.3, 128.7, 127.7, 127.5, 52.6, 52.1, 50.7, 43.5, 40.7, 40.4, 31.9, 27.3, 25.0, 23.1, 22.1 ppm; HRMS ( $m/z$ ):  $\text{MNa}^+$  calcd for  $\text{C}_{22}\text{H}_{36}\text{N}_4\text{O}_3$  405.2860, found 405.2865.

**(2S)-2-Amino-N'-(2,2-dimethylpropyl)-N-[(1S)-1-[(2-fluorophenyl)methyl]carbamoyl]-3-methylbutyl]butanediamide (IV-34b).**

Synthesis according to general procedure B using **IV-32b** (431 mg, 1.81 mmol), **IV-28** (548 mg, 1.81 mmol), HATU (689 mg, 1.81 mmol), and DIPEA (0.32 mL, 1.84 mmol, 1.0 eq) in DMF (15 mL) within 48 h afforded the Boc-protected intermediate **IV-33b** as an off-white solid which was directly treated according

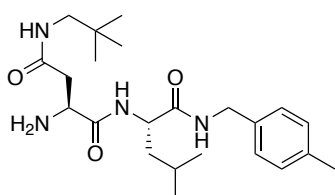
to general procedure C using TFA (15 mL) and DCM (60 mL). **IV-34b** was obtained as a white solid (587 mg, 1.39 mmol, 77% over 2 steps); mp 118–121 °C; <sup>1</sup>H NMR (400 MHz, CDCl<sub>3</sub>): δ 7.94 (d, *J* = 8.1 Hz, 1H, NH), 7.32–7.14 (m, 2H, arom.), 7.13–6.94 (m, 2H, arom.), 6.42 (s, 1H, NH), 4.51–4.32 (m, 3H, CH<sub>2</sub>, CH), 3.80 (t, *J* = 6.0 Hz, 1H, CH), 2.98 (d, *J* = 6.3 Hz, 2H, CH<sub>2</sub>), 2.70–2.55 (m, 4H, CH<sub>2</sub>, NH<sub>2</sub>), 1.75–1.51 (m, 3H, *i*-Pr-CH, CH<sub>2</sub>), 0.96–0.76 (m, 15H, *i*-Pr, *t*-Bu) ppm; <sup>13</sup>C NMR (101 MHz, CDCl<sub>3</sub>): δ 173.6, 172.1, 171.0, 162.2, 159.8, 130.1, 130.0, 129.3, 129.2, 125.3, 125.2, 124.39, 124.36, 115.5, 115.3, 52.5, 52.2, 50.7, 40.6, 39.8, 37.6, 37.5, 32.0, 27.3, 24.9, 23.0, 22.1 ppm; HRMS (*m/z*): MH<sup>+</sup> calcd for C<sub>22</sub>H<sub>35</sub>FN<sub>4</sub>O<sub>3</sub> 423.2766, found 423.2791.

**(2S)-2-Amino-N-[(1S)-1-[[2-chlorophenyl)methyl]carbamoyl]-3-methylbutyl]-N'-(2,2-dimethylpropyl)butanediamide (IV-34c).**



Synthesis according to general procedure B using **IV-32c** (461 mg, 1.81 mmol), **IV-28** (548 mg, 1.81 mmol), HATU (689 mg, 1.81 mmol), and DIPEA (0.32 mL, 1.84 mmol, 1.0 eq) in DMF (15 mL) within 48 h afforded the Boc-protected intermediate **IV-33c** as a white solid which was directly treated according to general procedure C using TFA (15 mL) and DCM (60 mL). **IV-34c** was obtained as a white solid (769 mg, 1.75 mmol, 97% over 2 steps); mp 151–153 °C; <sup>1</sup>H NMR (400 MHz, CDCl<sub>3</sub>): δ 7.95 (d, *J* = 8.1 Hz, 1H, NH), 7.40–7.21 (m, 4H, arom.), 7.16 (q, *J* = 6.4, 5.9 Hz, 1H, NH), 6.49 (s, 1H, NH), 4.59–4.36 (m, 3H, CH<sub>2</sub>, CH), 3.77 (dd, *J* = 7.1, 4.7 Hz, 1H, CH), 2.99 (d, *J* = 6.2 Hz, 2H, CH<sub>2</sub>), 2.76–2.47 (m, 4H, CH<sub>2</sub>, NH<sub>2</sub>), 1.81–1.57 (m, 3H, CH<sub>2</sub>, *i*-Pr -CH), 0.98–0.78 (m, 15H, *i*-Pr, *t*-Bu) ppm; <sup>13</sup>C NMR (75 MHz, CDCl<sub>3</sub>): δ 174.1, 172.1, 171.0, 135.6, 133.5, 129.8, 129.6, 128.9, 127.1, 52.6, 52.1, 50.7, 41.5, 40.6, 40.3, 31.9, 27.3, 24.9, 23.0, 22.1 ppm; HRMS (*m/z*): MNa<sup>+</sup> calcd for C<sub>22</sub>H<sub>35</sub>ClN<sub>4</sub>O<sub>3</sub> 461.2290, found 461.2288.

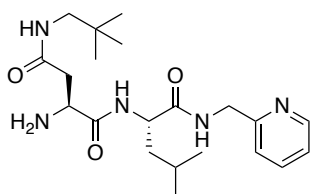
**(2S)-2-Amino-N'-(2,2-dimethylpropyl)-N-[(1S)-3-methyl-1-[[4-methylphenyl)methyl]carbamoyl]butyl]butanediamide (IV-34d).**



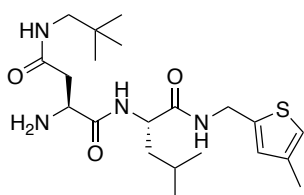
Synthesis according to general procedure B using **IV-32d** (424 mg, 1.81 mmol), **IV-28** (548 mg, 1.81 mmol), HATU (689 mg, 1.81 mmol), and DIPEA (0.32 mL, 1.84 mmol, 1.0 eq) in DMF (15 mL) within 48 h afforded the Boc-protected intermediate **IV-33d** as an off-white solid which was directly

treated according to general procedure C using TFA (15 mL) and DCM (60 mL). **IV-34d** was obtained as a white solid (651 mg, 1.56 mmol, 86% over 2 steps); mp 140–144 °C; <sup>1</sup>H NMR (400 MHz, CDCl<sub>3</sub>): δ 7.76 (d, *J* = 8.4 Hz, 1H, NH), 7.18–7.04 (m, 4H, arom.), 6.65 (t, 1H, NH), 6.08 (t, 1H, NH), 4.46–4.27 (m, 3H, CH<sub>2</sub>, CH), 3.66 (dd, *J* = 6.9, 4.7 Hz, 1H, CH), 2.99 (d, *J* = 6.3 Hz, 2H, CH<sub>2</sub>), 2.59 (qd, *J* = 14.7, 5.8 Hz, 2H, CH<sub>2</sub>), 2.32 (s, 3H, CH<sub>3</sub>), 1.70–1.49 (m, 3H, CH<sub>2</sub>, *i*-Pr-CH), 0.99–0.73 (m, 15H, *i*-Pr, *t*-Bu) ppm; <sup>13</sup>C NMR (75 MHz, CDCl<sub>3</sub>): δ 174.4, 171.7, 171.0, 137.2, 135.2, 129.5, 127.8, 52.8, 52.0, 50.7, 43.4, 40.7, 40.6, 31.9, 27.3, 25.0, 23.1, 22.1, 21.2 ppm; HRMS (*m/z*): MNa<sup>+</sup> calcd for C<sub>23</sub>H<sub>38</sub>N<sub>4</sub>O<sub>3</sub> 441.2836, found 441.2838.

**(2S)-2-Amino-N'-(2,2-dimethylpropyl)-N-[(1S)-3-methyl-1-[(pyridin-2-yl)methyl]carbamoyl]butanediamide (IV-34e).**

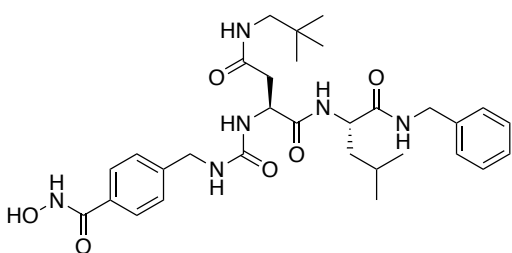


Synthesised according to general procedure B using **IV-32e** (400 mg, 1.81 mmol), **IV-28** (548 mg, 1.81 mmol), HATU (689 mg, 1.81 mmol), and DIPEA (0.32 mL, 1.84 mmol, 1.0 eq) in DMF (15 mL) within 48 h. Instead of washing with HCl, the crude mixture was dried *in vacuo* to remove excess DIPEA. The remaining Boc-protected intermediate **IV-33e** was directly treated according to general procedure C using TFA (15 mL) and DCM (60 mL). **IV-34e** was obtained as a brown oil (674 mg, 1.66 mmol, 92% over 2 steps); <sup>1</sup>H NMR (400 MHz, CDCl<sub>3</sub>): δ 8.81–8.67 (m, 1H, NH), 8.56–8.34 (m, 2H, arom.), 8.20 (s, 1H, NH), 7.68–7.49 (m, 2H, arom.), 7.17–7.06 (m, 1H, NH), 4.58–4.30 (m, 4H, 2 x CH, CH<sub>2</sub>), 3.16–2.83 (m, 4H, 2 x CH<sub>2</sub>), 1.70–1.52 (m, 3H, CH<sub>2</sub>, *i*-Pr-CH), 1.00–0.67 (m, 15H, *i*-Pr) ppm; <sup>13</sup>C NMR (101 MHz, CDCl<sub>3</sub>): δ 172.9, 172.7, 170.4, 170.2, 169.9, 169.8, 162.5, 162.2, 157.3, 157.1, 148.8, 148.6, 137.6, 137.4, 122.7, 122.4, 53.2, 52.9, 51.2, 51.0, 45.8, 44.9, 44.8, 40.7, 31.99, 31.95, 27.3, 24.9, 23.1, 22.9, 21.9, 21.7, 8.7 ppm; HRMS (*m/z*): MH<sup>+</sup> calcd for C<sub>21</sub>H<sub>35</sub>N<sub>5</sub>O<sub>3</sub> 406.2813, found 406.2810.

**(2S)-2-Amino-N'-(2,2-dimethylpropyl)-N-[(1S)-3-methyl-1-[[4-methylthiophen-2-yl)methyl]carbamoyl]butyl]butanediamide (IV-34f).**

Synthesis according to general procedure B using **IV-32f** (435 mg, 1.81 mmol), **IV-28** (548 mg, 1.81 mmol), HATU (689 mg, 1.81 mmol), and DIPEA (0.32 mL, 1.84 mmol, 1.0 eq) in DMF (15 mL) within 48 h afforded the Boc-protected intermediate **IV-33f** as a brown solid which was directly treated according to

general procedure C using TFA (15 mL) and DCM (60 mL). **IV-34f** was obtained as a brown solid (612 mg, 1.44 mmol, 80% over 2 steps); mp 81–83 °C; <sup>1</sup>H NMR (400 MHz, CDCl<sub>3</sub>): δ 7.85 (d, *J* = 8.4 Hz, 1H, NH), 7.07–6.93 (m, 1H, NH), 6.76–6.71 (m, 2H, arom.), 6.44–6.27 (m, 1H, NH), 4.51–4.47 (m, 2H, CH<sub>2</sub>), 4.41–4.33 (m, 1H, CH), 3.73–3.66 (m, 1H, CH), 3.00 (d, *J* = 6.3 Hz, 2H, CH<sub>2</sub>), 2.68–2.48 (m, 2H, CH<sub>2</sub>), 2.18 (s, 3H, CH<sub>3</sub>), 2.15 (s, 2H, NH<sub>2</sub>), 1.80–1.52 (m, 3H, *i*-Pr-CH, CH<sub>2</sub>), 0.97–0.85 (m, 15H, *i*-Pr, *t*-Bu) ppm; <sup>13</sup>C NMR (101 MHz, CDCl<sub>3</sub>): δ 174.0, 171.7, 171.0, 140.9, 137.6, 128.3, 120.2, 52.6, 52.0, 50.7, 40.5, 40.3, 38.5, 32.0, 27.4, 24.9, 23.1, 22.2, 15.8 ppm; HRMS (*m/z*): MH<sup>+</sup> calcd for C<sub>21</sub>H<sub>36</sub>N<sub>4</sub>O<sub>3</sub>S 425.2581, found 425.2584

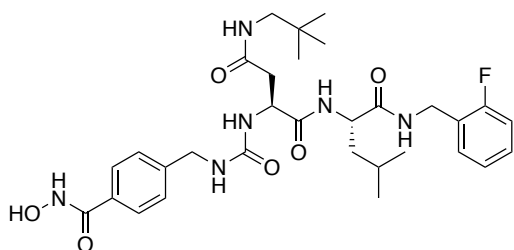
**(2S)-N-[(1S)-1-(Benzylcarbamoyl)-3-methylbutyl]-N'-(2,2-dimethylpropyl)-2-[[[4-(hydroxycarbamoyl)phenyl]methyl]carbamoyl]amino]butanediamide (IV-24a).**

Synthesis according to general procedure F using **IV-34a** (404 mg) yielded the ester **IV-35a** as a white solid (220 mg, 0.37 mmol, 37%) of which 178 mg (0.30 mmol) were directly treated according to general procedure G using hydroxylamine (50% solution in water; 0.55 mL,

8.98 mmol, 30 eq) and NaOH (120 mg, 3.00 mmol, 10 eq) within 2 h. Filtration over a layer of ISOLUTE PE-AX<sup>®</sup> afforded the desired product **IV-24a** as a pale-brown solid (93.0 mg, 0.16 mmol, 52%); mp 210 °C (decomp.); *t*<sub>R</sub>: 7.34 min, purity: 96.0%; <sup>1</sup>H NMR (400 MHz, DMSO-*d*<sub>6</sub>): δ 8.55 (t, *J* = 9.3, 7.7 Hz, 1H, NH), 8.10 (d, *J* = 8.2 Hz, 1H, NH), 7.98–7.87 (m, 1H, NH), 7.71–7.66 (m, 2H, arom.), 7.35–7.17 (m, 7H, arom.), 6.96 (t, *J* = 6.0 Hz, 1H, NH), 6.60 (d, *J* = 7.8 Hz, 1H, NH), 4.40 (q, *J* = 6.7 Hz, 1H, CH), 4.33–4.15 (m, 5H, 2 x CH<sub>2</sub>, CH), 2.80 (d, *J* = 6.1 Hz, 2H, CH<sub>2</sub>), 2.56 (d, *J* = 6.5 Hz, 2H, CH<sub>2</sub>), 1.65–1.45 (m, 3H, *i*-Pr-CH, CH<sub>2</sub>), 0.90–0.73 (m, 15H, *i*-Pr, *t*-Bu) ppm; <sup>13</sup>C NMR (75 MHz, DMSO-*d*<sub>6</sub>): δ 174.3, 172.0, 170.1, 163.7, 157.7, 143.8, 139.4, 131.3, 128.1, 127.1, 127.0, 126.70, 126.65, 126.6,

113.7, 51.2, 50.9, 49.7, 42.5, 42.1, 31.8, 27.2, 24.2, 24.0, 23.2, 21.3 ppm; HRMS (m/z): MNa<sup>+</sup> calcd for C<sub>31</sub>H<sub>44</sub>N<sub>6</sub>O<sub>6</sub> 619.3215, found 619.3228.

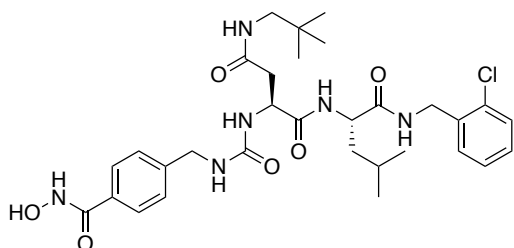
**(2S)-N'-(2,2-Dimethylpropyl)-N-[(1S)-1-[(2-fluorophenyl)methyl]carbamoyl]-3-methylbutyl]-2-[[[4-(hydroxycarbamoyl)phenyl]methyl]carbamoyl]amino]-butanediamide (IV-24b).**



Synthesis according to general procedure F using **IV-34b** (422 mg) yielded the ester **IV-35b** as a white solid (183 mg, 0.30 mmol, 30%) which was directly treated according to general procedure G using hydroxylamine (50% solution in water; 0.55 mL, 8.98 mmol, 30 eq) and NaOH (120 mg,

3.00 mmol, 10 eq) within 2 h. Filtration over a layer of ISOLUTE PE-AX<sup>®</sup> afforded the desired product **IV-24b** as a pale-brown solid (92.0 mg, 0.15 mmol, 50%); mp 210 °C (decomp.); t<sub>R</sub>: 7.42 min, purity: 98.5%; <sup>1</sup>H NMR (400 MHz, DMSO-*d*<sub>6</sub>): δ 8.55 (t, *J* = 6.0 Hz, 1H, NH), 8.11 (d, *J* = 8.2 Hz, 1H, NH), 7.89 (t, *J* = 6.2 Hz, 1H, NH), 7.72–7.62 (m, 2H, arom.), 7.33–7.25 (m, 4H, arom.), 7.20–7.08 (m, 2H, arom.), 6.82 (t, *J* = 6.0 Hz, 1H, NH), 6.41 (d, *J* = 7.9 Hz, 1H, NH), 4.44–4.35 (m, 1H, CH), 4.33–4.19 (m, 5H, CH<sub>2</sub>, CH<sub>2</sub>, CH), 2.82–2.75 (m, 2H, CH<sub>2</sub>), 2.57 (d, *J* = 6.5 Hz, 2H, CH<sub>2</sub>), 1.64–1.51 (m, 3H, CH<sub>2</sub>, *i*-Pr-CH), 0.91–0.74 (m, 15H, *i*-Pr, *t*-Bu) ppm; <sup>13</sup>C NMR (101 MHz, CDCl<sub>3</sub>): δ 172.1, 171.9, 170.1, 167.2, 166.1, 164.1, 163.9, 161.1, 158.7, 157.5, 144.0, 131.1, 129.3, 129.2, 128.7, 128.6, 126.8, 126.7, 126.2, 126.1, 126.0, 125.9, 124.2, 115.8, 115.0, 114.8, 51.2, 50.7, 49.6, 35.8, 31.8, 29.0, 27.2, 24.2, 23.2, 21.3, 19.5 ppm; HRMS (m/z): MNa<sup>+</sup> calcd for C<sub>31</sub>H<sub>43</sub>FN<sub>6</sub>O<sub>6</sub> 637.3120, found 637.3139.

**(2S)-N-[(1S)-1-[[[2-Chlorophenyl]methyl]carbamoyl]-3-methylbutyl]-N'-(2,2-dimethylpropyl)-2-[[[4-(hydroxycarbamoyl)phenyl]methyl]carbamoyl]amino]-butanediamide (IV-24c).**

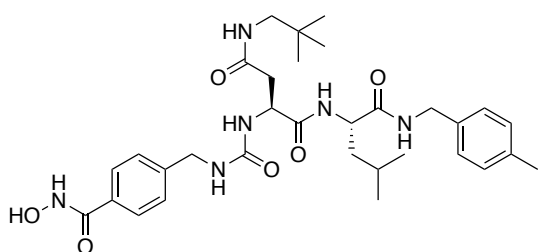


Synthesis according to general procedure F using **IV-34c** (483 mg, 1.00 mmol) yielded the ester **IV-35c** as a white solid (105 mg, 0.17 mmol, 17%) which was directly treated according to general procedure G using hydroxylamine (50%



solution in water; 0.30 mL, 4.90 mmol, 29 eq) and NaOH (60 mg, 1.50 mmol, 8.8 eq) within 3 h. Filtration over a layer of ISOLUTE PE-AX<sup>®</sup> afforded the desired product **IV-24c** as a pale-brown solid (65.0 mg, 0.10 mmol, 59%); mp 169 °C (decomp.);  $t_R$ : 7.71 min, purity: 95.1%; <sup>1</sup>H NMR (300 MHz, DMSO-*d*<sub>6</sub>): δ 8.63–8.55 (m, 1H, NH), 8.49 (t, *J* = 6.0 Hz, 1H, NH), 8.23–8.15 (m, 1H, NH), 7.96–7.86 (m, 1H, arom.), 7.79 (t, *J* = 6.4 Hz, 1H, NH), 7.71–7.65 (m, 1H, arom.), 7.46–7.22 (m, 6H, arom.), 6.93–6.83 (m, 1H, NH), 6.52 (d, *J* = 7.8 Hz, 1H, NH), 4.39–4.17 (m, 4H, CH<sub>2</sub>, 2 x CH), 3.50 (s, 2H, CH<sub>2</sub>), 2.83–2.71 (m, 2H, CH), 2.62–2.54 (m, 2H, CH<sub>2</sub>), 1.71 (s, 1H), 1.67–1.49 (m, 2H, CH<sub>2</sub>), 0.95–0.67 (m, 15H, *i*-Pr, *t*-Bu) ppm; <sup>13</sup>C NMR (101 MHz, DMSO-*d*<sub>6</sub>): δ 172.3, 172.2, 172.1, 171.3, 170.1, 169.6, 163.9, 163.8, 157.7, 156.2, 143.8, 136.2, 131.8, 131.8, 131.4, 129.0, 128.9, 128.5, 128.4, 127.1, 126.7, 126.7, 51.9, 51.5, 50.9, 49.7, 42.5, 37.7, 31.8, 27.2, 24.4, 24.2, 23.2, 23.1, 21.3, 21.3 ppm; HRMS (*m/z*): *M*<sup>-</sup> calcd for C<sub>31</sub>H<sub>43</sub>ClN<sub>6</sub>O<sub>6</sub> 629.2860, found 629.2817.

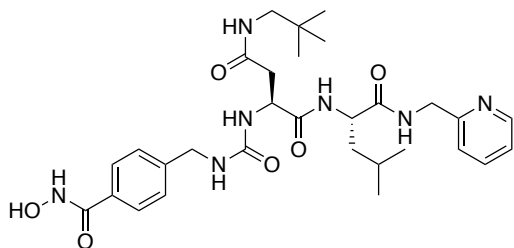
**(2S)-N'-(2,2-Dimethylpropyl)-2-[[{4-(hydroxycarbonyl)phenyl}methyl]carbamoyl]-amino]-N-[(1S)-3-methyl-1-[[{4-methylphenyl}methyl]carbamoyl]butyl]butane-diamide (**IV-24d**).**



Synthesis according to general procedure F using **IV-34d** (418 mg) yielded the ester **IV-35d** as a white solid (219 mg, 0.36 mmol, 36%) of which 180 mg (0.30 mmol) were directly treated according to general procedure G using hydroxylamine (50% solution in water; 0.55 mL,

8.98 mmol, 30 eq) and NaOH (120 mg, 3.00 mmol, 10 eq) within 90 min. Filtration over a layer of ISOLUTE PE-AX<sup>®</sup> afforded the desired product **IV-24d** as a pale-brown solid (101 mg, 0.17 mmol, 55%); mp 198 °C (decomp.);  $t_R$ : 7.61 min, purity: 96.9%; <sup>1</sup>H NMR (300 MHz, DMSO-*d*<sub>6</sub>): δ 8.49 (t, *J* = 6.0 Hz, 1H, NH), 8.04 (d, *J* = 8.3 Hz, 1H, NH), 7.89 (d, *J* = 6.2 Hz, 1H, NH), 7.73–7.64 (m, 2H, arom.), 7.33–7.24 (m, 2H, arom.), 7.15–7.05 (m, 4H, arom.), 6.89–6.78 (m, 1H, NH), 6.42 (d, *J* = 7.9 Hz, 1H, NH), 4.45–4.34 (m, 1H, CH), 4.31–4.07 (m, 5H, CH<sub>2</sub>, CH<sub>2</sub>, CH), 2.80 (d, *J* = 6.1 Hz, 2H, CH<sub>2</sub>), 2.56 (d, *J* = 6.4 Hz, 2H, CH<sub>2</sub>), 2.26 (s, 3H, CH<sub>3</sub>), 1.64–1.46 (m, 3H, CH<sub>2</sub>, *i*-Pr-CH), 0.94–0.73 (m, 15H, *i*-Pr, *t*-Bu) ppm; <sup>13</sup>C NMR (101 MHz, DMSO-*d*<sub>6</sub>): δ 171.83, 171.76, 170.1, 163.9, 157.6, 144.0, 136.4, 135.6, 131.1, 128.7, 127.1, 126.8, 126.7, 54.9, 51.2, 50.8, 49.7, 42.5, 41.8, 31.8, 27.2, 24.2, 23.2, 21.3, 20.7 ppm; HRMS (*m/z*): *M*Na<sup>+</sup> calcd for C<sub>32</sub>H<sub>46</sub>N<sub>6</sub>O<sub>6</sub> 633.3371, found 633.3380.

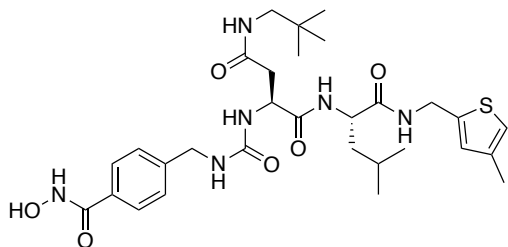
**(2S)-N'-(2,2-Dimethylpropyl)-2-[[{4-(hydroxycarbonyl)phenyl}methyl]carbamoyl]-amino]-N-[(1S)-3-methyl-1-[[{(pyridin-2-yl)methyl}carbamoyl]butyl]butanediamide (IV-24e).**



To a solution of **IV-34e** (405 mg, 1.00 mmol, 1.0 eq) and Et<sub>3</sub>N (0.14 mL, 1.00 mmol, 1.0 eq) in dry THF (5 mL) was added **IV-13** and the mixture was subjected to microwave irradiation at 70 °C and 150 W under vigorous stirring for 6 h. Upon completion of the reaction, the mixture was

diluted with DCM and washed with sat. aq. NaHCO<sub>3</sub> (5 x 10 mL), water (2 x 10 mL), and brine (1 x 10 mL). The organic layer was dried over MgSO<sub>4</sub> and the solvent was evaporated. The residue was purified by flash column chromatography (DCM/MeOH 10:0 to 9:1) to yield the ester **IV-35e** as a white solid (128 mg, 0.21 mmol, 21%) which was directly treated according to general procedure G using hydroxylamine (50% solution in water; 0.39 mL, 6.36 mmol, 30 eq) and NaOH (84.0 mg, 2.10 mmol, 10 eq) within 4 h. Due to incomplete precipitation after addition of HCl (pH 6), the aqueous mixture was extracted with EtOAc (3 x 50 mL) and the combined organics were dried over Na<sub>2</sub>SO<sub>4</sub> before the solvent was evaporated. Recrystallisation of the residue from MeOH (1 mL) and Et<sub>2</sub>O (10 mL) afforded **IV-24e** as a white solid (52.0 mg, 0.09 mmol, 41%); mp 139 °C (decomp.); t<sub>R</sub>: 6.07 min, purity: 96.9%; <sup>1</sup>H NMR (300 MHz, DMSO-*d*<sub>6</sub>): δ 11.15 (s, 1H, OH), 8.97 (s, 1H, NH-OH), 8.66–8.53 (m, 1H, NH), 8.45 (d, *J* = 4.8 Hz, 1H, NH), 8.10 (t, *J* = 7.8 Hz, 1H, NH), 7.90–7.61 (m, 4H, arom.), 7.32–7.17 (m, 4H, arom.), 6.87–6.72 (m, 1H, NH), 6.36 (t, *J* = 7.0 Hz, 1H, NH), 4.52–4.09 (m, 6H, CH<sub>2</sub>, CH<sub>2</sub>, 2 x CH), 2.79 (dd, *J* = 22.2, 6.2 Hz, 2H, CH<sub>2</sub>), 2.64–2.55 (m, 2H, CH<sub>2</sub>), 1.57 (s, 3H, CH<sub>2</sub>, *i*-Pr-CH), 0.97–0.64 (m, 15H, *i*-Pr, *t*-Bu) ppm; <sup>13</sup>C NMR (101 MHz, DMSO-*d*<sub>6</sub>): δ 172.22, 172.16, 172.0, 170.1, 169.6, 164.1, 158.6, 157.8, 157.5, 148.7, 144.0, 136.6, 131.1, 129.3, 126.7, 121.9, 120.5, 51.33, 51.28, 51.1, 50.7, 49.7, 49.6, 44.2, 42.5, 31.8, 31.8, 27.22, 27.18, 24.2, 23.2, 21.3 ppm; HRMS (*m/z*): MNa<sup>+</sup> calcd for C<sub>30</sub>H<sub>43</sub>N<sub>7</sub>O<sub>6</sub> 620.3167, found 620.3176.

**(2S)-N'-(2,2-Dimethylpropyl)-2-[[{4-(hydroxycarbamoyl)phenyl}methyl]carbamoyl]-amino]-N-[(1S)-3-methyl-1-[[{4-methylthiophen-2-yl}methyl]carbamoyl]butyl]-butanediamide (**IV-24f**).**



To a solution of **IV-34f** (410 mg, 1.00 mmol, 1.0 eq) and Et<sub>3</sub>N (0.14 mL, 1.00 mmol, 1.0 eq) in dry THF (5 mL) was added **IV-13** and the mixture was subjected to microwave irradiation at 70 °C and 150 W under vigorous stirring for 6 h. Upon completion of the reaction, the mixture was

diluted with DCM and insoluble residues were removed by filtration and rinsed with water. The organic filtrate was washed with sat. aq. NaHCO<sub>3</sub> (5 x 10 mL), water (2 x 10 mL), and brine (1 x 10 mL). After drying over MgSO<sub>4</sub>, the solvent was removed under reduced pressure. The crude extract and the insoluble residues were combined and purified by column chromatography (DCM/MeOH 19:1) to yield the ester **IV-35f** as a brown solid (63.0 mg, 0.10 mmol, 10%) which was directly treated according to general procedure G using hydroxylamine (50% solution in water; 0.22 mL, 3.59 mmol, 36 eq) and NaOH (50.0 mg, 1.25 mmol, 12 eq) in MeOH (2 mL) and DCM (0.5 mL) within 4 h. Filtration over a layer of ISOLUTE PE-AX<sup>®</sup> afforded the desired product **IV-24f** as a pale-brown solid (30.0 mg, 0.05 mmol, 50%); mp 191 °C (decomp.); t<sub>R</sub>: 7.55 min, purity: 96.6%; <sup>1</sup>H NMR (300 MHz, DMSO-*d*<sub>6</sub>): δ 8.61 (s, 1H, NH), 8.04 (s, 1H, NH), 7.92 (s, 1H, NH), 7.71–7.61 (m, 2H, arom.), 7.30–7.17 (m, 2H, arom.), 6.98–6.68 (m, 3H, 2 x arom., NH), 6.51 (s, 1H, NH), 4.47–4.15 (m, 6H, CH<sub>2</sub>, CH<sub>2</sub>, 2 x CH), 2.85 (s, 2H, CH<sub>2</sub>), 2.13 (s, 3H, CH<sub>3</sub>), 1.66 (s, 1H, CH<sub>2</sub>), 1.60–1.45 (m, 3H, CH<sub>2</sub>, *i*-Pr -CH), 1.25 (s, 1H, CH<sub>2</sub>), 0.92–0.75 (m, 15H, *i*-Pr, *t*-Bu) ppm; <sup>13</sup>C NMR (101 MHz, DMSO-*d*<sub>6</sub>): δ 171.8, 171.7, 170.1, 163.7, 157.7, 143.9, 142.1, 136.4, 131.2, 127.4, 126.73, 126.68, 119.8, 51.1, 50.9, 49.7, 42.5, 37.3, 31.9, 27.3, 24.1, 23.2, 21.3, 15.4 ppm; HRMS (m/z): MNa<sup>+</sup> calcd for C<sub>30</sub>H<sub>44</sub>N<sub>6</sub>O<sub>6</sub>S 639.2935, found 639.2968.

## 4.5 References

Adams J. 2004. The proteasome: A suitable antineoplastic target. *Nat Rev Cancer* **4**: 349–360.

Anighoro A, Bajorath J, Rastelli G. 2014. Polypharmacology: Challenges and opportunities in drug discovery. *J Med Chem* **57**: 7874–7887.

Atkinson SJ, Soden PE, Angell DC, Bantscheff M, Chung C-W, Giblin KA, Smithers N, Furze RC, Gordon L, Drewes G, Rioja I, Witherington J, Parra NJ, Prinjha RK. 2014. The structure based design of dual HDAC/BET inhibitors as novel epigenetic probes. *MedChemComm* **5**: 342–351.

Bali P, Pranpat M, Bradner J, Balasis M, Fiskus W, Guo F, Rocha K, Kumaraswamy S, Boyapalle S, Atadja P, Seto E, Bhalla K. 2005. Inhibition of histone deacetylase 6 acetylates and disrupts the chaperone function of heat shock protein 90. *J Biol Chem Vol.* **280**: 26729–26734.

Beck A, Goetsch L, Dumontet C, Corvaia N. 2017. Strategies and challenges for the next generation of antibody-drug conjugates. *Nat Rev Drug Discov* **16**: 315–337.

Bhatia S, Krieger V, Groll M, Osko JD, Reßing N, Ahlert H, Borkhardt A, Kurz T, Christianson DW, Hauer J, Hansen FK. 2018. Discovery of the first-in-class dual histone deacetylase-proteasome inhibitor. *J Med Chem* **61**: 10299–10309.

Blackburn C, Barrett C, Blank JL, Bruzzese FJ, Bump N, Dick LR, Fleming P, Garcia K, Hales P, Hu Z, Jones M, Liu JX, Sappal DS, Sintchak MD, Tsu C, Gigstad KM. 2010b. Optimization of a series of dipeptides with a P3 threonine residue as non-covalent inhibitors of the chymotrypsin-like activity of the human 20S proteasome. *Bioorg Med Chem Lett* **20**: 6581–6586.

Blackburn C, Barrett C, Blank JL, Bruzzese FJ, Bump N, Dick LR, Fleming P, Garcia K, Hales P, Jones M, Liu JX, Nagayoshi M, Sappal DS, Sintchak MD, Tsu C, Xia C, Zhou X, Gigstad KM. 2012. Optimization of a series of dipeptides with a P3 b-neopentyl asparagine residue as non-covalent inhibitors of the chymotrypsin-like activity of human 20S proteasome. *Med Chem Commun* **3**: 710–719.

Blackburn C, Gigstad KM, Hales P, Garcia K, Jones M, Bruzzese FJ, Barrett C, Liu JX, Soucy TA, Sappal DS, Bump N, Olhava EJ, Fleming P, Dick LR, Tsu C, Sintchak MD, Blank JL. 2010a. Characterization of a new series of non-covalent proteasome inhibitors with exquisite potency and selectivity for the 20S  $\beta$ 5-subunit. *Biochem J* **430**: 461–476.

Böhme D, Krieghoff J, Beck-Sickinger AG. 2016. Double methotrexate-modified neuropeptide Y analogues express increased toxicity and overcome drug resistance in breast cancer cells. *J Med Chem* **59**: 3409–3417.

Boyault C, Sadoul K, Pabion M, Khochbin S. 2007. HDAC6, at the crossroads between cytoskeleton and cell signaling by acetylation and ubiquitination. *Oncogene* **26**: 5468–5476.

Breslow R, Marks P, Mahendran A, Yao Y, inventors. The Trustees of Columbia University in the City of New York; Memorial Sloan-Kettering Cancer Center, assignees; White JP, Cooper & Dunham LLP, agents. *Selective HDAC6 inhibitors*. U.S. Patent Application US20160347732 A1. 2014-12-23 (filing date).

Chen M-C, Chen C-H, Wang J-C, Tsai A-C, Liou J-P, Pan S-L, Teng C-M. 2013. The HDAC inhibitor, MPT0E028, enhances erlotinib-induced cell death in EGFR-TKI-resistant NSCLC cells. *Cell Death Dis* **4**: e810.

Cincinelli R, Musso L, Artali R, Guglielmi MB, La Porta I, Melito C, Colelli F, Cardile F, Signorino G, Fucci A, Frusciante M, Pisano C, Dallavalle S. 2018. Hybrid topoisomerase I and HDAC inhibitors as dual action anticancer agents. *PLoS ONE* **13**: e0205018.

Depetter Y, Geurs S, De Vreese R, Goethals S, Vandoorn E, Laevens A, Steenbrugge J, Meyer E, de Tullio P, Bracke M, D'hooghe M, De Wever O. 2019. Selective pharmacological inhibitors of HDAC6 reveal biochemical activity but functional tolerance in cancer models. *Int J Cancer* **145**: 735–747.

Duan Y, Ma Y, Qin W, Ding L, Zheng Y, Zhu Y, Zhai X, Yang J, Ma C, Guan Y. 2017. Design and synthesis of tranlycypromine derivatives as novel LSD1/HDACs dual inhibitors for cancer treatment. *Eur J Med Chem* **140**: 392–402.

de Freitas RF, Harding RJ, Franzoni I, Ravichandran M, Mann MK, Ouyang H, Lautens M, Santhakumar V, Arrowsmith CH, Schapira M. 2018. Identification and structure-activity relationship of HDAC6 zinc-finger ubiquitin binding domain inhibitors. *J Med Chem* **61**: 4517–4527.

Greve G, Schiffmann I, Pfeifer D, Pantic M, Schüler J, Lübbert M. 2015. The pan-HDAC inhibitor panobinostat acts as a sensitizer for erlotinib activity in EGFR-mutated and -wildtype non-small cell lung cancer cells. *BMC Cancer* **15**: 947.

Gu S, Cui D, Chen X, Xiong X, Zhao Y. 2018. PROTACs: An emerging targeting technique for protein degradation in drug discovery. *BioEssays* **40**: 1700247.

Guerrant W, Patil V, Canzoneri JC, Oyelere AK. 2012. Dual targeting of histone deacetylase and topoisomerase II with novel bifunctional inhibitors. *J Med Chem* **55**: 1465–1477.

Guerrant W, Patil V, Canzoneri JC, Yao L-P, Hood R, Oyelere AK. 2013. Dual-acting histone deacetylase-topoisomerase I inhibitors. *Bioorg Med Chem Lett* **23**: 3283–3287.

Hai Y, Christianson DW. 2016. Histone deacetylase 6 structure and molecular basis of catalysis and inhibition. *Nat Chem Biol* **12**: 741–747.

Harding RJ, de Freitas RF, Collins P, Franzoni I, Ravichandran M, Ouyang H, Juarez-Ornelas KA, Lautens M, Schapira M, von Delft F, Santhakumar V, Arrowsmith CH. 2017. Small molecule antagonists of the interaction between the histone deacetylase 6 zinc-finger domain and ubiquitin. *J Med Chem* **60**: 9090–9096.

He S, Dong G, Li Y, Wu S, Wang W, Sheng C. 2020. Potent dual BET/HDAC inhibitors for efficient treatment of pancreatic cancer. *Angew Chem Int Ed* **59**: 3028–3032.

Hideshima T, Bradner JE, Wong J, Chauhan D, Richardson P, Schreiber SL, Anderson KC. 2005. Small-molecule inhibition of proteasome and aggresome function induces synergistic antitumor activity in multiple myeloma. *PNAS* **102**: 8567–8572.

Hideshima T, Richardson PG, Anderson KC. 2011. Mechanism of action of proteasome inhibitors and deacetylase inhibitors and the biological basis of synergy in multiple myeloma. *Mol Cancer Ther* **10**: 2034–2042.

Hoppenz P, Els-Heindl S, Beck-Sickinger AG. 2020. Peptide-drug conjugates and their targets in advanced cancer therapies. *Front Chem* **8**: 571.

Huber EM, Groll M. 2012. Inhibitors for the immuno- and constitutive proteasome: Current and future trends in drug development. *Angew Chem Int Ed* **51**: 8708–8720.

Jenke R, Reßing N, Hansen FK, Aigner A, Büch T. 2021. Anticancer therapy with HDAC inhibitors: Mechanism-based combination strategies and future perspectives. *Cancers* **13**: 634.

Kalin JH, Wu M, Gomez AV, Song Y, Das J, Hayward D, Adejola N, Wu M, Panova I, Chung HJ, Kim E, Roberts HJ, Roberts JM, Prusevich P, Jeliaskov JR, Burman SSR, Fairall L, Milano C, Eroglu A, Proby CM, Dinkova-Kostova AT, Hancock WW, Gray JJ, Bradner JE, Valente S, Mai A, Anders NM, Rudek MA, Hu Y, Ryu B, Schwabe JWR, Mattevi A, Alani RM, Cole PA. 2018. Targeting the CoREST complex with dual histone deacetylase and demethylase inhibitors. *Nature Commun* **9**: 53.

Karagöz GE, Rüdiger SGD. 2015. Hsp90 interaction with clients. *Trends Biochem Sci* **40**: 117–125.

Kawaguchi Y, Kovacs JJ, McLaurin A, Vance JM, Ito A, Yao T-P. 2003. The deacetylase HDAC6 regulates aggresome formation and cell viability in response to misfolded protein stress. *Cell* **115**: 727–738.

Kovacs JJ, Murphy PJM, Gaillard S, Zhao X, Wu J-T, Nicchitta CV, Yoshida M, Toft DO, Pratt WB, Yao T-P. 2005. HDAC6 regulates Hsp90 acetylation and chaperone-dependent activation of glucocorticoid receptor. *Mol Cell* **18**: 601–607.

Krieger V. Synthese, Konformationsanalyse und biologische Evaluierung von neuartigen antitumoraktiven Peptoid-Derivaten. PhD [dissertation]. Düsseldorf: Heinrich Heine University; 2017. Available from: <https://docserv.uni-duesseldorf.de/servlets/DocumentServlet?id=42955>.

Lai C-J, Bao R, Tao X, Wang J, Atoyan R, Qu H, Wang D-G, Yin L, Samson M, Forrester J, Zifcak B, Xu G-X, DellaRocca S, Zhai H-X, Cai X, Munger WE, Keegan M, Pepicelli CV, Qian C. 2010. CUDC-101, a multitargeted inhibitor of histone deacetylase, epidermal growth factor receptor, and human epidermal growth factor receptor 2, exerts potent anticancer activity. *Cancer Res* **70**: 3647–3656.

Lecker SH, Goldberg AL, Mitch WE. 2006. Protein degradation by the ubiquitin–proteasome pathway in normal and disease states. *J Am Soc Nephrol* **17**: 1807–1819.

de Lera AR, Ganesan A. 2016. Epigenetic polypharmacology: from combination therapy to multitargeted drugs. *Clin Epigenetics* **8**: 105.

de Lera AR, Ganesan A. 2020. Two-hit wonders: The expanding universe of multitargeting epigenetic agents. *Curr Opin Chem Biol* **57**: 135–154.

Li X, Song Y. 2020. Proteolysis-targeting chimera (PROTAC) for targeted protein degradation and cancer therapy. *J Hematol Oncol* **13**: 50.

Liu T, Wan Y, Xiao Y, Xia C, Duan G. 2020. Dual-target inhibitors based on HDACs: Novel antitumor agents for cancer therapy. *J Med Chem* **63**: 8977–9002.

Lötsch J, Geisslinger G. 2011. Low-dose drug combinations along molecular pathways could maximize therapeutic effectiveness while minimizing collateral adverse effects. *Drug Discov Today* **16**: 1001–1006.

Luan Y, Li J, Bernatchez JA, Li R. 2019. Kinase and histone deacetylase hybrid inhibitors for cancer therapy. *J Med Chem* **62**: 3171–3183.

Maher RL, Hanlon J, Hajjar ER. 2014. Clinical consequences of polypharmacy in elderly. *Expert Opin Drug Saf* **13**: 57–65.

Manasanch EE, Orlowski RZ. 2017. Proteasome inhibitors in cancer therapy. *Nat Rev Clin Oncol* **14**: 417–433.

Martin NI, Woodward JJ, Marletta MA. 2006. *N*<sup>G</sup>-Hydroxyguanidines from primary amines. *Org Lett* **8**: 4035–4038.

Masnoon N, Shakib S, Kalisch-Ellett L, Caughey GE. 2017. What is polypharmacy? A systematic review of definitions. *BMC Geriatrics* **17**: 230.

Mehndiratta S, Lin M-H, Wu Y-W, Chen C-H, Wu T-Y, Chuang K-H, Chao M-W, Chen Y-Y, Pan S-L, Chen M-C, Liou J-P. 2020. *N*-alkyl-hydroxybenzoyl anilide hydroxamates as dual inhibitors of HDAC and Hsp90, downregulating IFN- $\gamma$  induced PD-L1 expression. *Eur J Med Chem* **185**: 111725.

Moreau P. 2013. Panobinostat to revert bortezomib resistance. *Blood* **122**: 2292–2293.

Morera L, Lübbert M, Jung M. 2016. Targeting histone methyltransferases and demethylases in clinical trials for cancer therapy. *Clin Epigenetics* **8**: 57.

Morphy R, Kay C, Rankovic Z. 2004. From magic bullets to designed multiple ligands. *Drug Discov Today* **9**: 641–651.

Nakagawa T, Takeuchi S, Yamada T, Ebi H, Sano T, Nanjo S, Ishikawa D, Sato M, Hasegawa Y, Sekido Y, Yano S. 2013. EGFR-TKI resistance due to BIM polymorphism can be circumvented in combination with HDAC inhibition. *Cancer Res* **73**: 2428–2434.

Noguchi-Yachide T, Sakai T, Hashimoto Y, Yamaguchi T. 2015. Discovery and structure-activity relationship studies of *N*<sup>6</sup>-benzoyladenine derivatives as novel BRD4 inhibitors. *Bioorg Med Chem* **23**: 953–959.

Ojha R, Huang H-L, HuangFu W-C, Wu Y-W, Nepali K, Lai M-J, Su C-J, Sung T-Y, Chen Y-L, Pan S-L, Liou J-P. 2018. 1-Aroylindoline-hydroxamic acids as anticancer agents, inhibitors of Hsp90 and HDAC. *Eur J Med Chem* **150**: 667–677.

Ouyang H, Ali YO, Ravichandran M, Dong A, Qiu W, MacKenzie F, Dhe-Paganon S, Arrowsmith CH, Zhai RG. 2012. Protein aggregates are recruited to aggresome by histone deacetylase 6 via unanchored ubiquitin C termini. *J Biol Chem* **287**: 2317–2327.

Pearson, DA, Blanchette M, Baker ML, Guindon CA. 1989. Trialkylsilanes as scavengers for the trifluoroacetic acid deblocking of protecting groups in peptide synthesis. *Tet Lett* **30**: 2739–2742.

Pinzi L, Benedetti R, Altucci L, Rastelli G. 2020. Design of dual inhibitors of histone deacetylase 6 and heat shock protein 90. *ACS Omega* **5**: 11473–11480.



Pottier C, Fresnais M, Gilon M, Jérusalem G, Longuespée R, Sounni NE. 2020. Tyrosine kinase inhibitors in cancer: Breakthrough and challenges of targeted therapy. *Cancers* **12**: 731.

Proschak E, Stark H, Merk D. 2019. Polypharmacology by design: A medicinal chemist's perspective on multitargeting compounds. *J Med Chem* **62**: 420–444.

Qian C, Lai C-J, Bao R, Wang D-G, Wang J, Xu G-X, Atoyan R, Qu H, Yin L, Samson M, Zifcak B, Ma AWS, DellaRocca S, Borek M, Zhai H-X, Cai X, Voi M. 2012. Cancer network disruption by a single molecule inhibitor targeting both histone deacetylase activity and phosphatidylinositol 3-kinase signaling. *Clin Cancer Res* **18**: 4104–4113.

Rabal O, Sánchez-Arias JA, Cuadrado-Tejedor M, de Miguel I, Pérez-González M, García-Barroso C, Ugarte A, Estella-Hermoso de Mendoza A, Saéz E, Espelosin M, Ursua S, Haizhong T, Wei W, Musheng X, Garcia-Osta A, Oyarzabal J. 2019. Discovery of *in vivo* chemical probes for treating Alzheimer's disease: Dual phosphodiesterase 5 (PDE5) and class I histone deacetylase selective inhibitors. *ACS Chem Neurosci* **10**: 1765–1782.

Ramsay RR, Popovic-Nikolic MR, Nikolic K, Uliassi E, Bolognesi ML. 2018. A perspective on multi-target drug discovery and design for complex diseases. *Clin Trans Med* **7**: 3.

Reßing N, Sönnichsen M, Osko JD, Schöler A, Schliehe-Diecks J, Skerhut A, Borkhardt A, Hauer J, Kassack MU, Christianson DW, Bhatia S, Hansen FK. 2020. Multicomponent synthesis, binding mode, and structure-activity relationship of selective histone deacetylase 6 (HDAC6) inhibitors with bifurcated capping groups. *J Med Chem* **63**: 10339–10351.

Richardson PG, Hungria VTM, Yoon S-S, Beksac M, Dimopoulos MA, Elghandour A, Jedrzejczak WW, Guenther A, Nakorn TN, Siritanaratkul N, Schlossman RL, Hou J, Moreau P, Lonial S, Lee JH, Einsele H, Sopala M, Bengoudifa B-R, Corrado C, Binlich F, San-Miguel J-F. 2016. Panobinostat plus bortezomib and dexamethasone in previously treated multiple myeloma: outcomes by prior treatment. *Blood* **127**: 713–721.

Richardson PG, Schlossman RL, Alsina M, Weber DM, Coutre SE, Gasparetto C, Mukhopadhyay S, Ondovik MS, Khan M, Paley CS, Lonial S. 2013. PANORAMA 2: panobinostat in combination with bortezomib and dexamethasone in patients with relapsed and bortezomib-refractory myeloma. *Blood* **122**: 2331–2337.

Riva E, Gagliardi S, Mazzoni C, Passarella D, Rencurosi A, Vigo D, Martinelli M. 2009. Efficient continuous flow synthesis of hydroxamic acids and suberoylanilide hydroxamic acid preparation. *J Org Chem* **74**: 3540–3543.

Sakamoto KM, Kim KB, Kumagai A, Mercurio F, Crews CM, Deshaies RJ. 2001. Protacs: Chimeric molecules that target proteins to the Skp1–Cullin–F box complex for ubiquitination and degradation. *PNAS* **98**: 8554–8559.

San-Miguel JF, Einsele H, Moreau P. 2016. The role of panobinostat plus bortezomib and dexamethasone in treating relapsed or relapsed and refractory multiple myeloma: A European perspective. *Adv Ther* **33**: 1896–1920.

Scripture CD, Figg WD. 2006. Drug interactions in cancer therapy. *Nat Rev Cancer* **6**: 546–558.

Seo YH. 2015. Dual inhibitors against topoisomerases and histone deacetylases. *J Cancer Prev* **20**: 85–91.

Shao M, He L, Zheng L, Huang L, Zhou Y, Wanga T, Chen Y, Shen M, Wanga F, Yang Z, Chen L. 2017. Structure-based design, synthesis and *in vitro* antiproliferative effects studies of novel dual BRD4/HDAC inhibitors. *Bioorg Med Chem Lett* **27**: 4051–4055.

Sinatra L, Bandolik JJ, Roatsch M, Sönnichsen M, Schoeder CT, Hamacher A, Schöler A, Borkhardt A, Meiler J, Bhatia S, Kassack MU, Hansen FK. 2020. Hydroxamic acids immobilized on resins (HAIRs): Synthesis of dual-targeting HDAC inhibitors and HDAC degraders (PROTACs). *Angew Chem Int Ed* **59**: 22494–22499.

Smalley JP, Cowley SM, Hodgkinson JT. 2020. Bifunctional HDAC therapeutics: One drug to rule them all? *Molecules* **25**: 4394.

Soldatos TG, Jackson DB. 2019. Adverse event circumstances and the case of drug interactions. *Healthcare* **7**: 45.

Stenzel K, Hamacher A, Hansen FK, Gertzen CGW, Senger J, Marquardt V, Marek L, Marek M, Romier C, Remke M, Jung M, Gohlke H, Kassack MU, Kurz T. 2017. Alkoxyurea-based histone deacetylase inhibitors increase cisplatin potency in chemoresistant cancer cell lines. *J Med Chem* **60**: 5334–5348.

Subramanian S, Bates SE, Wright JJ, Espinoza-Delgado I, Piekarczyk RL. 2010. Clinical toxicities of histone deacetylase inhibitors. *Pharmaceuticals* **3**: 2751–2767.

Suraweera A, O'Byrne KJ, Richard DJ. 2018. Combination therapy with histone deacetylase inhibitors (HDACi) for the treatment of cancer: Achieving the full therapeutic potential of HDACi. *Front Oncol* **8**: 92.

Tang F, Yang Z, Tan Y, Li AY. 2020. Super-enhancer function and its application in cancer targeted therapy. *NPJ Precis Oncol* **4**: 2.

Tomaselli D, Lucidi A, Rotili D, Mai A. 2020. Epigenetic polypharmacology: A new frontier for epi-drug discovery. *Med Res Rev* **40**: 190–244.

Tu HJ, Lin YJ, Chao MW, Sung TY, Wu YW, Chen YY, Lin MH, Liou JP, Pan SL, Yang CR. 2018. The anticancer effects of MPT0G211, a novel HDAC6 inhibitor, combined with chemotherapeutic agents in human acute leukaemia cells. *Clin Epigenetics* **10**: 162.

Vogl DT, Raje N, Jagannath S, Richardson P, Hari P, Orlowski R, Supko JG, Tamang D, Yang M, Jones SS, Wheeler C, Markelewicz RJ, Lonial S. 2017. Ricolinostat, the first selective histone deacetylase 6 inhibitor, in combination with bortezomib and dexamethasone for relapsed or refractory multiple myeloma. *Clin Cancer Res* **23**: 3307–3315.

Vrettos EI, Mező G, Tzakos AG. 2018. On the design principles of peptide–drug conjugates for targeted drug delivery to the malignant tumor site. *Beilstein J Org Chem* **14**: 930–954.

Witt O, Deubzer HE, Milde T, Oehme I. 2009. HDAC family: What are the cancer relevant targets? *Canc Lett* **277**: 8–21.

Wobser M, Weber A, Glunz A, Tauch S, Seitz K, Butelmann T, Hesbacher S, Goebeler M, Bartz R, Kohlhof H, Schrama D, Houben R. 2019. Elucidating the mechanism of action of domatinostat (4SC-202) in cutaneous T cell lymphoma cells. *J Hematol Oncol* **12**: 30.

Xiao Y, Zhang X. 2020. Recent advances in small molecular modulators targeting histone deacetylase 6. *Future Drug Discov* **2**: FDD53.

Xie R, Li Y, Tang P, Yuan Q. 2017. Rational design, synthesis and preliminary antitumor activity evaluation of a chlorambucil derivative with potent DNA/HDAC dual-targeting inhibitory activity. *Bioorg Med Chem Lett* **27**: 4415–4420.

Xie R, Tang P, Yuan Q. 2018. Rational design and characterization of a DNA/HDAC dual-targeting inhibitor containing nitrogen mustard and 2-aminobenzamide moieties. *MedChemComm* **9**: 344–352.

Yang H, Lv W, He M, Deng H, Li H, Wu W, Rao Y. 2019. Plasticity in designing PROTACs for selective and potent degradation of HDAC6. *Chem Commun* **55**: 14848–14851.

Zhang Z, Hou S, Chen H, Ran T, Jiang F, Bian Y, Zhang D, Zhi Y, Wang L, Zhang L, Li H, Zhang Y, Tang W, Lu T, Chen Y. 2016. Targeting epigenetic reader and eraser: Rational design, synthesis and *in vitro* evaluation of dimethylisoxazoles derivatives as BRD4/HDAC dual inhibitors. *Bioorg Med Chem Lett* **26**: 2931–2935.

Zhijun H, Shusheng W, Han M, Jianping L, Li-Sen Q, Dechun L. 2016. Pre-clinical characterization of 4SC-202, a novel class I HDAC inhibitor, against colorectal cancer cells. *Tumor Biol* **37**: 10257–10267.

Zhou Y, Liu X, Xue J, Liu L, Liang T, Li W, Yang X, Hou X, Fang H. 2020. Discovery of peptide boronate derivatives as histone deacetylase and proteasome dual inhibitors for overcoming bortezomib resistance of multiple myeloma. *J Med Chem* **63**: 4701–4715.

Zhu M-K, Zhao J-F, Loh T-P. 2011. Palladium-catalyzed C-C bond formation of arylhydrazines with olefins via carbon-nitrogen bond cleavage. *Org Lett* **13**: 6308–6311.

# Chapter 5: Investigation of (difluoromethyl)-1,3,4-oxadiazole as a novel HDAC6-selective zinc-binding group

## 5.1 Introduction

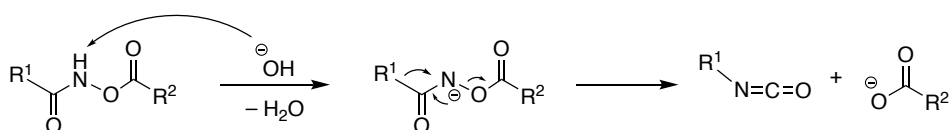
### 5.1.1 Drawbacks of hydroxamates as HDAC inhibitors

Crystallographic data obtained for HDAC6 CD2 revealed that zinc coordination of the substrate initiates the deacetylation process (Hai & Christianson 2016). The formation of such transition metal-ligand complexes requires the partially empty d-orbitals of the metal ion to be filled up with electrons donated by suitable ligands. This process yields polyhedral complexes of varying stabilities that depend on the quality of the metal-ligand interactions. Once more appropriate electron donors emerge, ligands in seemingly stable complexes may be replaced to optimise the stability constant or the coordination geometry, which may ultimately add up to virtually inert complexes. Sufficient chelating qualities of inhibitors that are supposed to compete against natural substrates are thus crucial and need to be aligned with structural demands.

As for the zinc ions present in HDAC enzymes, the hydroxamate motif  $C(=O)-NH-OH$  has been established as a reliable chelator which still dominates the majority of all preclinical HDACi and, except for the fatty acids, the entirety of non-natural pan-HDACi in clinical trials. A second ZBG common in class I-selective clinical candidates is the aryl-substituted *ortho*-aminoanilide group. It was specifically designed to engage the foot pockets in HDACs 1 and 2 and is not complementary to other isoforms except, to some extent, HDAC3 (Ho et al. 2020). Further discrimination in favour of HDACs 1 and 2 can be accomplished by attaching aryl groups in *para*-position to the amino group as those fit well into the foot pockets (Methot et al. 2008; Methot et al. 2014; Ho et al. 2020). If preferred, HDAC3 affinity can be promoted by introducing fluorine substituents in *para*-position to the amide group (Ho et al. 2020; Wagner et al. 2016). The potency of *ortho*-aminoanilide-based HDACi was initially doubted but meanwhile, it turned out that the compounds exert their activity after longer incubation times than hydroxamate-based inhibitors (Chou et al. 2008). This behaviour is attributed to

their characteristic *slow-on/slow-off* kinetics and typically results in delayed but prolonged histone acetylation (Chou et al. 2008; Methot et al. 2014; Ho et al. 2020).

In spite of the predominance in HDACi, it has long been acknowledged that the incorporation of hydroxamate groups into drugs is problematic (Wang & Lee 1977; Shen & Kozikowski 2016). Due to their low  $pK_a$  values ranging between 8 and 9, hydroxamates access the active site in a neutral state and are prone to being deprotonated upon metal-coordination (Shen & Kozikowski 2016; Porter et al. 2018). For HDAC6, both monodentate and bidentate binding modes have yet been observed (Porter et al. 2018; Porter et al. 2017). A drawback of the strong chelation by hydroxamates is the susceptibility to undergoing unpredictable off-target interactions. In complex organisms that assemble reams of metalloproteins, this point seems particularly relevant as it may be the source of severe adverse effects (Shen & Kozikowski 2016). The most obvious way to tackle such complications is target-specific drug design which may indeed help minimise the likelihood of unwanted interactions; nevertheless, there are other complications that may still arise.



**Scheme 5.1.** Mechanism of the Lossen rearrangement converting hydroxamate esters into isocyanates.

Under physiological conditions, hydroxamate groups bear the danger of being acetylated by acetyl-CoA. The resulting hydroxamate esters are, in turn, likely to undergo intramolecular rearrangements yielding toxic species (Shen & Kozikowski 2016). The underlying reaction was first described by Lossen in 1869 (Scheme 5.1; Yale 1943; Lossen 1869; Lossen 1872). In presence of bases, hydroxamates are able to transform into the corresponding isocyanates which act as strong and highly reactive electrophiles with the ability to attack DNA strands and other physiological targets, thus causing severe and irreversible mutagenic damage with carcinogenic potential (Shen & Kozikowski 2016). Accordingly, Shen and Kozikowski link the mutagenic and clastogenic effects of FDA-approved HDACi, which were apparent in the Ames test, mouse models, and several *in vitro* studies, to the hazardous potential of hydroxamates (Shen & Kozikowski 2016). The authors moreover mention the possibility that the mutagenic potential of hydroxamate-based HDACi could be triggered by metabolic transformation into the corresponding carboxylic acids which goes along with the

release of hydroxylamine, a highly reactive mutagen (Shen & Kozikowski 2016).

In conclusion, it cannot be ruled out that the side effects observed for hydroxamate-based HDACi are accompanied by serious mutagenic potential. The identification of alternative ZBGs for inhibitors of HDACs and other metal-dependent enzymes is therefore a crucial requirement for a less aggressive, more targeted cancer therapy.

### 5.1.2 Potential new zinc-binding groups

Attempts to overcome the drawbacks of the hydroxamate motif by finding a suitable replacement go back to the early days of epigenetic drug discovery. In 2007, Wang and co-workers reported on the results of a computer-aided density functional theory (DFT) study which helped to identify 3-hydroxy pyrones and  $\beta$ -amino ketones as possible zinc-chelators (Wang et al. 2007). Since then, several synthetic approaches afforded a variety of new ZBGs, but none of those are yet featured in clinical candidates. In this context, it is noteworthy that neither structure of a new generation of clinical HDAC6i has yet been disclosed (Zhang et al. 2021).

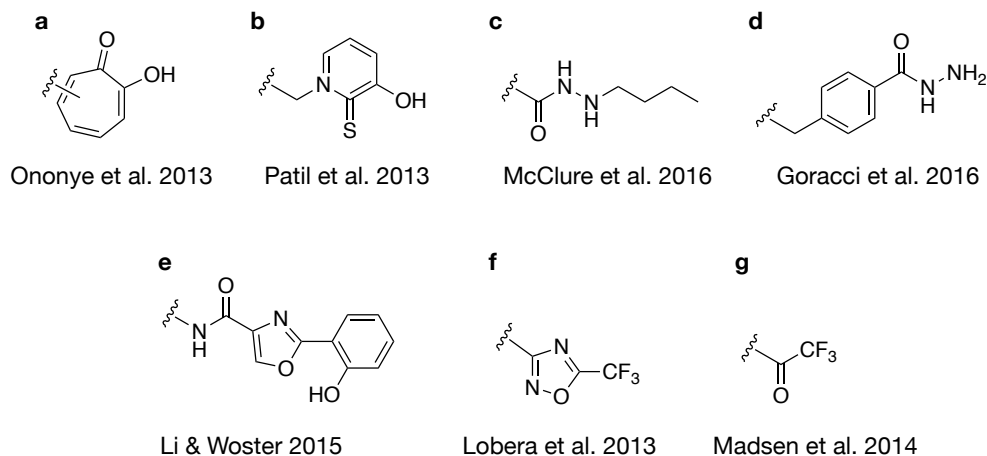


**Figure 5.1.** Examples of novel ZBGs. (a) tropolone group; (b) 3-hydroxypyridin-2-thione group; (c) alkylated benzoyl-hydrazide group; (d) hydrazide group; (e) 2-(oxazole-2-yl)-phenol group; (f) trifluoromethyloxadiazolyl group; (g) trifluoromethyl ketone group.

In a recent review, Zhang and colleagues summarise a number of promising ZBG candidates and highlight that some of the newly discovered motifs appear to be class- or isoform-selective (Figure 5.1; Zhang et al. 2018). Thus, they might be capable of circumventing the limitations to isoform specificity that are predefined by the similar cap group regions of the

enzymes. Examples for such isoform-selective ZBGs include the HDAC2-selective tropolone-derivatives (Ononye et al. 2013), the HDAC6-preferential 3-hydroxypyridin-2-thione group (Patil et al. 2013), and the alkylated benzoyl-hydrazide motif with a particular preference for HDAC3 and other class I HDACs (McClure et al. 2016; Wang et al. 2015). Interestingly, a computational study verified by biological assessment had previously led to the discovery of the same hydrazide motif, though devoid of the alkyl chain, as a promising ZBG with a preference for HDAC6 over isoforms 2, 4, and 8 (Goracci et al. 2016). Another group sought to avoid the aniline-derived toxicity of the *ortho*-aminoanilide group by creating structural mimics and presented the 2-(oxazole-2-yl)-phenol group which displayed moderate inhibition of class I and IIa isoforms (Li & Woster 2015; Zhang et al. 2018).

In addition to heterocycles becoming a common feature in novel ZBGs, there are several candidates containing fluorinated substituents (Figure 5.1). In 2013, Lobera et al. reported on a group of compounds featuring a trifluoromethyloxadiazolyl moiety that displayed excellent selectivity for the class IIa isoforms HDAC4, 5, 7, and 9 (Lobera et al. 2013). A similar ZBG, the 2-(difluoromethyl)-5-(pyrimidin-5-yl)-1,3,4-oxadiazole moiety, was developed by Yates and retained its excellent HDAC6 selectivity in combination with a wide range of cap groups (Yates 2019; see chapter 5.1.4). A comprehensive study undertaken by Olsen and co-workers led to the discovery of the trifluoromethyl ketone (TFMK) group as another fluorinated ZBG for non-selective HDACi (Madsen et al. 2014). However, by comparison with corresponding hydroxamates of the highly potent and HDAC6-selective tubathian series, it became obvious that the TFMK motif is unsuitable for selective HDAC6i (De Vreese et al. 2016; Depetter et al. 2018).

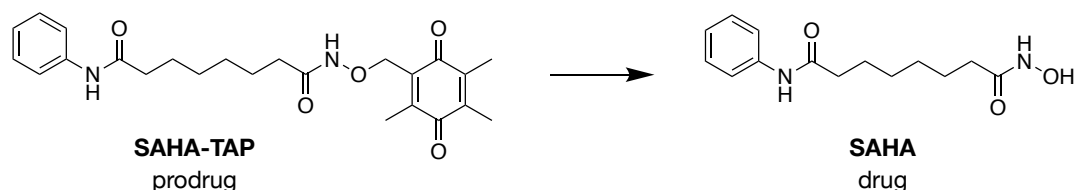
In respect of their chelating properties, new ZBGs are often considered inferior to hydroxamates and *ortho*-aminoanilides and hence, clinical examples are rare. Allowing for improved safety profiles, new ZBGs for HDACi are yet urgently required to widen the scope for clinical application. The design of potent but non-toxic ZBGs therefore remains as one of the key challenges in epigenetic drug discovery.

### 5.1.3 Prodrug concepts for HDAC inhibitors

The disadvantages of hydroxamates as ZBGs may indeed be limited by introducing masking groups to generate prodrugs with improved pharmacokinetic properties. In such cases, the administration of a drug precursor is followed by the partial or complete metabolic release of the active parent drug. One benefit of this method is the chance of increased bioavailability while off-target interactions may be reduced or delayed to a later stage of the metabolic

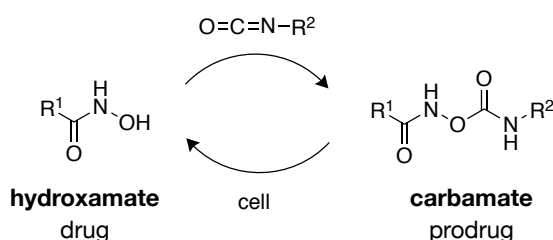


process.



**Scheme 5.2.** SAHA-TAP releases SAHA after activation by glutathione (Daniel et al. 2015).

In 2015, the Cohen group developed SAHA-TAP (thiol activated prodrug). Functioning as a quinone-protected vorinostat analogue, SAHA-TAP releases the drug upon Michael addition of nucleophiles, such as the thiol groups of cysteine residues present in the active sites of all HDACs (Scheme 5.2; Daniel et al. 2015). In addition to improving the plasma stability in comparison to vorinostat, SAHA-TAP offers a dual mode of inhibition through conventional zinc coordination and covalent cysteine modification (Daniel et al. 2015). Another prodrug concept was introduced by Schlimme et al. who discovered carbamates as cell-permeable precursors to hydroxamates (Schlimme et al. 2011). Following their initial studies on thiazole-based inhibitors with a preference for HDAC6, the group confirmed their results using non-selective vorinostat analogues with different carbamate residues and detected potent inhibition by the released hydroxamates as well as the carbamate species (Scheme 5.3; Schlimme et al. 2011; King et al. 2018).



**Scheme 5.3.** Carbamate groups are accessible from the reaction of hydroxamates and isocyanates. Hydrolysis affords the active species (Schlimme et al. 2011; King et al. 2018).

A common disadvantage of HDACi featuring hydroxamates is their limited ability to reach solid tumour sites due to rapid hydrolysis or other metabolic transformations (Flipo et al. 2009; Zheng et al. 2018). Hence, Wang and co-workers designed a belinostat analogue comprising a pinacol-protected *para*-boronate benzyl group which is supposed to be cleaved by hydrogen peroxide present in malignant tissue (Figure 5.2; Zheng et al. 2018). *In*

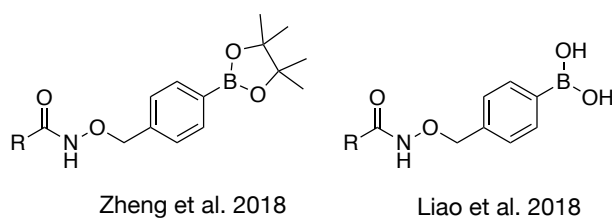
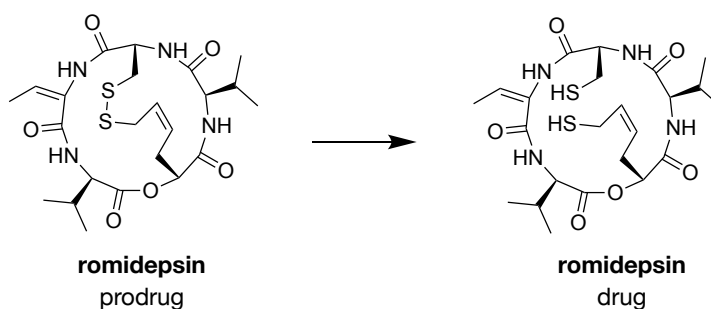


**Figure 5.2.** Promoiety containing pinacol-protected or unmasked boronic acids are suitable for the design of hydroxamate prodrugs.

(Zheng et al. 2018). Another study focused on unprotected aryl boronic acid prodrugs of vorinostat that assume their function after activation by hydrogen peroxide and peroxyxynitrite (Figure 5.2; Liao et al. 2018). Assayed against AML cell lines, the prodrug displayed promising antiproliferative potential and enhanced the efficacy of the antimetabolite cytarabine (Liao et al. 2018).

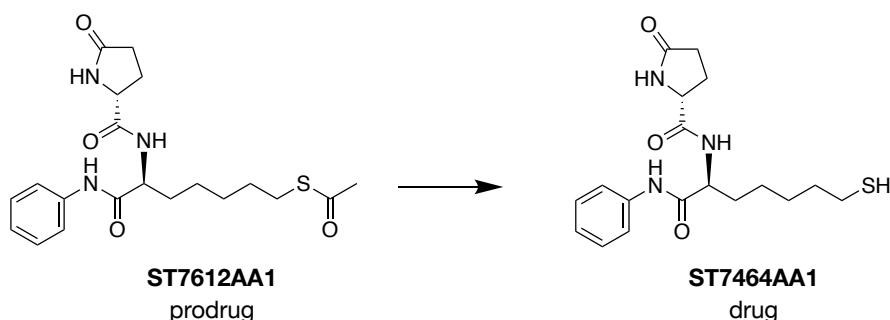
A particularly promising and potent alternative ZBG that has long been considered for the incorporation in HDACi is the thiol motif which is also eligible for prodrug concepts (Suzuki et al. 2004; Suzuki et al. 2006; Segretti et al. 2015). In fact, the FDA-approved drug romidepsin



**Scheme 5.4.** Cleavage of the disulfide bridge in romidepsin generates the active thiol species.

(Scheme 5.4) is administered as a disulfide serving as a prodrug for the thiol analogue which is accessible through reduction by glutathione (Poligone et al. 2011).

Other promoiety for the thiol group that have been reported in the literature include isobutyryl and, predominantly, acetyl groups (Suzuki et al. 2006; Giannini et al. 2014; Vesci et al. 2015). So far, there have been no thiol-based HDACi except romidepsin in clinical trials,



**Scheme 5.5.** Hydrolysis releases the active thiol species from thioacetate prodrugs.

but studies on preclinical stage yielded the thioacetate derivative ST7612AA1 (Scheme 5.5) which was subjected to advanced evaluation (Vesci et al. 2015; Battistuzzi & Giannini 2016).

### 5.1.4 Project outline

In 2019, Yates was granted a patent for his invention of new and highly HDAC6-selective ZBGs (Yates 2019). Bound to a pyrimidine linker, the new ZBGs consist of differently arranged oxadiazole moieties featuring either difluoro- or trifluoromethyl residues (Figure 5.3; Yates 2019). By screening all four ZBG types connected to the same group, Yates discovered that the 2-(difluoromethyl)-1,3,4-oxadiazole-based (DFMO) compound **V-la** exhibited high inhibitory potential for HDAC6 in the low nanomolar concentration range and a more than 1304-fold preference for HDAC6 over HDAC1 (Yates 2019, columns 429/430). The replacement of the difluoromethyl group by a trifluoromethyl residue (**V-lb**) reduced both the HDAC6 inhibition and the selectivity by a factor of nine. Upon switching to the 1,2,4-oxadiazole scaffold (**V-lc**), the inhibitory potential and isoform selectivity diminished altogether (Yates 2019). Inhibition assay results provided for a hydroxamate derivative built on the same scaffold (**V-le**) further indicate that the cap group-linker combination alone enables only moderate HDAC6-preference (SI: > 57; Yates 2019). Thus, it is clear that the high selectivity observed for **V-la** stems from the nature of the DFMO ZBG.

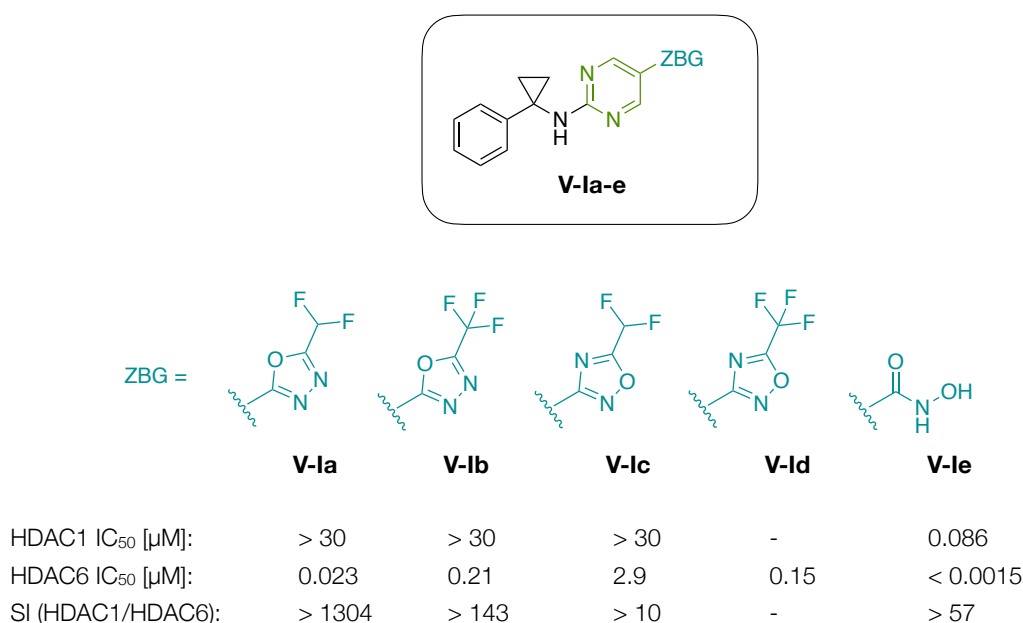
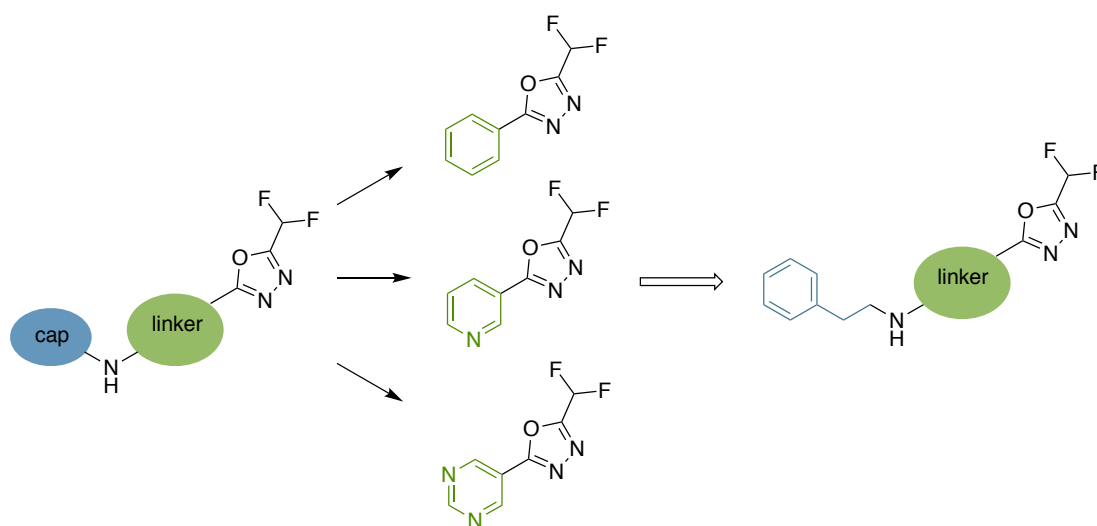


**Figure 5.3.** Inhibition of HDAC1 and HDAC6 by compounds featuring different oxadiazole-based ZBGs (Yates 2019).

On this basis, investigating the design and synthetic feasibility of new HDAC6-selective inhibitors featuring the DMFO motif emerged as a new option. Preliminary studies on drug fragments were supposed to elucidate the effect of phenyl or pyridine linkers in comparison to the pyrimidine unit chosen by Yates. Once identified, the most suitable linker was to be incorporated into a first HDAC6i prototype featuring the new ZBG (Scheme 5.6).

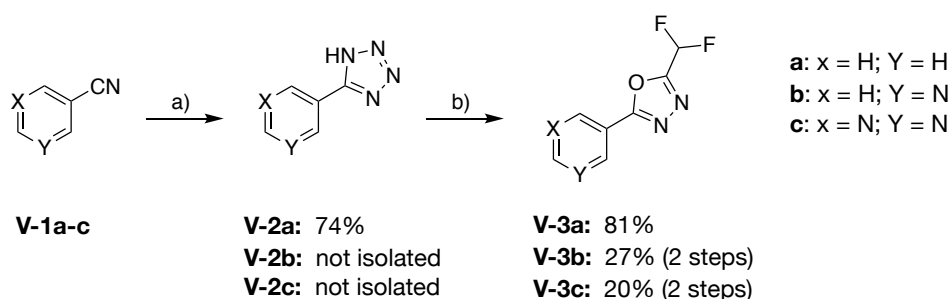


**Scheme 5.6.** Linker variation of HDACi fragments containing the 2-(difluoromethyl)-1,3,4-oxadiazole ZBG.

## 5.2 Results and Discussion

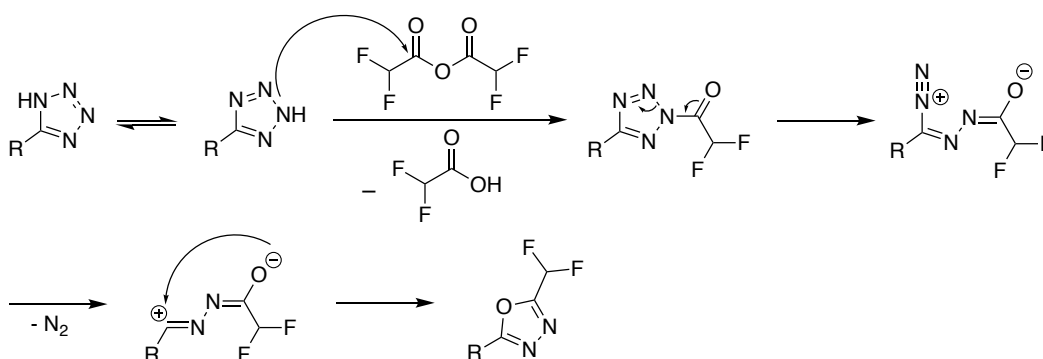
### 5.2.1 Synthesis of (difluoromethyl)-1,3,4-oxadiazole fragments

The synthesis of the three (difluoromethyl)-1,3,4-oxadiazole fragments **V-3a-c** started from commercially available carbonitriles and was based on the protocol provided by Yates (Scheme 5.7; Yates 2019). In the first step, 1,3-dipolar cycloaddition reactions of sodium azide and the respective carbonitriles **V-1a-c** were carried out under microwave conditions to generate the corresponding tetrazole intermediates **V-2a-c**.



**Scheme 5.7.** Synthesis of the fragments **V-3a-c**. Reagents and conditions: a)  $\text{NaN}_3$ ,  $\text{LiCl}$ ,  $\text{NH}_4\text{Cl}$ , DMF, MW, 150 W, 100 °C, 24 h; b) DFAA, DCM, rt, 24 h.

Prone to undergoing tautomerisation, the *2H*-tetrazole intermediates could then be treated with difluoroacetic anhydride (DFAA) to build the desired DFMOs **V-3a-c** (Scheme 5.8) via the Huisgen 1,3,4-oxadiazole synthesis under release of nitrogen (Huisgen et al. 1958; Wang et al. 2019). The resulting phenyl intermediate **V-2a** was easily isolated by aqueous workup, but due to their zwitterionic nature, this method could not be applied to the tetrazoles **V-2b** and



**Scheme 5.8.** Mechanism of the Huisgen 1,3,4-oxadiazole synthesis. Upon tautomerisation, the *2H*-tetrazoles react with acyl derivatives to yield 1,3,4-oxadiazoles.

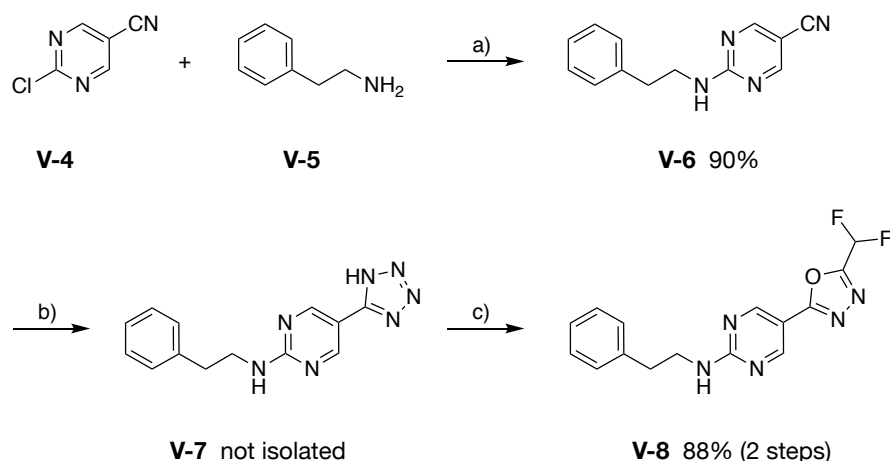
**V-2c**. Instead, they were filtered over a layer of silica in order to remove the inorganic byproducts of the first reaction. The crude products thus obtained were subsequently treated with DFAA. After 24 h of stirring at room temperature, all three fragments **V-3a-c** were afforded in sufficient purities of approximately 95% after aqueous workup.

### 5.2.2 HDAC inhibition of (difluoromethyl)-1,3,4-oxadiazole fragments

Due to the absence of cap groups, low HDAC inhibition was anticipated. Consequently, the percentage of isoform inhibition at a concentration of 100  $\mu\text{M}$  was determined in addition to  $\text{IC}_{50}$  values in biochemical assays. At the given concentration, neither of the three fragments inhibited HDAC1. With regard to HDAC6, the phenyl derivative **V-3a**, which impeded only 10% of HDAC6 activity, turned out to be the weakest inhibitor. The pyridine fragment **V-3b** was significantly more potent and suppressed the HDAC6 activity by approximately one half. With nearly 79% HDAC6 inhibition ( $\text{HDAC6 IC}_{50}$ :  $> 3.33 \mu\text{M}$ ), the pyrimidine motif **V-3c** stood out as the most suitable linker which was to be featured in the full prototype.

### 5.2.3 Synthesis of a (difluoromethyl)-1,3,4-oxadiazole-based HDAC6 inhibitor

For this proof-of-concept approach, an easily accessible phenylethyl group was selected as a model cap group for compound **V-8**. Compared to the examples presented by Yates, **V-8** differs by one methylene group in length and lacks the characteristic cyclopropyl group but shares the phenyl cap group, which is also characteristic for vorinostat. The carbonitrile was synthesised starting from 2-chloropyrimidine-5-carbonitrile (**V-4**) which was subjected to nucleophilic aromatic substitution by phenylethylamine to give **V-6** in 90% yield after recrystallisation (Scheme 5.9). The tetrazole formation was performed according to the aforementioned procedure, but owing to the low yields of the heterocyclic fragments **V-2b** and **V-2c**, the reaction time was extended to 36 h. Following the isolation by filtration over silica, the intermediate **V-7** was not characterised but directly used to build the (difluoromethyl)-1,3,4-oxadiazole **V-8**. Probably resulting from the deactivating properties of the phenylethyl group, TLC monitoring of this reaction indicated a slow conversion so that the reaction was allowed to stir for 96 h. After subsequent aqueous workup and recrystallisation, compound **V-8** was obtained in excellent yield (88% over 2 steps) and sufficient purity  $> 95\%$ . Although seemingly stable in general, the final compound could not be stored as a hydrochloride salt as it turned out to decompose under acidic conditions.



**Scheme 5.9.** Synthesis of the prototype HDAC6i **V-8**. Reagents and conditions: a) DCM, 0 °C, 60 min; b) NaN<sub>3</sub>, LiCl, NH<sub>4</sub>Cl, DMF, MW, 150 W, 100 °C, 36 h; c) DFAA, DCM, rt, 96 h.

### 5.2.4 HDAC inhibition of compound **V-8**

Unlike the fragments analysed in the first step, compound **V-8** was expected to display considerable activity in inhibition experiments so that the IC<sub>50</sub> values in presence of HDAC1 and HDAC6 were determined.<sup>20</sup> Similar to the results reported by Yates, no HDAC1 inhibition (> 30 μM) was detected (Yates 2019). In comparison to the pyrimidine-fragment **V-3c** (HDAC6 IC<sub>50</sub>: > 3.33 μM), the HDAC6 inhibition by **V-8** (1.31 ± 0.09 μM) was remarkably improved but, surprisingly, failed to fall below the micromolar concentration range. Regardless of the fact that the compounds developed by Yates were screened in different inhibition assays, it can thus be concluded that the cyclopropyl group adjacent to the pyrimidine ring is a crucial contributor to HDAC6 inhibition.

<sup>20</sup> HDAC inhibition assays for all compounds were performed by Andrea Schöler in the group of Finn K. Hansen, Leipzig University.

### 5.3 Conclusions

This study aimed to explore the synthetic accessibility of HDAC6i featuring the new ZBG invented by Yates. It succeeded in developing a simple, microwave-assisted protocol that afforded the desired (difluoromethyl)-1,3,4-oxadiazole fragments in sufficient purities without any need for extensive purification. Following the preparation and screening of the fragments **V-3a-c**, a full drug prototype, **V-8**, was designed and synthesised in a three-step procedure that afforded the compound in excellent yield. In biochemical assays, **V-8** exhibited a clear preference for HDAC6 over HDAC1 but since no effort towards cap group optimisation had been made at this stage, the inhibitory activity was yet poor. Although unstable under acidic conditions, DFMOs bring the advantage of being altogether easier to handle than hydroxamates.



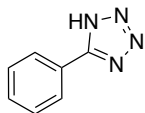
## 5.4 Experimental section

### 5.4.1 General information

Except for DCM, which was purified by distillation prior to use, all reagents and solvents were purchased from commercial sources and used without further purification. TLC was carried out using Macherey-Nagel pre-coated aluminium foil sheets which were visualised using UV light (254 nm).  $^1\text{H}$  NMR and  $^{13}\text{C}$  NMR spectra were recorded at rt using Bruker Avance III HD (400 MHz), and Varian/Agilent Mercury-plus (300 MHz & 400 MHz) spectrometers. Chemical shifts ( $\delta$ ) are quoted in parts per million (ppm). All spectra were standardised in accordance with the signals of the deuterated solvents (DMSO- $d_6$ :  $\delta_{\text{H}} = 2.50$  ppm,  $\delta_{\text{C}} = 39.5$  ppm;  $\text{CDCl}_3$ :  $\delta_{\text{H}} = 7.26$  ppm,  $\delta_{\text{C}} = 77.0$  ppm). Coupling constants ( $J$ ) are reported in Hertz (Hz). Mass spectra were measured by the Leipzig University Mass Spectrometry Service using electrospray ionisation (ESI) on Bruker Daltonics Impact II and Bruker Daltonics micrOTOF spectrometers. The uncorrected melting points were determined using a Barnstead Electrothermal 9100 apparatus. Analytical HPLC analysis were carried out using a Thermo Fisher Scientific UltiMate 3000 system equipped with an UltiMate<sup>TM</sup> HPG-3400SD pump, an UltiMate<sup>TM</sup> 3000 Diode array detector, an UltiMate<sup>TM</sup> 3000 autosampler, and a TCC-3000SD standard thermostatted column compartment by Dionex. The system was operated using a Macherey-Nagel NUCLEODUR 100-5  $\text{C}_{18}$  ec column (250 mm x 4.6 mm). UV absorption was detected at 254 nm with a linear gradient of 5% B to 95% B within 23 min. Acidified HPLC-grade water (0.1% TFA; solvent A) and acidified HPLC-grade acetonitrile (0.1% TFA; solvent B) were used for elution at a flow rate of 1 mL/min. The purity of the final compound was at least 95.0%.

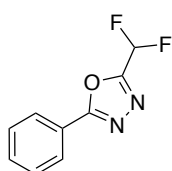
## 5.4.2 Experimental procedures

### 5-Phenyl-1*H*-1,2,3,4-tetrazole (**V-2a**).

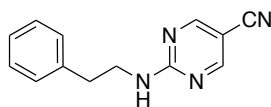


Benzonitrile (206 mg 2.00 mmol, 1.0 eq), NaN<sub>3</sub> (260 mg, 4.00 mmol, 2.0 eq), NH<sub>4</sub>Cl (213 mg, 4.00 mmol, 2.0 eq), and LiCl (66.0 mg, 1.56 mmol, 0.8 eq) were suspended in DMF (2 mL) and the resulting mixture was subjected to microwave irradiation at 150 W and 100 °C under vigorous stirring for 24 h. After evaporation of the solvent, the mixture was dissolved in 1M NaOH (20 mL) and washed with EtOAc (2x 10 mL) to remove excess benzonitrile. The aqueous layer was acidified using 10% HCl (pH 4) and extracted with DCM (3 x 50 mL). The combined organic layers were dried over MgSO<sub>4</sub> and concentrated under reduced pressure during which the product crystallised. The desired product **V-2a** was obtained as a white solid (216 mg, 1.47 mmol, 74%) and used without further purification; <sup>1</sup>H NMR (400 MHz; DMSO-*d*<sub>6</sub>): δ 8.11–7.94 (m, 1H, arom.), 7.70–7.18 (m, 3H, arom., NH) ppm; <sup>13</sup>C NMR (101 MHz; DMSO-*d*<sub>6</sub>): δ 155.3, 131.2, 129.4, 127.0, 124.2 ppm; HRMS (m/z): M<sup>-</sup> calcd for C<sub>7</sub>H<sub>6</sub>N<sub>5</sub> 145.0520, found 145.0523.

### 2-(Difluoromethyl)-5-phenyl-1,3,4-oxadiazole (**V-3a**).

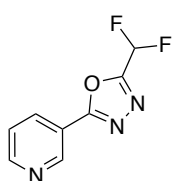


A solution of **V-2a** (180 mg, 1.22 mmol, 1.0 eq) in DCM (18 mL) was cooled to 0 °C and DFAA (0.75 mL, 6.1 mmol, 5.0 eq) was added dropwise. The resulting solution was allowed to warm to rt and stirred for 24 h before water (20 mL) was added. The mixture was extracted with DCM (3 x 30 mL) and the combined organic layers were washed with brine (10 mL) and dried over MgSO<sub>4</sub>. Removal of the solvent under reduced pressure and recrystallisation from EtOAc (2 mL) and petrol (20 mL) afforded the desired product **V-3a** as a white solid (193 mg, 0.98 mmol, 81%); mp 101–105 °C; t<sub>R</sub>: 8.86 min, purity: 94.7%; <sup>1</sup>H NMR (300 MHz, CDCl<sub>3</sub>): δ 8.19–8.07 (m, 2H, arom.), 7.67–7.46 (m, 3H, arom.), 6.92 (t, *J* = 51.7 Hz, 1H, CH) ppm; <sup>13</sup>C NMR (101 MHz, CDCl<sub>3</sub>): δ 166.3, 158.3, 132.91, 129.4, 127.6, 122.8, 108.4, 106.0, 103.6 ppm; HRMS (m/z): MH<sup>+</sup> calcd for C<sub>9</sub>H<sub>6</sub>F<sub>2</sub>N<sub>2</sub>O 197.0521, found 145.0523.

**2-[(2-Phenylethyl)amino]pyrimidine-5-carbonitrile (V-6).**

A solution of 2-chloropyrimidine-5-carbonitrile (558 mg, 4.00 mmol, 1.0 eq) in DCM (16 mL) was cooled to 0 °C and phenylethylamine (968 mg, 8.00 mmol, 2.0 eq) was added dropwise. After stirring at 0 °C for 2 h, the mixture was diluted with DCM and filtered over a layer of silica using DCM/MeOH (9:1) as eluent. The solvent was removed under reduced pressure and the remaining crude product was recrystallised from EtOAc (2 mL) and petrol (20 mL) to afford **V-6** as a white solid (811 mg, 3.61 mmol, 90%); mp 165–167 °C; <sup>1</sup>H NMR (400 MHz, CDCl<sub>3</sub>): δ 8.54 (s, 1H, arom.), 8.36 (s, 1H, arom.), 7.35–7.13 (m, 5H, arom.), 5.84 (br s, 1H, NH), 3.80–3.71 (m, 2H, NH-CH<sub>2</sub>), 2.92 (t, *J* = 6.9 Hz, 2H, Ar-CH<sub>2</sub>) ppm; <sup>13</sup>C NMR (75 MHz, CDCl<sub>3</sub>): δ 161.9, 161.6, 160.8, 138.5, 128.9, 128.9, 126.9, 116.5, 97.1, 42.9, 35.5 ppm; HRMS (*m/z*): M<sup>+</sup> calcd for C<sub>13</sub>H<sub>12</sub>N<sub>4</sub> 225.1135, found 225.1135.

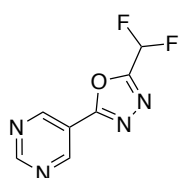
**General procedure for the preparation of compounds V-3b-c and V-8.** The respective heterocyclic carbonitrile (2.00 mmol, 1.0 eq), NaN<sub>3</sub> (260 mg, 4.00 mmol, 2.0 eq), NH<sub>4</sub>Cl (213 mg, 4.00 mmol, 2.0 eq), and LiCl (66.0 mg, 1.56 mmol, 0.8 eq) were suspended in DMF (2 mL) and the resulting mixture was subjected to microwave irradiation at 150 W and 100 °C under vigorous stirring for 24 h (**V-2b** and **V-2c**) or 36 h (**V-7**). The reaction mixture was then filtered over a 5 cm layer of silica using DCM/MeOH (9:1) as eluent until UV light no longer indicated the presence of product. Upon removal of the solvent under reduced pressure, the crude tetrazole was dissolved in DCM (30 mL) and DFAA (1.5 mL, 12.2 mmol, 6.1 eq) was added dropwise at 0 °C. The resulting solution was allowed to warm to rt and stirred for 24 h (**V-3b** and **V-3c**) or 96 h (**V-8**), respectively. After completion of the reaction, the mixture was diluted using DCM (30 mL) and washed with 1M NaOH (2 x 10 mL), water (1x 10 mL), and brine (1x 10 mL). Drying of the organic layer over Na<sub>2</sub>SO<sub>4</sub> and subsequent evaporation of the solvent afforded the desired product.

**3-[5-(Difluoromethyl)-1,3,4-oxadiazol-2-yl]pyridine (V-3b).**

Synthesis according to the general procedure starting from 5-cyanopyrimidine (210 mg) afforded **V-3b** as a white solid (108 mg, 0.54 mmol, 27%); mp 76–78 °C; *t<sub>R</sub>*: 6.63 min, purity: > 99%; <sup>1</sup>H NMR (400 MHz, CDCl<sub>3</sub>): δ 9.37–9.28 (m, 1H, arom.), 8.88–8.78 (m, 1H, arom.), 8.45–8.29 (m, 1H, arom.), 7.55–7.43 (m, 1H, arom.), 6.94 (t, *J* = 51.7 Hz,

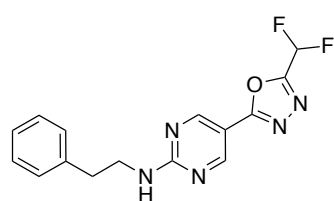
1H, CH) ppm;  $^{13}\text{C}$  NMR (75 MHz,  $\text{CDCl}_3$ ):  $\delta$  164.3, 162.7, 159.1, 158.8, 158.4, 153.5, 148.4, 134.8, 124.1, 119.5, 109.0, 105.8, 102.6 ppm; HRMS (m/z):  $\text{MH}^+$  calcd for  $\text{C}_8\text{H}_5\text{F}_2\text{N}_3\text{O}$  198.0473, found 198.0483.

#### 5-[5-(Difluoromethyl)-1,3,4-oxadiazol-2-yl]pyrimidine (**V-3c**).



Synthesis according to the general procedure starting from nicotinonitrile (208 mg) afforded **V-3c** as a yellow solid (80.0 mg, 0.41 mmol, 20%); mp 104–107 °C;  $t_R$ : 6.59 min, purity: 96.6%;  $^1\text{H}$  NMR (400 MHz,  $\text{CDCl}_3$ ):  $\delta$  9.49–9.40 (m, 3H, arom.), 6.97 (t,  $J = 51.6$  Hz, 1H, CH) ppm;  $^{13}\text{C}$  NMR (75 MHz,  $\text{CDCl}_3$ ):  $\delta$  162.1, 161.5, 159.6, 159.2, 158.8, 155.4, 118.4, 108.9, 105.7, 102.5 ppm; HRMS (m/z):  $\text{MH}^+$  calcd for  $\text{C}_7\text{H}_4\text{F}_2\text{N}_4\text{O}$  199.0426, found 199.0425.

#### 5-[5-(Difluoromethyl)-1,3,4-oxadiazol-2-yl]-N-(2-phenylethyl)pyrimidin-2-amine (**V-8**).



Synthesised according to the general procedure starting from **V-6** (448 mg). Recrystallisation from EtOAc (2mL) and petrol (20 mL) afforded **V-8** as a yellow solid (557 mg, 1.76 mmol, 88%); mp 83–86 °C;  $t_R$ : 9.66 min, purity: 95.2%;  $^1\text{H}$  NMR (400 MHz,  $\text{CDCl}_3$ ):  $\delta$  9.24 (s, 2H, arom.), 7.35–7.12 (m, 6H, arom,  $\text{CDCl}_3$ ), 7.10–6.73 (m, 1H, CH), 4.48–4.37 (m, NH- $\text{CH}_2$ ), 3.03–2.95 (m, 2H, Ar- $\text{CH}_2$ ) ppm;  $^{13}\text{C}$  NMR (75 MHz,  $\text{CDCl}_3$ ):  $\delta$  165.3, 161.9, 161.1, 159.2, 158.8, 158.4, 156.7, 138.1, 129.2, 129.0, 128.9, 128.6, 113.6, 111.2, 108.9, 107.9, 105.7, 104.7, 102.5, 48.2, 34.4 ppm; HRMS (m/z):  $\text{MH}^+$  calcd for  $\text{C}_{15}\text{H}_{13}\text{F}_2\text{N}_5\text{O}$  318.1161, found 318.1173.

## 5.5 References

Battistuzzi G, Giannini G. 2016. Synthesis of ST7612AA1, a novel oral HDAC inhibitor, via radical thioacetic acid addition. *Curr Bioact Compd* **12**: 282–288.

Chou CJ, Herman D, Gottesfeld JM. 2008. Pimelic diphenylamide 106 is a slow, tight-binding inhibitor of class I histone deacetylases. *J Biol Chem* **283**: 35402–35409.

Daniel KB, Sullivan ED, Chen Y, Chan JC, Jennings PA, Fierke CA, Cohen SM. 2015. Dual-mode HDAC prodrug for covalent modification and subsequent inhibitor release. *J Med Chem* **58**: 4812–4821.

Depetter Y, Geurs S, Vanden Bussche F, De Vreese R, Franceus J, Desmet T, De Wever O, D'hooghe M. 2018. Assessment of the trifluoromethyl ketone functionality as an alternative zinc-binding group for selective HDAC6 inhibition. *Med Chem Commun* **9**: 1011–1016.

Flipo M, Charton J, Hocine A, Dassonneville S, Deprez B, Deprez-Poulain R. 2009. Hydroxamates: relationships between structure and plasma stability. *J Med Chem* **52**: 6790–6802.

Giannini G, Vesce L, Battistuzzi G, Vignola D, Milazzo FM, Guglielmi MB, Barbarino M, Santaniello M, Fantò N, Mor M, Rivara S, Pala D, Taddei M, Pisano C, Cabri W. 2014. ST7612AA1, a thioacetate- $\omega$ ( $\gamma$ -lactam carboxamide) derivative selected from a novel generation of oral HDAC inhibitors. *J Med Chem* **57**: 8358–8377.

Goracci L, Deschamps N, Randazzo GM, Petit C, Dos Santos Passos C, Carrupt P-A, Simões-Pires C, Nurisso A. 2016. A rational approach for the identification of non-hydroxamate HDAC6-selective inhibitors. *Sci Rep* **6**: 29086.

Hai Y, Christianson DW. 2016. Histone deacetylase 6 structure and molecular basis of catalysis and inhibition. *Nat Chem Biol* **12**: 741–747.

Ho TCS, Chan AHY, Ganesan A. 2020. Thirty years of HDAC inhibitors: 2020 insight and hindsight. *J Med Chem* **63**: 12460–12484.

Huisgen R, Sauer J, Sturm HJ. 1958. Acylierung 5-substituierter Tetrazole zu 1,3,4-Oxadiazolen. *Angew Chem* **70**: 272–273.

King K, Hauser A-T, Melesina J, Sippl W, Jung M. 2018. Carbamates as potential prodrugs and a new warhead for HDAC inhibition. *Molecules* **23**: 321.

Li Y, Woster PM. 2015. Discovery of a new class of histone deacetylase inhibitors with a novel zinc binding group. *Med Chem Commun* **6**: 613–618.

Liao Y, Xu L, Ou S, Edwards H, Luedtke D, Ge Y, Qin Z. 2018. H<sub>2</sub>O<sub>2</sub>/peroxynitrite-activated hydroxamic acid HDAC inhibitor prodrugs show antileukemic activities against AML cells. *ACS Med Chem Lett* **9**: 635–640.

Lobera M, Madauss KP, Pohlhaus DT, Wright QG, Trocha M, Schmidt DR, Baloglu E, Trump RP, Head MS, Hofmann GA, Murray-Thompson M, Schwartz B, Chakravorty S, Wu Z, Mander PK, Kruidenier L, Reid RA, Burkhart W, Turunen BJ, Rong JX, Wagner C, Moyer MB, Wells C, Hong X, Moore JT, Williams JD, Soler D, Ghosh S, Nolan MA. 2013. Selective class IIa histone deacetylase inhibition via a nonchelating zinc-binding group. *Nat Chem Biol* **9**: 319–325.

Lossen H. 1869. Über die Oxalohydroxamsäure. *Liebigs Ann Chem* **150**: 314–322.

Lossen W. 1872. Über Benzoylderivate des Hydroxylamins. *Liebigs Ann Chem* **161**: 347–362.

Madsen AS, Kristensen HME, Lanz G, Olsen CA. 2014. The effect of various zinc binding groups on inhibition of histone deacetylases 1–11. *ChemMedChem* **9**: 614–626.

McClure JJ, Zhang C, Inks ES, Peterson YK, Li J, Chou CJ. 2016. Development of allosteric hydrazide-containing class I histone deacetylase inhibitors for use in acute myeloid leukaemia. *J Med Chem* **59**: 9942–9959.

Methot JL, Chakravarty PK, Chenard M, Close J, Cruz JC, Dahlberg WK, Fleming J, Hamblett CL, Hamill JE, Harrington P, Harsch A, Heidebrecht R, Hughes B, Jung J, Kenific CM, Kral AM, Meinke PT, Middleton RE, Ozerova N, Sloman DL, Stanton MG, Szewczak AA, Tyagarajan S, Witter DJ, Secrist JP, Miller TA. 2008. Exploration of the internal cavity of histone deacetylase (HDAC) with selective HDAC1/HDAC2 inhibitors (SHI-1:2). *Bioorg Med Chem Lett* **18**: 973–978.

Methot JL, Hoffman DM, Witter DJ, Stanton MG, Harrington P, Hamblett C, Siliphaivanh P, Wilson K, Hubbs J, Heidebrecht R, Kral AM, Ozerova N, Fleming JC, Wang H, Szewczak AA, Middleton RE, Hughes B, Cruz JC, Haines BB, Chenard M, Kenific CM, Harsch A, Secrist JP, Miller TA. 2014. Delayed and prolonged histone hyperacetylation with a selective HDAC1/HDAC2 inhibitor. *ACS Med Chem Lett* **5**: 340–345.

Ononye SN, Van Heyst MD, Oblak EZ, Zhou W, Ammar M, Anderson AC, Wright DL. 2013. Tropolones as lead-like natural products: The development of potent and selective histone deacetylase inhibitors. *ACS Med Chem Lett* **4**: 757–761.

Patil V, Sodji QH, Kornacki JR, Mrksich M, Oyelere AK. 2013. 3-Hydroxypyridin-2-thione as novel zinc binding group for selective histone deacetylase inhibition. *J Med Chem* **56**: 3492–3506.

Poligone B, Lin J, Chung C. 2011. Romidepsin: Evidence for its potential use to manage previously treated cutaneous T cell lymphoma. *Core Evid* **6**: 1–12.

Porter NJ, Mahendran A, Breslow A, Christianson DW. 2017. Unusual zinc-binding mode of HDAC6-selective hydroxamate inhibitors. *PNAS* **114**: 13459–13464.

Porter NJ, Osko JD, Diedrich D, Kurz T, Hooker JM, Hansen FK, Christianson DW. 2018. Histone deacetylase 6-selective inhibitors and the influence of capping groups on hydroxamate-zinc denticity. *J Med Chem* **61**: 8054–8060.

Schlimme S, Hauser A-T, Carafa V, Heinke R, Kannan S, Stolfa DA, Cellamare S, Carotti A, Altucci L, Jung M, Sippl W. 2011. Carbamate prodrug concept for hydroxamate HDAC inhibitors, *ChemMedChem* **6**: 1193–1198.

Segretti MCF, Vallerini GP, Brochier C, Langley B, Wang L, Hancock WW, Kozikowski AP. 2015. Thiol-based potent and selective HDAC6 inhibitors promote tubulin acetylation and T-regulatory cell suppressive function. *ACS Med Chem Lett* **6**: 1156–1161.

Shen S, Kozikowski AP. 2016. Why hydroxamates may not be the best histone deacetylase inhibitors — What some may have forgotten or would rather forget? *ChemMedChem* **11**: 15–21.

Suzuki T, Kouketsu A, Itoh Y, Hisakawa S, Maeda S, Yoshida M, Nakagawa H, Miyata N. 2006. Highly potent and selective histone deacetylase 6 inhibitors designed based on a small-molecular substrate. *J Med Chem* **49**: 4809–4812.

Suzuki T, Kouketsu A, Matsuura A, Kohara A, Ninomiya S, Kohda K, Miyata N. 2004. Thiol-based SAHA analogues as potent histone deacetylase inhibitors. *Bioorg Med Chem Lett* **14**: 3313–3317.

Vesci L, Bernasconi E, Milazzo FM, De Santis R, Gaudio E, Kwee I, Rinaldi A, Pace S, Carollo V, Giannini G, Bertoni F. 2015. Preclinical antitumor activity of ST7612AA1: a new oral thiol-based histone deacetylase (HDAC) inhibitor. *Oncotarget* **6**: 5735–5748.

De Vreese R, Depetter Y, Verhaeghe T, Desmet T, Benoy V, Haeck W, Van Den Bosch L, D'hooghe M. 2016. Synthesis and SAR assessment of novel Tubathian analogs in the pursuit of potent and selective HDAC6 inhibitors. *Org Biomol Chem* **14**: 2537–2549.

Wagner FF, Lundh M, Kaya T, McCarren P, Zhang Y-L, Chattopadhyay S, Gale JP, Galbo T, Fisher SL, Meier BC, Vetere A, Richardson S, Morgan NG, Christensen DP, Gilbert TJ, Hooker, Leroy M, Walpita D, Mandrup-Poulsen T, Wagner BK, Holson EB. 2016. An isochemogenic set of Inhibitors to define the therapeutic potential of histone deacetylases in  $\beta$ -cell protection. *ACS Chem Biol* **11**: 363–374.

Wang CY, Lee LH. 1977. Mutagenicity and antibacterial activity of hydroxamic acids. *Antimicrob Agents Chemother* **11**: 753–755.

Wang D, Helquist P, Wiest O. 2007. Zinc binding in HDAC inhibitors: A DFT study. *J Org Chem* **72**: 5446–5449.

Wang Q, Mgimpatsang KC, Konstantinidou M, Shishkina SV, Dömling A. 2019. 1,3,4-Oxadiazoles by Ugi-Tetrazole and Huisgen Reaction. *Org Lett* **21**: 7320–7323.

Wang Y, Stowe RL, Pinello CE, Tian G, Madoux F, Li D, Zhao LY, Li J-L, Wang Y, Wang Y, Ma H, Hodder P, Roush WR, Liao D. 2015. Identification of histone deacetylase inhibitors with benzoylhydrazide scaffold that selectively inhibit class I histone deacetylases. *Chem Biol* **22**: 273–284.

Yale HL. 1943. The hydroxamic acids. *Chem Rev* **33**: 209–256.

Yates CM, inventor. Selenity Therapeutics (Bermuda), Ltd., assignee. *Metalloenzyme inhibitor compounds*. U.S. Patent US10357493B2. 2019-07-23.

Zhang L, Zhang J, Jiang Q, Zhang L, Song W. 2018. Zinc binding groups for histone deacetylase inhibitors. *J Enzym Inhib Med Chem* **33**: 714–721.

Zhang X-H, Qin-Ma, Wu HP, Khamis MY, Li Y-H, Ma L-Y, Liu H-M. 2021. A Review of progress in histone deacetylase 6 inhibitors research: Structural specificity and functional diversity. *J Med Chem* **64**: 1362–1391.

Zheng S, Guo S, Zhong Q, Zhang C, Liu J, Yang L, Zhang Q, Wang G. 2018. Biocompatible boron-containing prodrugs of belinostat for the potential treatment of solid tumors. *ACS Med Chem Lett* **9**: 149–154.